Development of a Moving Front Kinetic Monte Carlo Algorithm to Simulate Moving Interface Systems

by

Donovan Chaffart

A thesis

presented to the University of Waterloo

in fulfilment of the

thesis requirement for the degree of

Doctor of Philosophy

in

Chemical Engineering

Waterloo, Ontario, Canada, 2023

©Donovan Chaffart 2023

Examining Committee Membership

The following served on the Examination Committee for this thesis. The decision of the Examination Committee was determined by majority vote.

External Examiner	Joseph Kwon Associate Professor, Kenneth R. Hall Career Development Professor Artie McFerrin Department of Chemical Engineering Texas A&M University
Supervisor	Luis Ricardez-Sandoval Associate Professor Department of Chemical Engineering University of Waterloo
Internal-External Examiner	Sushanta Mitra Executive Director, Professor Department of Mechanical and Mechatronics Engineering University of Waterloo
Internal Examiner	Eric Croiset Professor Department of Chemical Engineering University of Waterloo
	Boxin Zhao University of Waterloo Endowed Chair in Nanotechnology, Professor Department of Chemical Engineering University of Waterloo

Author's Declaration

I hereby declare that I authored or co-authored all of the material within this thesis; please see the Statement of Contributions included in the thesis. This is a true copy of the thesis, including any required final revisions, as accepted by my examiners.

I understand that my thesis may be made electronically available to the public.

Statement of Contributions

The text presented within this thesis was entirely written by me. My work was supervised by Prof. Ricardez-Sandoval, who provided insights and suggestions to help further clarify the text. The results of Chapters 1, 2, and 8 were entirely written by myself under the guidance of Dr. Luis Ricardez-Sandoval, and their contents are not written for publication. The remaining chapters were written based on four manuscripts, whose content was written solely by me, written for publication. These works were further supervised by Dr. Luis Ricardez-Sandoval.

In addition to the above information, I furthermore received the following aid within my manuscript:

Chapter 5: The contents of this chapter were solely written by myself, under the supervision of Dr. Luis Ricardez-Sandoval. I furthermore received suggestions and revisions from Dr. Cunjing Lv, Dr. Songlin Shi, and Chen Ma, whose suggestions helped hone the text and eliminate confusion.

Chapter 6: The contents of this chapters were solely written by myself, under the direction of my supervisor Dr. Luis Ricardez-Sandoval. Furthermore, I was the sole contributor to the modelling, simulations, and mathematical modelling aspects of these works. However, the experimental studies reported within this chapter were performed by Dr. Songlin Shi and Chen Ma under the supervision of Dr. Cunjing Lv, who are reported as co-authors for the papers published based on the contents this chapter. They additionally provided feedback and comments that helped revise this chapter.

Abstract

Moving interfaces play vital and crucial roles in a wide variety of different natural, technological, and industrial processes, including solids dissolution, capillary action, sessile droplet spreading, and superhydrophobicity. In each of these systems, the fundamental process behaviour is entirely dependent on the interface and on the underlying physics governing its movement. As a result, there is significant interest in studying and developing models to capture the behaviour of these moving interface systems over a wide variety of different applications. However, the simulation techniques used to model moving interfaces are limited in their application, as the molecular-level models are unable to simulate interface behaviour over large spatial and temporal scales, whereas the large-scale modeling techniques cannot account for the nanoscale processes that govern the interface behaviour or the molecular-scale fluctuations and deviations in the interface. Furthermore, methods developed to bridge the gap between the two scales are prone to error-induced force imbalances at the interface that can result in fictitious behaviour.

In order to overcome these challenges, this study developed a novel kinetic Monte Carlo (kMC)-based modelling technique referred to as Moving Front kMC (MFkMC) to adequately and efficiently capture the molecular-scale events and forces governing the moving interface behaviour over large length and timescales. This framework was designed to capture the movement of transiently-varying interfaces in a kinetic-like manner so that its movement can be described using Monte Carlo sampling. The MFkMC algorithm accomplishes this task by evaluating the behaviour of the interfacial molecules and assigning kinetic Monte Carlo-style rate equations that describe the transition probability that a molecule would advance into the neighbouring phase, displacing an interfacial molecule from the opposing phase and thus changing the interface. The proposed algorithm was subsequently used to capture the moving interface behaviour within crystal dissolution, capillary rise, and sessile droplet spreading on both smooth and superhydrophobic surfaces. The individual system models for each application were used to analyze the behaviour within each application and to tackle challenges within each field.

The MFkMC modelling method was initially used to capture crystal dissolution for applications in pharmaceutical drug delivery. The developed model was designed to predict the dissolution of a wide variety of crystalline minerals, regardless of their composition and crystal structure. The MFkMC approach was compared against a standard kMC model of the same system to validate the MFkMC approach and highlight its advantages and limitations. The proposed framework was used to explore ways of enhancing crystal dissolution processes by assessing the variability from environmental uncertainties and by performing robust optimization to improve the dissolution performance. The approach was used to simulate calcium carbonate dissolution within the human gastrointestinal system. Polynomial chaos expansions (PCEs) were used to propagate the parametric uncertainty through the kMC model. Robust optimization was subsequently

performed to determine the crystal design parameters that achieve target dissolution specifications using low-order PCE coefficient models (LPCMs). The results showcased the applicability of the kMC crystal dissolution model and the need to account for dissolution uncertainty within key biological applications.

The MFkMC approach was additionally used to capture capillary rise in cavities of different shapes. The proposed model was adapted to capture the movement of a fluid-fluid interface, such as the moving interface present in capillary action studies, using kMC type approaches based on the forces acting locally upon the interface. The proposed force balance-based MFkMC (FB-MFkMC) expressions were subsequently coupled with capillary action force balance equations to capture capillary rise within any axisymmetric cavity. The developed model was validated against known analytical models that capture capillary rise dynamics in perfect cylinders. Furthermore, the resulting multiscale model was used to analyze capillary rise within axisymmetric cavities of irregular shape and in cylinders subject to surface roughness. These studies highlighted that the FB-MFkMC algorithm can capture the macroscale behaviour of a system subject to molecular-level irregularities such as surface roughness. Furthermore, they highlighted that phenomena such as roughness can significantly affect moving interface behaviour and highlight the need to accommodate for these phenomena.

MFkMC was furthermore extended to capture sessile droplet spreading on a smooth surface. The developed approach adapted the capillary action FB-MFkMC model to capture the spreading behaviour of a droplet based on the force balance acting upon the droplet interface, which was developed using analytical inertial and capillary expressions from the literature. This study furthermore derived a new semi-empirical expression to depict the viscous damping force acting on the droplet. The developed viscous force term depends on a fitted parameter c, whose value was observed to vary solely depending on the droplet liquid as captured predominantly by the droplet Ohnesorge number. The proposed approach was subsequently validated using data obtained both from conducted experiments and from the literature to support the robustness of the framework. The predictive capabilities of the developed model were further inspected to provide insights on the sessile droplet system behaviour.

The developed FB-MFkMC model was additionally modified to capture sessile droplet spreading on pillared superhydrophobic surfaces (SHSs). These adjustments included developing the Periodic Unit (PU) method of capturing periodic SHS pillar arrays and accommodating for the changes necessary to capture the droplet spreading behaviour across the gaps between the pillars (i.e., Cassie mode wetting). The proposed SHS-based FB-MFkMC (SHS-MFkMC) model was furthermore adapted to accommodate for spontaneous Cassie-to-Wenzel (C2W) droplet transitions on the solid surface. The capabilities of the full SHS-MFkMC model to capture both radial sessile droplet spread and spontaneous C2W transitions were compared to experimental results from within the literature. Furthermore, a sensitivity analysis was conducted to assess the effects of the various system parameters on the model performance and compare them with the expected system results.

Acknowledgements

I would like to express the upmost sincere gratitude to my advisor, Dr. Luis Ricardez-Sandoval, for his invaluable support and guidance in helping me complete my PhD. His keen insights, constant support, and diligent feedback were immensely pivotal in helping me attain this significant milestone. Without his help and support, it is unlikely that I would have even embarked upon this journey toward my PhD, and I certainly could not have made it this far without him. Furthermore, I want to thank him specifically for encouraging me to pursue this degree in the first place. Without his guidance, I would have never discovered my love for academic research, nor would I have determined my ambitions to continue pursuing a career in academia. Furthermore, if it was not for him, I would have never met the love of my life, my beautiful wife Yue. Luis, working with you has completely changed my life for the better and I cannot thank you enough for all your help and support.

I would also like to give my sincerest of thanks to my research committee, to Dr. Kwon, Dr. Mitra, Dr. Croiset, and Dr. Zhao. Thank you so much for all feedback and guidance you provided me throughout my degree, and for providing me with a fair committee during my comprehensive exam and my thesis defense.

Furthermore, I would like to sincerely thank Dr. Cunjing Lv, his former student Dr. Songlin Shi, and his current student Ma Chen at Tsinghua University for all the help and assistance provided over the years as I worked towards my degree, and in particular for providing me with the experimental data used throughout my PhD research in order to validate my sessile droplet models. Their help was invaluable for helping me advance my knowledge in moving interface applications, and in particular with sessile droplet spread on smooth and superhydrophobic surfaces. I could not have made as much progress as I did without their help, support, advice, feedback, and results. 吕老师，非常感谢您！ 史松林和马晨，非常感谢你们!

I would also like to sincerely thank Prof. Jesse Zhu for all his amazing help, support, guidance, and encouragement over the past year. It has been an absolute honour to discuss my research ideas with him, and I could not have made it this far without his invaluable support. 非常感谢您，祝老师！ Furthermore, thank you so much for taking in Yue and providing her with the postdoctoral opportunity that allowed her to be here with me during this most critical time of my life.

In addition, I would like to thank the rest of my research group, past and present, for the constant, invaluable support, care, and friendship. We have all been through a lot over the last several years, we have gone through a pandemic, we have suffered losses, and we have all struggled to progress in our research. Yet in the end, we are all overcoming each and every challenge life (and Luis) has thrown at us over the course of this degree! I would especially like to thank my friends Yue Yuan, Huabei You, Mahshad Valipour, Han Wang, Yael Valdez, Oscar Flores, Piyush Agarwal, Kavitha Menon, Yanshuo Peng, Mina Rafiei, Grigoriy Kimaev, Gabriel Patron, and everyone else within this awesome group and beyond, for everything.

I would like to also thank my parents, Rob and Lynona Chaffart, my brother Darien and his wife Kim, my beloved deceased Grams, Wynona Gordon, my amazing in-laws Shizhong Yuan and Tao Ma, my uncle and aunt Al and Marion Gordon, my cousin Trent and his family, and everyone else from my amazing extended family who have been there for

me every step of the way throughout this wild ride that was my PhD. I could not have done any of this without your amazing help and support throughout the years. You all are amazing, and I am blessed to have you all in my life.

I would also like to thank my grandparents who did not live to see me begin my PhD adventure, to my Bopa, Albert Gordon, and my Belgian Grandpa and Marraine, Jimmy and Regine Chaffart, in addition to my Grams, Wynona Gordon, who was there at the start of my degree and who offered great encouragement and support before her passing. I know you all are celebrating with me in achieving this milestone, and I want to thank you all for all the love and support throughout the years. Thank you, Grams, for always being there and encouraging me throughout my degree. As much as I wish you could be here in person to attend my graduation, and as much as I know you would have wanted to attend, I bet you're glad you don't have to sit through that ceremony for a third time! And Bopa, thank you so much for inspiring in me a passion for discovery and learning, for designing and engineering. If it wasn't for you, I don't know if I would have ever been so keen to set off on this journey as an engineer! Marraine, tu as toujours été là pour moi de loin et pour me montrer ton amour malgré que tu habitasses en Belgique. Je me suis toujours réjoui de te rendre visite, je sais que tu es fière de moi ! Merci beaucoup pour tout ton aide, pour toujours être là pour moi. Et Grandpa, je n'ai pas pu avoir beaucoup de temps de te connaitre, mais je savais toujours que tu m'aimais et que tu étais fière de moi ! Je suis toujours fière de mon héritage belge et français, et je vais montrer à tout le monde ce que les Belges peuvent accomplir ! Merci beaucoup pour tout.

I would especially like to give thanks to my amazing and beautiful wife, Yue Yuan, for all her constant support, help, encouragement, and ideas over the course of my degree. I never knew that by starting this degree, I would find someone so perfect for me, someone who would not only gladly listen to my research ideas but would understand them and provide insightful comments in return. I cannot wait to spend the rest of my life with her, as we continue to grow our family and our careers together. 我非常爱你，我的最美的太太, xi nav ji eit！ Ma petite pêche mignonne, 非常感谢你!

I would furthermore like to thank all my friends outside of my research group, for all the invaluable help and support and comfort over the years. Ryan Stewart, you are like a brother to me, I seriously could not have handled all the chaos that has happened over the past several years, both from my degree and from the general turbulence of life, without your constant friendship and support. You are my nakama and my brother, and I cannot wait to see what adventures we will encounter next! Furthermore, I cannot wait until your Skygarde adventures get published! I also would like to sincerely thank my closest and dearest friends, my sisters Emily Boyce and Alysha McCann, Matt Haynes, Michelle Furneaux, Bryce Robson, Jeff McCauley, and everyone else. You all rock, and I would not have made it this far without you. Additionally, I would like to thank Lyn Chaffart and Ryan Stewart for taking the time to proofread this thesis. Your help was most invaluable to me.

Finally, and most importantly, I would like to thank Jesus Christ for giving me the motivation, creativity, encouragement, strength, and energy needed to get through my PhD, and for placing such amazing people in my life over the past several years.

Dedication

Dedicated to Wynona Gordon, my dearest grandmother who supported me wholeheartedly throughout my degree but who sadly passed away before my graduation.

I love you and I miss you a lot.

Table of Contents

List of Figures

List of Tables

List of Abbreviations

BCC	Body Centered Cubic
C2W	Cassie-to-Wenzel
CAH	Contact Angle Hysteresis
CFD	Computational Fluid Dynamics
FB-MFkMC	Force Balance-based Moving Front kinetic Monte Carlo
kMC	Kinetic Monte Carlo
LB	Lattice Boltzmann
LPCM	Low-order PCE Coefficient Model
MC	Monte Carlo
MD	Molecular Dynamics
MFkMC	Moving Front kinetic Monte Carlo
NISP	Non-Intrusive Spectral Projection
PCE	Polynomial Chaos Expansion
PDE	Partial Differential Equation
PDF	Probability Distribution Function
PRMSE	Percent Root Mean Squared Error
PU	Periodic Unit
SHS	Superhydrophobic Surface
SHS-MFkMC	Moving Front kinetic Monte Carlo for Superhydrophobic Surfaces
TLK	Terrace Ledge Kink model
W2C	Wenzel-to-Cassie

List of Symbols

Latin Symbols

$\measuredangle$	crystal shape
A	surface area, (mm^2)
$\mathcal{A}$	ratio of capillary forces to viscous forces in the Lucas-Washburn capillary rise equation, (m^2/s)
a	PCE coefficient
a	fitted constant term in the modified Hoerl equation
a_{ca}	empirical fitting parameter for cylindrical approximation of inertial force added in to prevent asymptoting, (m)
a_p	SHS pillar length, (μm)
$\boldsymbol{a}_{\boldsymbol{\chi}}(t_m)$	vector of χ^{th}-order PCE coefficients for a model observable $\boldsymbol{\Psi}(t_m)$ at a discretized time point t_m
$\mathcal{B}$	ratio of gravity forces to viscous forces in the Lucas-Washburn capillary rise equation, (m/s)
$\boldsymbol{b}$	vector of LPCM coefficients for a given LPCM
b	fitted exponential term in the modified Hoerl equation
b_p	SHS interpillar gap distance, (μm)
b_ι	ι^{th} LPCM coefficient for a given LPCM
$\boldsymbol{b}_{\chi}^{\mathbf{H}}(\boldsymbol{\Xi}_{\mathbf{H}})$	vector of χ^{th}-order polynomial basis functions orthogonal to the uncertain parameters **H** as a function of $\boldsymbol{\Xi}_{\mathbf{H}}$
Ca	dimensionless Capillary number
CPU	CPU cost
C_m	concentration of crystal precursor species in the surrounding fluid phase, (mol)
c	empirical dimensionless viscous damping parameter derived for the viscous damping force within a sessile droplet
d, d_1, d_2	general numbers

d_{VLV}	distance between a droplet VLV interface site and the nearest droplet-contacted pillar edge for sessile droplet spreading on an SHS, (mm)
E	activation energy of dissolution for a bond between two neighbouring ions in a $CaCO_3$ crystal, (eV)
F	probability distribution function
$\mathcal{F}$	collection of non-acceleration terms within the inertial force term of a sessile droplet, (kg)
$F^{-1}\left(\Pi\middle\vert\boldsymbol{\Psi}(\alpha_{cf}\vert t_m)\right)$	inverse cumulative distribution function of a model output $\boldsymbol{\Psi}(t_m)$ at a discretized time point t_m evaluated at a probability Π for a given confidence α_{cf}
$\vec{F}$	capillary force acting upon an interface, (N)
f	local force per unit length acting on a triple contact line interface site, (N/m)
$\not{f}$	fraction of the bottom surface of a sessile droplet in the Cassie state on a superhydrophobic surface that is in contact with the solid surface
g	acceleration due to gravity at the Earth's surface, (m/s^2)
H	height of a feature (capillary rise cavity segment, SHS pillar, sessile droplet etc.), (mm)
$He_\chi(\boldsymbol{\Xi}_\mathbf{H})$	χ^{th}-order Hermite polynomial for a vector of randomly-generated realizations with standard properties $\boldsymbol{\Xi}_\mathbf{H}$ dependent upon **H** for predicting output uncertainty distributions using PCE
h	rise height/drop of a fluid undergoing capillary action within a cavity, (mm)
$\not{h}_{release}$	release height of a droplet over-top of a solid surface
$\not{h}_{sag}$	sag height of a sessile droplet VLV interface site spreading between two pillars on an SHS, (nm)
I	number of interface sites i within a MFkMC/standard kMC system at any time t
$\mathcal{I}$	number of uncertain parameters $\eta_i \in \mathbf{H}$ for a system
$\mathcal{J}$	number of model outputs $\psi_j \in \boldsymbol{\Psi}$ for a system
K	number of non-moving interface events $\epsilon_{misc,k,i}$ accommodated in a moving interface system by the MFkMC algorithm
k'	pre-exponential rate constant for the movement of a triple contact interface, (s^{-1})

k_0	pre-exponential factor for the rate of crystal dissolution $W_{\boldsymbol{n},\boldsymbol{\Theta_n}}$, ($s^{-1}$)
k_b	Boltzmann constant, (eV/K)
L_{norm}	normalized distance from the utopia point for the bi-objective crystal dissolution optimization problem
l	length of a crystal edge or a PU, (Å)
ℓ	characteristic length of a system, (m)
$\ell^{\mathcal{p}}$-norm	$\mathcal{p}^{\text{th}}$ order norm, for use as the objective function in bi-objective optimization
M	number of discretized time points where the model outputs $\boldsymbol{\Psi}$ are analyzed under uncertainty
$Memory$	memory allocation requirements of a modelling method
m	mass, (kg)
N_v	number of discretization points used to sub-divide a design parameter ω_v for a given system
$\mathcal{N}(\overline{\mathcal{N}}, \sigma_{\mathcal{N}}^2)$	normal distribution with mean $\overline{\mathcal{N}}$ and variance $\sigma_{\mathcal{N}}^2$
$\widehat{\boldsymbol{n}}$	surface normal vector
n	number of datapoints measured from experimental results
n_{bd}	number of bonds shared between a molecule and its nearest neighbours
$\boldsymbol{n_{bd}}$	vector of number of bonds $n_{bd,\upsilon}$ between a particle and its neighbours in the υ^{th} direction; $\boldsymbol{n_{bd}} = [n_1 \dots n_\upsilon \dots n_\Upsilon]$
$n_d(t_m)$	number of molecules remaining within a dissolving crystal at a discretized time point t_m
n_v	discretized point of the v^{th} process design condition ω_v for a given system
Oh	dimensionless Ohnesourge number
$o(\delta\tau)$	probability that more than one event ϵ will occur over the vanishingly-small time interval $\delta\tau$
P	probability

$P(\delta t, \epsilon)$	probability that an event ϵ will occur at time $t + \delta t$, given the current system state at time t
$P_{cont}(\delta t)$	continuous probability that any event ϵ_i will occur at time $t + \delta t$, given the current system state at time t
$P_{disc}(\epsilon_i \mid \delta t)$	discrete probability that the next event to occur will be ϵ_i specifically, given that the event will occur at time $t + \delta t$
$P_0(\delta t)$	probability, given the current system state at time t, that no event will occur between time t and time $t + \delta t$
q	size of a single atom defect for surface roughness
R	radius, (mm); radial cylindrical coordinate
$\mathcal{R}$	radial cylindrical coordinate
Re	dimensionless Reynolds number
$r_d(t_m)$	crystal dissolution rate at a discretized time point t_m
$\boldsymbol{S_v}$	viscous stress tensor, (N/m^2)
s	crystal size, (number of particles)
T	temperature, (K, ^oC)
t	system time, (s)
t_d	total time required for a crystal to completely dissolve, (s)
t_f	stopping time for the MFkMC algorithm, (s)
u	fluid velocity, (m/s)
$\boldsymbol{u}$	fluid velocity vector, (m/s)
V	volume, (m^3)
V_{Rs}	volume accommodation term in the semi-empirical viscous damping force expression for sessile droplets, derived based on the radius of the droplet as a perfect sphere, (mm)
v	velocity of an interface site, (m/s)
v_0	initial local velocity of an interface site, (m/s)
$\mathcal{v}$	characteristic velocity of a system, (m/s)

$\mathcal{W}$	Lambert W function
W	rate equation, (s^{-1})
We	dimensionless Weber number
w_{pareto}	weighted term for determining the pareto front
w_{SHS}	ratio of the surface area of a sessile droplet in contact with the solid surface to the surface area of the bottom side of a sessile droplet
w	fitted power term in the modified Hoerl equation
$\boldsymbol{x}$	vector of spatial coordinates for a given point
x	cartesian x-axis coordinate
$x_{0,\Delta}$	initial crystal size guess for crystal dissolution optimization for a crystal of shape Δ
y	cartesian y-axis coordinate
y_{Δ}	binary variable to represent the discrete nature of the crystal shape Δ when performing optimization; $y_{\Delta} = 1$ for the selected Δ and $y_{\Delta} = 0$ for all other Δ
$\eth$	axial cylindrical coordinate

Greek Symbols

α_{cf}	confidence level for the probabilistic bounds
β_s	local angle of a cavity wall relative to a horizontal surface for capillary action, (°)
$\Gamma(\boldsymbol{x}, t)$	an interface at spatial coordinates $\boldsymbol{x}$ and at time t
γ	interfacial (surface) tension, (N/m)
$\boldsymbol{\Delta}$	vector of considered crystal shapes for crystal dissolution
ΔE	correction activation energy/stabilization energy to accommodate for crystal surface particles dependent on their coordination number, (eV)
$\Delta\mu_{cp}$	difference in chemical potential between the crystal precursor species and the solid crystal, (eV)
$\Delta\omega_v$	distance between each discretized point used to sub-divide a design parameter ω_v for a given system

δR	molecular-level surface roughness within a cavity for capillary rise action, (nm)
δt	stochastically-determined kMC time interval
$\delta \tau$	vanishingly-small time interval describing the probability that an event ϵ will take place between time $t + \delta t$ and time $t + \delta t + \delta \tau$
$\delta \Omega$	interface of a volume of fluid
ϵ	kMC/MFkMC event
ζ	surface roughness, (μm)
$\mathbf{H}$	vector of uncertain parameters for a system
η_i	value of the i^{th} uncertain parameter
$\boldsymbol{\Theta}_{\boldsymbol{n_{bd}}}$	angle orientation configuration for a particle with $\boldsymbol{n_{bd}}$ nearest neighbour configuration
θ	contact angle of a fluid droplet interface point, (°)
θ_{wall}	contact angle between droplet sag and a pillar wall on an SHS, (°)
ϑ	interaxial angle for a pristine crystal, where $\vartheta \in \{\vartheta_\alpha, \vartheta_\beta, \vartheta_\gamma\}$, (°)
κ^{-1}	capillary length; ratio between a fluid's capillary and gravity forces, (μm)
λ	spatial discretization and step size parameter for fluid-fluid interface movement, (m)
μ	viscosity, (Pa s)
N	number of process design conditions under which a PCE model is developed for a given system
$\boldsymbol{\Xi}_{\mathbf{H}}$	vector of randomly-generated realizations with standard properties dependent upon **H** for predicting output uncertainty distributions using PCE
ξ	random number
ξ_{cont}	random number generated from a uniform distribution used to calculate the MFkMC time interval δt
ξ_{disc}	random number generated from a uniform distribution used to select the discrete event ϵ_i that will take place using MFkMC

Π	probability at which the inverse cumulative distribution function $F^{-1}\left(\Pi\middle\|\boldsymbol{\Psi}^{\varsigma}\left(\alpha_{cf}\middle\|t_m\right)\right)$ is evaluated
ρ	density, (kg/m^3)
ς	line tension of the triple contact line in a solid/fluid/atmosphere interface system, (pN)
σ^2	variance
φ_{lsm}	implicit boundary surface of the level set method
φ_p	SHS pillar base angle, (°)
ϕ	azimuthal angle in polar and cylindrical coordinates
$\boldsymbol{\Psi}$	vector of model outputs for a system
$\psi_j(t_m)$	j^{th} model output for a system at a given discretized time point t_m
$\boldsymbol{\omega}$	vector of design conditions under which a PCE model is developed
ω_v	v^{th} process design condition under which a PCE model is developed

Subscripts and Superscripts

$\vartriangle$	crystal shape
a	acute interaxial angle marker for a pristine crystal
aaa	acute-acute-acute interaxial angle marker for a kink ($n_{b,tot} = 3$) crystal particle
$\vec{a}$	primary axis of a pristine crystal
adv	advancing
ai	property of an atmosphere interface time
avg	parameter modified to prevent phantom pinning
b	pertaining to the base of an SHS structure
$\vec{b}$	secondary axis of a pristine crystal
bd	pertaining to the solid-solid bonds of a solid surface particle
$\vec{c}$	tertiary axis of a pristine crystal
ca	cylindrical approximation

cap	capillary
cb	Cassie state
cf	confidence
$cone$	conical geometry parameter
$cont$	continuous probabilities and parameters
cp	chemical potential
cr	capillary rise/capillary action
$cube$	cubic (rhombohedral) crystal parameter
cyl	cylindrical geometry parameter
cw	Cassie wetting
d	dissolution
db	bottom surface of a sessile droplet
di	property of a droplet interface time
$disc$	discrete probabilities and parameters
$dode$	dodecahedral crystal parameter
$drop$	droplet
E	property applied to the activation energy of dissolution
e	equilibrium (intrinsic)
eq	equivalent
exp	experimental
f	final
fc	accommodating for impossible droplet spreading in non-radial directions and the formation of satellite droplets
g	gravity
$\mathcal{I}$	total number of uncertain parameters **H**
i	site index number for the skMC and MFkMC algorithms
$\dot{\imath}$	index number for a system's uncertain parameters **H**

$impact$	vertical impact
int	interpolated
$inta$	inertia
j	index for a bulk phase molecule advancing into a given interface site for MFkMC
$\not{j}$	index for time points measured from experimental results
j_i	index for the nearest neighbours to a given site i
k	index for non-moving interface events
l	lower probabilistic bound
low	lower
lsm	level set method parameter
lv	fluid-atmosphere (liquid-vapour) property
$l_{\vec{a}}$	pertaining to the primary axis length of a pristine crystal
$l_{\vec{b}}$	pertaining to the secondary axis length of a pristine crystal
$l_{\vec{c}}$	pertaining to the tertiary axis length of a pristine crystal
$MFkMC$	measure of MFkMC algorithm performance
m	index number for the discretized time points
max	pertaining to the *MaxTime* optimization study
$maximum$	maximum value
mf	MFkMC events pertaining to the movement of an interface
min	pertaining to the *minVar* optimization study
$minimum$	minimum value
$misc$	MFkMC events pertaining to non-interfacial movement events
mol	molar
n_ν	discretized point index of the ν^{th} process design condition ω_ν for a given system
$\boldsymbol{n_{bd}}$	parameter for a surface particle with $n_{b,\upsilon}$ number of bonds between itself and its nearest neighbours in the υ^{th} direction
na	property of a parameter before it is modified to accommodate for phantom pinning

nc	property that does not accommodate for unphysical droplet spreading deviations
$norm$	normalized
o	obtuse interaxial angle marker for a pristine crystal
ooa	obtuse-obtuse-acute interaxial angle marker for a kink ($n_{b,tot} = 3$) crystal particle
ord	accommodating for unphysical droplet radius deviations
PU	property of a periodic unit
$PUint$	parameter value inside a periodic unit
p	property of an SHS pillar
$\mathscr{p}$	$\mathscr{p}^{\text{th}}$ order term, used to determine the norm objective functions for optimization
p, b	property at the base of an SHS pillar
p, t	property at the top of an SHS pillar
pin	property of a receding fluid interface pinned along the edge of an SHS pillar
$pareto$	parameter for determining the pareto front
$prev$	parameter value at the previous timestep $t - \delta t$
ps	perfect sphere projected onto the spherical cap formed by a droplet
q	index for selecting an event to occur according to kMC
Rs	volume accommodation term
$\mathcal{R}$	radial cylindrical component of a vector quantity
$\mathcal{R}_i$	i^{th} radial cylindrical coordinate
rec	receding
SHS	parameter pertaining to the solid-fluid contact on an SHS
s	property pertaining to solid and roughness structures
sag	property pertaining to the sag of a VLV between SHS pillars
$sdbi$	bottom surface of a sessile droplet in contact with a solid surface
$skMC$	measure of standard kMC algorithm performance
sl	solid-fluid (solid-liquid) property
$sphere$	spherical crystal parameter, spherical cavity geometry parameter

$step$	property related to the step site of an etch pit
sv	solid-atmosphere (solid-vapour) property
T	parameter pertaining to cleavage face stabilization for a terrace crystal site ($n_{b,tot} = 5$)
t	pertaining to the top of an SHS structure
t_d	property applied to the crystal dissolution time
$tetra$	tetrahedral crystal parameter
tot	total
tvf	property for droplet spread on an SHS, for an interface site if the site were a VLV site instead of a TCL site, or vice versa
u	upper probabilistic bound
up	upper
VLV	property of a VLV interface site
v	viscous
vd	pertaining to the triple contact interface site vertical movement along a pillar wall
w	Wenzel state
$wall$	property pertaining to the wall of an SHS structure
x	x-axis
y	y-axis
$\mathfrak{z}$	axial cylindrical component of a vector quantity
$\mathfrak{z}_i$	i^{th} axial cylindrical coordinate
α	interaxial angle between $l_{\vec{b}}$ and $l_{\vec{c}}$ for a pristine crystal, (°)
β	interaxial angle between $l_{\vec{a}}$ and $l_{\vec{c}}$ for a pristine crystal, (°)
γ	interaxial angle between $l_{\vec{a}}$ and $l_{\vec{b}}$ for a pristine crystal, (°)
ε	advancing ($\varepsilon = adv$) and receding ($\varepsilon = rec$) index
H	set of all uncertain parameters for a system
η_i	i^{th} uncertain parameter of a system

$\boldsymbol{\Theta}_{\boldsymbol{n_{bd}}}$	parameter for a surface particle with a given angle orientation $\boldsymbol{\Theta}$ for an $\boldsymbol{n_{bd}}$ nearest neighbour configuration
ι	index number for LPCM coefficients
N	total number of process design conditions under which a PCE model is developed for a given system
ν	index number for a process's design conditions $\boldsymbol{\omega}$ under which a PCE model is developed
$\nu\epsilon$	index of different types of MFkMC events that can occur; $\nu\epsilon = 1$ denotes a moving interface event and $\nu\epsilon > 1$ denotes one of the non-moving interface events
ξ_{i,η_i}	randomly-generated realization with standardized properties of the i^{th} uncertain parameter η_i, for predicting output uncertainty distributions using PCE
ς	designation for the upper ($\varsigma = u$) and lower ($\varsigma = l$) probabilistic bounds of an output $\boldsymbol{\Psi}(t_m)$
Υ	number of orthogonal lattice vectors for a given crystal structure
υ	index number for the different orthogonal lattice vectors (i.e., axis directions) of a given crystal structure
ϕ_i	i^{th} azimuthal cylindrical coordinate
χ	order of the series expansions used for PCE
$\boldsymbol{\Psi}(t_m)$	parameter applied to the vector of model outputs at a discretized timepoint t_m

Additional Notation

$\bar{d}$	average value of a parameter d
$\tilde{d}$	dimensionless value of a parameter d
$\hat{d}$	nominal value of a parameter d
$\lfloor d \rceil$	rounding of a parameter d to the nearest integer value
$mod(d_1, d_2)$	remainder of division between numerator d_1 and denominator d_2

Chapter 1 - Introduction & Motivation

The interfacial phenomena that occur at the boundary between two or more phases are critical to a wide variety of different processes throughout engineering.[1] The interfaces within these systems do not frequently remain static and are known to move and undergo surface fluctuations in time. Accordingly, these processes can be referred to as moving interface systems, and they play a crucial role in fields ranging from emulsions and micelle formation to ice melts and ocean waves.[2,3] Consequently, it is crucial to accommodate for the boundary displacement and the various interfacial phenomena that occur in order to capture these processes. The fundamental processes and challenges affecting a moving interface system differ depending on the composition of the phases on each side of the interface. For example, the motion of a solid moving interface can be readily captured based on the physiochemical kinetic events taking place, such as adsorption and desorption. Conversely, the dynamics of moving fluid-fluid interfaces are better described using the underlying forces and energy balances acting along the interface.

Moving interface systems play important roles in a variety of different systems as highlighted above, and as a result there is significant interest in developing models to capture, study, and improve upon these processes. In general, moving interface systems are often macroscale in nature and typically evolve over large spatial (mm-km) and temporal (ms-h) scales. However, these interfaces frequently include intricate detailed topologies and morphologies that are highly sensitive to microscale and molecular-level perturbations such as roughness and surface structures.[4] For example, the dissolution of a solid is highly dependent on the molecular-level configuration of a surface particle with respect to its nearest neighbours. In addition, the inclusion of microscale and molecular-level roughness on a solid surface is known to drastically affect the spreading behaviour of fluid droplets on the surface, and can result in superhydrophobic surface behaviour. Therefore, due to the discrepancies in the length and time scales within these systems, moving interface processes can be challenging to capture using conventional modelling techniques. For instance, large-scale modelling techniques such as computational fluid dynamics (CFD) are incapable of capturing detailed molecular analyses of the systems, and thus are only useful for capturing the general (macroscale) behaviour of the system.[5] These techniques additionally require specific methodologies to capture the movement of the interface, such as front-tracking or front-capturing.[4,6] In comparison to the large-scale modelling techniques, microscale techniques such as Molecular Dynamics (MD) are capable of capturing the movement of the interface at the molecular level and therefore they are able to achieve unprecedented accuracy in simulating interfaces with complex geometries. However, those methods are computationally intensive and can only be used to simulate small systems (~nm) over short timescales (~ns).[7] These challenges can be overcome using mesoscale modelling methods such as the Lattice-Boltzmann method, which aims to balance the molecular-level and macroscale evolution of a system.[8] However, this latter approach is prone to error-induced force imbalances and fictitious behaviour near

the boundaries of multi-phase interfaces.[9] This can be disadvantageous for moving interface systems, where the key properties of the system are often directly related to the interface.[10]

Kinetic Monte Carlo (kMC) is an alternative mesoscale modeling technique that uses random sampling to analyze a system's dynamic behaviour. kMC only considers the key events contributing to a system's evolution, and thus it is capable of simulating larger systems over long periods of time.[7] Furthermore, a kMC system is able to directly account for the crucial phenomena present at a multiphase interface. The kMC method has already been previously implemented to study solid moving interface applications ranging from thin film deposition to crystal growth and dissolution.[11–13] In these applications, the solid-fluid interface can be evolved by adding or removing molecules from the solid surface according to kinetic event rates. However, it is not inherently obvious as to how kinetic surface events could be used to capture the interfacial dynamics of more complex systems involving fluid-fluid interfaces, such as capillary action or sessile droplet spreading, or whether kinetic surface events are even applicable to these systems. Furthermore, standard kMC is typically only used to directly model the solid surface at the interface, and consequently the behaviour of the remaining phases is usually only captured indirectly through the kinetic rate equations governing the surface evolution. As a result, this technique cannot be directly applied to simulate a dynamic fluid-fluid interface. Therefore, in order to capture moving interface systems using kMC, it is necessary to develop new approaches that can accommodate for both solid-based and fluid-fluid-based moving interfaces. This PhD study will particularly focus on developing a general kMC-based moving interface algorithm and applying it to key applications including solids and crystal dissolution, as well as fluid-fluid triple contact interface-based processes such as capillary action, sessile droplet spreading, and superhydrophobic surfaces.

Solids and crystal dissolution is a prominent moving interface field of study where the interface exists at the boundary between a fluid and a shrinking solid phase.[14–19] One of the key attributes for this application pertains to the rate at which the solid disintegrates within its intended environment, and thus it is desirable to control the dissolution rate within a given system.[20] These rates strongly depend upon the local microstructure of the surface as well as the system environment,[12] and therefore they are highly sensitive to environmental variability and uncertainties.[21,22] As a result, it is necessary to accommodate for the effects of both the local surface structure and environmental uncertainties when conducting dissolution studies. However, this remains an emerging field within the literature. Capillary action-driven transport is another crucial moving interface system that significantly impacts a variety of different natural and artificial applications. This phenomenon utilizes the differences in surface energies between fluids and solids to propel a fluid-fluid interface along the surface of a narrow cavity without requiring external energy. This process does not depend on physiochemical kinetics and must be quantified through fundamental physical laws (e.g., the force or energy balances affecting the system) and therefore it can be challenging to analyze the interfacial movement.[23] This process is essential in many different scientific and engineering disciplines, and thus there has been significant interest in studying

capillary action processes in order to maximize their applicability.[24–26] The observed behaviour within a capillary action system is dependent on the shape and properties of the solid cavity through which the fluid is rising or falling, and on the local microstructure and roughness of the cavity.[27] However, capillary action is a macroscale process that can drive fluids over distances that can range from mm to km.[28] As a result, it is necessary to accommodate the disparity in scales and cavity surface properties when studying and designing processes where capillary action plays a critical role.

One of the most important moving interface applications can be found in the spreading of sessile droplets on solid surfaces. Sessile droplet systems are triple contact interface processes where the moving interface consists of two different fluids, and therefore its behaviour is best quantified based on the fundamental forces affecting the system. However, these droplet systems are further limited due to a lack of knowledge in the underlying forces responsible for the droplet spreading behaviour. Sessile droplet spreading is relevant to a wide variety of different engineering designs and processes.[29–33] Superhydrophobicity, in particular, has emerged as one of the most critical sessile droplet applications. Solid surfaces are prone to contamination from various pollutants, and there are many instances where these can lead to adverse results. Consequently, there is significant motivation to develop surfaces that are self-cleaning, anti-fouling, and anti-wetting, in order to minimize or eliminate both solid and liquid surface contamination. These properties can be induced by designing extremely water-repellant surfaces, known as superhydrophobic surfaces (SHSs), where any water contacting the surface will form mobile drops that are readily removed by gravity or other external forces.[34,35] This superhydrophobic behaviour can be induced by creating low-energy material surfaces textured with microscale roughness structures to minimize the contact between water and the surface. However, SHSs suffer from a number of different problems that limit their wide-scale applicability. Most notably, these surfaces are susceptible to deactivation due to Cassie-to-Wenzel (C2W) transitions, where the droplets pin and impale on the surface roughness asperities to the extent where they are nearly impossible to remove.[36] This process has the potential to critically sabotage SHS antiwetting behaviour, and consequently, there has been a substantial amount of research dedicated to preventing C2W from occurring.[37–39] Furthermore, there are many model-based studies conducted within the literature with the intention of overcoming C2W.[8,39–41] These works employ techniques such as MD and LB to depict the dynamic response of fluid droplets to the micro- and nano-scale roughness structures present within SHSs. However, these modelling studies are limited by the same restrictions outlined previously for each method, i.e., computational limitations and force imbalances.[7,9]

1.1 Research Objectives & Contributions

Motivated by the challenges highlighted above, this PhD thesis presents the development of a novel Moving Front kinetic Monte Carlo (MFkMC) algorithm to capture and simulate general moving interface systems. This proposed kMC-based method only considers the behaviour of the interface and how it moves at

the molecular level. The MFkMC method defines the interface as the border separating interface molecules of different phases, and it uses kinetic-like rate equations to capture the interface movement based on the fundamental physics affecting the interface movement. As a result, the MFkMC algorithm possesses good generality. The applicability of the MFkMC algorithm is demonstrated through application in four case studies involving crystal dissolution, capillary rise, sessile droplet spread, and superhydrophobic surfaces. The MFkMC models developed for each case study are subsequently implemented to tackle key challenges experienced within each moving interface application. The specific research objectives considered are as follows:

- Develop a generalized kMC-based MFkMC algorithm to capture the dynamic behaviour of any moving interface system. Validate the model performance through comparisons to standard kMC, known system behaviour, and experimental results for different case studies.
- Adapt the MFkMC algorithm to capture the dissolution of crystalline solids within a solvent fluid. Use the developed model, in conjunction with uncertainty propagation techniques, to provide insight on the impact of environmental uncertainties on crystal dissolution with particular focus on pharmaceutical drug delivery. Determine the optimal conditions to encourage crystal dissolution while minimizing the impact of uncertainty.
- Develop a method to capture fluid-fluid moving interfaces based on the fundamental physics affecting the interface behaviour and apply it to capture capillary rise. Utilize the developed method to evaluate the effects of cavity shape and surface roughness on the capillary action process.
- Investigate the balance of forces acting upon the interfaces of sessile droplet systems. Couple this force balance with MFkMC to develop a sessile droplet spreading model and use it to study sessile droplet spread on flat surfaces.
- Expand the sessile droplet FB-MFkMC model to accommodate for irregular solid surface geometries and to capture droplet spread on superhydrophobic surfaces. Adapt the model to predict whether spontaneous C2W transitions will occur based on the surface geometry. Evaluate the effects of the surface structures on the droplet spreading and C2W behaviour.

The study of moving interface systems is a diverse multiscale field filled with processes that evolve on the macroscale but that are sensitive to microscale fluctuations along the interface. Consequently, it is essential to develop modelling methodologies that can accurately and efficiently capture the complete behaviour of a moving interface system while still accommodating for critical molecular-level deviations such as surface roughness. However, there are limited options that are able to achieve these conflicting objectives despite their relevance, as highlighted above. This study aims to fill this gap by developing the novel MFkMC algorithm to capture the general behaviour of any moving interface system, including both solid-based and fluid-fluid-based interfaces, so long as the underlying physiochemical processes that drive the interface movement are known.

Although this model has its own limitations and challenges, it is not subject to the same shortcomings as previously-developed moving interface approaches and therefore shows significant potential to improve model-based studies for these systems.

This study furthermore implements MFkMC to study and gain new insights in the fields of crystal dissolution, capillary rise, and sessile droplet spread on both ideally smooth and superhydrophobic surfaces. For crystal dissolution, this study explores the significant impact of environmental variability on dissolving solids, particularly within pharmaceutical drug delivery. This study furthermore contributes towards the development of efficient robust and bi-objective optimization policies for crystal dissolution applications like drug coating design. Within the field of capillary action, this work additionally develops a modelling tool that can be used to efficiently capture capillary rise for irregular pore geometries and for pores subject to molecular-level surface asperities. Furthermore, it explores and highlights the importance of accommodating for phenomena such as surface roughness within these systems. Finally, with regards to sessile droplet spreading, this research develops a semi-empirical force balance to describe and capture each of the forces acting on the droplet interface. In addition, it explores the effects of superhydrophobic surface structures on the droplet spreading and contributes towards the designs of SHSs that resist C2W transitions. Overall, this work contributes towards the development of a novel modelling framework to capture and study moving interface systems that accommodates for both their macroscopic behaviour and microscale variations.

1.2 Outline

The remainder of this thesis is organized as follows:

- Chapter 2 provides a review of the literature and presents an overview of the key moving interface systems (i.e., crystal growth and dissolution, capillary action, sessile droplet spreading, and superhydrophobicity), and discusses the key challenges facing each system. Furthermore, this section outlines the various modelling methods that can be used to capture moving interface systems and discusses their usage within the literature, with particular focus on the kMC approach that serves as the basis for the proposed MFkMC framework.
- Chapter 3 provides a detailed overview of the developed MFkMC algorithm and showcases the fundamental theory behind this method. This section furthermore outlines many of the key challenges and considerations necessary when designing an MFkMC model for a given system. The information presented in this chapter has been adapted from a paper previously published in *The Journal of Physical Chemistry B*.[23]
- Chapter 4 adapts the proposed MFkMC algorithm to capture the complete dissolution of crystals for biological applications. The developed model is compared to a standard kMC model previously developed within the literature for the same system.[12] Furthermore, PCE is used to

propagate uncertainty in the environmental parameters through the dissolution process, and LPCMs are derived to predict the PCE coefficients for a range of different crystal shapes and sizes. The LPCM-based framework is used to perform robust and bi-objective optimization on the crystal dissolution system. The work presented in this chapter is a combination of information previously published in *The Journal of Physical Chemistry B*[23] and *Computers & Chemical Engineering*.[42]

- Chapter 5 describes a variation of the MFkMC algorithm adapted to capture moving fluid-fluid interfaces based on the force balances acting upon the interface. This model is subsequently used to capture capillary rise of a fluid within cavities that are perfectly cylindrical, that have an irregular geometry, and that have a roughened surface. The information presented in this chapter has been previously published in *The Journal of Physical Chemistry B.*[23]
- Chapter 6 describes the study of the forces impacting the interface movement of a sessile droplet on an ideally smooth surface. This information is used to derive a semi-empirical force balance that is coupled with MFkMC to form the FB-MFkMC algorithm for sessile droplet spreading. The FB-MFkMC model is validated against experimental data and subsequently used to study sessile droplet spreading for different fluid droplets on different solid surfaces. This work has been previously published in *Physics of Fluids*.[43]
- Chapter 7 modifies the FB-MFkMC algorithm to capture sessile droplet spread on SHSs. The developed model is adapted to accommodate for the changes in surface geometry and their effects on the droplet force balance. In addition, the model is modified to simulate C2W transitions. The model is validated against experimental data from the literature and it is used to subsequently study the effects of SHS structures on the droplet spreading behaviour. This model is furthermore used to determine the surface structures that minimize the likelihood of C2W transitions. The contents of this chapter will be submitted for publication to Chemical Engineering Science.
- Chapter 8 presents the conclusions gained throughout this thesis. Furthermore, it outlines suggestions for further avenues of research to pursue in the future.

Chapter 2 – Background & Literature Review

The objective of this chapter is to give a summary of the moving interface background knowledge pertinent to this study. This section particularly focuses on moving interface systems such as solids dissolution, capillary action, sessile droplet spread, and superhydrophobicity. Additionally, it highlights the advantages and disadvantages of the core modelling techniques previously applied to capturing moving interface systems. This section is organized as follows. Section 2.1 provides an overview of the different modelling methods used to depict moving interfaces, with particular focus on the fundamental modelling theories behind kMC. Section 2.2 provides the necessary background information for each of the main moving interface systems depicted within this work. Subsection 2.2.1 discusses the mechanisms behind the solid moving interface-based crystal growth and dissolution processes. Furthermore, Subsection 2.2.2 discusses the relevant background information on the fluid-fluid-based capillary action, sessile droplet spread, and superhydrophobic surface applications respectively. Section 2.3 summarizes the gaps within the literature that highlight the overall objectives of this study.

2.1 Modelling Methods

Moving interface systems comprise exclusively of processes that contain a dynamically propagating interface between two or more phases. These interface displacements are expected to occur due to fluid flows, erosion, and deformations between the different phases.[44,45] Such moving interface systems can be found in many critical applications, ranging from ice to fluid flows to mathematical finance.[46–48] The properties of an interface differ significantly from those of the bulk and are critical for developing an understanding of how a system behaves and evolves. This interfacial behaviour are especially prominent on the microscale, and consequently there is a strong need to study moving interface systems as technology trends toward significantly smaller devices.[49,50] Accordingly, there is substantial interest and strong motivation in developing models to capture and simulate the behaviour of these dynamic interface processes.

The objective of this section is to discuss the various modelling methods that have been developed for moving interfaces and discuss how they have been implemented within the literature. This section will specifically focus on the kMC algorithm, which is the basis of the MFkMC algorithm developed in this work. Each modelling method described within this section are summarized in Table 2.1. This table additionally highlights the advantages and disadvantages of each method. The following subsection will provide a general overview of some of the most prominent moving interface modelling tools. Subsequently, Section 2.1.2 will provide a brief introduction to the kMC algorithm to highlight its potential and discuss its challenges and limitations in capturing moving interface system behaviour.

Table 2.1: Comparison of different moving interface modelling techniques

Method	Description	Advantages	Disadvantages	Relevant References
Continuum Modelling: Front-Tracking	Continuum PDE-based modelling; Interface captured directly through computational nodes	• Simple • Computationally Fast	• Cannot capture molecular-level behaviour • Large number of nodes required to model microscale fluctuations	4,6,53
Continuum Modelling: Front-Capturing; Level-Set Method	Continuum PDE-based modelling; Interface modelled implicitly (e.g., as an arbitrary surface)	• Computationally efficient • Flexible • Can handle complex geometries	• Cannot capture molecular-level behaviour • Numerical instabilities at the interface	4,6,54
Molecular Dynamics	Movement of each molecule captured based on intermolecular forces	• Captures molecular behaviour and fluctuations • Detailed	• Computationally slow • Only capture ~nm systems over ~ns timeframes	59,60,7
Lattice Boltzmann	Model movement of molecules over discretized space using Boltzmann equations	• Captures molecular behaviour and fluctuations • Reasonably great computational costs	• Force imbalances and ficticious behaviour at interfaces • Computationally slow compared to continuum modelling • Requires solving entire fluid space	8,9
Kinetic Monte Carlo	Stochastically models state-by-state evolution of a system based on kinetic transition rates	• Captures molecular behaviour and fluctuations • Reasonable computational costs	• Require duplicate simulations to capture average behaviour • Computationally slow compared to continuum modelling • No clearcut method to capture fluid-based moving interfaces	7,67,68

2.1.1 Modelling Approaches for Moving Interface Systems

There are many different modelling methods that have been developed to capture the behaviour of moving interface systems. These problems frequently entail complex interface topologies and geometries that are sensitive to slight changes and perturbations.[4] These interfaces furthermore frequently depict discontinuities in the system properties between the materials in each phase.[51] As a result, they can be challenging to model using conventional techniques. Despite this, myriads of different modelling approaches have been proposed

and implemented to capture the dynamic behaviour of moving interface systems for a variety of different applications, including the applications considered in this work, i.e., crystal growth and dissolution, capillary action, and droplet spread on flat and textured surfaces. Moving interface problems are frequently tackled using large-scale modelling techniques such as computational fluid dynamics or other continuum modelling approaches. These processes frequently denote the movement of the interface with a unique partial differential equation (PDE) designed to capture the underlying physical processes governing the interface movement. The solution to the interface PDE can be furthermore used as boundary conditions of other relevant PDEs (e.g., mass, momentum, or energy conservation equations). A common example of these kinds of moving interface models is the Stefan Problem, which aims to study the change in properties such as heat conduction over an interface between the two phases, where at least one phase is changing into the other.[52] Although Stefan problems are not exclusively applied to moving interface systems, they are frequently employed in applications where the interface can change significantly, such as heat exchange during ice melts. In general, continuum-based analyses of moving interface systems are comparably fast and can efficiently capture the dynamics of large systems over realistically-long time periods. However, these techniques require specific methodologies to capture the movement of the interface, such as front-tracking or front-capturing.[4,6] In the front-tracking method, the moving interface is assigned computational nodes to capture the location of the moving interface. These nodes are evolved discretely based on the underlying interface PDE to capture the interface movement.[53] The front tracking method can accurately capture the evolution of an interface, however it requires a prohibitively-large number of points to sufficiently capture systems with sophisticated surface geometries that evolve on a molecular level or systems whose interfacial movement is spatially heterogeneous based on the local interfacial microstructure. On the other hand, front-capturing methods implicitly model the moving interface as a high variation region instead of tracking the interface directly. The most common form of front-capturing method is the level-set method, which captures the interface using an arbitrary implicit boundary surface φ_{lsm}, where $\varphi_{lsm} = 0$ denotes the current location of the interface. In this method, the interface is evolved in time and space based on its normal velocity v according to the level set equation $\frac{\partial \varphi_{lsm}}{\partial t} + v|\nabla \varphi_{lsm}| = 0$. This approach is versatile and can readily handle complex interface geometries in an accurate and efficient manner.[54] Furthermore, its implicit interface definition allows for easier interface propagation and property calculation. However, it suffers from numerical instabilities at the interfaces that limit its applicability to accurately capture moving interface behaviour.[5] Furthermore, this method requires detailed insights in order to properly set up the system. As highlighted in Table 2.1, both front-tracking and front-capturing methods are able to adequately capture the movement of an interface with sufficient implementation. Consequently, they have been used to capture a wide variety of different moving interface systems, including crystal growth,[55] capillary rise,[56,57] and sessile droplet spread.[6,58] However, these methods struggle to capture detailed and

discrete microscale information about the interface, such as its reactions to molecular-level perturbations, and are better reserved for applications where these features are not as crucial to the interface dynamics.

In comparison to the large-scale continuum-based modelling techniques, microscale techniques such as Molecular Dynamics (MD) are capable of capturing the movement of the interface on the molecular level and therefore they are able to achieve unprecedented accuracy in simulating interfaces with complex geometries and spatially-heterogeneous systems, as documented in Table 2.1. The MD method is one of the most commonly-implemented molecular-level modelling technique. In MD, the positions and momentum of every molecule in the system are approximated based on Newton's equations of motion.[59,60] MD is able to accurately capture the dynamics of every particle within a considered system, and therefore it is able to achieve molecular-level accuracy while simulating the behaviour of moving interfaces. Consequently, MD has found a lot of use in molecular-level moving interface studies, such as the dissolution of individual surface features of a crystal,[61] studying C2W transitions inside individual SHS features,[40,41] and capillary action within nanoscale pores.[62] However, this approach, alongside other molecular-level modelling methods, is computationally intensive due to the number of particles considered and can only be used to simulate small systems (~nm) over short timescales (~ns).[7]

The behaviour of moving interface problems frequently involve complex topologies and geometries that are sensitive to small perturbations.[4] Furthermore, many moving interface problems involve phenomena that span multiple length and timescales, and consequently there is a need for modelling techniques that can bridge the disparate scales. This has previously been accomplished via mesoscale methods such as the Lattice-Boltzmann (LB) approach.[8] These methods still consider the molecular-level evolution of the system, however they apply key assumptions to simplify the problem and thus allow them to capture the behaviour of larger systems over longer time scales. The LB method is one of the most prominent mesoscale methods that can be used to capture moving interface behaviour in multiphase flows. In LB, the fluid phases of a moving interface system are depicted using a distribution of fictitious particles within a discretized space that are restricted by the degrees of freedom in which they can travel. These particles are subsequently evolved based on modified versions of the Boltzmann equation. LB is capable of capturing the behaviour of realistically-large moving interface systems while still accommodating for the underlying molecular-level behaviour, as highlighted in Table 2.1. As a result, it has been frequently used to capture fluid-fluid interface behaviour, including capillary rise,[63] sessile droplet spread,[64] and superhydrophobicity.[65,66] However, LB simulations are still computationally constrained by their need to solve the entire fluid space of the droplet rather than only considering key interfacial events that govern the droplet dynamics. Additionally, this approach is prone to error-induced force imbalances and fictitious behaviour near the boundaries of multi-phase interfaces.[9] This can be disadvantageous for moving interface systems, where the key properties of the system are often directly related to the interface.[10]

Each of the aforementioned modelling methods have different advantages and disadvantages that restrict their general applicability, as highlighted in Table 2.1. Continuum methods are computationally cheap, but they struggle to capture the microscale phenomena and fluctuations that govern many moving interface systems. On the other hand, molecular methods such as MD are able to achieve excellent accuracy on the microscale but are too computationally intensive to scale up. The trade-off between these two methods can be addressed using the LB method, however this method suffers from force imbalances along interfaces that limit its applicability to moving interface systems. Alternatively, these issues can be overcome through mesoscopic stochastic event algorithms such as kinetic Monte Carlo (kMC), which only considers the key events contributing to the system evolution and can be designed to directly account for the fundamental physics affecting a system. Given the relevance of kMC to this research, this method will be briefly reviewed in detail within the next section.

2.1.2 Kinetic Monte Carlo

Kinetic Monte Carlo (kMC) is an iterative stochastic modelling technique that can be used to evolve a system from one state into another based on transition rates, as summarized in Table 2.1. Given a system in its initial state, the kMC approach will identify any currently-accessible states and will transition the system into one of these at random, where the new system state is selected using Monte Carlo sampling based on its kinetic rate of occurrence. Therefore, kMC can be considered a stochastic realization of the Chemical Master Equation, a series of ordinary differential equations (ODEs) that describe the probabilistic state-wise system evolution.[67] The transitions considered in kMC simulations solely consist of the key events that transpire within the system. These events typically consist of molecular-level physical chemistry processes such as adsorption, reactions, and surface/bulk diffusion. During each kMC iteration, an event is selected at random based on its kinetic rate W_i according to the following expression:

$$\sum_{q=1}^{i-1} W_q \leq \xi_{disc} W_{tot} \leq \sum_{q=1}^{i} W_q \tag{2.1}$$

where W_i denotes the kinetic rate of the i^{th} event, W_{tot} denotes the total sum of all the kinetic rates, and ξ_{disc} is a random number generated from the standard uniform distribution. Following its selection, the chosen kinetic event is subsequently executed to propagate the system into a new state. Note that the kinetic rates for each event can remain fixed for the duration of the kMC simulation, or they can be dynamically updated after each transition depending on the nature of the processes taking place. The kMC technique keeps track of time using a stochastic logarithmic equation that takes the sum of all rates into account, as shown below:[68]

$$\delta t = -\ln(\xi_{cont}) / W_{tot} \tag{2.2}$$

where δt denotes the time increment between two kMC events and ξ_{cont} is a second randomly-generated number from the standard uniform distribution. kMC is therefore capable of evolving the system in real time.

However, it is important to note that since kMC is a stochastic process, it often requires averaging over multiple independent simulations in order to determine the average properties of the system.[67]

A key advantage of kMC is that this technique is not focused on keeping track of the exact positions and properties of each molecular object in the system. Rather, it analyzes the system's movement between fixed states in order to determine the average system behaviour.[7] This allows it to simulate far larger models over far longer timescales than would be possible using more detailed molecular modelling approaches such as MD. Furthermore, kMC can be coupled with lattice meshes such that the locations of each molecule/molecular object is approximated onto discrete lattice sites. This limits the positional degrees of freedom and allows for much longer simulation times to be reached.[67] However, one of the greatest strengths of the kMC approach is that it is only necessary to apply this method to the domains where the key system events are taking place (i.e. in the sessile droplet system on a flat surface, it is only necessary to apply kMC at the triple contact line). The remainder of the system domains (i.e. the bulk fluid phase) can therefore be disregarded by the kMC algorithm in order to greatly reduce the overall simulation computational cost. However, despite its advantages, kMC still suffers from drawbacks that can limit its implementation for a given system. Although kMC is significantly faster than MD and can be used to capture the dynamic behaviour of realistically large systems, it is still computationally intensive and can require extensive computational resources compared to continuum modelling or LB.[7] Furthermore, kMC is a stochastic process where each full simulation only depicts a single possible model outcome. As a result, kMC results must be averaged over multiple independent simulations in order to capture the general expected behaviour of a system.[13]

The kMC discussions thus far have primarily considered its molecular-level modelling capabilities. However, kMC is not necessarily constrained to simulating molecules and molecule-sized objects, as by definition it merely captures the state-by-state evolution of a system. As a result, the kMC approach can be readily expanded to simulate larger systems at reduced computational costs. These approaches still capture the fundamental molecular-level processes governing the system evolution, while applying them to larger scale objects. Furthermore, these approaches can help reduce the kMC computational drawbacks discussed previously. These approaches can be implemented through spatial clustering methods such as spatial coarse-graining or Object kinetic Monte Carlo. If the kMC system consists of interacting atoms or molecules, the spatial coarse-graining technique can be applied, in which clusters of identical molecules are grouped together to form a larger "mesoparticle". These mesoparticles are subjected to the same kinetic transition events applied to the molecules, although the kinetic rates for each event need to be modified to account for the larger mesoparticle size. Therefore, spatial coarse-graining kMC can efficiently simulate the behaviour of larger systems by considering the actions of these molecular clusters rather than the actions of individual molecules.[69] Similarly, if the system considered consists of molecular-level items (e.g. single surface defects, vacancies, or points along an interface), it can be simulated using Object kinetic Monte Carlo (OkMC), in which a cluster of

similar items are grouped together to form a larger object (e.g. a cluster of neighbouring vacancies can be defined as a void). Subsequently, OkMC will evolve each of the objects based on the kinetic rules that govern them.[70,71] Much like coarse-grained kMC, OkMC events are applied to the objects as a whole rather than the elements they are composed of. As a result, OkMC algorithms are capable of simulating large systems over long timescales at reasonable computational costs so long as the objects are sufficiently large in scale.

The kMC algorithm is highly versatile, and consequently it has been applied to describe a wide variety of systems. Most notably for the processes discussed within this work, kMC has previously been applied to simulate a variety of different moving interface processes, such as crystal growth,[11,72,73] thin film depostion,[13,74–78] solids dissolution,[12,79–81] and quantum dot synthesis.[82,83] In addition, kMC-based multiscale frameworks have been used to capture the growth and erosion of solid-based moving interfaces within a fluid for applications such as dendrite growth in Li-ion batteries[84,85] and delignification in wood fiber.[86–89] However, these processes have all been restricted to capturing the evolution of solid moving interfaces, which are frequently driven by physical chemistry events such as adsorption and surface reaction and therefore can be readily described using known kinetic expressions.[13,90,91] These approaches cannot be readily applied to capture fluid-based moving interfaces, which are driven by physical processes such as the balance of forces acting upon the interface, and therefore lack concise kinetic expressions. Furthermore, solid moving interface systems only use kMC to directly model the solid surface at the interface, and consequently the behaviour of the remaining phases is usually only captured indirectly through the kinetic rate equations governing the surface evolution. As a result, this technique cannot be directly applied to simulate a dynamic fluid-fluid interface. Consequently, the approach necessary to model these systems using kMC would differ significantly.

2.2 Moving Interface Systems

An interface is the boundary region between two different phases, and they define the spatial boundaries where the properties of one phase stop and give way to the properties of one or more adjacent phases. Furthermore, interfaces are seldom static and can evolve in both space and time. The evolution of an interface $\Gamma(\boldsymbol{x}, t)$ as a function of space $\boldsymbol{x}$ and time t is most readily accomplished by analyzing the normal local interface velocity $v(\boldsymbol{x}, t)$ along the length of the interface. This velocity is subject to the underlying laws governing the system behaviour; these laws can take the form of force and energy balances acting over the interface, of kinetic representations of physical events taking place, and of partial differential equations (PDEs) for the mass, energy, and momentum conservation expressions acting on the system.[12,23,44] Once the velocity is known, it can be used to evolve the interface in time and to determine the new system shape. Note that there are a large variety of different moving interface processes governed by a myriad of different fundamental principles, and consequently the nature of the moving interface system can vary significantly from problem to problem. Specifically, there is a fundamental difference in the key underlying physics between different moving interface

systems depending on the composition of each phase on each side of the interface. These distinctions are most apparent between interfaces where one or more of the moving phases is a solid (e.g., crystal growth and dissolution) and interfaces where the moving phases are all fluids (e.g., capillary action and sessile droplet spread). Therefore, each of the subsequent sections will provide specific details about each the moving interface systems studied in this PhD thesis.

2.2.1 Crystal Growth & Dissolution Behaviour

The growth and dissolution of crystalline materials is an important field of study in numerous different disciplines with various engineering, geological, and medical applications, ranging from the developments of cements and paints,[14,15] to the study of erosion and ocean acidity,[16,17] to the study of bone implants.[18,19] The crystal growth and dissolution processes are of particular importance in a number of biological fields such as the pharmaceutical, medical, and food industries, and have found usage in a number of different applications including the formation and disintegration of mineral supplements, nano-apatites for biomedical purposes, and capsules for food and drug delivery.[11,92–96] One of the key critical quality attributes for many of these biological applications pertains to the rate at which the crystal dissolves within its intended environment. For example, in the pharmaceutical industry, it is critical to control the release rate at which a nano-encapsulated drug is administered within the human body.[20] As a result, it is desirable to control the crystal dissolution rate for a given system. This can be achieved by modifying the size and shape distribution of the produced crystals,[11] and consequently, there has been significant interest in studying the underlying mechanisms behind the growth and dissolution of crystals in order to design and manufacture crystals with specific shapes and sizes such that they can meet explicit bioavailability criteria. This has motivated the development of several different model-based approaches in order to analyze the crystal production and disintegration process.[97–100] These methodologies have been furthermore implemented to optimize, control, and enhance these crystallization-based processes in applications such as protein crystallization.[72,101–103] Similarly, this has inspired the development of multiscale crystallization models for use in non-biological processes such as size control in the synthesis of quantum dots.[82,104–107]

Crystals can adopt a wide variety of different shapes and structures depending on factors including their composition, the temperature and pressure of the environment, crystal growth conditions, and vapour absorption.[108] As a result, there are a wide range of techniques that can be used to capture crystal growth and dissolution processes. Crystals are typically classified according to a number of different metrics, including the structure of their unit cell, the spacing and angles between particles, their symmetry, and the crystal coordination number, i.e. the number of nearest neighbours surrounding a bulk crystal particle on average. For the sake of simplicity, this work will predominantly focus on crystals with a coordination number of six, as depicted in Fig. 2.1. Crystals with this coordination can be described using a general unit cell of edge lengths $l_{\vec{a}}$, $l_{\vec{b}}$, and $l_{\vec{c}}$ and interaxial angles ϑ_α, ϑ_β, and ϑ_γ. To distinguish the interaxial angles from their supplementary

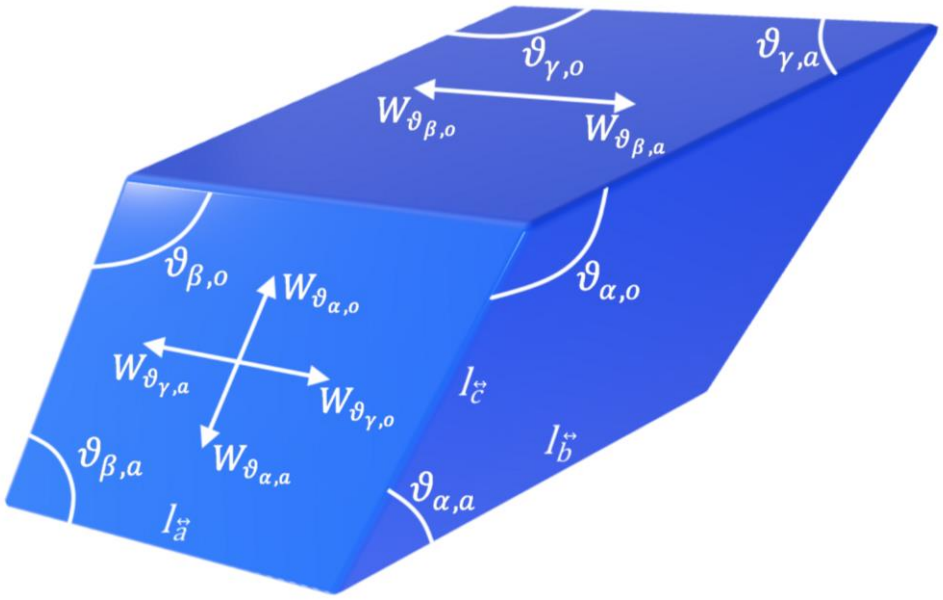

Figure 2.1: Labelling the dimensions and angles, including acute (a) and obtuse (o) angles, for a crystal with coordination number of six. Note that similar terminology can be derived for crystals of different coordination numbers

counterparts, each of the interaxial angles are further indexed as acute ($\vartheta_{\alpha,a}$, $\vartheta_{\beta,a}$, and $\vartheta_{\gamma,a}$) and obtuse ($\vartheta_{\alpha,o}$, $\vartheta_{\beta,o}$, and $\vartheta_{\gamma,o}$), where $\vartheta_a = 180° - \vartheta_o$ for $\vartheta_a \in \{\vartheta_\alpha, \vartheta_\beta, \vartheta_\gamma\}$. Crystals with a coordination number of six can be characterized using the Terrace Ledge Kink (TLK) model, which analyzes the kinetic and thermodynamic properties of the ion based on the number of bonds $n_{bd,tot}$ it shares with its coordinated neighbouring ions. According to TLK, an ion with $n_{bd,tot}$ = 6 bonds is classified as a bulk ion, whereas ions with $n_{bd,tot}$ = 5, 4, 3, 2, and 1 are characterized as terrace ions, ledge ions, kink ions, ledge adatoms, and adatoms, respectively.[90,109] Note that similar crystal surface formation models exist for crystals with a different coordination number.[110] However, discussions about these modelling methods will not be included here for the sake of brevity.

Crystal growth and dissolution mechanisms are frequently described kinetically based on the rates that molecules are added or removed from the crystal. There are three main events that are known to occur on the crystal surface: deposition, elimination (dissolution), and surface diffusion;[111] each of these events is assumed to be governed by sets of kinetic equations that overall shape the evolution of the crystal surface. In crystal deposition, an atom, ion, or molecule adsorbs onto the crystal surface from the fluid phase surrounding it. In contrast, crystal surface particle elimination via dissolution involves the detachment of a crystal particle from the surface back into the surrounding fluid phase. Crystal growth and disintegration mechanisms can additionally undergo surface diffusion, where a crystal surface particle detaches and re-attaches at a different location on the crystal surface. Surface diffusion is typically decomposed into a surface dissolution and a re-adsorption event, and therefore the kinetic rate for this event can be derived by combining the kinetic growth

and dissolution rate equations.[111] Note that the studies considered in this work consist of crystal dissolution studies where it is assumed that deposition and surface migration will not occur, and consequently this section will specifically focus on the kinetics of the surface molecule elimination events. However, kinetic equations for the remaining events can be readily found within the literature.[111–113]

In order to dissolve, a crystal surface particle must break its bonds with each of its nearest neighbours and migrate into the surrounding fluid phase. Consequently, the energy required for a surface species to dissolve is proportional to the number of bonds it shares with its neighbouring species and the identity of its neighbouring species. Furthermore, the energy required for dissolving a surface particle is dependent on the angle and spacing between it and its neighbours, which can be determined based on the base lengths and angles of the crystal lattice for a perfect crystal. Consequently, it is necessary to know the local atomic surface configuration in order to determine the dissolution rate for a given surface species. The dissolution rate for a crystal surface particle with a known local surface configuration can be described as follows:

$$W_{cd,\boldsymbol{n_{bd}},\boldsymbol{\Theta}_{\boldsymbol{n_{bd}}}} = k_0 \, exp\left(-\frac{\sum_{\upsilon} n_{bd,\upsilon} E_{\upsilon} + \Delta E_{\boldsymbol{\Theta}_{\boldsymbol{n_{bd}}}}}{k_b T}\right) \tag{2.3}$$

where k_0 is a pre-exponential factor; $\boldsymbol{n_{bd}} = \left[n_{bd,1}, \dots, n_{bd,\upsilon}, \dots, n_{bd,\Upsilon}\right]$ is a vector that stores the number of bonds $n_{bd,\upsilon}$ between a particle and its neighbours in the υ^{th} direction, where $\sum \boldsymbol{n_{bd}} = n_{bd,tot}$ is the number of nearest neighbours; E_{υ} denotes the activation energy of dissolution of the bond in the υ^{th} direction; k_b is the Boltzmann constant; and T is the temperature. Furthermore, the term $\Delta E_{\boldsymbol{\Theta}_{\boldsymbol{n_{bd}}}}$ represents the correction activation energy necessary to account for the angle orientations $\boldsymbol{\Theta}_{\boldsymbol{n_{bd}}}$ for a surface species with neighbour configuration $\boldsymbol{n_{bd}}$. Note that the nearest neighbour vector $\boldsymbol{n_{bd}}$ and the possible angle orientation values $\boldsymbol{\Theta}_{\boldsymbol{n_{bd}}}$ are dependent on the lattice structure of the considered crystal material. For a perfect primitive cell crystal with a coordination number of six, illustrated in Fig. 2.2, each ion in the bulk phase is coordinated with two nearest neighbours along each of the crystal lattice primitive vectors, and consequently the neighbour vector can be denoted as $\boldsymbol{n_{bd}} = [n_{bd,l_{\vec{a}}}, n_{bd,l_{\vec{b}}}, n_{bd,l_{\vec{c}}}]$. Furthermore, the angle orientation vector can take the values of $\boldsymbol{\Theta}_{\boldsymbol{n_{bd}}} = [\vartheta_{\alpha,a}, \vartheta_{\beta,a}, \vartheta_{\gamma,a}, \vartheta_{\alpha,o}, \vartheta_{\beta,o}, \vartheta_{\gamma,o}]$ for $n_{bd,tot} = 4$ and $n_{bd,tot} = 2$ (ledge and ledge adatom ions, respectively) and $\boldsymbol{\Theta}_{\boldsymbol{n_{bd}}} = [\vartheta_{\alpha,a}\vartheta_{\beta,o}\vartheta_{\gamma,o},\ \vartheta_{\alpha,o}\vartheta_{\beta,a}\vartheta_{\gamma,o},\ \vartheta_{\alpha,o}\vartheta_{\beta,o}\vartheta_{\gamma,a},\ \vartheta_{\alpha,a}\vartheta_{\beta,a}\vartheta_{\gamma,a}]$ for $n_{bd,tot} = 3$ (kink ions), depending on the location of the nearest neighbours. Note that crystal cleavage face stabilization effects can be taken into account on terrace ions by assigning a corrector value $\Delta \mathrm{E}_{\boldsymbol{\Theta}_{\boldsymbol{n_{bd}}}} = \Delta E_T$ when $n_{bd,tot} = 5$, if it is required for the crystal dissolution problem.[90] Also note that the aforementioned values of $\boldsymbol{\Theta}_{\boldsymbol{n_{bd}}}$ provide a general overview of all possible number of angle configurations and are most adept at describing triclinic crystals, where $\vartheta_{\alpha} \neq \vartheta_{\beta} \neq \vartheta_{\gamma}$; and the values of $\boldsymbol{\Theta}_{\boldsymbol{n_{bd}}}$ can be simplified depending on the crystal lattice structure (e.g. for cubic/tetragonal/orthorhombic crystals, where $\vartheta_{\alpha} = \vartheta_{\beta} = \vartheta_{\gamma} = 90°$, there is only one

possible angle configuration of $\boldsymbol{\Theta}_{\boldsymbol{n_{bd}}} = 90°$ for all values of n_{bd}.) Fig. 2.2 provides an illustration of the different acute/obtuse angle orientations and their respective reaction rates.

Crystal growth and dissolution are the two main branches that study how a crystal changes size and shape based on its environment. In both crystal size changing modes, all three of the aforementioned crystal surface events (deposition, elimination, and surface diffusion) are expected to occur. However, both crystal growth and dissolution are expected to occur under different environmental conditions, and therefore they are both typically studied in isolation and for different applications. Crystal growth studies consider the formation and expansion of crystals within a fluid with a high concentration of precursor crystal species. These studies seek to analyze the crystal growth mechanisms and to optimize and control the process in order to obtain crystals with desirable shape and size distributions.[11,72,73,98,114] On the other hand, crystal dissolution studies consider the key processes responsible for the breakdown of a crystal within a system. Many practical dissolution applications (e.g., timed release drug delivery) naturally occur under low solute conditions, such that crystal dissolution dominates whereas growth and surface diffusion can be considered negligible.[115] As a result, the crystal dissolution process

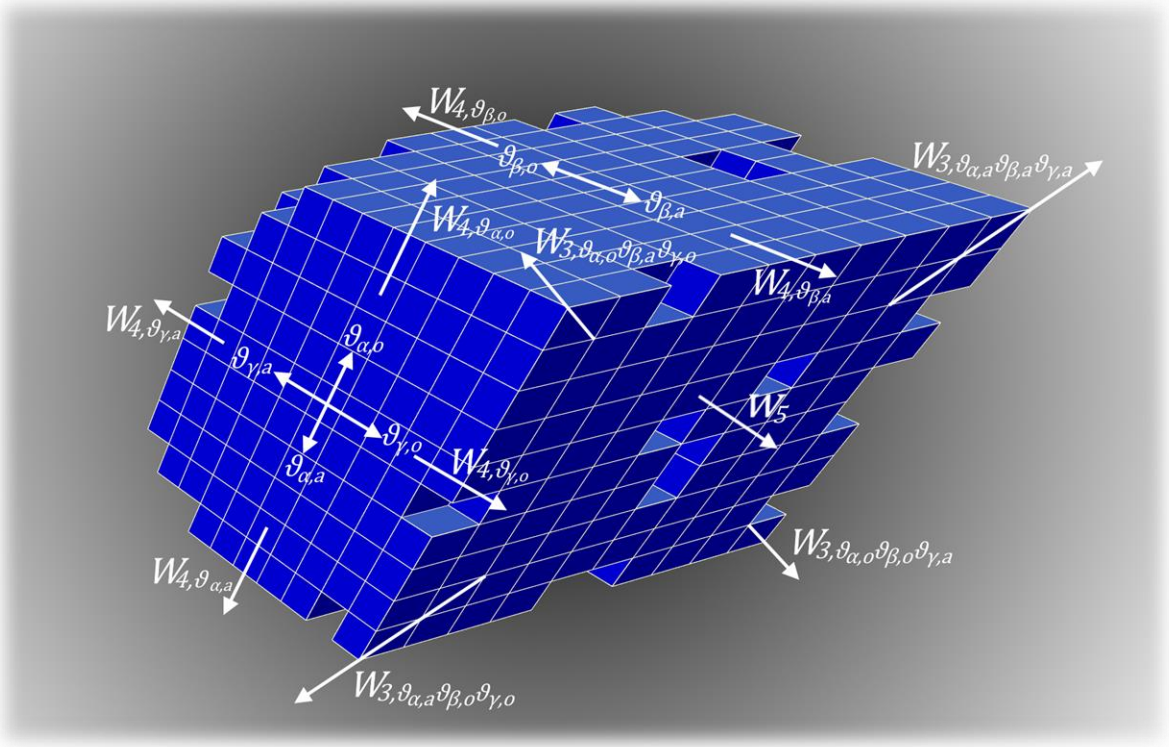

Figure 2.2: Assigning labels to the edge lengths, angle orientations, and kinetic rates for a rhombohedral crystal. Due to the rhombohedral crystal shape, this crystal can be described using TLK, such that the kinetic rates correspond to terrace (W_5), ledge (W_{4,Θ_4}), and kink (W_{3,Θ_3}) crystal sites; note that similar notation can be derived for crystals of different coordinate numbers

is typically studied in a solvent or some other system that encourages the desorption of particles and the overall disintegration of the crystal. These studies are performed in order to gain insights into the dissolution process and are frequently used to either study how to prevent crystal dissolution (e.g., dental caries studies),[116] to control the rate and duration of the dissolution within a target system (e.g., timed release drug delivery),[115] or to study the effects of dissolution on the surrounding system (e.g., permafrost melt studies).[17] Crystal dissolution studies were initially performed by measuring the bulk dissolution rates of crystals within solutions, wherein the crystal surface was assumed to dissolve at a uniform rate regardless of its surface geometry.[117,118] Although primitive, these early works helped establish the overall relationship between crystal dissolution and environmental factors such as pH, temperature, and solvent saturation.[119–122] Building upon the works of these predecessors, subsequent crystal dissolution works began to analyze the dissolution rates of individual crystal surface particles and study the effects of the surface microstructure on these dissolution rates. These studies were often performed by analyzing the formation and propagation of etch pits on a crystalline surface.[123,124] These etch pits form at defects in the crystal surface and rapidly enlarge as the crystal dissolves due to containing a higher number of faster-dissolving ledge and kink-type surface sites. The rates at which the etch pit expands can therefore provide a useful metric for analyzing the kinetics of the surface particles based on their numbers of nearest neighbours.[125,126] The dissolution rates of an etch pit are frequently observed by analyzing the speed at which the etch pit walls recede. These step velocities v_{step} can be compared for crystals with anisotropic etching in order to observe the effects of the crystal geometry in the crystal particle dissolution rate.[127,128] For example, crystals subject to acute and obtuse crystal structure angles are observed to have different rates of etching depending on whether the exposed surface particle has more acute or obtuse angles. This observation can be measured by comparing the step velocities in etch pits along the acute ($v_{step,a}$) and obtuse ($v_{step,o}$) directions.[127,128] These studies can further be upscaled to predict the dissolution kinetics of the entire crystal, and therefore provide detailed integrated analyses on crystal erosion operations that can be used to optimize and control the crystal dissolution process.

These studies overall highlighted the importance of accommodating for the microscale surface structure when studying crystal growth and dissolution processes. Furthermore, they highlight how the processes are sensitive to environmental factors, such as the temperature and pH of the surrounding fluid. These variables are often subject to uncertainty and environmental variability, which can significantly alter the dissolution process and its kinetics.[21,22,129] These issues are of particular importance for natural processes such as crystal dissolution within a biological system, where the environmental variability cannot be controlled and can experience significant fluctuations. Furthermore, this natural variability can critically affect processes such as pharmaceutical drug delivery, where it is necessary to control the rate and time of dissolution in order to prevent harm.[20] Consequently, it has been previously suggested within the literature that the event rate constants for crystal dissolution and growth cannot be depicted with a single value, and instead a possible range of rates

should be used when predicting dissolution mechanics.[130,131] The effects of dissolution on crystal growth processes have already been analyzed and taken into consideration within studies performed within the literature.[11,72,73] However, the effects of uncertainty on crystal dissolution are not as frequently studied, which can impose limitations on pharmaceutical studies and other critical fields of research. In addition, it is important to develop process models that can capture the complete dissolution of a crystal from the microscale, as highlighted previously. However, to the author's knowledge, none of the modelling methods discussed in Section 2.1 can adequately accurately capture the entire molecular crystal dissolution process without requiring prohibitive computational costs. Modelling approaches such as MD and kMC still require modelling the entire crystal structure, which is computationally infeasible for sufficiently large crystals. In addition, the continuum-based approaches are not able to capture the microscale surface processes critical to the crystal dissolution behaviour. As a result, there is a need to develop modelling methods to address these challenges and efficiently capture the dissolution of an entire crystal.

2.2.2 Fluid-Fluid Interface Behaviour

A volume of liquid in a vacuum will create a completely spherical shape in the absence of outside factors. This phenomenon can be most readily explained by analyzing the balance of intermolecular forces within the liquid. In the bulk phase of the fluid, a molecule is completely surrounded by its neighbouring molecules of the same fluid and thus the net intermolecular forces experienced by the molecule is negligible. However, molecules at the fluid surface are only partially surrounded by molecules of the same phase, and therefore they will experience only a fraction of the intermolecular forces from their neighbours, resulting in a force imbalance.[29,132] This imbalance is the basis of surface tension γ, or the force per unit length exerted by the surface on the environment.[133] This imbalance can also be defined as a surface energy, or the energy per unit area necessary for the surface to form.[132] Note that surface tension and surface energy are equivalent within a fluid, and are thus used interchangeably. It is because of surface energy that a liquid will assume a spherical shape within a vacuum, as a fluid will modify its shape to minimize its overall potential energy. The minimum surface energy attained by a fluid is only dependent on the intermolecular forces present in the fluid and therefore it remains constant at fixed temperatures, regardless of the mass or volume of the fluid.[133]

The concept of surface tension can be additionally expanded to describe the interface between multiple different bodies, such as when a fluid contacts a different material. In these cases, due to the differing intermolecular forces present at each side of the interface, the surface energy at the interface between the two phases will deviate from the individual surface energies of each phase, and consequently, the shape of the fluid will differ. The exact behaviour of these fluid interfaces varies from application to application, and consequently there has been a substantial amount of research performed to study this phenomenon for different systems. The following sub-sections will discuss this process as it relates to key fluid interface-based systems including capillary action, sessile droplet spread, and superhydrophobic surfaces.

2.2.2.1 Capillary Action Systems

When a narrow cavity is placed into a fluid, the fluid will either rise up or be repelled from the cavity, depending on the surface energies between the fluid, the solid capillary material, and the surrounding air. If the surface energy of the liquid on the surface is lower than the air-solid surface energy (i.e., the solid surface is wetting), then the liquid will rise up in order to minimize the overall energy of the system. Furthermore, if the cavity material is wetting, the tip of the fluid column will rise up the cavity with a concave quasi-hemispherical shape that intersects the cavity wall at an acute contact angle θ, as showcased in Fig. 2.3a. On the other hand, if the cavity material is non-wetting, then the liquid will be pushed down the cavity and its tip will maintain a convex quasi-hemispherical cap with an obtuse contact angle, as illustrated in Fig. 2.3b. Note that in both cases, the point at the edge of the fluid cap, where there is three-phase contact between the fluid, the solid cavity wall, and the surrounding atmosphere, is referred to as the triple contact line. The steady state relationship between the contact angle and the surface energies at the triple contact line can be expressed using Young's Equation, which describes the interfacial force balance of the contact line along the solid surface as follows:[29]

$$\gamma_{lv}\, cos(\theta_e) = \gamma_{sv} - \gamma_{sl} \tag{2.4}$$

where γ_{lv}, γ_{sv}, and γ_{sl} denote the interfacial tension of the fluid/atmosphere, solid/atmosphere, and solid/fluid interfaces respectively; and θ_e denotes the contact angle at equilibrium. This surface energy-driven movement is referred to as the capillary force and it is the basis for capillary rise.

When a fluid rises up a wetting cavity, it will experience a balance of forces, in addition to the capillary force, that will dictate the dynamic fluid behaviour. The balance of forces can be captured using an equation

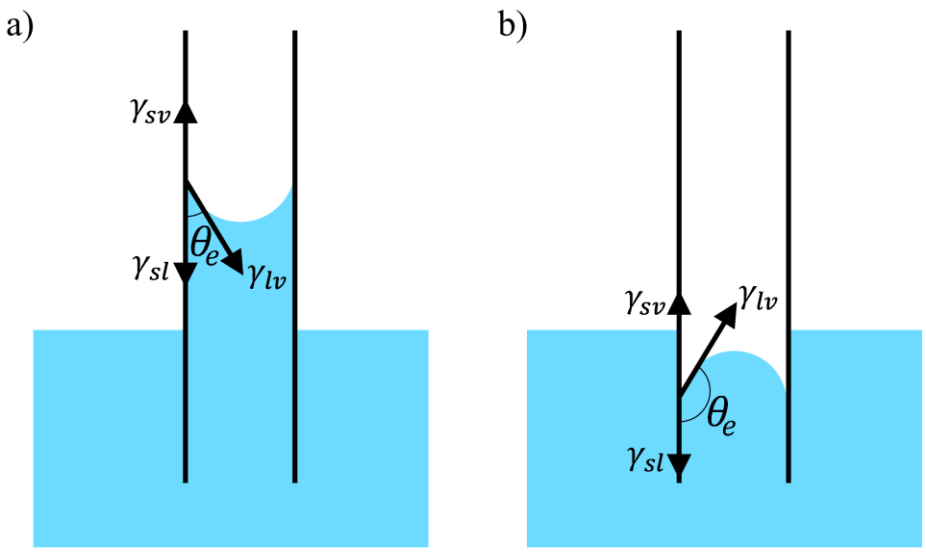

Figure 2.3: Liquid column shape in a capillary tube: a) wetting surface ($\theta_e < 90°$); b) non-wetting surface ($\theta_e > 90°$)

such as the Lucas-Washburn equation, which models the fluid rise as a balance between capillary, viscous damping, and gravity forces in a vertical cylindrical cavity according to the following relationship:

$$\frac{2}{R_{cr}}\gamma_{lv}\,cos(\theta_e) - \frac{8}{R_{cr}^2}\mu h\frac{dh}{dt} - \rho g h = 0 \tag{2.5}$$

where R_{cr} denotes the radius of the cavity at the triple contact line, μ denotes the dynamic viscosity of the fluid, ρ denotes the density of the fluid, $g = 9.81$ m/s^2 is the gravitational acceleration due to gravity at the Earth's surface, h denotes the rise height (i.e. the height of the fluid within the cavity relative to the fluid surface outside the cavity), and $\frac{dh}{dt} = v_{cr}$ denote the vertical velocity of the fluid as it rises. This model can be further adapted to accommodate for inertial effects as follows:[56,134]

$$\rho h\frac{d^2h}{dt^2} + \rho\left(\frac{dh}{dt}\right)^2 + \frac{2}{R_{cr}}\gamma_{lv}\,cos(\theta_e) - \frac{8}{R_{cr}^2}\mu h\frac{dh}{dt} - \rho g h = 0 \tag{2.6}$$

Note that Eqs. (2.5) and (2.6) above assumes that the cavity is perfectly cylindrical and therefore has a constant radius R_{cr}. In order to consider more complex cavity geometries, it is necessary to modify these equations to accommodate for changes in the radius R_{cr} as a function of the cavity height h. This is accomplished through the inclusion of the local cavity angle β_s, which describes the local angle of the cavity wall relative to a horizontal surface and can be calculated based on the local variation in the cavity wall radius over an incremental change λ in the cavity height (i.e., a change between $h-\lambda$ and h) as follows:[135]

$$\beta_s(h) = cos^{-1}\left(\frac{h-(h-\lambda)}{R_{cr}(h)-R_{cr}(h-\lambda)}\right) = cos^{-1}\left(\frac{\lambda}{R_{cr}(h)-R_{cr}(h-\lambda)}\right) \tag{2.7}$$

Furthermore, it is important to note that a change in the radius R_{cr} will also impact the contact angle θ of the fluid triple contact line and cause it to deviate from its equilibrium value θ_e. The deviation in θ for a tube of varying R_{cr} can be described according to the following equation:[135]

$$cos(\theta(h)) = cos(\theta_e) - \frac{\varsigma}{\gamma_{lv}}\frac{cos(\beta_s)}{R_{cr}(h)} \tag{2.8}$$

where ς denotes the line tension of the triple contact line. The cavity wall angle β_s and dynamic contact angle θ can be incorporated into the Lucas-Washburn equation as follows:

$$\frac{2}{R_{cr}}\gamma_{lv}\,sin(\beta_s - \theta) - \frac{8}{R_{cr}^2}\mu h v_{cr} - \rho g h = 0 \tag{2.9}$$

Note that Eq. (2.9) becomes Eq. (2.5) when the cavity wall is completely vertical (i.e., when $\beta_s = 90°$ and therefore $\theta = \theta_e$). These processes illustrate that microscale variability within the cavity can have notable impacts on the capillary behaviour of the fluid within it. As a result, it is necessary to accommodate for the molecular-level deviations when studying capillary action, especially within irregular cavity geometries.

2.2.2.2 Sessile Droplet Spreading

When a liquid comes into contact with a solid surface, it will adapt a spherical cap shape and will move along the surface in order to minimize the interfacial energies between the liquid, the solid, and the surrounding atmosphere, as illustrated in Fig. 2.4. If the solid/air interface has a higher surface energy than the sum of the liquid/air and liquid/solid interface energies, then the liquid will spread along the solid to form a film. On the other hand, if the solid/air interface has a lower surface energy, then the liquid will form a quasi-hemispherical droplet with a contact angle θ, as shown in Fig. 2.4b.[29] Note that θ is defined between the solid surface and the droplet's triple contact line, as highlighted within the figure. The droplet contact angle and its contact radius are dependent on the surface energies of each interface. On an ideally flat surface, the relationship between the contact angle and the surface energies at steady state can be expressed using Young's Equation according to Eq. (2.4).[136] Since the contact angle of a droplet is dependent on the interfacial surface energies of the system, it can therefore serve as an important measure of the liquid's ability to wet the solid, as discussed for capillary action within the previous section. Typically, the liquid and solid are considered wetting/partially wetting if the equilibrium contact angle of the droplet is below 90°; similarly, contact angles above 90° are generally associated with non-wetting interactions between the solid and liquid. In the case of water, these wetting regimes are referred to as hydrophilic ($\theta_e < 90°$) and hydrophobic ($\theta_e > 90°$), respectively.[137] It is important to note, however, that the switching angle of 90° is generally used for the sake of convenience, as in reality, the processes involved are quite complicated and there is no clear switch point between hydrophobicity and hydrophilicity for sessile droplet systems. Therefore, it is best to analyze this switch point based on the affinity between the liquid and the surface, that is, how readily water can be removed from the surface.[138]

While the previous discussions have considered the sessile droplet at steady state, it is also important to consider the droplet's dynamic behaviour. When a droplet is placed on a solid surface, it will spread and recede until it minimizes the overall surface energy between the droplet, the surface, and the atmospheric phase surrounding them as discussed previously. This minimization of the interfacial energies exerts a continuous restoration force on the drop (i.e. the capillary force) that drives the droplet to spread so long as there is a surface energy imbalance. These capillary forces are opposed by inertial forces, which resist droplet

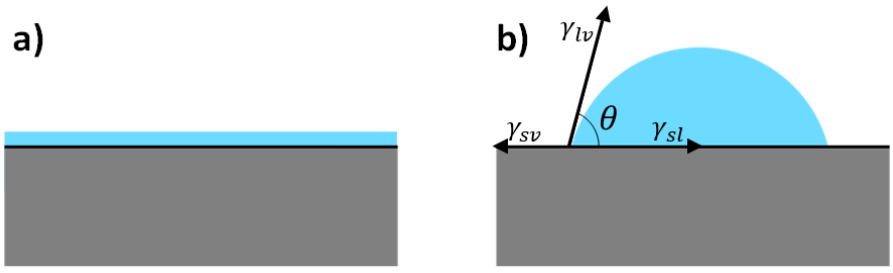

Figure 2.4: Liquid droplet shape on a solid surface based on surface energy minimization.
a) $\gamma_{sv} > \gamma_{sl} + \gamma_{lv}$ (complete wetting), b) $\gamma_{sv} < \gamma_{sl} + \gamma_{lv}$ (partial/non wetting)

deceleration and acceleration and can drive the droplet to expand or contract past the capillary equilibrium size. For sufficiently large droplets, gravity has been observed to provide an additional driving force for the system.[29] These driving forces, however, are countered largely by viscous damping forces that continuously dissipate energy from the system. The dynamic behaviour of a sessile droplet is considered to be predominantly driven by the aforementioned forces.[29,139] Therefore, it is necessary to have a detailed understanding of these forces in order to capture crucial droplet spreading behaviour. There have been many studies published within the literature that have derived analytical expressions for many of the key sessile droplet forces, i.e., capillary, inertial, and gravitational forces.[140–142] However, there has yet to be developed any concretely analytical models to capture the viscous damping force within droplet systems, despite its overall importance to the sessile droplet spreading behaviour.

The capillary force is one of the most important forces governing the behaviour of a fluid droplet, and therefore its effects on a sessile droplet behaviour are some of the most studied within the literature. As described above, this force is the result of the intermolecular force imbalances between the solid, droplet, and surrounding atmosphere phases, and therefore its analytical expression is dependent upon the fluid surface tension γ_{lv} and the droplet contact angle θ. The complete analytical expression for the capillary force at a given location $\boldsymbol{x}$ along the interface and at a given time point t can be derived in terms of these variables by integrating the differential pressure and the energy dissipation equations along the fluid-vapour interface in order to yield the following equation:[56,140–142]

$$\vec{F}_{cap}(\boldsymbol{x},t) = 2\pi R_{drop}(\boldsymbol{x},t)\gamma_{lv}\big(cos\,\theta_e - cos\,\theta\,(\boldsymbol{x},t)\big) \tag{2.10}$$

where R_{drop} and θ denote the dynamic droplet contact radius and the dynamic contact angle for the interface at position $\boldsymbol{x}$ and at time t, respectively. Note that if the droplet maintains a spherical cap shape, the contact angle can also be determined geometrically based on its volume V and the contact radius R_{drop}, according to:

$$\theta = 2\,tan^{-1}\left(\left(\left(\sqrt{9V^2+\pi^2R_{drop}^6}+3V\right)^{\frac{2}{3}} - \pi^{\frac{2}{3}}R_{drop}^2\right)\Big/ R_{drop}\pi^{\frac{1}{3}}\left(\sqrt{9V^2+\pi^2R_{drop}^6}+3V\right)^{\frac{1}{3}}\right) \tag{2.11}$$

The expression in Eq. (2.10) highlights how capillary action affects the sessile spreading depending on the state of the droplet. For example, if the droplet has a smaller contact radius than at equilibrium (i.e. $\theta > \theta_e$ according to Eq. (2.10)), then the capillary force will be positive and will drive the droplet to expand and increase its surface contact. On the other hand, if the droplet contact radius exceeds its equilibrium radius (i.e. $\theta < \theta_e$), then the capillary force will be negative and will push the droplet to recede and decrease its contact with the surface.

As a sessile droplet expands or contracts along the solid surface, it additionally experiences inertial forces that resist droplet deceleration. In order to determine an analytical expression for a droplet's inertia, Newton's second law can be applied to express the inertial force acting upon a differential element within the droplet. These differential inertia values can be subsequently integrated to derive a general inertial expression for the entire spherical droplet.[141] The compete inertial force equation at a given time point t can be expressed in terms of θ and R as follows:

$$\vec{F}_{inta}(\boldsymbol{x},t) = \pi\rho R_{drop}(\boldsymbol{x},t)^3 \left(\frac{\cos\theta(\boldsymbol{x},t)}{6\sin\theta(\boldsymbol{x},t)} + \frac{\cos\theta(\boldsymbol{x},t)}{4\sin^3\theta(\boldsymbol{x},t)} - \frac{\theta(\boldsymbol{x},t)}{4\sin^4\theta(\boldsymbol{x},t)}\right)\frac{d^2R_{drop}(\boldsymbol{x},t)}{dt^2} = \mathcal{F}(\boldsymbol{x},t)\frac{d^2R_{drop}(\boldsymbol{x},t)}{dt^2} \quad (2.12)$$

where:

$$\mathcal{F}(\boldsymbol{x},t) = \pi\rho R_{drop}(\boldsymbol{x},t)^3 \left(\frac{\cos\theta(\boldsymbol{x},t)}{6\sin\theta(\boldsymbol{x},t)} + \frac{\cos\theta(\boldsymbol{x},t)}{4\sin^3\theta(\boldsymbol{x},t)} - \frac{\theta(\boldsymbol{x},t)}{4\sin^4\theta(\boldsymbol{x},t)}\right).$$

This expression highlights how the inertial force is proportional to the local acceleration experienced by the droplet. Note that this expression was derived based on inertial force expressions reported previously within the literature,[141,142] as described within Appendix A. Furthermore, the contact angle and radius terms within the inertial expression produce negative values over $0 < \theta \leq \pi$ that are greater in magnitude for larger contact angle values, as highlighted in Appendix A. These results showcase that the inertial force works in opposition to the droplet acceleration and that it is most significant when the droplet maintains low contact with the surface (large θ). These results further highlight that the inertial force is greatest when the droplet first contacts the surface, which has been previously observed within the literature.[29,143]

In addition to the capillary and inertial forces, gravity is also known to affect both the shape and the spreading behaviour of sufficiently large droplets. Within a small droplet, the capillary forces will dominate over the gravitational forces and therefore gravity will have a negligible effect on the droplet behaviour. However, if the droplet is too large, then gravity forces will dominate and will act as an additional driving force on the droplet spreading. The cut-off at which gravitational forces become negligible is defined according to the capillary length, κ^{-1}, as follows:[144]

$$\kappa^{-1} = \sqrt{\gamma_{lv}/\rho g} \quad (2.13)$$

For droplets with greater radius than κ^{-1}, the effects of the gravity forces can play a significant role on the droplet spreading behaviour. Under this scenario, the effects of gravity on the droplet at a given location $\boldsymbol{x}$ along the interface and at a time point t can be expressed according to the following analytical formulation:[142]

$$\vec{F}_g(\boldsymbol{x},t) = \pi\rho g R_{drop}(\boldsymbol{x},t)^3 \left(\frac{\theta(\boldsymbol{x},t)}{sin^3\,\theta(\boldsymbol{x},t)} - \frac{cos\,\theta(\boldsymbol{x},t)}{sin^2\,\theta(\boldsymbol{x},t)} - \frac{2}{3}\right) \quad (2.14)$$

This equation illustrates that the gravitational force experienced by the droplet is greatest for large contact angles (i.e., when the droplet has minimal contact with the surface) and is smallest when the droplet

has maximal contact with the surface. Note that when the effects of gravity cannot be neglected, the gravitational force will additionally influence the shape of a sufficiently large droplet, causing it to form a flattened pancake shape rather than a hemispherical cap.[29,142] Consequently, Eq. (2.11) cannot be used to relate the contact angle to the contact radius for droplets larger than κ^{-1}.

Viscous damping is another crucial force that plays a significant role in the spreading behaviour of a sessile droplet. It is through viscous damping that the droplet's energy is dissipated, and consequently it is the viscous damping force that prevents the droplet from oscillating indefinitely around its equilibrium contact angle. However, despite its overall importance to the sessile droplet spreading behaviour, there has yet to be developed any concretely analytical models to capture the viscous damping force within this system. This is due to the nature of how this force is calculated in general. For a given arbitrary system, the force due to viscosity is calculated based on integrating the viscous stress tensor $\boldsymbol{S_v}$ over the surface of the system $\delta\Omega$ as follows:

$$\vec{F}_v = \int\int_{\delta\Omega} \boldsymbol{S_v} \cdot \hat{\boldsymbol{n}}\, do = \mu \int\int_{\delta\Omega} (\nabla \boldsymbol{u} + \nabla \boldsymbol{u}^T) \cdot \hat{\boldsymbol{n}}\, do \tag{2.15}$$

where $\boldsymbol{u}$ is the vector components of the fluid velocity at some point in space within the droplet, and $\hat{\boldsymbol{n}}$ denotes the normal to the system surface $\delta\Omega$. This equation highlights that in order to derive a complete analytical expression for viscous damping, it is necessary to determine the fluid velocity at all points along the system surface. Deriving closed-form expressions for $\boldsymbol{u}$ requires solving the Navier Stokes equations for the given system, which has yet to be accomplished for sessile droplets. Furthermore, fluid droplets are known to have complex internal flow patterns,[145,146] further complicating the derivation. There have not been any reported work within the literature that have attempted to develop a purely-explicit mechanistic viscous force equation due to the challenges highlighted above. Instead, efforts have been focused on deriving assumption-based empirical viscous damping expressions, such as the following cylindrically-based viscous damping force:[140]

$$\vec{F}_v \approx \frac{6\pi\mu\left(1+\frac{R_{drop}(x,t)^2-H_{drop}(x,t)^2}{R_{drop}(x,t)^2+H_{drop}(x,t)^2}\right)\frac{2H_{drop}(x,t)R_{drop}(x,t)^2}{H_{drop}(x,t)^2+R_{drop}(x,t)^2}}{\left(1-\frac{R_{drop}(x,t)^2-H_{drop}(x,t)^2}{R_{drop}(x,t)^2+H_{drop}(x,t)^2}\right)\left(2+\frac{R_{drop}(x,t)^2-H_{drop}(x,t)^2}{R_{drop}(x,t)^2+H_{drop}(x,t)^2}\right)} ln\left(\frac{R_{drop}(\boldsymbol{x},t)}{a_{ca}}\right)\left(\frac{dR_{drop}(\boldsymbol{x},t)}{dt}\right)^2 \tag{2.16}$$

where $H_{drop}(\boldsymbol{x},t)$ is the height of the droplet above the surface and a_{ca} is an empirically-fit parameter. This expression was constructed using assumptions to simplify the complex geometry and flow patterns of the sessile droplet system, such as assuming that the drop is a cylinder, or that the axial velocity profiles within the drop were negligibly small. However, these assumptions are only valid under very special conditions and can lead to significant errors in the predicted results. Furthermore, these forces rely on a fitted model parameter a_{ca} and therefore they do not provide a true mechanistic expression for the viscous damping force. Consequently, further research is desired in order to overcome this obstacle.

The dynamic behaviour of the droplet can be assessed by considering the ratios of each of the forces mentioned above. These ratios can be captured through the use of dimensionless numbers such as the Reynolds (Re, inertia vs viscosity), Capillary (Ca, viscosity vs capillarity), and Ohnesourge (Oh, viscosity vs inertia and capillarity) numbers, which can be depicted for sessile droplet systems as follows:

$$Re = \frac{\mathcal{v}\rho\ell}{\eta} \tag{2.17}$$

$$Ca = \frac{\eta\mathcal{v}}{\gamma_{lv}} \tag{2.18}$$

$$Oh = \frac{\mu}{\sqrt{\rho\gamma_{lv}\ell}} \tag{2.19}$$

where $\mathcal{v}$ and ℓ denote a characteristic velocity and characteristic length respectively; these values for a sessile droplet system are typically represented by the average velocity of the droplet contact line $\bar{v}_{drop}$ and the average droplet contact radius $\bar{R}_{drop}$. These numbers provide estimates on droplet properties such as the number of oscillations (Re, Ca), the period of oscillation (Re, Oh), and the recoil strength (Oh, Ca) that a droplet would experience before reaching equilibrium.[29,147,148]

When a sessile droplet is dynamically spreading/receding, it will adapt different contact angle values than the equilibrium value defined in Eq. (2.4). In particular, it has been observed that a droplet will adapt two different contact angles depending on whether the droplet edge is advancing or receding. When the contact line is expanding away from the droplet center, it will have a higher contact angle than at equilibrium, which is called the advancing contact angle θ_{adv}. On the other hand, the contact line will have a lower contact angle than at equilibrium when it is contracting back into the droplet; this is referred to as the receding contact angle θ_{rec}. The difference between θ_{adv} and θ_{rec} is defined as the contact angle hysteresis (CAH).[29] The origins of advancing/receding contact angles and CAH are not completely understood, and is therefore a field still under study. CAH is most commonly attributed to surface roughness and heterogeneous surface materials. The effects of surface heterogeneities on a droplet's behaviour would produce different surface energies depending on the different materials, and thus the droplet would adapt a different contact angle in order to minimize the overall potential energy. On the other hand, there are several different surface roughness effects that are associated with CAH. Surface roughness allows for pockets of air to be trapped between the droplet and the surface, resulting in a heterogeneous surface composition. In addition, the changes in the solid surface height will require more energy for the droplet's triple line to overcome. In particular, the triple line can often become pinned on surface asperities, and will not become unpinned until sufficient force has been applied.[149] In this case, the contact line will remain in place while the droplet continues to advance/recede, resulting in larger/smaller contact angles approaching $\theta_{adv}/\theta_{rec}$. The droplet will de-pin once θ_{adv} or θ_{rec} has been reached for advancing and receding droplets, respectively.

In addition to contributing towards CAH, surface roughness has been established to affect the wettability of the solid by the liquid droplet. When a liquid is placed on a rough surface, it can either occupy the extra surface area created by the roughness (Wenzel state), or it can choose to sit on top of the surface asperities, leaving vapour-phase gaps between the droplet and the lower parts of the surface (Cassie state), as illustrated in Fig. 2.5. When the droplet is in the Wenzel state, the contact surface area between the droplet and the surface will be much larger than it appears, and consequently the droplet will appear to adopt different measured contact angles (θ_w) than the true contact angle (θ). When the droplet is in a Cassie state, it will similarly adopt larger apparent contact angles (θ_{cb}) than the ideal case (θ) in order to account for the heterogeneous solid-vapour surface composition. This increase in the contact angle is due to the hydrophobic nature of air ($\theta_{air/water} = 180°$). The contact angle modifications observed in both Wenzel and Cassie wetting can be characterized using the Wenzel and Cassie-Baxter equations, respectively.[150] Note that the Cassie-Baxter model can be naturally adjusted to describe heterogeneous surfaces composed of two or more different solid materials by taking into account the contact angle and the fraction of the solid surface occupied by each material. Furthermore, note that despite the widespread use of the Cassie-Baxter and Wenzel equations to describe the Cassie and Wenzel state wetting respectively, there is much debate about their validity within the literature.[151,152] These validity concerns predominantly arise as it is known that the droplet dynamics are affected by the movement of the droplet's advancing line (i.e. the triple contact line on a solid surface), and therefore roughness profiles and composite surfaces only affect the droplet when they are in contact with this three-way interface.[10] However, the general consensus seems to be that while these models might not be completely accurate on a molecular level, they are highly useful when taken as global surface descriptors that can be applied locally to droplets in the Cassie and Wenzel states.[152]

The effect of roughness on the wettability of a surface is predominantly determined by the wetting state of the droplet. If a water droplet is in the Wenzel wetting regime, then the surface asperities will amplify the liquid behaviour on the surface, and therefore hydrophilic surfaces will appear more hydrophilic ($\theta_w < \theta$), whereas hydrophobic surfaces will appear more hydrophobic ($\theta_w > \theta$). Alternatively, if the water droplet is undergoing Cassie wetting, then the contact angle will be larger than on an ideal surface and the surface will behave more hydrophobically, regardless of the affinity between the droplet and the surface. This is due to the

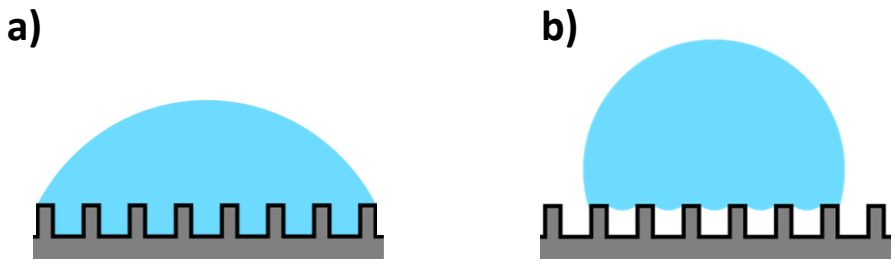

Figure 2.5: Liquid droplet in the a) Wenzel state, b) Cassie State

high contact angle between liquids and air (e.g. $\theta_{air/water} = 180°$).[153] Consequently, if a rough solid surface can be designed such that a contacting droplet of water is always in the Cassie state, then the droplet will have larger contact angles and can be removed more readily from the surface. This effect is referred to as superhydrophobicity, and it is the basis of self-cleaning and anti-wetting surfaces.

2.2.2.3 Superhydrophobicity

In nature, there are many biological surfaces, such as the lotus leaves, cicada wings and duck feathers, which exhibit extraordinary hydrophobic properties beyond what is achievable via capillary effects on an ideal surface. Specifically, the lotus leaf has been reported to achieve water contact angles greater than 150°, whereas the most hydrophobic solid surface materials cannot produce water contact angles higher than 120° on their own.[154] This natural superhydrophobicity has been attributed to multi-scaled textures on the surfaces, where the surfaces are water-repellant due to roughness asperities that keep water droplets in the Cassie wetting state. Consequently, these surfaces are able to achieve higher contact angles and lower hysteresis than if they were perfectly flat.[155] These surfaces have thus served as an inspiration for the design and fabrication of artificial superhydrophobic surfaces (SHSs), where roughness is combined with low surface energy materials in order to maximize the surface's water repellency.

There are numerous different approaches that have been implemented within the literature in order to produce artificial SHSs. For example, roughened surfaces can be fabricated by damaging pre-existing flat surfaces, by depositing nanoparticles, or by creating highly-porous surfaces.[156,157] These methods produced surfaces with contact angles between 120-175° depending on the techniques and the surface material used. However, one of the most promising routes for fabricating SHSs involves creating periodic micro- or nano-scale pillars on a solid surface.[150,156,157] For these surfaces, the height, shape, width, and spacing between the pillars can be adjusted in order to achieve intrinsic contact angles between 125° and 165°. In general, superior intrinsic contact angles can be achieved for structures that minimize the contact between the solid and the droplet while still maintaining a Cassie wetting state. Additionally, lower CAH can be obtained by using simple pillar shapes (i.e. cylinders and rectangular prisms), whereas complicated pillar structures tend to have high hysteresis due to pinning on the complex geometry.[158] In general, droplet pinning has been observed to cause large CAH on micro-pillared SHSs. This can be overcome by combining micro-textured surfaces with nanoscale features, which inhibit contact line pinning, in order to create structures with hierarchical roughness.[159] Hierarchical SHSs have additionally been observed to have higher contact angles and sustain higher dynamic pressures, with contact angles as high as 173° and CAH as low as 1-2°.[37,156,157,160] Consequently, there has been significant interest in developing periodic SHSs with multi-scale roughness, and numerous different surface designs have been produced.

Despite the promise of textured surfaces in achieving superhydrophobicity, these surfaces are still prone to issues that deteriorate their liquid repellency. Micro- and nano-structured surfaces can be fragile, and thus

SHSs are prone to deterioration due to wear and tear. Surface degradation not only reduces the SHS effectiveness, but also results in the formation of sharp edges that are prone to pinning, resulting in higher CAH.[161,162] This can be overcome by fabricating surfaces with higher mechanical durability, or by designing surfaces with microstructures that shield the more-vulnerable nanostructures. SHSs are also subject to contamination and corrosion damage.[163] As a result, further research has been performed towards designing surfaces that resist common forms of corrosion.[162] However, one of the most significant forms of SHS deterioration occurs if a droplet becomes embedded on the surface, i.e. undergoes a Cassie-to-Wenzel (C2W) transition.[36]

There are several methods for sessile droplets to enter the impaled Wenzel state. Wenzel drops form readily due to fogging and droplet nucleation, when microdroplets condense directly within the gaps between asperities on an SHS. These microdroplets can coalesce with each other to form Wenzel state droplets, or they can coalesce with Cassie-state macrodroplets and impale them on the surface.[164] Even the lotus plant, often considered the posterboy of superhydrophobicity, will lose its water-repellant tendencies if water is condensed on its surface.[150] Droplets can additionally be transitioned into the Wenzel state directly from the Cassie state (C2W transition). This can occur during evaporation due to the increasing Laplace pressure within a shrinking droplet.[9] Cassie droplets can also transition into the Wenzel state via application of an external force[165,166] Additionally, C2W frequently takes place due to the impact of the droplets themselves on the surface.[167,168] Note that the amount of force needed to undergo a C2W transition depends on the energy barrier between the Cassie and Wenzel states, which is furthermore dependent on the structure of the SHS. As a result, it is also possible to design an SHS where the C2W energy barrier is negligible and the C2W transition happens spontaneously. In this highly undesirable case, the Wenzel state is monostable and the Cassie state will not occur.[169] These spontaneous transitions can occur due to droplet sliding, when the local contact angle between the droplet and the asperity exceeds the advancing contact angle, thus allowing the droplet to advance into the gap between asperities. C2W transitions can also occur due to droplet sag. For a droplet in the Cassie state on an SHS, the liquid-vapour interface across a gap between roughness asperities will experience a local curvature due to gravity and surface tension forces and will sag downward. If the height of the curvature exceeds the height of the gap, then the droplet will readily fill the gap and enter a Wenzel state.[36]

In order to prevent SHS deterioration due to C2W, it is necessary to determine pathways to transition drops out of the Wenzel state or to prevent the Wenzel drops from ever forming. Due to the presence of an energy barrier for the C2W transition, it can be inferred that the reverse transition from Wenzel to Cassie (W2C) wetting can also occur as long as the Cassie state is stable and sufficient energy is applied to the system. This has been observed numerous times experimentally, where a successful W2C transition was induced via external stimuli such as electrowetting,[166] vibration,[170] and application of heat.[171] However, many superhydrophobic applications such as anti-wetting and self-cleaning surfaces involve systems where external energy cannot be

so readily applied. As a result, there is keen interest in developing SHSs where the transition to the Wenzel state is difficult to achieve, or where the inverse W2C transition could occur spontaneously, i.e. where the Cassie state is monostable. This potential state is theorized to occur on any SHS so long as the following condition is met:[37]

$$\frac{1-\not{f}}{\zeta-\not{f}} = -cos\ (\theta_{rec}) \tag{2.20}$$

where $\not{f}$ denotes the fraction of the surface occupied by the solid for a droplet in the Cassie state and ζ is a measure of the surface roughness. Similarly, conditions for high-stability Cassie state surfaces has been proposed based on the height of the surface asperities and the liquid, liquid-gas, and liquid-solid interaction properties.[172] Additionally, monostable Cassie states have been observed to occur in surfaces with a two-layered roughness scheme (i.e. by depositing hydrophobic nanoparticles over a periodic micropillar structure)[37,173] and on surfaces etched with periodically-structured nanocones.[38] However, despite these advances, the transition mechanism for spontaneous W2C is still not completely understood and is an active area of research.

2.3 Summary

This section has reviewed the pertinent theory behind different moving interface systems and the various phenomena that govern these processes. This chapter furthermore has summarized the various studies that have already been performed within this field. This review provided particular focus on the fields of solids dissolution, capillary action, droplet spreading, and superhydrophobicity, which serve as the critical fields of study analyzed within this work. It furthermore provided a brief overview of the kMC modelling method that serves as the basis for the MFkMC algorithm proposed within this study.

This chapter has illustrated the challenges faced in modelling moving interface systems and highlighted some of the remaining gaps within each of the moving interface systems considered. It discussed how there is currently a lack of model studies that are able to both efficiently simulate the molecular-level evolution of large moving interface systems over long timescales, while still accurately capturing the underlying physics governing the interface movement. In addition, while kMC has the potential to overcome the aforementioned challenges, there is a current lack of knowledge on how it could be implemented to simulate systems where the moving interface is not a solid. Furthermore, this chapter has highlighted how kMC is computationally-limited in its ability to capture large solid moving interface systems, such as the complete dissolution of large crystals. This section has additionally outlined some of the individual challenges experienced by the key studied moving interface systems. In the field of crystal dissolution, the dissolution of the solids is significantly affected by uncertainty and environmental variability. This uncertainty can cause significant issues in critical fields such as pharmaceutical drug delivery, where it is crucial to control key parameters such as the dissolution time and dissolution rate. In the field of capillary action, the movement of a fluid in a cavity is significantly affected by

the cavity shape and its microscale structure, which are not often taken into consideration by standard modelling approaches. In addition, sessile droplet systems suffer from a lack of knowledge on the complete balance of forces acting upon them. Furthermore, SHSs are prone to deactivation due to fowling mechanisms such as spontaneous C2W transitions and therefore there is considerable interest in designing surfaces that prevent this behaviour from occurring. These gaps provide the key motivation to perform this PhD study focused on developing a novel moving interface algorithm that can be applied to study and improve upon each of the moving interface processes analyzed within this thesis.

Chapter 3 – Development of the Moving Front Kinetic Monte Carlo Method*

Moving interface problems encompass a wide variety of different systems, such as ice melt, emulsion dynamics, ocean wave propagation, and droplet spread on a surface.[2,3,174] These problems often involve complicated interface geometries and topologies that are sensitive to small scale variations.[4] Consequently, they can be difficult to capture using traditional modelling methods. These issues can be addressed through the use of the kinetic Monte Carlo (kMC) method, which has the potential to bridge the gap between highly detailed molecular-level system descriptions and the larger space and time scales associated with continuum-level descriptions.[7,67] Nevertheless, the application of kMC to moving interface systems is fundamentally limited by a lack of clear direction on how it can be implemented for such systems. Previously-developed kMC models can only be applied to solid-solid interface systems, where the underlying surface evolution can be captured kinetically, as discussed in Section 2.1.2. However, these approaches cannot be used to capture moving fluid-fluid interfaces. In addition, existing kMC models for solid-based moving interfaces such as crystal dissolution require mapping of the entire solid affected by the kMC processes (e.g., in crystal dissolution kMC models need to capture the entire molecular structure of the crystal to simulate the dissolution of the entire crystal), and consequently it can be computationally infeasible to capture the behaviour of large systems using standard kMC.

Based on the above, the objective of this chapter is to present a novel general kMC algorithm that can efficiently capture the movement of any dynamic interface. This kMC algorithm, which shall be referred to as Moving Front kMC (MFkMC), focuses primarily on the interface and how it advances or recedes on a molecular level. The MFkMC algorithm defines the interface as the boundary between the interface molecules, and it captures the interface movement using kinetic-like rate equations based on the fundamental physics responsible for the interface movement. Consequently, MFkMC is widely applicable and can be adjusted to capture any moving interface system, regardless of the physical processes or the composition of each phase. Section 3.1 provides an overview of the background theory and basic structure of the MFkMC method. Subsequently, the full general MFkMC algorithm is presented in Section 3.2. Furthermore, Section 3.3 outlines some of the general challenges and considerations that must be taken into account when developing a MFkMC model for a given application, such as time-dependent event rates, the initialization of new interface sites, dimensionality challenges, and the efficient storage of the system information. Summarizing remarks are provided at the end in Section 3.4.

* The contents of this chapter were published in the Journal of Physical Chemistry B.[23]

3.1 Moving Front Kinetic Monte Carlo Theory & Overview

This section presents the MFkMC algorithm proposed in this work to capture the behaviour of a moving interface system. This approach predominantly focuses on the local dynamic movement of an interface and the prevalent forces that govern its displacement. Taking inspiration from the object characterization approaches found in Object kinetic Monte Carlo,[70,71] the MFkMC approach defines the interface based on the positions of the molecules on every side of this boundary, as illustrated in Fig. 3.1a. Consequently, MFkMC only concerns

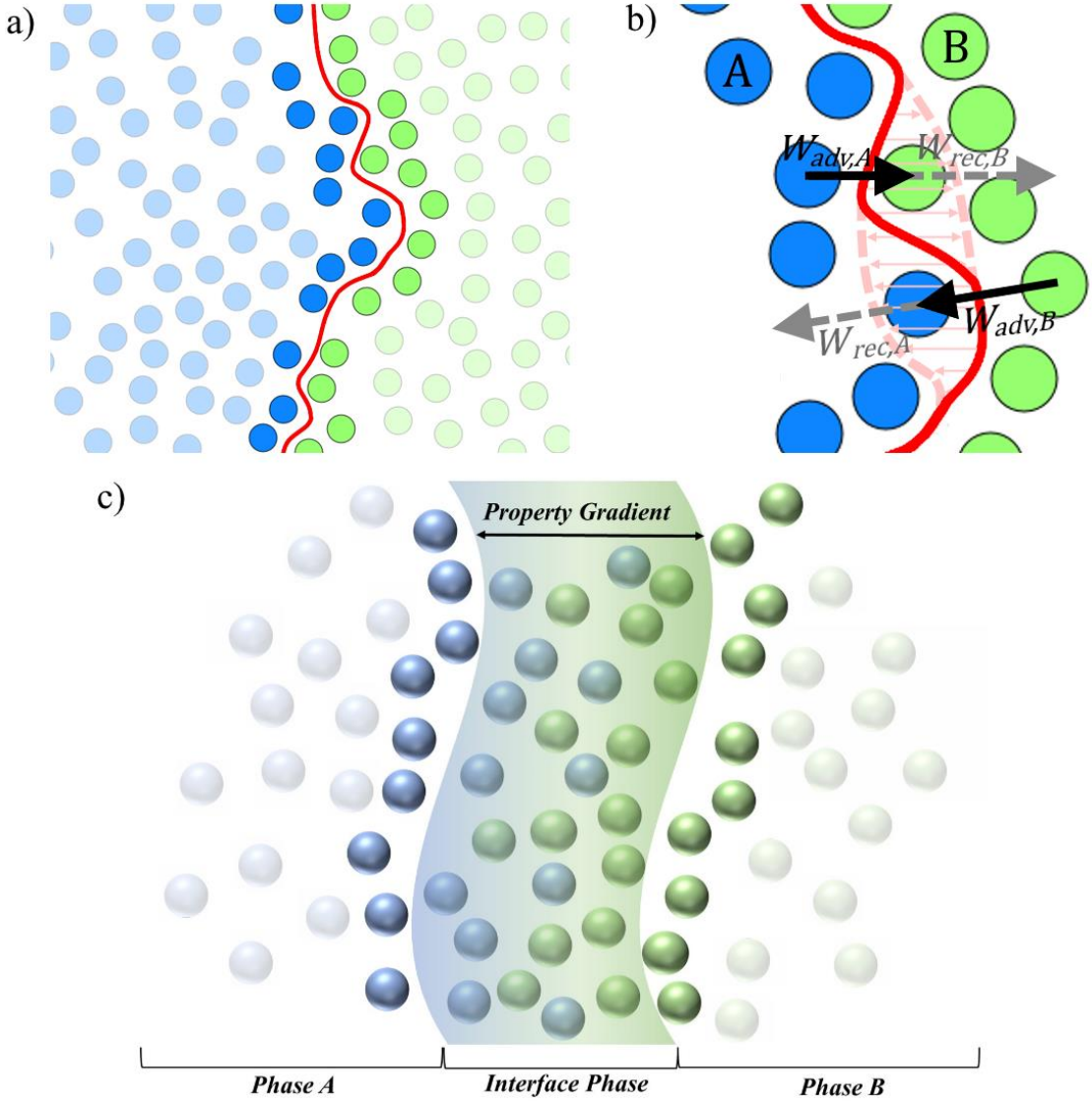

Figure 3.1: a) The interface region modelled by MFkMC. The coloured blue/green circles represent the interfacial molecules of each considered phase, the faded circles represent the bulk phase molecules that are excluded, and the red line denotes the interface; b) The movement of the interface can be subdivided into advancing ($\epsilon_{adv,i}$) and receding ($\epsilon_{rec,i}$) components; c) Illustration of how the MFkMC algorithm can represent a diffuse interface

itself with tracking the interfacial molecules in each phase and disregards the molecules within the phase bulks. To further reduce the degrees of freedom within the system, the MFkMC can be optionally combined with a lattice such that the positions of each interface molecule are restricted to a single lattice point.[67] However, the MFkMC approach does not necessitate lattices and can be readily implemented lattice-free. Note that MFkMC still accounts for the effects of the bulk ions on the interface through the rate equations used to govern the interface site movement; specifically, MFkMC rate equations consider the probability that a bulk phase molecule could advance into the interface and replace a molecule of the adjacent phase, as detailed below. However, MFkMC does not explicitly keep track of the positions or properties of the bulk molecules directly. As a result, MFkMC has to disregard any former interface sites that move into the bulk phase due to the interface movement. Similarly, MFkMC has to construct a new interface every time it considers a former bulk phase site that becomes an interface site due to the movement of the interface. Note that since MFkMC does not explicitly keep track of the positions of bulk phase molecules, each MFkMC model must contain a problem-specific set of rules to determine when and where to initialize new interface sites based on the bulk system properties whenever the interface moves. These rules vary depending on the application and therefore special care must be taken when adapting MFkMC for a new system. However, this initialization process is trivialized in lattice-based systems, as each empty lattice site adjacent to the interface following the interface movement can be assumed to contain a new interface molecule. As a result, it is recommended to implement an MFkMC lattice whenever the lattice-based assumption can be applied, although this is not a stringent requirement for MFkMC. Also note that the MFkMC algorithm can be adapted to accommodate for bulk phase sites if it is needed by coupling it with a separate bulk-phase kMC model; however, details concerning this method are beyond the scope of this work. Finally note that the above framework implies that the interface is sharp and that the properties of the phase on one side of the interface discontinuously jump to the property values of the adjacent phases on the other side of the interface. However, the framework discussed within this work can be readily extended to include diffuse interfaces. This can be accomplished by defining the diffuse interface as its own phase separated from each of the bulk phases by its own sharp interfaces, as illustrated in Fig. 3.1c. Each of the molecules within the interface phase would need to be considered (i.e., they cannot be disregarded unlike the bulk phase molecules) and each molecule's properties would be assigned via a gradient function depending on their position in space relative to the bulk phases. However, this work is predominantly focused on developing moving interface models for sharp interface systems, and therefore the development of MFkMC algorithms for diffuse interface systems will need to be the subject of future work.

The MFkMC algorithm defines the movement of the interface (mf) as a series of probabilistic events where each event $\epsilon_{mf,i}$ describes how a given interface molecule i is replaced by a molecule from the neighbouring phase. These events are each composed of two interchangeable and interdependent sub-events. The first sub-event describes the movement of the selected interface molecule i as it recedes into its own bulk

phase or the bulk of an adjacent phase (receding (rec) sub-event $\epsilon_{rec,i}$). On the other hand, the second sub-event describes the replacement of the previously-mentioned molecule i by a molecule within the neighbouring phase that advances into and occupies molecule i's initial position (advancing (adv) sub-event $\epsilon_{adv,i}$). Therefore, the movement of the interface at molecule i consists of both a receding event $\epsilon_{rec,i}$ and an advancing event $\epsilon_{adv,i}$ where $\epsilon_{mf,i} = \epsilon_{rec,i} + \epsilon_{adv,i}$. Note that the order of these sub-events $\epsilon_{rec,i}$ and $\epsilon_{adv,i}$ is not relevant (i.e., these sub-events are interchangeable), as the interface will move regardless of whether the selected molecule recedes and is subsequently replaced by a molecule from the adjacent phase, or whether a molecule from the adjacent phase advances and displaces the selected interface molecule.

Each event $\epsilon_{mf,i}$ is captured using a kinetic-like rate equation $W_{mf,i}$ that describes the transition probability $P(\delta t, \epsilon_{mf,i})$, given the current state of the system at time t, that the interface movement event $\epsilon_{mf,i}$ takes place at time $t + \delta t$ (where δt denotes a stochastically-generated time interval), as per the rules of kinetic Monte Carlo.[68] This probability can be decomposed into three components: the probability $P_0(\delta t)$ that no event will occur between time t and time $t + \delta t$; the probability $P_{rec}(\delta t, \epsilon_{rec,i})$ that the receding sub-event $\epsilon_{rec,i}$ will occur at time $t + \delta t$; and the probability $P_{adv}(\delta t, \epsilon_{adv,i})$ that the advancing sub-event $\epsilon_{adv,i}$ will occur at time $t + \delta t$. Note that the probability $P_{adv}(\delta t, \epsilon_{adv,i})$ for sub-event $\epsilon_{adv,i}$ does not represent the probability of movement for a specific molecule but rather it represents the probability that any molecule from within the adjacent neighbouring phase will advance into the site presently occupied by interface molecule i. As a result, in order to calculate $P_{adv}(\delta t, \epsilon_{adv,i})$, it is necessary to express this probability based on the individual probabilities $P(\delta t, \epsilon_{adv,i,j})$ that a specific molecule j within the adjacent phase will advance into the specified site i at time $t + \delta t$. In order to calculate $P_{adv}(\delta t, \epsilon_{adv,i})$ as a function of the probabilities $P(\delta t, \epsilon_{adv,i,j})$, consider the probability that any event $\epsilon_{adv,i,j}$ will occur over a vanishingly-small time interval $\delta\tau$ (i.e. the probability that any event $\epsilon_{adv,i,j}$ will occur between time $t + \delta t$ and time $t + \delta t + \delta\tau$). Note that the time interval $\delta\tau$ is different from the larger, unvanishing, and stochastically-generated time interval δt that is used to indicate the system time when the interface movement event $\epsilon_{mf,i}$ takes place. Therefore, the probability $P_{adv}(\delta t, \epsilon_{adv,i})$ can be expressed as follows:

$$P_{adv}\big(\delta t, \epsilon_{adv,i}\big)\delta\tau = \sum_j P\big(\delta t, \epsilon_{adv,i,j}\big)\,\delta\tau + o(\delta\tau) \tag{3.1}$$

where $o(\delta\tau)$ is the probability that more than one event $\epsilon_{adv,i,j}$ will occur over $\delta\tau$, i.e., the probability that multiple molecules j will advance into the site currently or formerly occupied by molecule i between times $t + \delta t$ and $t + \delta t + \delta\tau$. Note that it is expected that $o(\delta\tau) \to 0$ as $\delta\tau \to 0$,[68] and therefore by taking this limit, Eq. (3.1) simplifies to $P_{adv}\big(\delta t, \epsilon_{adv,i}\big) = \sum_j P\big(\delta t, \epsilon_{adv,i,j}\big)$. As a result, the complete expression for the probability $P(\delta t, \epsilon_{mf,i})$ that $\epsilon_{mf,i}$ will take place at time $t + \delta t$ can be expressed as follows:

$$P(\delta t, \epsilon_{mf,i}) = P_0(\delta t)P_{rec}(\delta t, \epsilon_{rec,i})P_{adv}(\delta t, \epsilon_{adv,i}) = P_0(\delta t)P_{rec}(\delta t, \epsilon_{rec,i})\sum_j P(\delta t, \epsilon_{adv,i,j}) \quad (3.2)$$

This equation can be further simplified by defining $W_{mf,i} = P_{rec}(\delta t, \epsilon_{rec,i})\sum_j P(\delta t, \epsilon_{adv,i,j})$ as the rate of occurrence for interface movement event $\epsilon_{mf,i}$. Note that this definition of $W_{mf,i}$ highlights that the rate equation for a given event $\epsilon_{mf,i}$ must simultaneously accommodate for both sub-events $\epsilon_{rec,i}$ and $\epsilon_{adv,i}$ (i.e., it must accommodate for both the rate that interface molecule i will recede into a bulk phase, and that a molecule from the adjacent phase will take the place of molecule i, thus moving the interface.)

The MFkMC algorithm is not restricted to only capturing the movement of the interface and can be readily adapted to consider additional interfacial kinetic events depending on the application, such as interfacial reactions or evaporation and condensation. If the system considers K different kinds of non-moving interface events in addition to the moving interface events, then each of these miscellaneous ($misc$) events ($\epsilon_{misc,k,i}$) can be captured using a kinetic rate equation $W_{misc,k,i}$ that describes the probability $P(\delta t, \epsilon_{misc,k,i})$ that the kth event $\epsilon_{misc,k,i}$ will take place at interface molecule i and at time $t + \delta t$.[68] Note that the subscript $misc$ is used to differentiate the non-moving interface events from the moving interface events, which are depicted using the subscript mf. The probability equation $P(\delta t, \epsilon_{misc,k,i})$ can be similarly decomposed into two (or more) components: the probability $P_0(\delta t)$ that no event will occur between time t and time $t + \delta t$, and the probability $P_{misc}(\delta t, \epsilon_{misc,k,i})$ that the kth non-moving event $\epsilon_{misc,k,i}$ will occur exactly at time $t + \delta t$ and at interface molecule i. By combining the probabilities for both $\epsilon_{mf,i}$ and $\epsilon_{misc,k,i}$, the total probability that event ϵ_i will occur can be expressed as follows:

$$P(\delta t, \epsilon_i) = \begin{cases} P_0(\delta t)P_{rec}(\delta t, \epsilon_{rec,i})\sum_j P(\delta t, \epsilon_{adv,i,j}), & \epsilon_i = \epsilon_{mf,i} \\ P_0(\delta t)P_{misc}(\delta t, \epsilon_{misc,k,i}), & \epsilon_i = \epsilon_{misc,k,i} \end{cases} \quad (3.3)$$

According to the kinetic Monte Carlo framework,[68] the probability $P_0(\delta t)$ can be expressed as follows:

$$P_0(\delta t) = exp(-W_{tot}\delta t) \quad (3.4)$$

where $W_{tot} = \sum_i [W_{mf,i} + \sum_k W_{misc,k,i}] = \sum_i [P_{rec}(\delta t, \epsilon_{rec,i})\sum_j P(\delta t, \epsilon_{adv,i,j}) + \sum_k P_{misc}(\delta t, \epsilon_{misc,k,i})]$ defines the total rate of event ϵ_i taking place at $t + \delta t$. Therefore, the complete expression for $P(\delta t, \epsilon_i)$ can be written as follows:

$$P(\delta t, \epsilon_i) = \begin{cases} P_{rec}(\delta t, \epsilon_{rec,i})\sum_j P(\delta t, \epsilon_{adv,i,j})e^{-W_{tot}\delta t}, & \epsilon_i = \epsilon_{mf,i} \\ P_{misc}(\delta t, \epsilon_{misc,k,i})e^{-W_{tot}\delta t}, & \epsilon_i = \epsilon_{misc,k,i} \end{cases} \quad (3.5)$$

The objective of the MFkMC algorithm is to stochastically evaluate the state-by-state evolution of the moving interface system whose events are governed by the probabilistic distribution in Eq. (3.5). Therefore, in order to advance the system from one state to another, it is necessary to use Eq. (3.5) to stochastically select

both the event ϵ_i taking place and the time increment δt between the selected event and the previously-executed event (i.e. Eq. (3.5) is used to select both the event ϵ_i and the time $t + \delta t$ when the selected event will occur). This probability density function spans both discrete and continuous probability spaces (i.e., the event ϵ_i is selected from a discrete list of *I* possible events $\epsilon = \epsilon_1, \dots, \epsilon_i, \dots, \epsilon_I$, whereas the time increment δt is selected from a continuous distribution $0 \leq \delta t < \infty$) and consequently there is a need to sub-divide $P(\delta t, \epsilon_i)$ into separate discrete and continuous density functions. Using conditioning, the probability density function can be written as follows:

$$P(\delta t, \epsilon_i) = P_{cont}(\delta t) P_{disc}(\epsilon_i | \, \delta t) \tag{3.6}$$

where $P_{cont}(\delta t)$ denotes the probability that any event will occur at $t + \delta t$, and $P_{disc}(\epsilon_i | \, \delta t)$ denotes the probability that the next event to occur will be ϵ_i, given that it will occur at $t + \delta t$. The continuous probability $P_{cont}(\delta t)$ can be calculated using probability addition theorem as follows:[68]

$$\begin{aligned} P_{cont}(\delta t) &= \textstyle\sum_i P(\delta t, \epsilon) \\ &= \textstyle\sum_i \left[P_{rec}\left(\delta t, \epsilon_{rec,i}\right) \sum_j P\left(\delta t, \epsilon_{adv,i,j}\right) e^{-W_{tot}\delta t} + \sum_k P_{misc}\left(\delta t, \epsilon_{misc,k,i}\right) e^{-W_{tot}\delta t} \right] \end{aligned} \tag{3.7}$$

By re-arranging the aforementioned equation and substituting in $W_{tot} = \sum_i \left[P_{rec}\left(\delta t, \epsilon_{rec,i}\right) \sum_j P\left(\delta t, \epsilon_{adv,i,j}\right) + \sum_k P_{misc}\left(\delta t, \epsilon_{misc,k,i}\right) \right]$, the probability $P_{cont}(\delta t)$ simplifies to:

$$P_{cont}(\delta t) = W_{tot} e^{-W_{tot}\delta t} \tag{3.8}$$

On the other hand, the discrete density function $P_{disc}(\epsilon_i | \, \delta t)$ can be obtained by re-arranging Eq. (3.6) as follows:[68]

$$P_{disc}(\epsilon_i | \, \delta t) = \frac{P(\delta t, \epsilon_i)}{P_{cont}(\delta t)} \tag{3.9}$$

By substituting Eqs. (3.5) and (3.8) into Eq. (3.9), the MFkMC event probability $P_{disc}(\epsilon_i | \, \delta t)$ can be expressed as follows:

$$P_{disc}(\epsilon_i | \, \delta t) = \begin{cases} \frac{W_{mf,i}}{W_{tot}}, & \epsilon_i = \epsilon_{mf,i} \\ \frac{W_{misc,k,i}}{W_{tot}}, & \epsilon_i = \epsilon_{misc,k,i} \end{cases} \tag{3.10}$$

where $W_{mf,i} = P_{rec}\left(\delta t, \epsilon_{rec,i}\right) \sum_j P\left(\delta t, \epsilon_{adv,i,j}\right)$ and $W_{misc,k,i} = P_{misc}\left(\delta t, \epsilon_{misc,k,i}\right)$ denote the rates of occurrence for events $\epsilon_{mf,i}$ and $\epsilon_{misc,k,i}$, respectively. Subsequently, the kMC expressions traditionally used to select the time increment δt and the event ϵ_i can be determined by inverting the corresponding continuous and discrete probability distribution functions $F_{cont}(\delta t)$ and $F_{disc}(\epsilon_i | \delta t)$ for Eqs. (3.8) and (3.10), respectively, as follows:[68]

$$\delta t = -\frac{ln(\xi_{cont})}{W_{tot}} \tag{3.11}$$

$$\sum_{m=1}^{i}\sum_{n=1}^{\nu\epsilon-1} W_{m,n} \leq \xi_{disc} W_{i,\nu\epsilon} \leq \sum_{m=1}^{i}\sum_{n=1}^{\nu\epsilon} W_{m,n} \tag{3.12}$$

where $W_{i,\nu\epsilon}$ is the rate of occurrence for event $\epsilon_{i,\nu\epsilon} \in \epsilon_i = \{\epsilon_{mf,i}, \epsilon_{misc,k,i}\}$, where $\epsilon_{i,\nu\epsilon=1} = \epsilon_{mf,i}$ denotes a moving interface event for interface molecule i and $\epsilon_{i,\nu\epsilon>1} = \epsilon_{misc,k=\nu\epsilon-1,i}$ denotes one of the additional non-moving interface events for interface molecule i; and ξ_{cont} and ξ_{disc} denote random numbers generated from a uniform distribution used to calculate δt and select ϵ_i, respectively. Note that Eqs. (3.11)-(3.12) share the same form as the standard kMC time and event selection equations (Eqs. (2.1)-(2.2)) reported within the previous chapter. These concepts serve as the fundamental mathematical principle for the kinetic Monte Carlo methodology, which is the foundation of the proposed MFkMC framework.[68] This furthermore illustrates that the MFkMC moving interface expressions derived above can be captured using kMC techniques, and therefore the MFkMC algorithm can be considered as a branch of kMC extended to describe general moving interface systems. Note that the relevant events and the exact form of the rate equations $W_{mf,i}$ and $W_{misc,k,i}$ varies from application to application. Therefore, the process of event selection and rate determination is described in more detail for each of the systems considered in Chapters 4-7 within this work.

The MFkMC algorithm defines the position and movement of an interface based on the positions and movements of the interfacial molecules on each side of the interface. Each time the interface moves, the algorithm re-defines the interface by removing any former interface molecules that move into the bulk phase and by adding in any former bulk phase molecules that become a part of the interface as a result of the move. Furthermore, the MFkMC method takes into account the known structural features and spatial heterogeneities of any solid surfaces involved in solid-fluid interfaces on a molecular level. As a result, the MFkMC algorithm is able to accurately capture the shape of an interface regardless of its complexity and regardless of the intricacy of any surrounding solid geometries.

The MFkMC algorithm is derived from kinetic Monte Carlo, and therefore it features the same limitations as standard kMC algorithms. However, the MFkMC algorithm has an additional limitation based on the assumptions used to define the moving interface events $\epsilon_{mf,i}$. As indicated above, the moving interface events assume that the two sub-events $\epsilon_{rec,i}$ and $\epsilon_{adv,i}$ occur near-simultaneously at time $t + \delta t$. Although this assumption holds for the majority of moving interface systems, it cannot be assumed for diffusion-limited phases that contain very few bulk molecules such that $\sum_j P(\delta t, \epsilon_{adv,i,j}) \ll P_{rec}(\delta t, \epsilon_{rec,i})$. In these cases, the interface molecules i in one phase recede significantly faster than they can be replaced by molecules in the opposing phase. In order to simulate these kind of systems, it would be necessary to separate the advancing and receding sub-events $\epsilon_{adv,i}$ and $\epsilon_{rec,i}$ into their own separate kinetic events; however this process is beyond the scope of this work.

3.2 MFkMC Algorithm

The proposed general MFkMC algorithm is illustrated in Fig. 3.2 and can be summarized as follows.

1. Initialize the system by defining the location and other relevant parameters for each of the interfacial molecules in every phase of each dynamic interface considered, based on the initial conditions.
2. Determine the initial rates $W_{mf,i} = P_{rec}(\delta t, \epsilon_{rec,i}) \sum_j P(\delta t, \epsilon_{adv,i,j})$ for the local movement of each interface molecule i using their respective rate equations. If there is more than one event that can take place for a given molecule (i.e., if the MFkMC algorithm considers more kinetic events than just moving the interface), then calculate the rate for any remaining kinetic events ($W_{misc,k,i} = P_{misc}(\delta t, \epsilon_{misc,k,i})$, where $\epsilon_{misc,k,i}$ denotes the k^{th} non-moving interface event taking place at the i^{th} interface molecule).
3. Generate a random number ξ_{cont} from a uniform distribution to increment the system time t by the continuous variable δt according to Eq. (3.11). Update any event rates that directly depend on the system time t or the increment time δt.
4. Generate a second random number ξ_{disc} from a uniform distribution to select an event ϵ_i (i.e. an interfacial molecule) from discrete space based on the event rates of occurrence, according to Eq. (3.12). Note that these events include moving the interface ($W_{mf,i}$) or any other interfacial event that is allowed to take place ($W_{misc,i}$).
5. Execute the selected event and update any affected rates at the neighbouring sites, accordingly.
6. Update the list of interfacial molecules to add new interface sites and remove new bulk phase sites created by the change in the interface. If the interface moves, initialize new interfacial sites created by the move (i.e., new interfacial molecules that were in the bulk phase prior to the move), as illustrated in Fig. 3.3. Similarly, remove interfacial sites that become bulk phase sites.
7. Repeat steps 3-6 until a pre-specified end condition has been met (e.g., the system time reaches a final integration time t_f; the system has reached steady state; the interface has completely disappeared, etc.)

3.3 Challenges & Considerations

The framework proposed in the previous section provides a general overview of the MFkMC methodology and its implementation. However, there are still a number of different aspects and challenges that must be addressed so that it can be properly implemented for a given application. Motivated by this, the following sub-sections will outline four main concerns and considerations with developing an MFkMC model, including time-dependent event rates, initializing former bulk phase sites, system dimensionality, and efficient storage of MFkMC information.

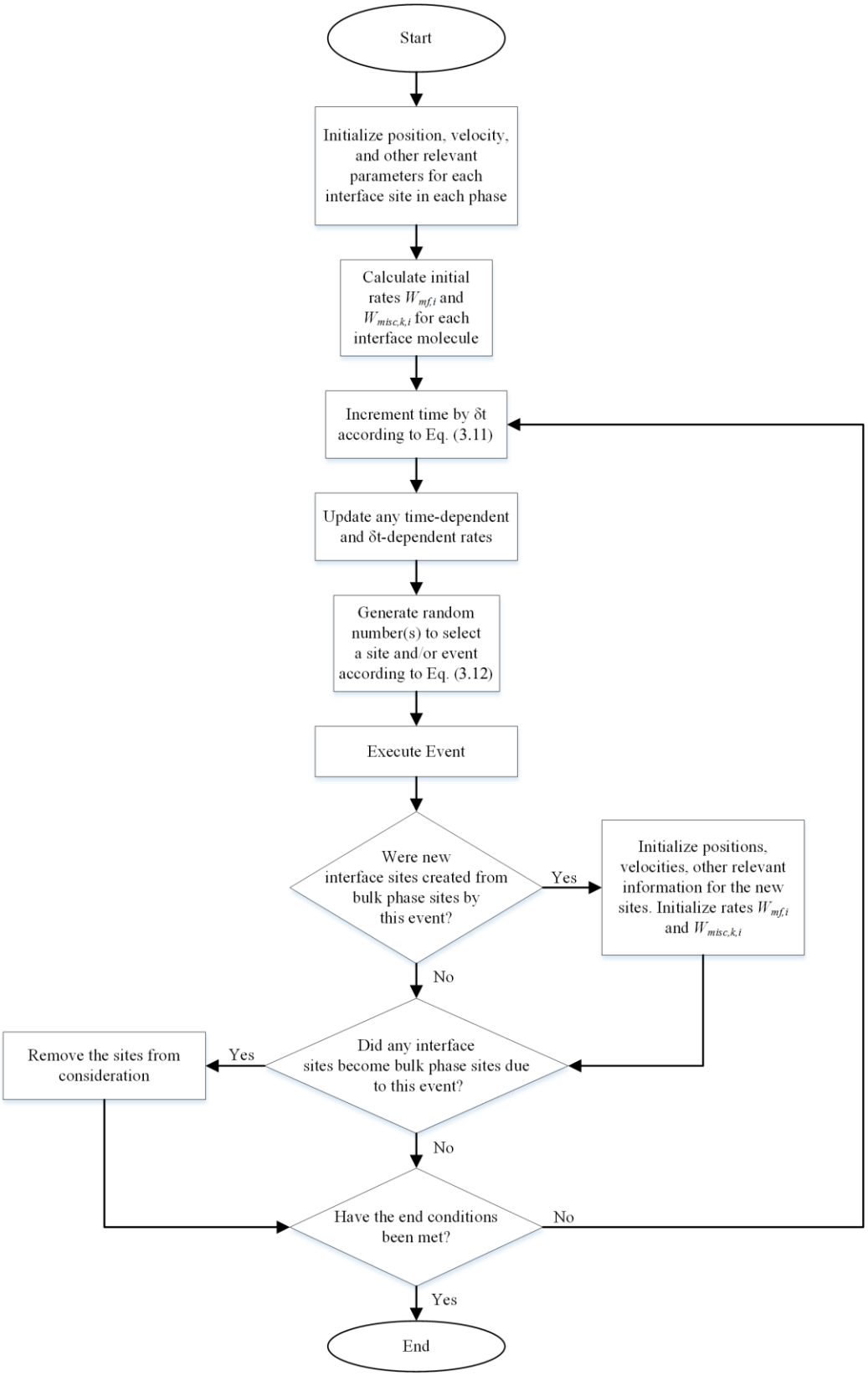

Figure 3.2: Flowchart of the general MFkMC algorithm

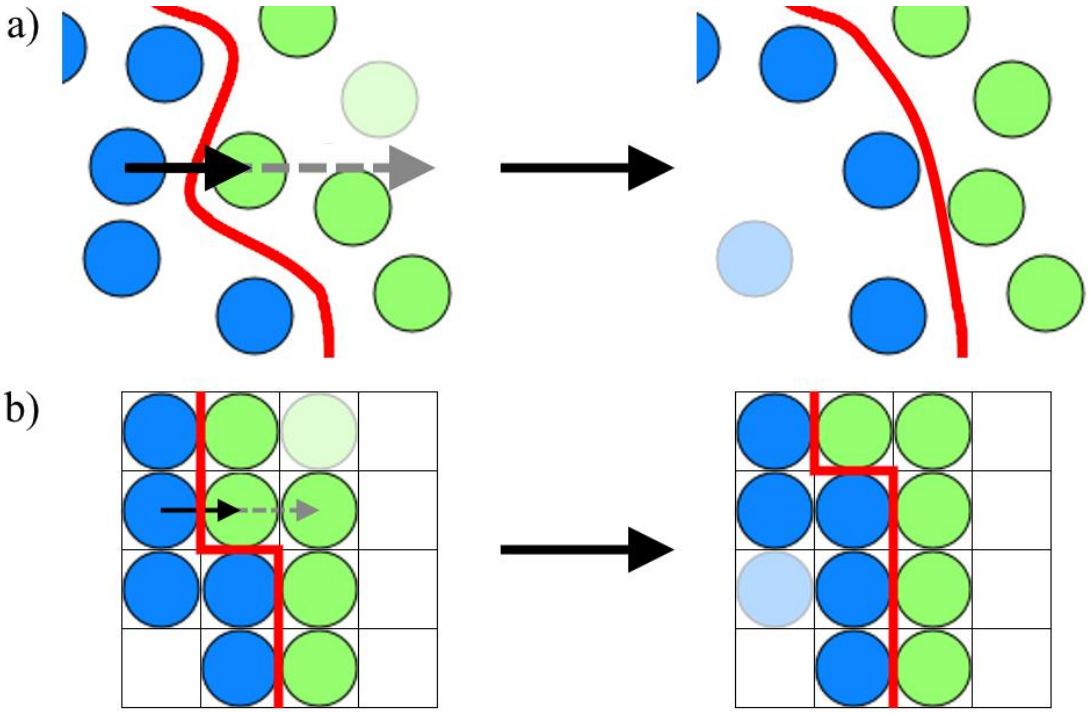

Figure 3.3: The interface region before (left) and after (right) a kMC event is executed using a) lattice-free and b) lattice-based kMC. The pale green circles (on the left) represent bulk phase sites that become interface sites after the event is executed. Similarly, the pale blue circles (on the right) represent bulk phase sites that were on the interface prior to the event

3.3.1 MFkMC for Systems with Time-Dependent Probabilistic Rates

Moving interface systems are dynamic processes whose properties change in time, and consequently, it is expected that the rate equations governing the interfacial movement in MFkMC will vary as the system evolves. However, MFkMC is stochastic in nature, and therefore the system properties and MFkMC rate equations affected by the state-by-state system evolution vary sporadically in time and cannot be represented using a closed-form transient expression. As a result, these system rate equations do not always depend directly on the time t or the rate of change in time δt, i.e., they often only depend indirectly on t or δt through the stochastic MFkMC fluctuations. When a system only involves rates that do not directly depend on t or δt, the order in which the random numbers ξ_{cont} and ξ_{disc} are generated is not relevant, and consequently Step 3 in the algorithm above (calculating the time increment δt) can be performed after Steps 4-6 (selecting and executing an event). Note that there are numerous kMC algorithms reported within the literature where the event selection and execution occurs before time is incremented.[12,13,175–177]

However, MFkMC can also accommodate for systems containing rate equations that depend directly on the time t or the change in time δt. These direct-time-dependent rate equations can occur due to controlled

predictable changes in external variables (e.g., subjecting the system to an externally-controlled temperature gradient in a system whose rates are temperature dependent but whose system evolution does not affect the temperature) or due to time derivative terms within the rate equations themselves that are approximated using finite differences. The latter case is expected to occur in systems whose rate equations are derived based on force balances, such as the sessile droplet studies presented in Chapters 6 & 7. In both of these cases, the order in which the random numbers ξ_{cont} and ξ_{disc} are generated is important. Consider the probability $P(\delta t, \epsilon_i)$ that the system will undergo a specific event ϵ_i at time $t + \delta t$. This probability density function can be separated into discrete and continuous functions $P(\delta t, \epsilon_i) = P_{cont}(\delta t)P_{disc}(\epsilon_i|\, \delta t)$ as illustrated in Eq. (3.6). In this expression, the discrete probability $P_{disc}(\epsilon_i|\, \delta t)$ denotes the probability that the next event to occur will be event ϵ_i, given that it is already known when the event will occur (i.e., δt has already been determined). As a result, it is necessary to calculate δt and determine the time at which the event takes place (i.e., $t + \delta t$) before selecting the event as long as the rates for an event ϵ_i are direct-time-dependent ($\epsilon_i(t)$) or time increment-dependent ($\epsilon_i(\delta t)$). Therefore, in order to provide a general algorithm that can be applied to the largest number of moving interface systems possible, the MFkMC algorithm calculates the time increment δt in Step 3 before determining and executing the event ϵ_i in Steps 4-6. Note that this ordering of steps can still be readily applied to systems whose rate equations that are not direct-time-dependent, as the order in which the random numbers are generated does not matter for these systems.

3.3.2 Initializing Interfacial Particles at Former Bulk Sites

Over the course of the MFkMF algorithm, new interfacial sites must be created and old sites removed whenever the interface moves, as highlighted in Fig. 3.3 and in step 6 of the MFkMC algorithm in Section 3.2. Whenever a new interfacial site is established, special care must be taken to initialize the particle properties such that they reflect the underlying attributes of the system. In a lattice-based MFkMC system, each of the molecules in each phase are assumed to occupy fixed positions according to a pre-set lattice,[67] and therefore new interface molecules are readily initialized by identifying the empty lattice sites that sit adjacent to the interface. On the other hand, in lattice-free MFkMC, the positions of newly-formed interface molecules can be stochastically initialized based on the fluid density using stochastic approaches such as particle swarm optimization[178] or probability distribution-based initialization schemes.[179] An example that can be used for lattice-free initialization is pseudo-lattice, as illustrated in Fig. 3.4. In this technique, the fluid domain is discretized into uniformly-spaced mathematical points separated by the average inter-particle distance, which can be calculated based on the fluid density ρ and particle molar mass m_{mol}.[180] Once the interface moves, this method subsequently identifies the points adjacent to the new interface boundary that do not have an interface molecule within close proximity, and initializes a new interface particle around this point at a position stochastically-generated from a uniform or a normal distribution. In addition to the position, it is also necessary to initialize other relevant parameters, such as the molecule velocity, for each newly-formed interface molecule

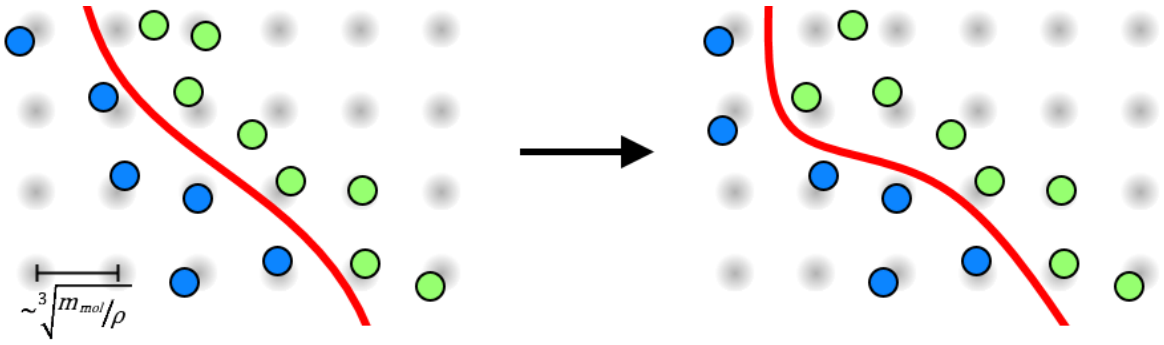

Figure 3.4: Illustration of the pseudo-lattice initialization scheme, where the spatial domains are sub-divided into a grid of evenly-spaced points, and new interface sites are placed at a randomly-placed position around any unoccupied point adjacent to the interface after the interface moves

for both lattice-based and lattice-free systems. These parameters can be assigned either deterministically or stochastically based on either the bulk properties of the system, or the properties of the nearby surrounding molecules. For example, the velocity of a freshly-created interface molecule for a water droplet spreading on a surface can be readily derived based on the velocity of its nearest neighbouring interface sites.[140] On the other hand, in applications such as micelle formation under fluid flow,[181] the velocities of new interface sites are more readily determined based on the overall velocity gradient of the surrounding fluid. Note that the method of initializing new interface molecules should be adapted depending on the application. More specifics are provided when discussing the different moving interface systems studied within each of the subsequent chapters.

3.3.3 Dimensionality of the Moving Interface System

The proposed MFkMC algorithm can be adapted to capture moving interface systems regardless of their underlying physics or their dimensionality. In general, higher-dimensional problems involve more complicated nearest neighbour interactions and often require additional application-specific rules that allow the interface to evolve in a realistic manner; detailed illustrations of this subject matter can be found in the sessile droplet models presented in Chapters 6 & 7. However, as a simple example, consider the spreading of a droplet on a smooth solid surface. In this case, the droplet interface is expected to spread uniformly around a center point, as illustrated in Fig. 3.5a. However, in a fully 3D model, this axisymmetric behaviour is not guaranteed and in the absence of additional rules, the droplet can readily adapt non-physical shapes, as illustrated in Fig. 3.5b. As a result, this 3D system model would require additional restrictions in place to prevent impossible moving interface events from occurring so that the interface will spread in a quasi-axisymmetric manner, as illustrated in Fig. 3.5c. Further details concerning this topic are provided in Chapters 6 & 7. Due to the aforementioned challenges associated with higher-dimensional systems, it is generally recommended to minimize the dimensionality of the considered problem whenever possible to reduce the complexity of the developed

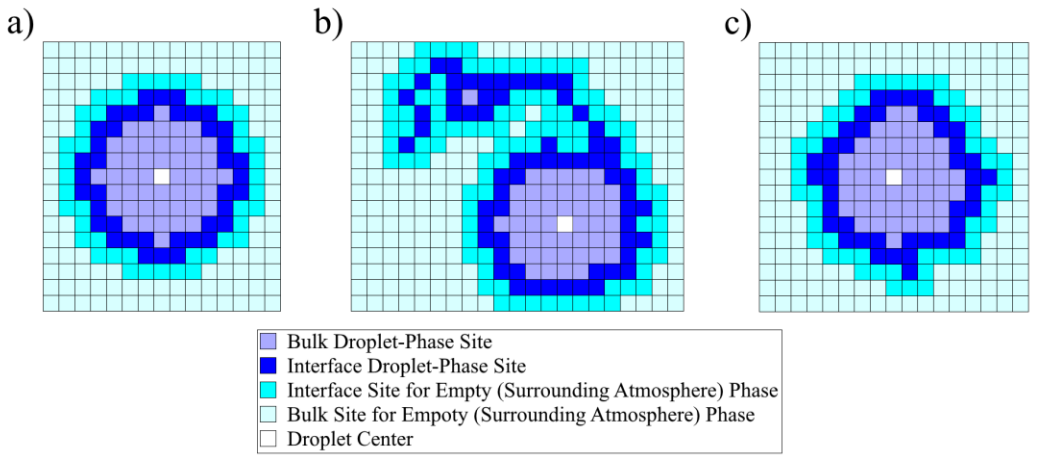

Figure 3.5: a) Expected axisymmetric droplet spreading on a solid surface; b) non-physical droplet spreading for a higher-dimensional model in the absence of model restrictions; c) realistic droplet spreading for a higher-dimensional model under sufficient model restrictions

MFkMC model. However, the reduction in dimensionality can interfere with the model accuracy for systems such as those subject to isotropic molecular-level perturbations, and therefore special care must be taken when deciding on the dimensionality of the proposed MFkMC model to balance both the model complexity/efficiency and the model accuracy.

3.3.4 Information Storage in MFkMC Models

The interfaces in moving interface problems seldom remain the same length and can undergo drastic and significant changes in size over the course of the system evolution, e.g., sessile droplet spread, emulsification of two immiscible liquids, etc. As a result, the MFkMC algorithm needs to be adaptable to account for changes in the sizes of the interfaces and the amount of system information necessary to store. Furthermore, moving interface problems often require knowledge about an interface molecule's nearest neighbour interface sites or other spatial heterogeneities. For lattice-based MFkMC models, the interfacial neighbors can be defined as the particles located in the lattice sites next to a given particle. On the other hand, for lattice-free MFkMC models, the interfacial nearest neighbors are best defined as the particles within a certain distance of a given particle. These nearest neighbor heterogeneities are particularly difficult to identify and store efficiently, and therefore it is imperative that the MFkMC information storage system provide an efficient means to determine a molecule's nearest neighbour information to minimize the system computational cost. There are many different methods that can be used to efficiently store moving interface information, depending on the system and the applied assumptions. Two key storage methods that can be used to efficiently store the relevant interface and nearest neighbor information, the list indexing approach and the sparse matrix approach, are discussed next.

The first potential method for information storage when implementing the MFkMC algorithm is to borrow from the list indexing approaches used in porous network modelling, as shown in Fig. 3.6a.[182] This approach would involve the creation of two lists: one that stores all the relevant information for each interface particle, and one that maps the interface particle "connectivity" (i.e., keeping track of each particle's interfacial nearest neighbors). However, special care must be taken to efficiently update all relevant information, especially the interfacial nearest neighbor information, after every kMC event. In order to avoid having to search through all the currently-stored interface sites to identify the nearest neighbors every time a new interface particle is added, the lists can be updated such that the particle information is stored based on their distance relative to a fixed point, so that the nearest neighbor search can be limited to searching through a handful of particle entries. For example, in Fig. 3.6a, the interface molecule information inside the primary table are ordered according to their proximity to the center of interface molecule A_1. Assuming that nearest neighbor molecules are defined as molecules that are 100 units or less apart, in order to determine the nearest neighbor information for molecule A_4 (197 units from the origin) for the first time, it is only necessary to consider the table entries for molecules situated within ±100 units (between 97 and 297 units from the origin), which are all adjacent to molecule A_4 in the main table, to see if they are nearest neighbors to A_4 or not. In this

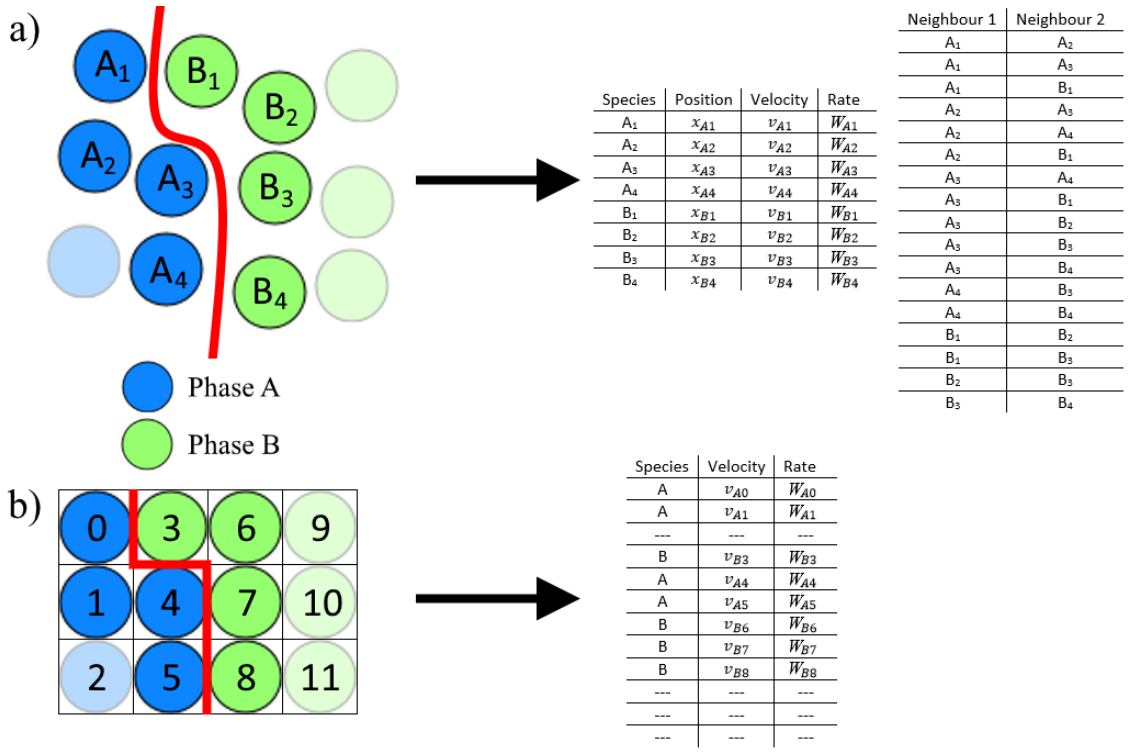

Species	Position	Velocity	Rate
A_1	x_{A1}	v_{A1}	W_{A1}
A_2	x_{A2}	v_{A2}	W_{A2}
A_3	x_{A3}	v_{A3}	W_{A3}
A_4	x_{A4}	v_{A4}	W_{A4}
B_1	x_{B1}	v_{B1}	W_{B1}
B_2	x_{B2}	v_{B2}	W_{B2}
B_3	x_{B3}	v_{B3}	W_{B3}
B_4	x_{B4}	v_{B4}	W_{B4}

Neighbour 1	Neighbour 2
A_1	A_2
A_1	A_3
A_1	B_1
A_2	A_3
A_2	A_4
A_2	B_1
A_3	A_4
A_3	B_1
A_3	B_2
A_3	B_3
A_3	B_4
A_4	B_3
A_4	B_4
B_1	B_2
B_1	B_3
B_2	B_3
B_3	B_4

Species	Velocity	Rate
A	v_{A0}	W_{A0}
A	v_{A1}	W_{A1}
---	---	---
B	v_{B3}	W_{B3}
A	v_{A4}	W_{A4}
A	v_{A5}	W_{A5}
B	v_{B6}	W_{B6}
B	v_{B7}	W_{B7}
B	v_{B8}	W_{B8}
---	---	---
---	---	---
---	---	---

Figure 3.6: a) Storing a (lattice-free) interface using a list indexing approach, where the interfacial molecule properties and the list of neighboring molecules are stored in separate tables; b) Storing a (lattice-based) interface using a sparse matrix, where the location of a molecule corresponds to its location within the matrix. Note that the sparse elements are shown as --- for the sake of illustration

example, there are only four molecules that need to be considered (molecules A_3, B_2, B_3, and B_4). Subsequently, the intermolecular distance can be calculated between each considered molecule and molecule A_4 to determine which molecules are its nearest neighbors (i.e. within 100 units of A_4.) Only molecules A_3 and B_4 are within 100 units of A_4, and therefore these are the only molecules marked on the connectivity table as A_4's nearest neighbors. Note that there are many other methods that can be used to further simplify the nearest neighbor search for a new molecule. For example, the nearest neighbor search procedure can be further simplified for an N-dimensional system by creating N copies of the main information storage table, where particle information is stored in each table relative to their distance in a single dimension with respect to a fixed point, and each table organizes their molecules based on a different dimension. However, these approaches are beyond the scope of this work.

The second information storage method, which works particularly well for lattice-based MFkMC approaches, is to use large sparse arrays to store all the data, where the location of an interfacial particle's data within the array is correlated to its position in space as illustrated in Fig. 3.6b. This approach greatly simplifies finding information about the molecule's nearest neighbors as the locations of the neighbors within the array can be readily determined. This is critical for determining whether new interface sites should be created or old sites removed. However, sparse arrays must be defined with a pre-determined size, and therefore it is possible for systems subject to fast-expanding interfaces or other large interfacial displacements to exceed the pre-allocated sparse matrix dimensions. In order to prevent this issue, it is necessary to include a subroutine within the MFkMC code to re-assign the moving interface system to a sufficiently larger sparse matrix should the system exceed the current matrix dimensions.

3.4 Summary

This chapter provided a detailed general overview of the Moving Front kinetic Monte Carlo algorithm, a novel kMC-based modelling technique designed to simulate moving interface systems. The proposed model defines the location of a time-varying interface based on the positions of the interface molecules on either side of the boundary and assigns rates to capture their ability to advance into or recede away from the opposing phase. The algorithm subsequently stochastically selects an interface molecule to advance/recede based on their rates and executes it in order to migrate the interface. The proposed algorithm is designed to be compatible with other kMC-based techniques so that it could readily account for additional kinetic interfacial phenomena such as interfacial reactions. This chapter additionally provided a brief analysis of key challenges that must be taken into account when constructing an MFkMC model to capture the moving interface behaviour of a given system. For one, the order in which the MFkMC steps should be executed is dependent on whether the MFkMC event rates are directly dependent on changes in time, and therefore special care should be taken to design the algorithm around its events. In addition, MFkMC models suffer from the curse of dimensionality and therefore

additional rules may need to be instated to prevent unrealistic system behaviour at higher dimensions. Finally, the MFkMC algorithm requires proper care and consideration must be taken into account when designing how new interface sites are implemented and when deciding the method of information storage so that MFkMC can both accurately and efficiently capture the general system behaviour. The information presented in this chapter consequently serve as a baseline for the MFkMC algorithms developed and implemented throughout the remainder of this work.

Chapter 4 – MFkMC Crystal Dissolution Model for Biological Systems with Applications in Uncertainty Analysis and Robust Optimization[†]

The dissolution of crystalline minerals is an emerging field of study with wide variety of applications in critical fields such as medicine, geology, and engineering.[19,97,183] The rate and the way in which the materials dissolve is of critical importance in many of these systems. These dissolution mechanisms are highly dependant on the microscale surface structure and consequently, there has been significant interest in studying and modelling the underlying mechanisms behind dissolution on a molecular level in order to control the dissolution rate for a given application. It is thus necessary to simulate crystal dissolution processes using a molecular-level modelling technique such as MFkMC to accurately capture the spatially-heterogeneous nature of the dissolution process. However, this process is complicated by environmental uncertainty in the crystal dissolution systems.[21,22,129] Consequently, it is important to implement techniques in order to accommodate for uncertainty when studying, optimizing, and controlling crystal dissolution processes.

The objective of this chapter is to develop a general 3D MFkMC framework to predict the dissolution of nanoscale defect-free crystals regardless of shape and crystal structure. This study particularly focuses on the dissolution of crystalline drug delivery capsules within the human body, which is of importance in the pharmaceutical industry. The developed MFkMC algorithm is subsequently compared and contrasted with standard kMC crystal dissolution models in order to validate its performance and to showcase the performance difference between the two kinetic Monte Carlo methods. This study furthermore utilizes the developed MFkMC framework to analyze the impact of various crystal sizes and shapes on the dissolution results. This chapter also investigates the effects of environmental uncertainties (e.g. the temperature and pH of the system) on the crystal capsule dissolution process through the use of Polynomial Chaos Expansions (PCEs). Furthermore, low-order PCE coefficient models (LPCMs) are constructed and used to perform computationally-efficient robust optimization on the dissolution model. This combination of methods provides key tools that can be used to further study and improve the design of pharmaceutical drugs and other biological nanocrystal designs to optimize and control their dissolution properties. Section 4.1 presents the 3D MCkMC and standard kMC frameworks developed and implemented to simulate complete crystal dissolution. This section additionally reviews the PCE and LPCM modelling methods implemented within this work. Section 4.2 compares and contrasts both the MFkMC and standard kMC methods for the calcium carbonate case study

[†] The contents of this chapter were published in the Journal of Physical Chemistry B[23] and in the Computers & Chemical Engineering[42]

considered in this work. Section 4.3 subsequently performs uncertainty analysis on the crystal dissolution system, and Section 4.4 presents the robust optimization on the selected case study. Concluding remarks are provided in Section 4.5.

4.1 Modelling Methods

This section provides an overview of the various modelling methods utilized within this chapter. The Moving Front kinetic Monte Carlo and standard kinetic Monte Carlo approaches are presented here to capture the stochastic dissolution behaviour for a crystal of any given composition, shape, and size. The provided kMC algorithms provide a general framework that can be applied to a wide variety of different crystal materials. Furthermore, this section briefly overviews the Polynomial Chaos Expansion and low-order PCE coefficient models used to efficiently propagate parametric uncertainty and perform efficient robust optimization on crystal dissolution systems, respectively.

4.1.1 MFkMC & Standard kMC Algorithms for Pristine Crystal Dissolution

The objective of this subsection is to provide general standard kMC and MFkMC frameworks to simulate complete crystal dissolution for any desired perfect (defect-free) nanoscale crystal regardless of composition or crystal structure. Note that the proposed algorithm can be readily adapted to a wide variety of different crystals regardless of composition, crystal lattice structure, crystal lattice centering, or coordination number, and consequently the algorithm detailed in this section is presented in as general of terms as possible. Furthermore, the model can be readily adapted to accommodate for dissolution for crystals whose structures and compositions entail complex multi-step dissolution processes. However, for the case of simplicity, the algorithm detailed below predominantly focuses on dissolution in crystals with simple dissolution methods, such as in ionic crystals.

In the crystal dissolution process, the surface species break their bonds with their surrounding neighbours and migrate into the bulk fluid phase surrounding the crystal. The energy required for a surface species to dissolve is proportional to the number of bonds it shares with its neighbouring species and the identity of its neighbouring species, and therefore it is necessary to know the local atomic surface configuration in order to determine the dissolution rate for a given surface species. Furthermore, the energy required for dissolving a surface particle is dependent on the angle and spacing between it and its neighbours, which can be determined based on the base lengths and angles of the crystal lattice for a perfect crystal. Consequently, it is additionally necessary to know distances and angles between each surface species and its neighbours, as highlighted in Section 2.2.1. In order to capture these surface heterogeneities, the crystal dissolution process is modeled using lattice-based approaches for both the MFkMC and standard kMC models. These latticing techniques represent

the entire crystal using a 3D mesh, such that each crystal particle is located within its own individual lattice site. Note that the lattice is used within these models as an organizational tool that maps the locations of the crystal particles relative to their neighbours, and consequently the type of lattice needed to adequately describe the crystal depends on the type of centering used (i.e., primitive, face-centered, body-centered, etc.). However, it is possible to capture all the different basic crystal centerings by changing the lattice shape. For example, a primitive cubic lattice is most easily denoted using a cubic lattice, as illustrated in Fig. 4.1a. On the other hand, a body-centered cubic (BCC) can be readily captured using an octahedral lattice, where each lattice site is considered to neighbour four lattice sites above and below it, as illustrated in Fig. 4.1b. Additionally, since the lattice is used to store the locations of each atom, ion, or molecule within the crystal, it is easiest to denote the lattice information of ionic or other polyatomic crystals based on the basic lattice shape formed by all of the species together rather than based on the sublattice occupied by a single species. For example, it is easiest to consider a NaCl crystal as a simple cubic lattice of alternating Na^+ and Cl^- ions, as illustrated in Fig. 4.1a, rather than a face-centered cubic Cl^- lattice with Na^+ cations located between the anions. The lattice stores critical information about each of the crystal particles, and therefore this modelling approach can directly account for crystal structure information of the surface particles such as their species composition, the number of neighbours, the distance between neighbours as indicated by the crystal lattice edge lengths, and the interaxial angles. The angle orientations and crystal edge lengths are determined at each lattice site by assigning labels in each direction, as depicted for a rhombohedral crystal in Fig. 2.2. Note that the angle labels differentiate between each interaxial angle and their supplement (i.e., the angle labels differentiate between acute and obtuse angles for each angle). These labels are determined based on the angle formed between the two planes intersecting at a given direction, as depicted in Fig. 4.2. Note that though this figure depicts a rhombohedral crystal, the methods mentioned in this section can be generally extended and applied to crystals of different shapes and coordination numbers.

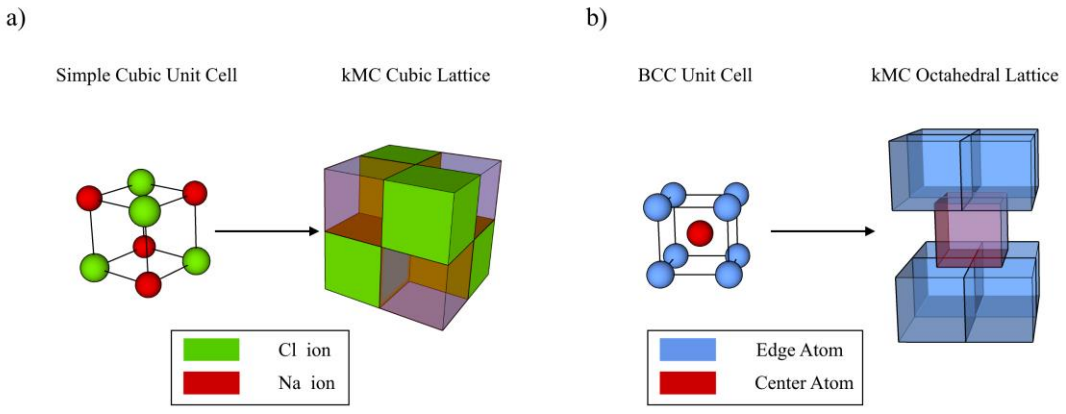

Figure 4.1: Mapping crystal lattices onto kMC lattices: a) mapping a 'simple cubic' NaCl crystal onto a cubic kMC lattice; b) mapping a BCC crystal onto an octahedral kMC lattice

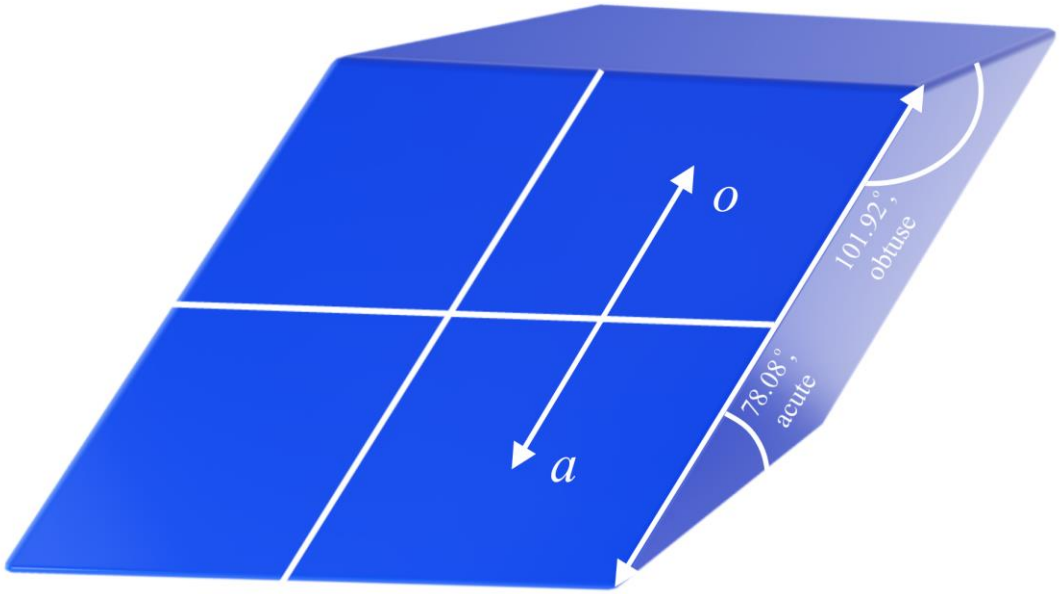

Figure 4.2: Labeling the acute (a) and obtuse (o) directions on the standard kMC/MFkMC lattice

In the present kMC-based algorithms, each surface crystal site is assigned a kinetic rate of dissolution based on its local surface structure, as detailed in Section 2.1.1 and as illustrated in Eq. (2.3). These kinetic rates are locally updated each time that a surface species is removed via dissolution. Note that in addition to the dissolution of the surface molecules, the inverse reaction (i.e., the re-adsorption of dissolved species back onto the surface of the crystal) and surface diffusion of existing crystal surface particles can also occur during the crystal dissolution process, if the concentration of dissolved particles in the fluid adjacent to the crystal is sufficiently high. Under these circumstances, the kinetic rate of re-adsorption and surface diffusion can be captured using kinetic models available within the literature.[72,98] However, it is predominantly assumed within the literature that the dissolved species are rapidly transported away from the surface of the crystals such that the concentration of dissolved species at the crystal surface is inconsequential, and therefore the rates of re-adsorption and surface migration during crystal dissolution are negligible.[80,90] As a result, the general kMC model presented within this work assumes that the dissolved particles are transported away from the crystal surface fast enough such that re-adsorption would only insignificantly affect the model results, and therefore the kinetic rate of re-adsorption is neglected.

The crystal dissolution process considered in this study is modeled using both standard kMC and MFkMC techniques. In both methods, the crystal shape and structure are captured using lattice-based approaches due to the well-ordered nature of crystals. In standard lattice-based kMC, the crystal is mapped to a 3D cubic lattice such that each ion within the crystal occupies its own unique lattice site, as illustrated (in 2D) in Fig. 4.3a. The crystal is then dissolved according to the standard kMC algorithm listed in Section B.1. In

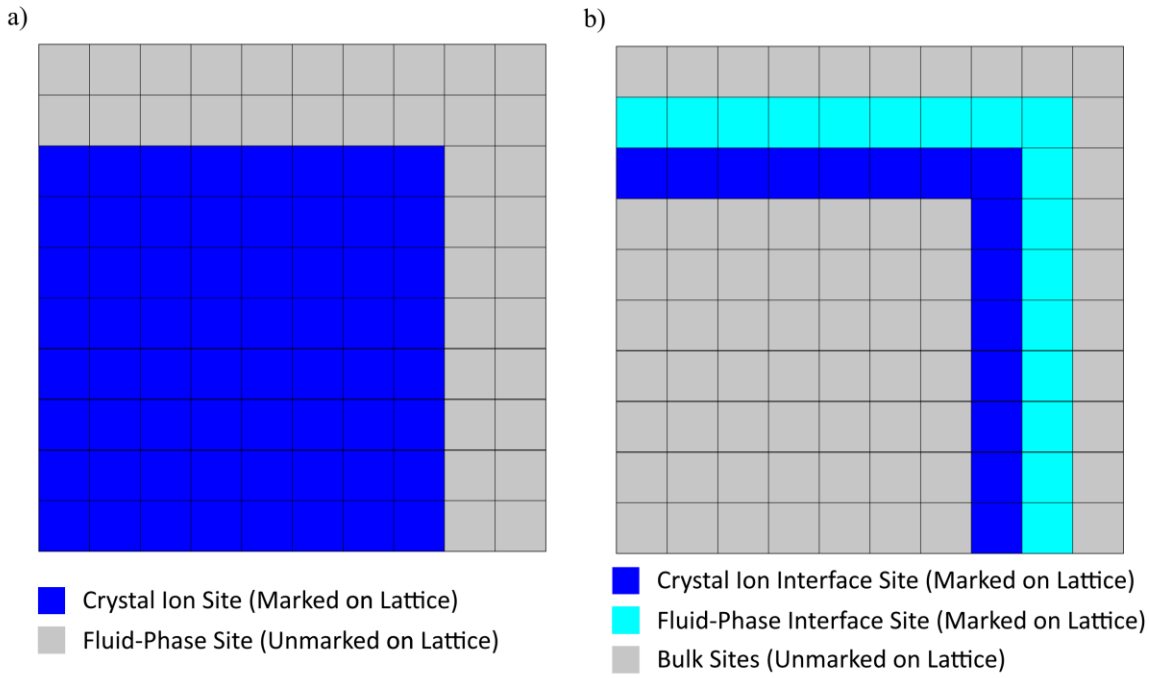

Figure 4.3: 2D representation of initializing a section of a kMC lattice for crystal dissolution applications: a) Lattice initialization according to standard kMC; b) Lattice initialization according to MFkMC

contrast, the MFkMC algorithm only maps the locations of the crystal surface ions and their neighbouring fluid phase sites on the lattice (i.e., it only maps the locations of the interface sites). As a result, all bulk crystal ions and all bulk phase fluid sites are marked as empty on the MFkMC lattice, as illustrated (in 2D) in Fig. 4.3b. Since the crystal dissolution model does not consider any crystal growth mechanisms, the MFkMC crystal dissolution model is most readily captured using the sparse lattice-based approach discussed at the end of Section 3.3.4. Note that in the absence of crystal growth, there is no need to assign a moving interface event rate to any of the fluid-phase interface sites, since the fluid molecules will not be displaced by the solid crystal. In addition, the only relevant information to store for the MFkMC algorithm corresponds to the number of nearest neighbours in each direction $\boldsymbol{n_{bd}}$, the corresponding angle information $\boldsymbol{\Theta_{n_{bd}}}$, and the dissolution rate $W_{cd,\boldsymbol{n_{bd}},\boldsymbol{\Theta_{n_{bd}}}}$ for each surface ion. The complete MFkMC algorithm for crystal dissolution is listed in Section B.2. Note that since the kinetic rate of dissolution $W_{cd,\boldsymbol{n_{bd}},\boldsymbol{\Theta_{n_{bd}}}}$ (Eq. (2.3)) does not directly depend on the time t or the time increment δt, it does not matter whether δt is calculated before or after the event selection step within both the standard kMC and MFkMC algorithms, as discussed in Section 3.2.2. However, the time increment δt was calculated before selecting an event in both of the algorithms presented above in order to mirror the MFkMC structure presented in Section 3.2.

4.1.2 Polynomial Chaos Expansions

The kMC approaches discussed above are unable to explicitly account for the parametric uncertainty that is expected to occur in the crystal dissolution system. Often, scenario-based kMC-type simulations would be required to take uncertainty into account. For example, for crystal dissolution within a gastrointestinal system, the kinetic rates of dissolution are sensitive to properties of the dissolving fluid that are expected to vary and cannot be known with complete certainty, such as the fluid temperature and its pH. Therefore, in order for a kMC or MFkMC model to accurately capture the crystal dissolution process within the gastrointestinal tract, it is necessary for the simulation to account for the uncertainty in these parameters and their effects on the kinetic rates of dissolution. However, this technique is computationally prohibitive since it involves multiple simulations of the kMC-type model under different operating conditions. The way uncertainty is addressed in this study is described next.

Parametric uncertainty was propagated through the crystal dissolution model via the use of Polynomial Chaos Expansions (PCEs). These low order expansions approximate the variability in the model outputs $\boldsymbol{\Psi}$ at specific time points as a function of the uncertain parameters $\mathbf{H}$ using chaos polynomials functions according to Eq. (4.1). Note that any spatial or temporal variations in the model outputs $\boldsymbol{\Psi}(\boldsymbol{x}, t)$ can be taken into account by discretizing the relevant space and time domains ($\boldsymbol{x}$ and t, respectively) into a set number of distinct points and measuring the variability due to uncertainty at each point. A unique PCE model can be subsequently constructed to capture the effects of uncertainty at each discrete point in space and time. The PCE algorithm implemented within this work only considers temporal variability within the model outputs, which is discretized into *M* distinct timepoints t_m, i.e. $\boldsymbol{\Psi}(t_m)$. Consequently, the PCE notation used throughout the remainder of this study will only denote time dependence; examples of PCE models with spatial dependencies can be found elsewhere within the literature.[176,184,185] The polynomial chaos expansion models can be expressed as follows:

$$\boldsymbol{\Psi}(t_m) = \sum_{\chi=0}^{\infty} \boldsymbol{a}_{\chi}(t_m)\, \boldsymbol{b}_{\chi}^{\boldsymbol{H}}(\boldsymbol{\Xi}_{\boldsymbol{H}}) \tag{4.1}$$

where $\boldsymbol{a}_{\chi}(t_m)$ represent the PCE coefficients of the χth order at a discretized timepoint t_m whereas $\boldsymbol{b}_{\chi}^{\mathbf{H}}(\boldsymbol{\Xi}_{\mathbf{H}})$ denotes a χth order polynomial basis function orthogonal to the uncertainty distribution $\mathbf{H}$. Note that these orthogonal polynomials are functions of $\boldsymbol{\Xi}_{\mathbf{H}} = \left[\xi_{1,\eta_1}, \ldots, \xi_{i,\eta_i}, \ldots, \xi_{\mathcal{I},\eta_{\mathcal{I}}}\right]$, where ξ_{i,η_i} denotes a random value generated based on the uncertainty probability distributions applied to the i^{th} uncertain parameter $\eta_i \in \mathbf{H}$. Furthermore, note that the PCE coefficients $\boldsymbol{a}_{\chi}$ can be determined via different methods, such as the intrusive Galerkin projection,[186] non-intrusive spectral projection (NISP),[187,188] or least-squares methods.[176,184] In this study, the least-squares method is used to fit the PCE coefficients to sample data generated by propagating random realizations in the uncertain parameters through the kMC models. The time-dependent

PCE algorithm considered in this study is based off of PCE methods developed previously within the literature,[186–188] and is described within Section B.3.

The PCE algorithm provides a computationally efficient means to propagate uncertainty through the crystal dissolution system. However, the computational speed of sample-based PCE is restricted by the number of sampling points used to determine the PCE coefficients $\boldsymbol{a}_\chi$, in addition to the number of uncertain parameters $\mathcal{I}$ in **H** and the PCE order χ. Lower order PCE polynomials and coefficients determined with fewer sampling points are more computationally efficient. However, these models are prone to larger computational errors and are thus more inaccurate. On the other hand, higher order PCE polynomials and coefficients determined with a larger number of sampling points may be able to achieve greater accuracy; however, more intensive offline calculations are needed to obtain such models. As a result, it is necessary to determine *a priori* the optimal number of sample points and PCE order to achieve sufficient accuracy while maintaining the lowest-possible computational time. In addition, it can be computationally expensive to perform optimization on a system model using PCE. This is because the PCE models are only defined for a single realization in the known design and operational parameters that influence the system performance, and therefore a unique PCE model would need to be developed for every design parameter combination considered within the optimization process. As a result, it is necessary to minimize the computational cost of PCE model development for a given system. The key computational sinkhole within least-squares and other non-intrusive PCE methods is due to the determination of the PCE coefficients, which require generating numerous sample points using the kMC-based models. To overcome this computational limitation, low-order PCE coefficient models (LPCMs) can be developed to approximate the values of the coefficients for a given set of design and operational parameters. The LPCM method is discussed next.

4.1.3 Low-Order PCE Coefficient Models

The PCE method is only capable of propagating parametric uncertainty under a single set of design conditions **ω** at which the PCE model was established. Consequently, it is necessary to develop a method to determine the PCE coefficients for an arbitrary set of design parameters. In order to accomplish this objective, a series of data-driven low order models were developed to predict each PCE coefficient $\boldsymbol{a}_\chi(t_m)$ as a function of **ω**. These low order PCE coefficient models (LPCMs) were determined by discretizing the set of design parameters **ω** into a finite number of realizations and developing a unique PCE model at each design parameter combination. Low order models were then selected to approximate the relationship between each PCE coefficient $\boldsymbol{a}_\chi(t_m)$ and the design parameters **ω**. The LPCM coefficients were subsequently determined using model regression techniques. The full LPCM algorithm considered in this work was adapted based on previous works in the literature[74,189] and can be found in Section B.4. Note that a unique LPCM was constructed for each PCE coefficient $\boldsymbol{a}_\chi(t_m)$ considered, i.e., a unique LPCM model was constructed for each coefficient within

the total dissolution time (t_d) PCE model and for each coefficient within the PCE models constructed for the number of atoms remaining within the crystal $n_d(t_m)$ at each timepoint t_m.

The developed LPCMs are computationally efficient and capable of generating a PCE model for a given **ω** within short computational times. However, the LPCMs rely on low order model fittings and therefore require careful design in order to minimize errors and achieve sufficient accuracy. The LPCMs implemented in this study were developed using PCE coefficient data determined for each of the key system outputs $\boldsymbol{\Psi}(t_m)$ at defined set points in the design parameters **ω**. The discretization of **ω** was selected *a priori* in order to determine the minimum number of design parameter points necessary to adequately capture the relationship between the PCE coefficients and **ω** with sufficient accuracy while still minimizing the number of required PCE models and therefore minimizing the required amount of computational resources. The corresponding LPCM models were selected and fit to the PCE coefficients using CurveExpert Professional 2.6. Furthermore, the LPCM methods are only defined over a specific range of design and operational parameters, and therefore they cannot be used to predict PCE models outside of this region of parameter space. It is thus necessary to determine in advance the parameter range in **ω** over which the LPCM models are to be defined.

4.2 Comparison of MFkMC and Standard kMC Crystal Dissolution Models

The MFkMC and standard kMC crystal dissolution schemes proposed in Section 4.1.1 were implemented in this work to study the complete dissolution of defect-free ionic Calcium Carbonate ($CaCO_3$) crystals dissolving within the human gastrointestinal system. This mineral has been previously simulated using a 2D standard kMC model that captured dissolution along the surface of a single crystal face, and the model kinetics were validated via comparison to experimental results.[90,109] Therefore, this mineral was selected for the case study as its kinetics have already been previously reported and validated within the literature. $CaCO_3$ has a rhombohedral crystal structure and therefore each of the bulk $[CO_3]^{2-}$ anions are coordinated with six metallic Ca^{2+} ions; similarly, each of the Ca^{2+} cations are coordinated with the oxygens from six different carbonate ions. Consequently, each ion can be characterized using the Terrace Ledge Kink (TLK) model, as detailed in Section 4.1.1.[90,109]

Due to its rhombohedral crystal structure ($l_{\vec{a}} = l_{\vec{b}} = l_{\vec{c}}$; $\vartheta_\alpha = \vartheta_\beta = \vartheta_\gamma \neq 90°$), $CaCO_3$ will predominantly cleave along three planes that intersect each other at non-right angles, as highlighted in Fig. 4.4. These planes intersect at an acute angle of $\vartheta_{\alpha,a} = 78.08°$ or at the supplementary obtuse angle of $\vartheta_{\alpha,o} = 101.92°$, depending on their orientation. Consequently, ledge and ledge adatom ions located at the intersection of two crystal planes can take on either an acute (a) or an obtuse (o) orientation ($\boldsymbol{\Theta}_{\boldsymbol{n_{bd}}} = [a, o]$ for $n_{bd,tot} = 2$ and $n_{bd,tot} = 4$ in Eq. (2.3)). Similarly, kink ions occur at the intersection of all three crystal planes and thus

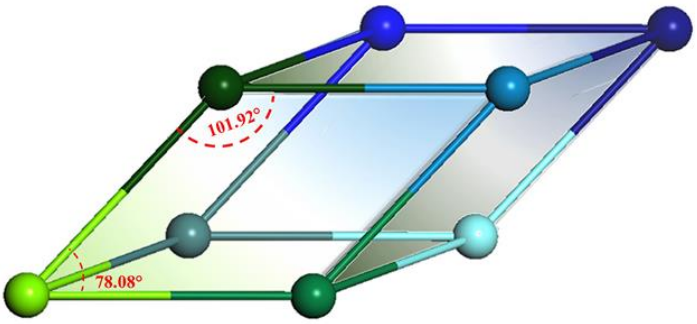

Figure 4.4: The rhombohedral crystal structure of $CaCO_3$

can take on two different (acute-acute-acute (aaa) and obtuse-obtuse-acute (ooa)) configurations ($\boldsymbol{\Theta}_{\boldsymbol{n_{bd}}} = [aaa, ooa]$ for $n_{bd,tot} = 3$ in Eq. (2.3)). In general, surface ions with a larger number of obtuse angles (e.g., obtuse ledge sites or ooa kink sites) dissolve faster as these sites are more exposed to the surrounding fluid. As a result, each of the different ledge and kink orientations dissolve at different rates depending on their angles of intersection with the crystal planes. Note that the present study assumes that the terrace ($n_{bd,tot} = 5$) stabilization effects described in Section 4.1.1 do not occur; hence, $\Delta E_T = 0$. Furthermore, because the lattice edge lengths are the same for a rhombohedral crystal ($l_{\vec{a}} = l_{\vec{b}} = l_{\vec{c}} = 3.2$ Å),[128] the activation energy term E_υ in Eq. (2.3) is the same in all directions υ and therefore the activation energy is represented using the symbol E. The full list of kinetic parameter values are derived from the literature[90] and are listed in Table 4.1.

The kMC model considered in this work is constructed to perform dissolution on $CaCO_3$ crystals with a wide variety of different designs. Consequently, this model takes as inputs the size (s) and shape ($\measuredangle$) of the

Table 4.1. $CaCO_3$ dissolution kinetic parameters

Parameter	Symbol	Value
Temperature	T	310 K
Dissolution pre-exponential constant	k_0	5.22×10^{10} s^{-1}
Activation energy of dissolution for a Ca-CO_3 bond (Activation energy for $CaCO_3$ ionic bond hydrolysis)	E	0.164 eV
Acute ledge/ledge adatom correction activation energy	ΔE_a	0.0465 eV
Obtuse ledge/ledge adatom correction activation energy	ΔE_o	0 eV
Acute/acute/acute kink correction activation energy	ΔE_{aaa}	0.0465 eV
Obtuse/obtuse/acute kink correction activation energy	ΔE_{ooa}	0.0388 eV
Cleavage face stabilization energy	ΔE_T	0 eV

$CaCO_3$ crystal to be studied. Note that the crystal shape is not a feature that can be easily quantified, and as a result there are several ways that can be used to define this design parameter. During crystal growth, the shape of the crystal can be quantified by the relative growth rates of the key crystal planes, and consequently these growth rates have been used to define crystal shape within previous works in the literature.[98,102] However, a much wider variety of crystal shapes can be achieved via processes such as physical and chemical etching.[190] This work considered four distinct crystal shapes that were applied to the $CaCO_3$ model, i.e., rhombohedral cubic ($cube$), spherical ($sphere$), tetrahedral ($tetra$), and dodecahedral ($dode$). Note that these shapes were selected to consider a wider diversity in the types of surface sites present on the crystal (e.g., terrace, edge, or kink sites). Shapes such as the tetrahedral and spherical crystals have higher ratios of the ledge ($n_{bd,tot} = 4$) and kink ($n_{bd,tot} = 3$) sites, whereas shapes such as the cubic and dodecahedral crystals have higher ratios of the terrace ($n_{bd,tot} = 5$) sites. Note that most of these shapes cannot be obtained through normal $CaCO_3$ growth methods, and therefore it is assumed that the calcium carbonate crystals were templated or cut and etched after growth in order to obtain the desired shapes. These techniques have been previously used within the literature to synthesize crystal nanoparticles of various different shapes.[191,192] Note that the objective of this study is to quantify the effects of different crystal shapes on the dissolution process under uncertainty in the system's parameters. Consequently, the synthesis of the aforementioned shapes is beyond the scope of this research. In contrast to the crystal shape, the sizes of the crystals were well-defined for the kMC model and measured by the total number of calcium and carbonate ions within the crystal, i.e., through the atomic volume of the crystal.

For a given set of design parameters s and $\measuredangle$, the kMC algorithms simulate the crystal dissolution process and subsequently output the total dissolution time t_d and the number of particles remaining in the crystal $n_d(t)$ at various time points $t = t_m$. The number of particles remaining are used to estimate the crystal dissolution rates in time according to the following backward finite difference expression:

$$r_d(t_m) \approx \frac{n_d(t_m) - n_d(t_{m-1})}{t_m - t_{m-1}} \tag{4.2}$$

Note that the dissolution rates were estimated in this manner to simplify the application of the PCE models described in Section 4.3.3, as the crystal dissolution rates calculated directly from the kMC models were extremely noisy and highly sensitive to the inherent kMC stochastic fluctuations. As a result, it was difficult to observe the effects of uncertainty on the directly-calculated dissolution rates. Hence, the dissolution rates were calculated based on the rate of change in the number of atoms within the crystal for the sake of simplicity. The dissolution rates were calculated in this manner as it was observed that this method could capture the dissolution rate with sufficient accuracy and without excessive fluctuations due to stochastic noise over the intervals of time considered in this work.

The MFkMC and standard kMC crystal dissolution models discussed above were implemented to model the dissolution of $CaCO_3$ crystals of various sizes s in water. The crystals simulated within this study were

cubic rhombohedrons with equal base length $l_{\vec{a}}$, width $l_{\vec{b}}$, and height $l_{\vec{c}}$ (i.e. $l_{\vec{a}} = l_{\vec{b}} = l_{\vec{c}}$, where the crystal size $s = l_{\vec{a}} l_{\vec{b}} l_{\vec{c}}$). This study considered the dissolution of crystals of five different sizes $s = [8^3, 18^3, 28^3, 38^3, 48^3]$. Both the standard kMC and the MFkMC crystal dissolution models were used to calculate the total dissolution time t_d necessary for the crystal to completely dissolve, and the number of ions remaining within the crystal as a function of time, $n_d(t_m)$. To minimize the kMC-induced inherent stochastic variability in the results, each crystal was simulated 10 independent times using both methods; the results were averaged to showcase the expected model performance for each method.

Table 4.2 lists the average crystal dissolution time t_d for each crystal size as calculated via standard kMC and MFkMC. In addition, Fig. 4.5 illustrates the variability in n_d as a function of time for each of the crystal

Table 4.2. Total dissolution times, computational costs, and memory usage requirements of the standard kMC and MFkMC $CaCO_3$ dissolution models for crystals of different sizes

Size (ions)	Modelling Method	t_d (s) (% Error)	CPU Time (s) (% of Standard kMC speed)	Peak Memory Allocation (GB) (% of Standard kMC memory)
$s = 8^3$	Standard kMC	0.0966574	0.781239	30.7853
	MFkMC	0.0965378 (0.124%)	7.94446 (1017%)	15.4243 (50.10%)
$s = 18^3$	Standard kMC	0.375573	69.7685	32.6622
	MFkMC	0.371833 (0.996%)	108.414 (155.3%)	16.7918 (51.41%)
$s = 28^3$	Standard kMC	0.684406	879.631	37.6286
	MFkMC	0.693743 (1.364%)	618.339 (70.30%)	17.5095 (46.53%)
$s = 38^3$	Standard kMC	1.0223	4112.16	47.3686
	MFkMC	1.01848 (0.374%)	2005.45 (48.77%)	19.925 (42.06%)
$s = 48^3$	Standard kMC	1.35121	20005.3	63.4289
	MFkMC	1.3383 (0.956%)	7036.34 (35.17%)	29.0104 (45.74%)

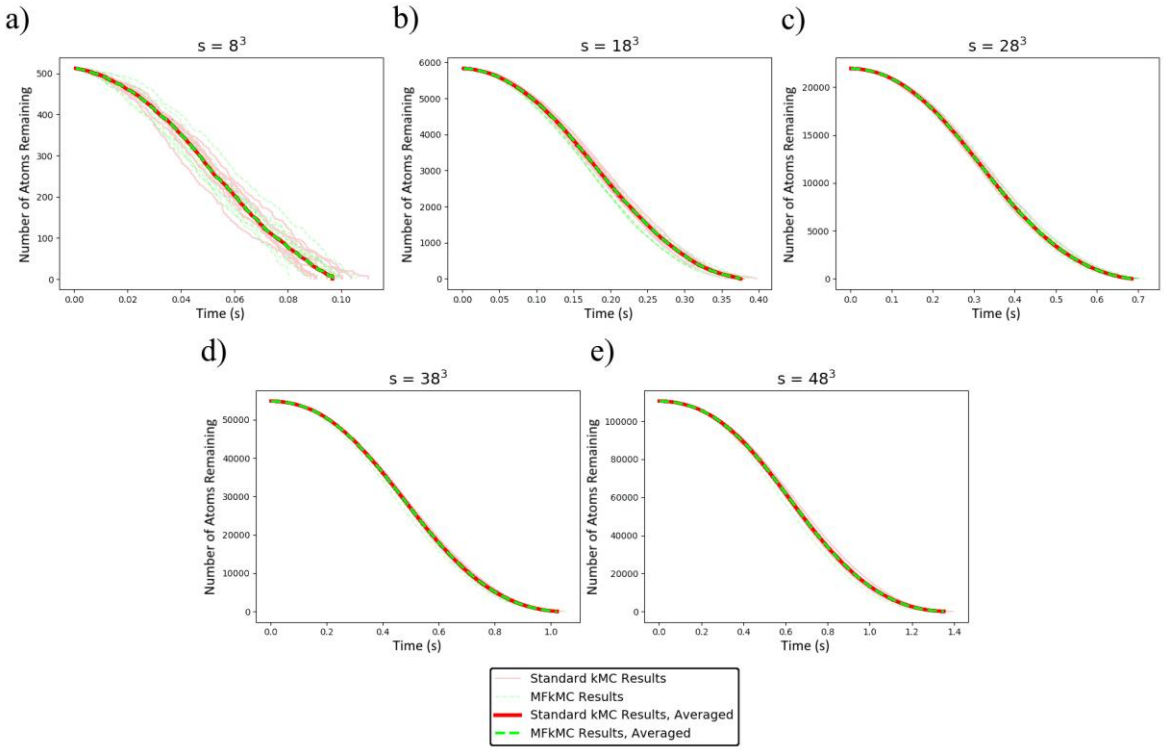

Figure 4.5: Number of atoms remaining $\boldsymbol{n_d(t)}$ in the $CaCO_3$ crystal as a function of time generated using standard kMC (blue) and MFkMC (green): a) for $s = 8^3$ ions; b) for $s = 18^3$ ions; c) for $s = 28^3$ ions; d) for $s = 38^3$ ions; e) for $s = 48^3$ ions

sizes using both standard kMC (blue solid lines) and MFkMC (green dashed lines). Note that in this figure, the fainter lines of each colour showcase the results of each independent standard kMC and MFkMC simulation, whereas the single darker line depicts the average n_d value at each point in time, averaged over each of the 10 independent runs for each method. These results illustrate that the MFkMC and standard kMC modelling approaches exhibit a similar performance and output similar results (percent errors <2%, as shown in Table 4.2). The results in Fig. 4.5 also illustrate the natural stochastic variability experienced by both kMC modelling methods. Note that the effects of the noise are more significant for the smaller crystal sizes, whereas they are insignificant for the larger crystals. The results furthermore showcase the nonlinear nature of the crystal dissolution process. This nonlinear behaviour occurs due to the ratio of the slow-dissolving terrace sites ($n_{bd,tot} = 5$) to the faster-dissolving ledge ($n_{bd,tot} = 4$) and kink ($n_{bd,tot} = 3$) sites, where the number of nearest neighbours $n_{bd,tot}$ impacts the kinetic dissolution rates as highlighted in Eq. (2.3). At the beginning of the dissolution process, the cubic rhombohedral crystal predominantly consists of terrace sites, resulting in slower initial kinetics. As the crystal dissolution process evolves, the crystal surface roughens and contains a higher ratio of the fast-dissolving kink sites, producing faster dissolution rates. The dissolution rate slows down as the crystal nears complete dissolution and the number of available surface ions decrease to zero. Table 4.2

additionally lists the computational costs and memory usage requirements for both the MFkMC and standard kMC methods for each of the crystal sizes. Note that the % kMC speed and % kMC memory values reported for the MFkMC results were calculated as follows:

$$\frac{CPU_{MFkMC}}{CPU_{skMC}} \times 100\% \tag{4.3}$$

$$\frac{Memory_{MFkMC}}{Memory_{skMC}} \times 100\% \tag{4.4}$$

These results showcase the superiority of the MFkMC algorithm in terms of memory allocation, as the MFkMC algorithm at its peak required on average only 50% of the total memory demanded by the standard kMC algorithm at its peak, regardless of the crystal size. Furthermore, they highlight that the MFkMC algorithm is computationally faster for larger systems, whereas it is slower for smaller systems compared to standard kMC. For the smallest crystal size considered ($s = 8^3$ ions), the MFkMC algorithm required an order of magnitude more computational cost compared to standard kMC. However for the largest crystal size ($s = 48^3$ ions), the MFkMC algorithm required an order of magnitude less computational time to simulate compared to standard kMC. This computational behaviour is due to the fundamental differences between the standard kMC and MFkMC approaches. Over the course of the execution of a single event, the MFkMC algorithm has more to accomplish as it must create new interface sites and remove new bulk sites brought about by the interface movement, in addition to executing the same tasks as standard kMC. However, the MFkMC algorithm disregards any molecules or sites within the bulk phase, and therefore it keeps track of significantly fewer molecules/sites on average compared to standard kMC, especially for large systems. Note that even though the bulk crystal sites have a zero reaction rate, the standard kMC model still needs to accommodate for them when selecting the molecule/site at which to execute the kMC event. As a result, the event selection process is faster for MFkMC since there are fewer molecules/sites to choose from compared to standard kMC. Although these computational savings are insignificant for small systems, they become notable as the crystal size increases, to the point where they completely overcome the additional MFkMC computational costs during the event execution. These results highlight the computational superiority of the MFkMC algorithm for modelling moving interface problems that can be otherwise captured using standard kMC techniques.

4.3 $CaCO_3$ Dissolution Model Validation, Analysis, and Sensitivity

In order to validate the performance of the kMC-based crystal dissolution models proposed in this study, the step velocities of the $CaCO_3$ dissolution process were calculated along the simulated crystal surfaces and compared to those observed experimentally using atomic force microscopy.[127,128] Note that since the MFkMC and standard kMC models output similar results, as highlighted in Table 4.2 and Fig. 4.5, it is not necessary to

validate the performance of both models and thus this study was performed for just the MFkMC model. $CaCO_3$ crystals are predicted to have two key step velocities $v_{step,o}$ and $v_{step,a}$ that capture the rate of etching for crystal ledges that are obtuse and acute, respectively. Note that these step velocities are often referred to as fast and slow velocities respectively within the literature. The acute and obtuse step velocities have also been calculated within previous kMC-based crystal dissolution studies, and therefore the step velocities reported in this work were calculated according to measurement schemes used within those studies.[90] The MFkMC model developed within this work was observed to have step velocities of $v_{step,o} = 3.3$ nm/s and $v_{step,a} = 1.2$ nm/s. These are well within the ranges of the step velocities observed experimentally within the literature ($v_{step,o} = 3.4 \pm 0.6$ nm/s and $v_{step,a} = 1.5 \pm 0.2$ nm/s),[127,128] as well as those measured from previously-developed crystal dissolution models ($v_{step,o} = 3.3$ nm/s and $v_{step,a} = 0.9$ nm/s).[90] These results validate the proposed MFkMC model, since it is able to adequately capture the crystal dissolution process.

The crystal dissolution model performance is presented at different combinations of the crystal shape s and size $\vartriangle$, as outlined in Table 4.3. The kMC model is specifically analyzed for each of the four considered crystal shapes ($\vartriangle \in \mathbf{\Delta} = \{cube, sphere, tetra, dode\}$) at two different sizes. Note that the number of ions in a perfect crystal etched into a precise shape varies depending on the shape of the crystal itself (i.e. a perfect rhombohedral $CaCO_3$ crystal with a base length of 15 ions would have a size $s = l_{\vec{a}} l_{\vec{b}} l_{\vec{c}} = 3375$ ions, whereas a perfect spherical crystal with a diameter of 15 ions would have a size $s = 672$ ions). In order to provide a fair comparison between the different crystal shapes, the sizes for each shape are selected such that they exhibit an equivalentnumber of ions, i.e. $s = s_{eq,\vartriangle}$ for $\vartriangle \in \mathbf{\Delta}$. Furthermore, preliminary results have shown that the number of atoms remaining $n_d(t_m)$ could not be readily captured over a linear timescale. This is because the effects of uncertainty were observed to introduce a large variation (over five orders of magnitude difference) in the crystal dissolution times, and consequently a linear timescale cannot provide meaningful analyses as most of the n_d distributions were dominated by large peaks at $n_d = 0$. Therefore, the number of atoms remaining $n_d(t_m)$ were calculated over a logarithmic timescale at nine independent time points that were selected from previous simulations, i.e. $t_m = [t_0 = 4.14 \times 10^{-8}, t_1 = 5.04 \times 10^{-7}, t_2 = 6.14 \times 10^{-6}, t_3 = 7.49 \times 10^{-5}, t_4 = 9.12 \times 10^{-4}, t_5 = 1.11 \times 10^{-2}, t_6 = 1.35 \times 10^{-1}, t_7 = 1.65, t_8 = 20.09]$.

The results and the computational times needed to run these simulations are displayed in Table 4.3. Furthermore, Figs. 4.6a and 4.6b showcase the evolution in the number of atoms remaining ($n_d(t_m)$) as a function of time for the smaller and larger crystal sizes, respectively. In order to illustrate the stochastic variability in the kMC methods, each of the results in Fig. 4.6 were generated using three independent realizations of the crystal dissolution model, highlighted using different shades of the same colour for each shape. These figures show that the stochastic noise inherent to kMC does not significantly affect the temporal evolution of the crystal dissolution. On the other hand, the results in Fig. 4.6 and in Table 4.3 demonstrate that

Table 4.3. Outputs and computational costs of the $CaCO_3$ dissolution kMC model for crystals of different sizes and shapes

Shape	*cube*	*cube*	*sphere*	*sphere*	*tetra*	*tetra*	*dode*	*dode*
Size (ions)	3375	15625	3071	15408	3098	14958	2880	15296
CPU Time (s)	13.92	227.13	26.93	492.08	60.76	1419.5	34.00	546.30
t_d (s)	0.259	0.583	0.180	0.422	0.186	0.410	0.209	0.443
$r_d(t_1)$ (ions/s)	2.16 $\times 10^6$	2.16 $\times 10^6$	3.02 $\times 10^7$	2.16 $\times 10^6$	2.16 $\times 10^6$	2.16 $\times 10^6$	3.02 $\times 10^7$	2.16 $\times 10^6$
$r_d(t_2)$ (ions/s)	1.77 $\times 10^5$	1.77 $\times 10^5$	7.98 $\times 10^6$	1.77 $\times 10^5$	1.77 $\times 10^5$	1.77 $\times 10^5$	1.03 $\times 10^7$	1.77 $\times 10^5$
$r_d(t_3)$ (ions/s)	1.46 $\times 10^4$	1.46 $\times 10^4$	4.80 $\times 10^5$	1.46 $\times 10^4$	1.46 $\times 10^4$	8.73 $\times 10^4$	3.35 $\times 10^5$	4.37 $\times 10^4$
$r_d(t_4)$ (ions/s)	1195	2.99 $\times 10^4$	4.66 $\times 10^4$	3584	1195	8.00 $\times 10^4$	1.16 $\times 10^5$	1.67 $\times 10^4$
$r_d(t_5)$ (ions/s)	686.5	2.86 $\times 10^4$	3.53 $\times 10^4$	1.60 $\times 10^4$	1275	7.17 $\times 10^4$	9.28 $\times 10^4$	2.55 $\times 10^4$
$r_d(t_6)$ (ions/s)	1.32 $\times 10^4$	1.90 $\times 10^4$	1.80 $\times 10^4$	1.76 $\times 10^4$	1.56 $\times 10^4$	6.20 $\times 10^4$	5.74 $\times 10^4$	5.17 $\times 10^4$
$r_d(t_7)$ (ions/s)	1136	254.4	245.1	342.3	9032	4556	4419	5679
$r_d(t_8)$ (ions/s)	0	0	0	0	0	0	0	0

the size and shape of the crystals notably affect the simulation results. The larger crystals have longer dissolution times and higher dissolution rates compared to the smaller crystals of the same shape. The longer dissolution times can be readily attributed to the larger number of ions in the larger $CaCO_3$ crystals. In terms of the shape, the tetrahedral crystals have the largest dissolution rates and require less time to fully dissolve on average. However, the spherical crystals are able to achieve similarly low dissolution times ($t_d = 0.180$ s and

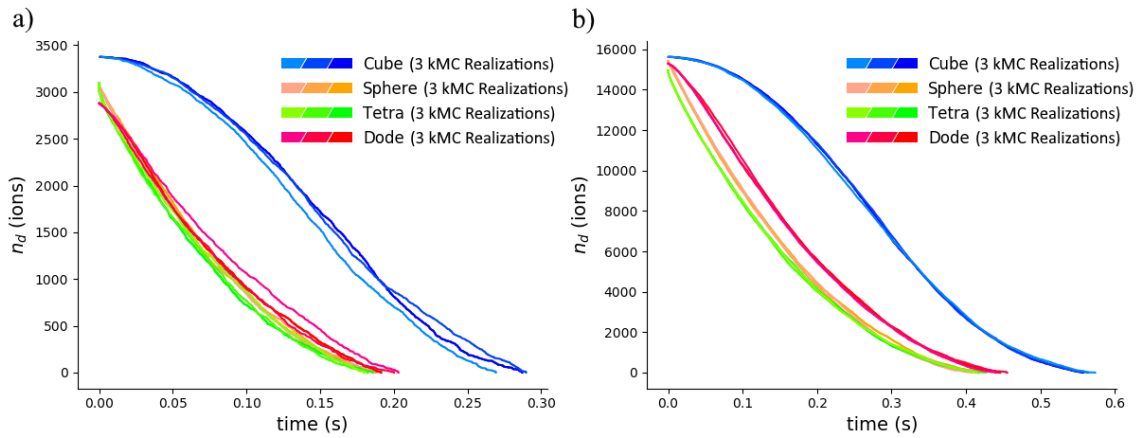

Figure 4.6: Number of atoms remaining in the $CaCO_3$ crystal as a function of time: a) for the smaller crystal sizes ($s_{cube} = 3375$, $s_{sphere} = 3071$, $s_{tetra} = 3098$, $s_{dode} = 2880$); b) for the larger crystal sizes ($s_{cube} = 15625$, $s_{sphere} = 15408$, $s_{tetra} = 14958$, $s_{dode} = 15296$). Note the differently-shaded lines for each colour correspond to independent kMC runs for each shape to showcase the amount of stochastic variability present within the model

0.422 s for the smaller and larger crystal sizes, respectively), although their overall dissolution rates are lower throughout most of the dissolution process. On the other hand, the rhombohedral cubic crystals have the lowest dissolution rates overall and take the longest to dissolve compared to the other shapes (t_d = 0.259 s and 0.583 s for the smaller and larger crystal sizes, respectively), as shown in Table 4.3. The changes in behaviour between the different shapes can be explained by the variation in the ratios of the different types of surface sites for each of the shapes. The faster-dissolving tetrahedral and spherical shapes have a higher ratio of the faster-dissolving kink and ledge sites. Consequently, these $CaCO_3$ shapes have notably higher dissolution rates and therefore dissolve faster. On the other hand, the dodecahedral and rhombohedral cubic crystals have higher ratios of the higher-stability terrace sites. As a result, they dissolve slower and take longer to completely dissolve. In terms of the computational cost, the smaller crystal sizes require less time to compute than the larger crystal sizes, as expected. Furthermore, Table 4.3 highlights that the tetrahedral and dodecahedral crystals require 2-5 times longer on average to compute compared to the rhombohedral cubic and spherical crystals. This increase in the computational cost is due to the approach used to initialize the crystals within the model, and not due to the model process itself. The rhombohedral cubic and spherical crystal shapes are relatively simple to implement and do not require significant computational time to create a crystal of these shapes within the kMC lattice network. On the other hand, the tetrahedral and dodecahedral shapes are relatively complicated to model and implement and therefore require more computational resources.

The current results highlighted in Fig. 4.6 provide reasonable comparisons of the differences in the dissolution behaviour between crystals of different shapes. However, they only provide a basic understanding

of the effects that the crystal size has on the dissolution dynamics. In general, it is expected that smaller crystals would have higher dissolution rates on average since they have a higher surface area-to-volume ratio, i.e., a larger percentage of their ions are on the crystal surface. Fig. 4.7 provides a direct comparison of the number of atoms remaining in the crystal (n_d) as a function of time for crystals of the same shape and different sizes. Figs. 4.7a and 4.7e plot the evolution of n_d for rhombohedral crystals of four different sizes $s_{cube} = [125, 3375, 15625, 42875]$ ions, i.e., the rhombohedral crystals listed in Table 4.3 as well as a larger crystal and a smaller crystal. Furthermore, Figs. 4.7b-4.7d and 4.7f-4.7h depict the evolution of n_d for spherical, tetrahedral, and dodecahedral crystals with sizes that are equivalent to the cubic crystal sizes, i.e. $s_{sphere} = [123, 3071, 15408, 41472]$, $s_{tetra} = [121, 3098, 14958, 41741]$, and $s_{dode} = [99, 2880, 15296, 41615]$. The results in Fig. 4.7 were generated by simulating three independent simulations for each crystal shape and size and averaging the results to minimize the stochastic noise. Note that Figs. 4.7e-4.7h plot the same results as Figs. 4.7a-4.7d; the only difference is that the results in Figs. 4.7e-4.7h have been normalized to provide better comparison of the results according to $\tilde{n}_d = n_d/s$ and $\tilde{t} = t/t_d$, where $\tilde{t}$ and $\tilde{n}_d$ denote the non-dimensional time and number of ions remaining respectively for each crystal shape and size. The results in Figs. 4.7a-4.7d illustrate that the larger crystals take longer to dissolve than the smaller crystals, which is to be expected due to the larger number of ions that require dissolution. On the other hand, the results in Figs. 4.7e-4.7h provide a better comparison on how the rates of dissolution vary between the crystals of each size. These results illustrate that the behaviour of the three larger crystal sizes are very similar and do not notably deviate from each other with regards to the shapes of their dissolution curves. However, the smallest crystal (in blue) deviates significantly from the results of the other three crystal sizes and has a drastically different profile shape. Note that the transient variation in n_d for the smallest size of crystals is much coarser compared to the larger crystals since they contain fewer atoms overall. However, this appearance was not observed to significantly alter the general behaviour as increasing the number of independent kMC simulations did not notably affect the curve appearances. These results illustrate that the overall dissolution behaviour for the smallest crystal sizes is quite different from the larger crystals, and therefore they highlight the effects of the surface area-to-volume ratio for smaller crystals. Smaller crystals have a higher ratio of the highly-reactive kink ($n_{bd,tot} = 3$) and ledge ($n_{bd,tot} = 4$) sites compared to the slower terrace ($n_{bd,tot} = 5$) sites and non-reactive bulk ($n_{bd,tot} = 6$) sites, especially in the case of the tetrahedral crystal shapes. As a result, the smaller crystals experience significant dissolution during the initial time periods, as illustrated by the sharp near-vertical decrease in n_d at the onset of the dissolution process. On the other hand, the larger crystal sizes have slower initial dissolution rates due to the lower ratio of highly-reactive sites. However, as the crystal dissolution process evolves, the larger crystals become rougher and rougher creating higher ratios of kink and ledge sites, and therefore the ratio of fast-dissolving sites increases as the crystal dissolves. As a result, the average rates of dissolution increase at moderate time periods for the larger crystals, as showcased in the middle of Figs. 4.7e-4.7h. Towards the end

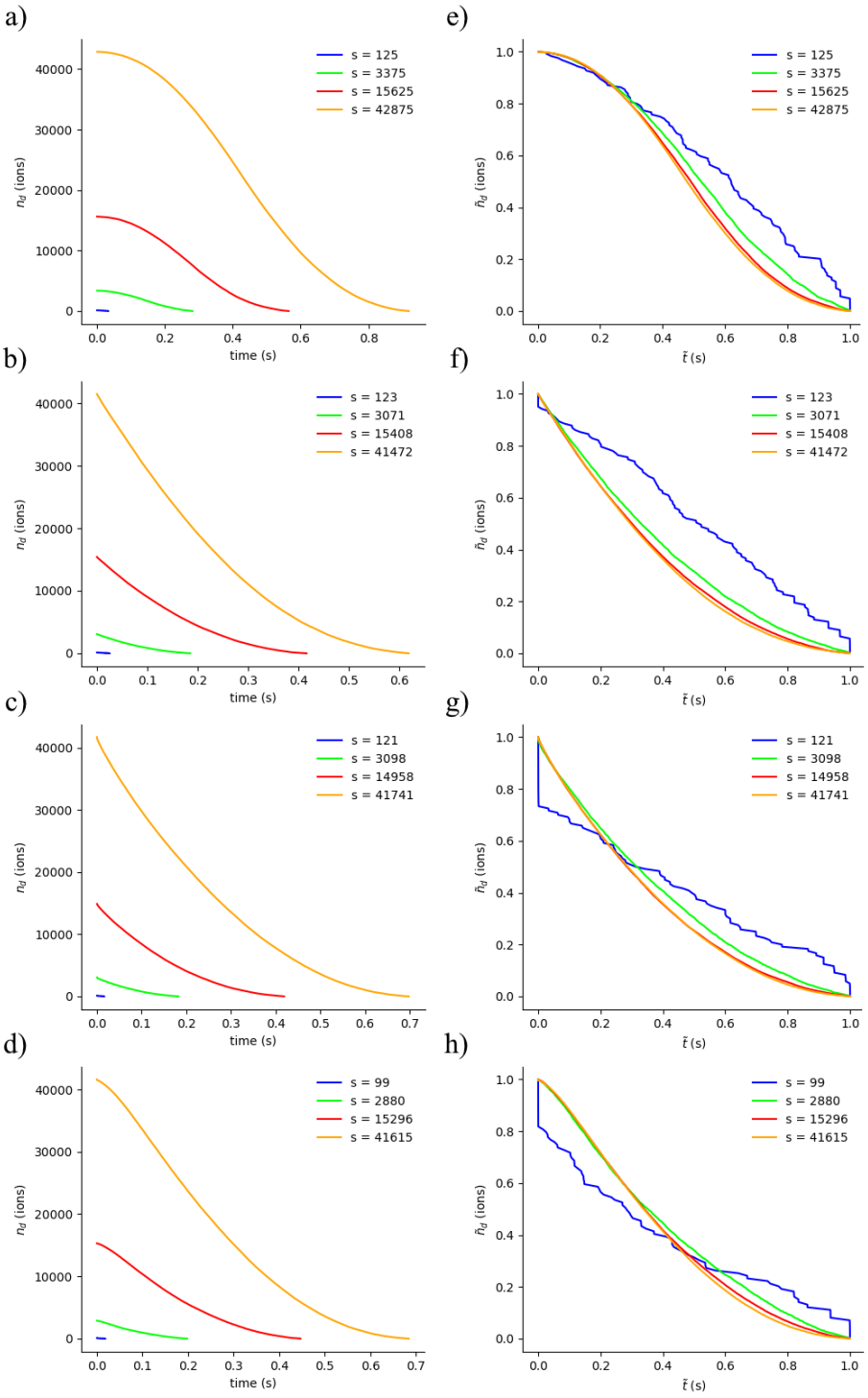

Figure 4.7: Number of atoms remaining in the $CaCO_3$ crystal as a function of time, a)-d), and normalized number of atoms remaining $\tilde{n}_d$ as a function of normalized time $\tilde{t}$, e)-h): a)/e) for rhombohedral crystals ($s_{cube} = [125,3375,15625,42875]$); b)/f) for spherical crystals ($s_{sphere} = [123,3071,15408,41472]$); c)/g) for tetrahedral crystals ($s_{tetra} = [121,3098,14958,41741]$); d)/h) for dodecahedral crystals ($s_{dode} = [99,2880,15296,41615]$)

of the dissolution process, the rates slow down as the fast-dissolving sites are removed. On the other hand, the smallest crystal size does not exhibit similar behaviour towards the middle and end of the dissolution process. This is because the number of fast-dissolving sites is highest at the onset of the crystal dissolution process, and it steadily decreases over time for the smallest crystals. After these sites dissolve, the rate of dissolution slows and maintains a near-constant rate for the remainder of the dissolution process as the ratio of different reactive sites stagnate.

The $CaCO_3$ dissolution process is dependent on a number of external environmental factors, such as the temperature and the pH of the system where the crystal is dissolving. Within the human gastrointestinal system, these environmental parameters are known to vary depending on a number of external factors. The average human body temperature has been documented as 37 ^oC;[193,194] however, the exact temperature of the human body is known to vary between 35.2-38 ^oC depending on a number of factors such as time of day, age, gender, health, menstrual and biological rhythms, diet, and lifestyle.[194–196] In addition, the pH of the human stomach has been reported to vary between 1.3 and 6.4 depending on a number of factors such as the location within the stomach and whether or not the person had recently eaten.[197] Consequently, it is important to analyze the impact of the variability of these environmental factors on the $CaCO_3$ dissolution behaviour.

Motivated by this, a brief sensitivity analysis is performed on the kMC calcium carbonate crystal dissolution model subject to the key model parameters affected by variations in the temperature and pH. Note that the pH is not directly involved in the $CaCO_3$ dissolution kinetics model; hence, the variability in the pH is evaluated in the model by modifying the activation energy of desorption E (i.e. the parameter within the kMC model that the pH would affect the most significantly). The objective of this sensitivity analysis is to analyze the need to perform uncertainty analysis on the crystal dissolution model, and to determine the most influential uncertain parameters within the system. Consequently, the sensitivity analysis is performed by directly propagating realizations of E and the temperature T independently through the dissolution model to assess the model sensitivity to each uncertain parameter individually. In order to accommodate for the stochastic tendency of kMC methods, each realization of E and T were passed through the model four separate times and the results were averaged.

Based on the above, this study analyzes the temperature and activation energies at their nominal value (i.e. $T = 37\ ^oC$ and $E = 0.164$ eV as shown in Table 4.1). Furthermore, this work also analyzes the crystal dissolution behaviour subject to a $\pm 2^oC$ variability in the temperature and a ± 0.0164 eV variability in the activation energy. Note that the variability in the system temperature was derived based on the expected temperature fluctuations within the human body as discussed above. Furthermore, a 10% variability was considered in the activation energy to account for the fluctuations in the pH described previously. These sensitivity analyses are applied to the same crystal design case studies considered above in Table 4.3.

Fig. 4.8 illustrates the variability in the transient crystal dissolution profiles through n_d. These results illustrate that the variation in the pH through the activation energy has a significant effect on the $CaCO_3$ dissolution performance, as a 0.0164 eV increase and decrease in E resulted in approximately an 85% increase and a 535% decrease on average, respectively, in the dissolution time as shown in Figs. 4.8e-4.8h. On the other hand, the variability in the system temperature was observed to have a minimal impact on the crystal dissolution behaviour. More specifically, a 2°C change in the temperature resulted in approximately a 13% change in the overall dissolution time, as highlighted in Figs. 4.8a-4.8d. As a result, the studies presented throughout the

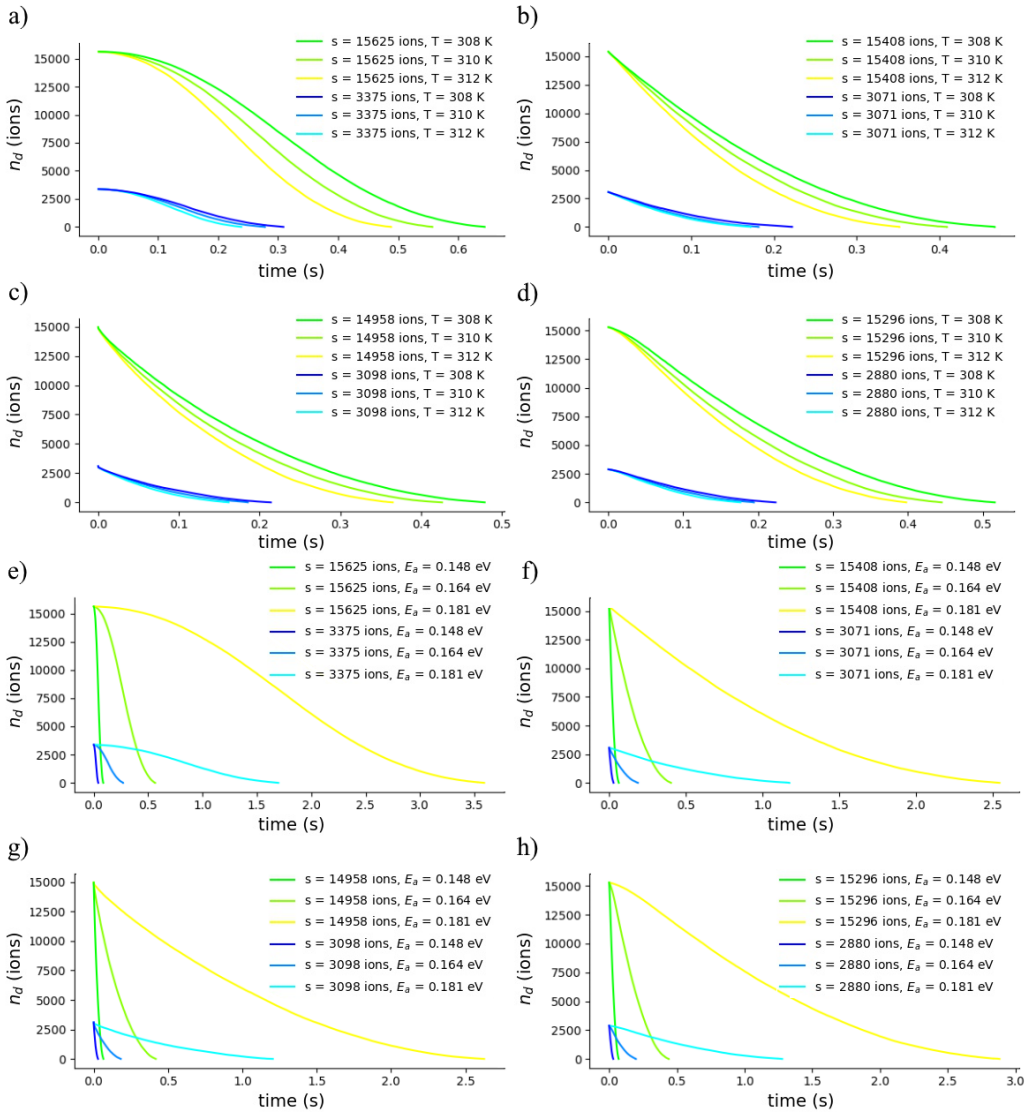

Figure 4.8: Sensitivity of the transient $CaCO_3$ dissolution profile subject to changes in temperature, parts a)-d), and pH through the activation energy, parts e)-h): a) temperature variability, $cube$; b) temperature variability, $sphere$; c) temperature variability, $tetra$; d) temperature variability, $dode$; e) pH variability, $cube$; f) pH variability, $sphere$; g) pH variability, $tetra$; h) pH variability, $dode$

remainder of this work will only consider uncertainty in the stomach pH (i.e. the remaining studies will only consider parametric uncertainty in the activation energy). Note that the low variability in the crystal dissolution behaviour due to fluctuations in the system temperature do not indicate that the crystal dissolution model is insensitive to variations in the system temperature. Rather, the low variability is due to the narrow temperature range considered in this study (i.e., the temperature within the human body is only expected to fluctuate between 35.2-38 ^{o}C, and therefore the temperature was only assigned a variability of ±2 ^{o}C). On the other hand, the pH within the human gastrointestinal system is expected to vary significantly. In the sensitivity analysis, this resulted in large fluctuations in the crystal dissolution behaviour as observed in Figs. 4.8e-4.8h. If the sensitivity analysis had been conducted with a larger variation in the system temperature, then it is expected that the fluctuations in the crystal dissolution behaviour would be much more significant.

4.4 Uncertainty Analysis via PCE and LPCMs

The objective of this section is to propagate parametric uncertainty due to environmental fluctuations through the $CaCO_3$ dissolution models using PCE and LPCM. This study considered variability in the stomach pH, which is captured by adding uncertainty to the crystal activation energy E as described in Section 4.3. The uncertainty in the activation energy was assumed to be normally distributed with its nominal value as the mean (i.e. $\bar{E} = 0.164$ eV) and a variance $\sigma_E^2 = 0.269 \times 10^{-3}$ eV^2. Furthermore, the uncertainty was assumed to remain invariant in time and space. Note that both the PCE models and LPCMs suffer from the curse of dimensionality and therefore increasing the number of uncertain parameters also increases the size and number of resources needed to generate these models. A larger number of uncertain parameters will increase the number of terms in the developed PCE model and will require more sampling from the kMC-based models to determine the PCE coefficient values thus requiring additional simulation costs. Similarly, increasing the number of uncertain parameters will increase the dimensionality of the developed LPCMs. Consequently, the addition of further uncertain parameters would raise the challenge of determining adequate models that can fit the data and they would necessitate the simulation of additional data points (and therefore additional computational resources) to achieve an acceptable model fit.

The PCE models considered for the uncertainty analysis were constructed using 1st, 2nd, and 3rd order probabilistic Hermite polynomials as the polynomial basis function (i.e. $\chi = 1 - 3$ and $\boldsymbol{b}_\chi^{\mathbf{H}} = He_\chi$ in Eq. (3)). The Hermite family of polynomials were selected for this study as they are orthogonal to the normal distribution, and they are therefore ideal for propagating normal uncertainty through the crystal dissolution model. Furthermore, the order of the PCE models were selected independently for each of the kMC model outputs (ie. t_d and $n_d(t_m)$). The PCE orders were determined *a priori* to be the lowest order of chaos polynomials needed to capture the uncertainty variability for their respective model outputs. The probabilistic Hermite polynomials are denoted as follows:

$$He_{\chi}(\boldsymbol{\Xi_H}) = (-1)^{\chi} e^{\boldsymbol{\Xi_H^2}/2} \frac{d^{\chi}}{d\boldsymbol{\Xi_H^{\chi}}} e^{\boldsymbol{\Xi_H^2}/2} \quad (4.5)$$

Consequently, the full 3rd order polynomial chaos expression for a single uncertain parameter considered in this work can be denoted as follows:

$$\boldsymbol{\Psi}(t_m) = a_0(t_m) + a_1(t_m)\Xi_H + a_2(t_m)(\Xi_H^2 - 1) + a_3(t_m)(\Xi_H^3 - 3\Xi_H) \quad (4.6)$$

where a_0, a_1, a_2, and a_3 denote the 0th, 1st, 2nd, and 3rd order PCE coefficients at each time instant t_m. Note that the corresponding 1st and 2nd order PCE models can be derived by truncating Eq. (4.6) after the 1st and 2nd order PCE coefficient terms, respectively. The PCE coefficients were determined via least squares regression using 500 sample points. The sample points were determined by propagating randomly-generated realizations in the uncertain parameter through the kMC models and recording their outputs at each time instant (t_m). Note that the number of sample points were determined *a priori* to be the lowest number of points needed to capture the variability in the outputs t_d and $n_d(t_m)$, respectively. Further note that both the lowest PCE order and the minimum number of sample points required were determined by fitting the PCE models to output uncertainty distributions generated using 10,000 randomly-generated MC sampling points propagated through the actual kMC model.

On the other hand, the LPCMs were developed to approximate the values of the coefficients for a given set of $CaCO_3$ design parameters (i.e. $\boldsymbol{\omega} = [s_{eq,\Delta}, \Delta]$). These LPCMs were generated using coefficient data generated for each of the selected crystal shapes ($\Delta \in \boldsymbol{\Delta} = \{cube, sphere, tetra, dode\}$) using the PCE algorithm described within Section 4.1.2. For the rhombohedral cubic ($cube$) crystals, the coefficient data was generated for crystals with a base length $l_{cube} \in \{8, 13, 18, 23, 28, 33, 38\}$ atoms (i.e. with a base length within the range $8 \leq l_{cube} \leq 38$, at intervals spaced five atoms apart.) Note that these correspond to rhombohedral cubic crystals of size $s_{cube} \in \{512, 2197, 5832, 12167, 21952, 35937, 54872\}$ atoms. The sizes for the remaining crystal shapes were selected to be comparable (in terms of number of atoms) to the rhombohedral cubic crystal shapes. In other words, the sizes for the other crystals were selected by finding the crystal with a perfect shape (e.g. a perfectly spherical, tetrahedral, or dodecahedral crystal with no vacancies or missing segments) that exhibited the closest number of atoms to the selected rhombohedral cubic crystals. The crystal sizes considered for the spherical, tetrahedral, and dodecahedral crystals were $s_{sphere} \in \{360, 2109, 5575, 11513, 20479, 35880, 54088\}$, $s_{tetra} = \{512, 2124, 5470, 12012, 20238, 35754, 53794\}$, and $s_{dode} = \{451, 2080, 5144, 11575, 21592, 33920, 53455\}$, respectively. In order to develop the LPCMs, the PCE coefficients at each crystal shape were subsequently fit to a variety of low-order models using the least squares method, and the model with the best fit was selected for each coefficient. A full list of the models and their coefficients for each PCE coefficient can be found in Section B.5.

The aforementioned PCE and LPCM algorithms were used to propagate parametric uncertainty in the pH through the $CaCO_3$ crystal dissolution system under five different crystal size and shape combinations listed in Table 4.4. The PCE and LPCM models were validated via comparison to probability distribution functions determined for each crystal design by propagating uncertainty directly through the kMC models using 10,000 MC sampling points. Table 4.4 lists the key statistical parameters for each uncertainty distribution generated via MC sampling, PCE, and LPCM. This table furthermore lists the computational times required to determine the output uncertainty distributions using each method. In addition, Figs. 4.9 and 4.10 illustrate the effects of uncertainty on the crystal dissolution time t_d and on the number of atoms remaining in the crystal $n_d(t_m)$ at each timepoint t_m, respectively, using the uncertainty propagation methods considered in this work, i.e. MC sampling, PCE, and the LPCMs. Note that the probability distribution curves for the PCE and LPCM methods were developed by generating histograms for their respective output uncertainty variability data and by plotting the peaks and peak locations for each histogram as a 2D curve. Additionally note that the results showcased in Figs. 4.9f)- 4.9j) showcase a close-up view of the PDFs in Figs. 4.9a)- 4.9e) over the time interval 0-10 s. The results in Figs. 4.9 and 4.10 and in Table 4.4 illustrate that the PCE model predictions can accurately capture the output variability, as the majority of the deviations between the PCE and MC sampling results remain below 1%. Similarly, the results demonstrate that the LPCM-generated PCE models are acceptable as the majority of the errors in the LPCM method compared to both the PCE and MC sampling methods remain below 5%. In addition, the PCE method showed an order of magnitude improvement on average in the computational cost compared to MC sampling, demonstrating the computational efficiency of the series expansion. On the other hand, the LPCMs have attractive computational efficiency compared to the PCE and the MC sampling methods. Table 4.4 highlights that the LPCMs require less than 3 seconds to compute the variability in t_d and $n_d(t_m)$ regardless of the crystal size and shape. This is in contrast to the PCE and MC sampling methods, where the computational times vary depending on the crystal design due to the influence of the kMC models. Note that the computational cost for both the PCE and LPCM methods includes the time needed to determine the PCE coefficients via least squares and the LPCM equations, respectively. For the crystal designs considered in this study, the LPCM method was approximately 2 and 3 orders of magnitude faster than the PCE and MC sampling methods (10,000 sample points) respectively for the fastest dissolving crystal design. Furthermore, LPCM was about 3 orders of magnitude faster than the PCE method and 4 orders of magnitude faster than the MC sampling method for the slowest dissolving crystal design. These computational savings are expected to be even greater for larger crystals. However, note that the computational costs for the PCE and MC sampling methods are dependent on the number of sample points used in either method, and therefore the computational advantage of the LPCM method would be lessened if fewer points were used for the other methods. The results in Table 4.4 and Figs. 4.9 and 4.10 furthermore highlight that the variability in the pH (as captured through the activation energy E) has a notable effect on the crystal dissolution model. These results highlight that the total dissolution

Table 4.4. Uncertainty variability statistics in the $CaCO_3$ dissolution outputs for different crystal shapes and sizes using MC sampling, PCE, and LPCM

Shape		*cube*			*cube*			*sphere*			*tetra*			*dode*		
Size (ions)		15625			3375			3071			3098			2880		
Method		MC	PCE	LPCM	MC	PCE	LPCM	MC	PCE	LPCM	MC	PCE	LPCM	MC	PCE	LPCM
CPU Time (s)		61260	6156	2.778	3854	393.9	2.808	7626	730.2	2.736	17430	1830	2.760	8556	903.6	2.832
t_d (s)	$\bar{t}_d$	3.146	3.373	3.554	1.447	1.557	1.904	1.091	1.542	1.336	1.046	1.652	1.184	1.130	1.352	1.325
	$t_d^u(0.95)$	12.41	17.38	17.93	5.503	8.085	9.752	3.882	7.393	6.634	3.968	7.831	6.045	3.939	6.821	6.833
	$t_d^l(0.95)$	0.027	0	0	0.012	0	0	0.008	0	0	0.008	0	0	0.009	0	0
n_d (t_0) (ions)	$\bar{n}_d(t_0)$	1.56 ×10⁴	1.56 ×10⁴	1.56 ×10⁴	3375	3375	3375	3065	3065	3020	3095	3095	3093	2880	2880	2887
	$n_d^u(0.95\|t_0)$	1.56 ×10⁴	1.56 ×10⁴	1.56 ×10⁴	3375	3375	3375	3066	3066	3021	3097	3096	3093	2880	2880	2887
	$n_d^l(0.95\|t_0)$	1.56 ×10⁴	1.56 ×10⁴	1.56 ×10⁴	3375	3375	3375	3065	3065	3020	3090	3090	3089	2880	2880	2887
n_d (t_2) (ions)	$\bar{n}_d(t_2)$	1.56 ×10⁴	1.56 ×10⁴	1.56 ×10⁴	3373	3373	3373	3063	3063	3017	3041	3042	3048	2878	2878	2887
	$n_d^u(0.95\|t_2)$	1.56 ×10⁴	1.56 ×10⁴	1.56 ×10⁴	3373	3373	3373	3064	3063	3019	3084	3085	3081	2878	2878	2891
	$n_d^l(0.95\|t_2)$	1.56 ×10⁴	1.56 ×10⁴	1.56 ×10⁴	3373	3373	3373	3061	3060	3012	3004	2996	3015	2878	2877	2880
n_d (t_4) (ions)	$\bar{n}_d(t_4)$	1.56 ×10⁴	1.56 ×10⁴	1.56 ×10⁴	3344	3353	3349	2947	2951	2908	2865	2873	2888	2798	2806	2821
	$n_d^u(0.95\|t_4)$	1.56 ×10⁴	1.58 ×10⁴	1.57 ×10⁴	3371	3401	3395	3062	3087	3068	3006	3021	3042	2876	2923	2910
	$n_d^l(0.95\|t_4)$	1.56 ×10⁴	1.52 ×10⁴	1.52 ×10⁴	3310	3213	3215	2518	2451	2330	2370	2321	2429	2514	2412	2539
n_d (t_6) (ions)	$\bar{n}_d(t_6)$	9797	9911	9922	1640	1664	1751	973.1	1016	1023	928.8	961.5	991.3	976.3	1033	1055
	$n_d^u(0.95\|t_6)$	1.56 ×10⁴	1.61 ×10⁴	1.63 ×10⁴	3365	3414	3650	2886	2929	2994	2775	2807	2868	2795	2835	2858
	$n_d^l(0.95\|t_6)$	0	0	0	0	0	0	0	0	0	0	0	0	0	0	0
n_d (t_7) (ions)	$\bar{n}_d(t_7)$	2614	2722	2884	298.1	324.7	129.1	136	146.4	501.3	128.7	137.3	123.8	137	153.9	1704
	$n_d^u(0.95\|t_7)$	1.50 ×10⁴	1.53 ×10⁴	1.58 ×10⁴	2690	2760	1353	1199	1318	3571	1162	1223	608.5	1240	1376	6439
	$n_d^l(0.95\|t_7)$	0	0	0	0	0	0	0	0	0	0	0	0	0	0	0

time follows an exponential distribution where the variation spans over five orders of magnitude. On the other hand, the variation in n_d begins as a single peak at the maximum crystal size and transitions to a single peak at zero through an intermediary bimodal distribution with peaks at both extremes. Note that a third-order PCE model was necessary for the intermediate values of n_d due to their bimodal nature, as this behaviour could not be accurately captured using 2nd or 1st order PCE models (not shown for brevity). These results indicate that the variability in n_d is very low at $t = 4.14 \times 10^{-8}$ s, and that therefore it is expected that the crystal would have not begun dissolving at this timepoint. As time evolves, the crystal dissolves and the effects of uncertainty begin to produce a binormal distribution with shallow peaks at $n_d = s$ and $n_d = 0$, indicating that the

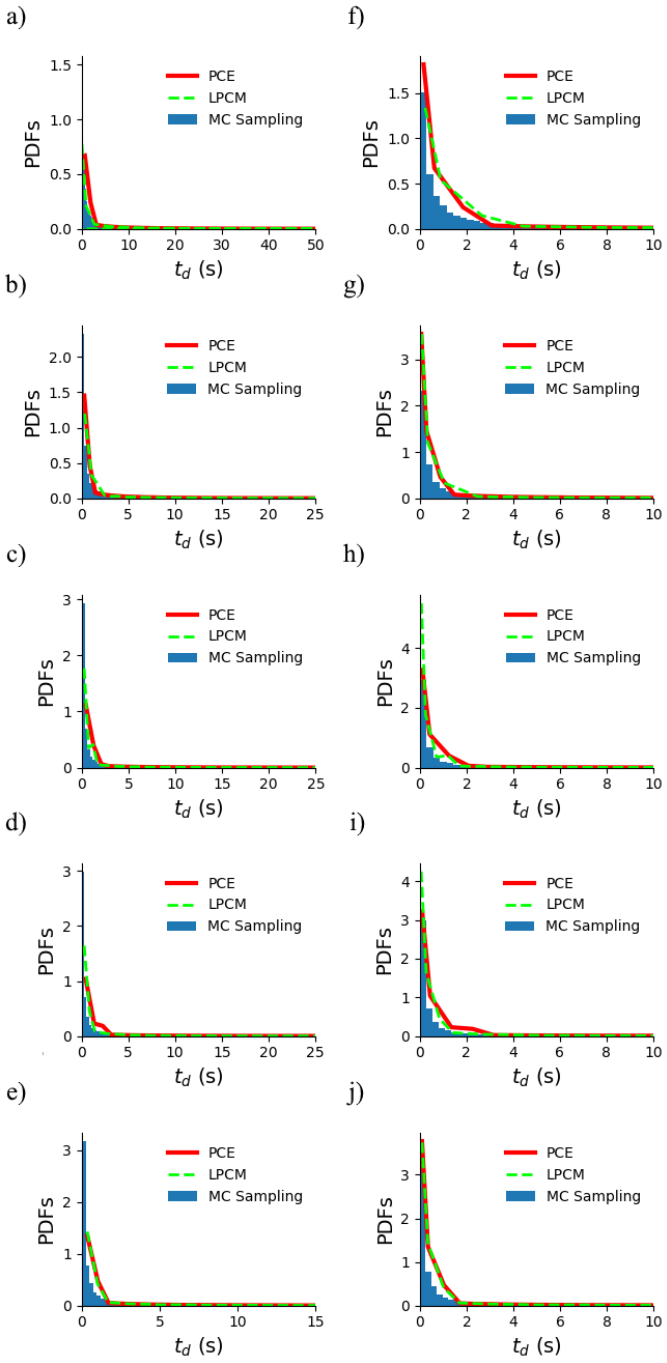

Figure 4.9: PDFs of the total crystal dissolution time, t_d, for different crystal designs generated using MC sampling (blue), 3rd order PCE (red), and the LPCMs (green): a)/f) rhombohedral cubic crystal, $s = 15625$ ions; b)/g) rhombohedral cubic crystal, $s = 3385$ ions; c)/h) spherical crystal, $s = 3071$ ions; d)/i) tetrahedral crystal, $s = 3098$ ions; e)/j) dodecahedral crystal, $s = 2880$ ions; where a)-e) showcase the full PDFs for each crystal design and f)-j) showcase a close-up view of each PDF over the time interval 0-10s

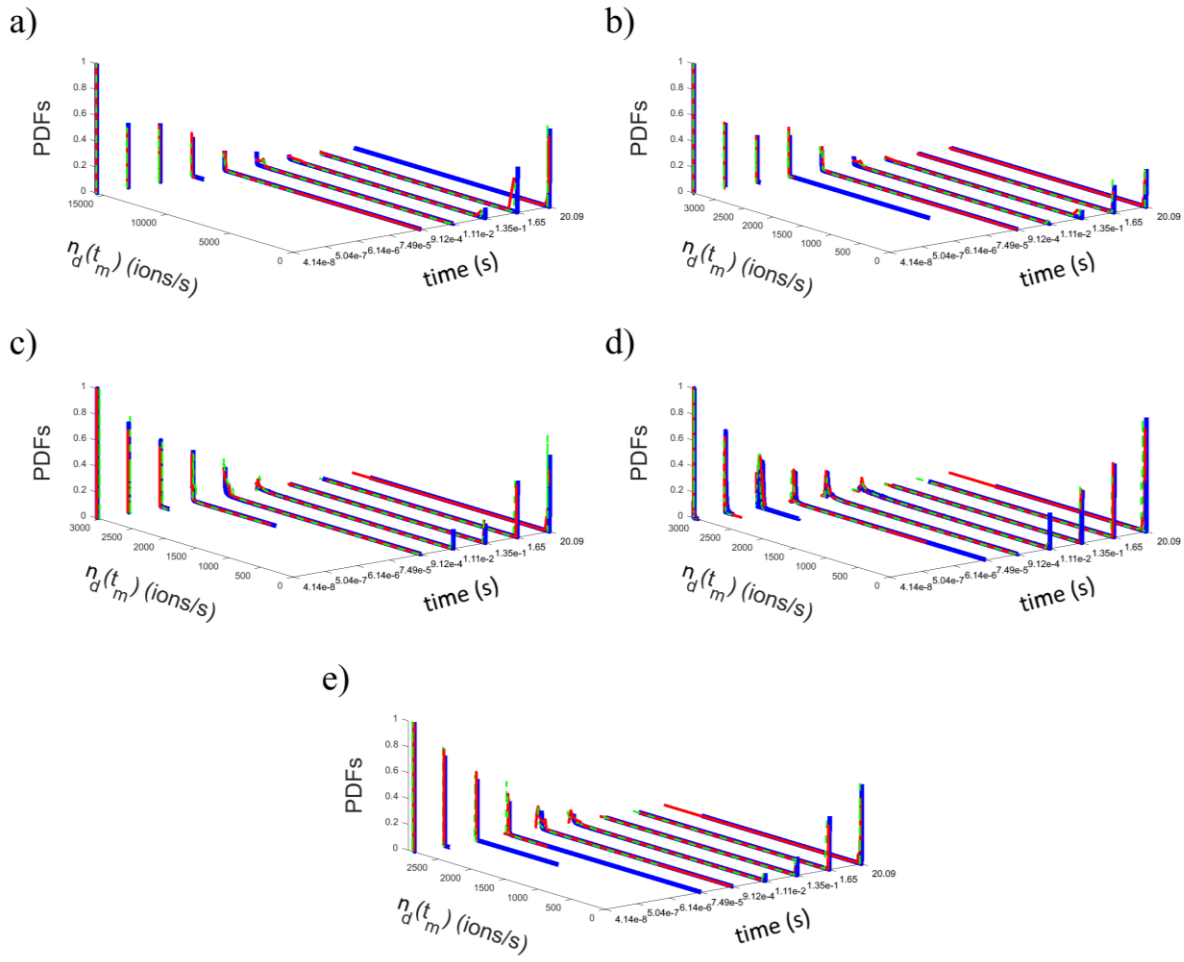

Figure 4.10: PDFs of the number of atoms remaining in the $CaCO_3$ crystal $n_d(t_m)$ at each of the timepoints t_m (where $m \in [0,8]$ denotes the timepoint index) for different crystal designs generated using MC sampling (blue), PCEs (red), and the LPCMs (green): a) rhombohedral cubic crystal, $s = 15625$ ions; b) rhombohedral cubic crystal, $s = 3385$ ions; c) spherical crystal, $s = 3071$ ions; d) tetrahedral crystal, $s = 3098$ ions; e) dodecahedral crystal, $s = 2880$ ions

variability in n_d due to uncertainty in the pH is substantial and that therefore it is unknown whether the crystal remains completely intact, has completely dissolved, or is somewhere in-between during these intermediary timepoints. Towards the end of the simulation ($t_8 = 20.09$ s), it is expected that the crystal would have completely dissolved for most of the considered uncertainty realizations, and therefore the PDF for n_d at this timepoint consists of a peak at $n_d = 0$. These results highlight that environmental uncertainties can have significant and sizeable effects on the crystal dissolution behaviour, and therefore they should be accommodated for when modelling $CaCO_3$ dissolution within the human body.

4.5 Robust Optimization

According to the pharmaceutical standards listed by the US Food and Drug Administration,[20] one of the key critical quality attributes of a pharmaceutical drug is its dissolution performance (i.e. dissolution rate). Additionally, many pharmaceutical drugs require controlled or sustained releases within the human body in order to prolong the drug's therapeutic efficiency.[198,199] Consequently, it is desirable to select drug crystal designs that can extend the crystal dissolution time while controlling their dissolution rate. These aforementioned drug performance markers are additionally subject to environmental uncertainties due to variability in the gastrointestinal pH and temperatures.[193,197] Therefore, it is also desirable to minimize the impact of variability due to uncertainty on the drug dissolution. However, these objectives are in direct conflict with each other, as the conditions that increase the dissolution time also increase the uncertain variability, as observed in Fig. 4.8.

The aim of this section is to perform optimization on the studied $CaCO_3$ dissolution system in order to address the trade-off between minimizing uncertainty and maximizing the drug release time while simultaneously controlling the dissolution rate. Note that this optimization problem is non convex and therefore only local optimality can be guaranteed; further analysis on this issue is beyond the scope of this work. This study assumes that the $CaCO_3$ crystals are being used as a delivery system for a sustained-release drug, as $CaCO_3$ has been previously proposed for this application within the literature.[200] Consequently, it is desirable to extend the dissolution time of the crystals while limiting the maximum dissolution rate to prevent a significant peak in the drug release. The $CaCO_3$ dissolution behaviour is influenced by the crystal size s and shape $\measuredangle$, which are the key crystal design parameters considered in this study. Note that the crystal shape can be adjusted through cutting and etching techniques, as described in Section 4.3. However, the formation process necessary to develop each of these shapes is beyond the scope of this research. Nevertheless, it is still critical to gain insight on how certain crystal shape and sizes impact the $CaCO_3$ dissolution properties under uncertainty. The optimization studies presented in this section solved using a 2.1 GHz Intel Xeon E5-2620 Processor. The proposed optimization study was performed under multiple different scenarios, which are described next.

4.5.1 Scenario I: Optimization under Nominal Conditions

The objective of this scenario is to study the crystal dissolution process under nominal conditions (i.e. in the absence of uncertainty). In order to analyze the nominal $CaCO_3$ dissolution behaviour, an optimization study was performed in order to determine the optimal crystal shape and size that maximizes the dissolution time while still keeping the dissolution rate below a certain threshold. The proposed optimization formulation is as follows:

$$\max_{s_{\Delta},\Delta} \hat{t}_d \tag{4.7}$$

Subject to:

$$LPCMs \tag{4.8}$$

$$\Delta \in \boldsymbol{\Delta} = \{cube, sphere, tetra, dode\} \tag{4.9}$$

$$y_{\Delta} \in \{0,1\}, \forall \Delta \in \boldsymbol{\Delta} \tag{4.10}$$

$$\sum_{\Delta \in \boldsymbol{\Delta}} y_{\Delta} = 1 \tag{4.11}$$

$$y_{\Delta} = 1 \Longrightarrow s_{l,\Delta} \leq s_{\Delta} \leq s_{u,\Delta}, \forall \Delta \in \boldsymbol{\Delta} \tag{4.12}$$

$$\hat{r}_d(t_m) \leq 7 \times 10^6 \; ions/s \tag{4.13}$$

where $\hat{t}_d$ and $\hat{r}_d$ denote the nominal time needed for the crystal to completely dissolve t_d and the nominal dissolution rate r_d (i.e. the dissolution observables in the absence of uncertainty), respectively; s_{Δ} denotes the size of a crystal with shape Δ; and $s_{l,\Delta}$ and $s_{u,\Delta}$ denote the lower and upper bounds applied to the crystal size for each shape Δ. The upper and lower bounds were set to $s_{l,\Delta} = [512{,}360{,}512{,}451]$ and $s_{u,\Delta} = [54872{,}54088{,}53794{,}53455]$ for $\Delta = [cube, sphere, tetra, dode]$. These bounds were selected based on the perfect crystal sizes that contain a comparable number of atoms for each of the considered shapes. Furthermore, note that the LPCMs are only being used in the present scenario to compute the model output assuming a nominal value in the activation energy, i.e. $E = 0.164$ eV. As shown in equations (4.7)-(4.13), the crystal shape (Δ) is discrete and cannot be optimized using gradient-based optimization techniques. To overcome this limitation and reduce the computational costs, the optimization study was performed four times, i.e. once for each of the four considered crystal shapes. The optimal crystal shape was subsequently selected from the optimization results *a posteriori*. The corresponding optimization problems were solved using the interior point solver within the *fmincon* built-in function, a gradient-based optimizer available in MATLAB R2020a, using an initial guess $x_{0,\Delta}$, where $x_{0,\Delta} = [12167{,}12712{,}12717{,}12680]$ for $\Delta = [\text{cube}, \text{sphere}, \text{tetra}, \text{dode}]$. As shown in Table 4.5, the optimal crystal design corresponds to a rhombohedral cubic crystal that is 54872 ions in size. These results illustrate that the crystal dissolution time can be maximized by considering large crystals with a higher ratio of terrace surface ions. In general, the results in Table 4.5 highlight that the largest crystal sizes maximize the dissolution time for each crystal shape. However, the optimal size determined for each crystal shape was limited by the restriction on the dissolution rate. For the rhombohedral cubic and dodecahedral crystals, the dissolution rates remained below the specified threshold for all considered crystal sizes, and therefore the optimal crystal size for these shapes corresponded to the maximum allowed crystal size. This is due to the higher ratio of the slower-dissolving terrace surface sites

Table 4.5 Nominal optimization results for each of the considered $CaCO_3$ crystal shapes

Optimization Scenario	Nominal Optimization			
Shape	*cube* **optimal**	*sphere*	*tetra* *infeasible*	*dode*
Size	54872	15408	512	53455
$\hat{t}_d$ (s)	5.75	2.63	0.26	4.89
$\sigma_{t_d}^2$ (s^2)	218.17	44.31	0.06	180.23
$\hat{r}_d(t_1)$ (ions/s)	2.16×10^6	7.00×10^6	1.13×10^7 *infeasible*	5.66×10^6
$\hat{r}_d(t_2)$ (ions/s)	1.81×10^5	1.86×10^6	3.06×10^6	2.40×10^6
$\hat{r}_d(t_3)$ (ions/s)	6.55×10^4	7.45×10^5	5.91×10^5	1.06×10^6
$\hat{r}_d(t_4)$ (ions/s)	9.84×10^5	6.17×10^5	7.09×10^4	1.44×10^6
$\hat{r}_d(t_5)$ (ions/s)	4.25×10^5	2.06×10^5	1.51×10^4	6.28×10^5
$\hat{r}_d(t_6)$ (ions/s)	1.70×10^5	5.34×10^4	1427.5	1.65×10^5
$\hat{r}_d(t_7)$ (ions/s)	1.89×10^4	3277.1	59.39	1.53×10^4
$\hat{r}_d(t_8)$ (ions/s)	1049.7	0	5.93	0

documented for these crystal shapes, which limited their maximum dissolution rates. On the other hand, the spherical and tetrahedral crystal sizes contain higher ratios of the faster-dissolving ledge and kink sites and therefore they were subject to higher dissolution rates. As a result, the optimal sizes for these crystal shapes were limited due to the restriction applied to the dissolution rate. In particular, the maximum dissolution rate within the tetrahedral crystal remained above the threshold specified in Eq. (4.13) for all considered crystal sizes, and consequently it is an infeasible solution. Note that the infeasible tetrahedral results listed in Table 4.5 were determined by finding the tetrahedral crystal size whose maximum reaction rate was the closest to meeting the restriction specified in Eq. (4.13), i.e. the smallest tetrahedral crystal size.

4.5.2 Scenario II: Robust Optimization

The uncertainty in the gastrointestinal acidity (as captured through the activation energy) is known to induce significant variability in the $CaCO_3$ dissolution results, as highlighted in Figs. 4.8e-4.8h and Table 4.5. Motivated by this, the objective of this scenario is to assess the impact of the uncertainty on the crystal

dissolution process. This objective was attained by implementing a robust optimization study to maximize the dissolution time under uncertainty in the environmental pH (i.e. through E, as described in Section 4.3). Note that the uncertainty in E was assumed to be normally distributed with mean $\bar{E} = 0.164$ eV and variance $\sigma_E^2 = 0.269 \times 10^{-3}$ eV^2. The robust optimization formulation is as follows:

$$\max_{s,\Delta} \bar{t}_d \tag{4.14}$$

Subject to:

Constraints, Eq. (4.8)-(4.12)

$$E \sim \mathcal{N}(\bar{E} = 0.164\ eV, \sigma_E^2 = 0.269 \times 10^{-3}\ eV^2) \tag{4.15}$$

$$r_d^u(\alpha_{cf}|t_m) \leq 7 \times 10^6\ atoms/s \tag{4.16}$$

Here, $\bar{t}_d$ denotes the average total crystal dissolution time subject to uncertainty and $r_d^u(\alpha_{cf}|t_m) = F^{-1}\left(1 - \frac{\alpha_{cf}}{2}\middle| r_d^u(\alpha_{cf}|t_m)\right)$ denotes the upper bound applied to the dissolution rate under uncertainty at every timepoint t_m at a confidence interval α_{cf}, where $F^{-1}\left(\Pi|\boldsymbol{\Psi}(\alpha_{cf}|t_m)\right)$ denotes the inverse cumulative distribution function of a model output $\boldsymbol{\Psi}(t_m)$ at time t_m evaluated at a probability Π. This scenario was implemented twice at two different confidence intervals. The first robust scenario applies an upper bound on the dissolution rate at 84.1% confidence (i.e. at one standard deviation above the expected value; $\alpha_{cf} = 31.8\%$ so $\Pi = 1 - \frac{\alpha_{cf}}{2} = 0.841$), whereas the second robust scenario analyzes the dissolution rate upper bound at 99.9% confidence ($\alpha_{cf} = 2\%$ so $\Pi = 1 - \frac{\alpha_{cf}}{2} = 0.99$). This problem was solved following the same approach described in Scenario I, i.e., problem was solved once for each crystal shape (Δ) using the *fmincon*'s built-in gradient-based optimization function available in MATLAB 2020a. The results from these optimization studies are displayed in Table 4.6. This table shows that there was a 1% difference on average in the total dissolution time between the nominal simulation results and the robust optimization results at 84.1% confidence. Similarly, it showcases that there is a 7% , 46%, and 94% difference in the total dissolution time between the nominal optimization results and the robust optimization results at a 99.9% confidence for the $cube$, $sphere$, and $dode$ crystal shapes, respectively. The results in Table 4.6 further show that under 84.1% confidence, the effects of uncertainty on the optimization performance is negligible, and consequently the results from the robust optimization (i.e. the crystal shape and size that maximize the dissolution time while limiting the maximum dissolution rate under uncertainty) are the same as those predicted from the nominal optimization study (Scenario I). On the other hand, the optimization results under 99% confidence show notable deviations from the nominal optimization results. These results highlight that due to the effects of uncertainty, it is necessary to consider notably smaller crystal sizes in order to ensure that the maximum dissolution rate remains below the

Table 4.6. Robust optimization results for $max\ \bar{t}_d$ for each of the considered $CaCO_3$ crystal shapes

Optimization Scenario	Robust Optimization: $max\ \bar{t}_d$ ($\alpha_{cf} = 31.8\%$)				Robust Optimization: $max\ \bar{t}_d$ ($\alpha_{cf} = 2\%$)			
Shape	*cube* **optimal**	*sphere*	*tetra* *infeasible*	*dode*	*cube* **optimal**	*sphere*	*tetra* *infeasible*	*dode* *infeasible*
Size	54872	15408	512	53455	46656	3544	512	451
$\bar{t}_d$ (s)	5.72	2.59	0.25	4.92	5.35	1.41	0.25	0.31
$\sigma_{t_d}^2$ (s^2)	217.36	42.78	0.06	184.34	191.95	14.41	0.06	0.55
$r_d^u(\alpha_{cf}\|t_1)$ (ions/s)	2.18×10^6	7.00×10^6	2.22×10^7 *infeasible*	6.70×10^6	2.28×10^6	6.92×10^6	4.74×10^7 *infeasible*	1.47×10^7 *infeasible*
$r_d^u(\alpha_{cf}\|t_2)$ (ions/s)	1.89×10^5	1.89×10^6	3.96×10^6	3.14×10^6	2.87×10^5	3.73×10^6	4.01×10^6	1.91×10^6
$r_d^u(\alpha_{cf}\|t_3)$ (ions/s)	8.35×10^4	8.60×10^5	6.74×10^5	1.18×10^6	6.06×10^5	4.88×10^6	5.06×10^6	1.74×10^6
$r_d^u(\alpha_{cf}\|t_4)$ (ions/s)	9.02×10^5	1.01×10^6	1.16×10^5	1.66×10^6	6.99×10^6	2.37×10^6	1.26×10^5	1.25×10^5
$r_d^u(\alpha_{cf}\|t_5)$ (ions/s)	7.95×10^5	4.31×10^5	3.18×10^4	1.28×10^6	3.30×10^6	2.81×10^5	3.86×10^4	3.79×10^4
$r_d^u(\alpha_{cf}\|t_6)$ (ions/s)	3.58×10^5	9.23×10^4	2659.3	3.24×10^5	3.47×10^5	2.48×10^4	3036.0	3496.3
$r_d^u(\alpha_{cf}\|t_7)$ (ions/s)	3.40×10^4	6692.7	182.05	2.82×10^4	3.06×10^4	1604.4	288.09	317.22
$r_d^u(\alpha_{cf}\|t_8)$ (ions/s)	3163.9	0	1.08	0	0	0	113.57	66.91

specified threshold with high confidence. This observation is most apparent in the dodecahedral shaped crystal, where the maximum dissolution rate is not guaranteed to fall below 7×10^6 ions/s with 99% certainty over the range of crystal sizes considered in this study. However, both the rhombohedral cubic and spherical crystals are also noticeably impacted by the effects of uncertainty on the dissolution rate, as the optimal crystal sizes predicted for both of these shapes are noticeably lower than for the nominal optimization study. Note that in addition to the dodecahedral shaped crystal at 99% certainty, the maximum dissolution rate within the tetrahedral crystal for both confidence intervals remained above the threshold specified in Eq. (4.16) for all considered crystal sizes, and consequently it is an infeasible solution. As in the previous scenario, the infeasible results listed in Table 4.6 were determined by finding the crystal sizes for their respective shapes whose maximum reaction rate was the closest to meeting the restriction specified in Eq. (4.16).

4.5.3 Scenario III: Bi-objective Optimization

The results above indicate that uncertainty can impact the optimal crystal sizes and shapes under high confidence and highlights the need to minimize the variability while maximizing the dissolution time. The present scenario aims to determine the optimal trade-off point between these opposing objectives using an ℓ^p-

norm bi-objective optimization scheme. This optimization approach identifies an infeasible yet desirable optimal point (the utopia point) that simultaneously addresses both conflicting objectives, and subsequently determines the point within the feasible objective search space that is closest to this point.[201]

In order to identify the utopia point and thus perform bi-objective optimization, it is necessary to perform two independent optimization studies *a priori*, one with respect to each conflicting objective. In the $CaCO_3$ dissolution process considered in this work, the first study (*minVar*) seeks to minimize the variability in the dissolution time while keeping the dissolution rate below a specific threshold, as follows:

$$\min_{s,\Delta} \sigma_{t_d}^2 \tag{4.17}$$

Subject to:

$$\text{Constraints, Eq. (4.8)-(4.12); Eq. (4.15)-(4.16)}$$

where $\sigma_{t_d}^2$ denotes the variance of t_d under uncertainty. The second optimization study (*maxTime*) seeks to maximize the dissolution time while still controlling the dissolution rate, as expressed in the robust optimization study denoted in Scenario II; these results are shown in Table 4.6 (*maxTime*). The results from the *minVar* optimization study are presented in Table 4.7. The results in both tables highlight that the uncertain variability is minimized for smaller crystals and crystals with shorter dissolution times. These results are to be expected, as the variability in the dissolution performance is directly correlated to the magnitude of the dissolution properties. Furthermore, the optimal conditions that minimize the variability are significantly different depending on the level of confidence applied to the maximum dissolution rate. Under a higher level of confidence, the dodecahedral crystal is no longer the optimal crystal shape since the maximum dissolution rate cannot be guaranteed to remain below the specified threshold with 99% confidence. Furthermore, the tetrahedral crystal remained above the specified threshold for both confidence intervals, and thus it was considered an infeasible solution. Note that the infeasible results listed in Table 4.7 were determined following the approach used to report the infeasible solutions for Scenarios I and II.

The results in Tables 4.6 and 4.7 additionally highlight that the optimal crystal proportions necessary to minimize the variation due to uncertainty are in direct contrast with the optimal crystal designs necessary to maximize the crystal dissolution time. However, these optimization results can be used to define the infeasible optimal utopia point according to the coordinate pair $(\bar{t}_{d,max}, \sigma_{t_d,min}^2)$, where $\bar{t}_{d,max}$ denotes the mean dissolution time under uncertainty determined from the *maxTime* optimization study, whereas $\sigma_{t_d,min}^2$ denotes the variance in t_d due to uncertainty under the *minVar* optimization study. After determining the utopia point, the optimal trade-off point can be determined using the ℓ^p-norm bi-objective optimization expression. This work implemented a ℓ^2-norm bi-objective optimization scheme as shown below in Eq. (4.18). This study considered a ℓ^2-norm optimization scheme as the relationship between the two objectives was determined to

Table 4.7. Robust optimization results for $min\ \sigma_{t_d}^2$ for each of the considered $CaCO_3$ crystal shapes

Optimization Scenario	Robust Optimization: $min\ \sigma_{t_d}^2$ ($\alpha_{cf} = 31.8\%$)				Robust Optimization: $min\ \sigma_{t_d}^2$ ($\alpha_{cf} = 2\%$)			
Shape	*cube*	*sphere*	*tetra* *infeasible*	*dode* **optimal**	*cube*	*sphere* **optimal**	*tetra* *infeasible*	*dode* *infeasible*
Size	512	360	512	576	512	672	512	451
$\bar{t}_d$ (s)	0.77	0.54	0.25	0.36	0.77	0.69	0.25	0.31
$\sigma_{t_d}^2$ (s^2)	5.64	2.48	0.06	0.84	5.57	3.99	0.06	0.56
$r_d^u(\alpha_{cf}\|t_1)$ (ions/s)	2.16×10^6	3.72×10^6	2.22×10^7 *infeasible*	6.99×10^6	2.17×10^6	6.92×10^6	4.73×10^7 *infeasible*	1.47×10^7 *infeasible*
$r_d^u(\alpha_{cf}\|t_2)$ (ions/s)	1.78×10^5	8.13×10^5	3.96×10^6	1.80×10^6	1.88×10^5	4.37×10^6	4.01×10^6	1.91×10^6
$r_d^u(\alpha_{cf}\|t_3)$ (ions/s)	3.02×10^4	6.00×10^5	6.74×10^5	2.03×10^5	1.32×10^5	4.27×10^6	5.04×10^6	1.74×10^6
$r_d^u(\alpha_{cf}\|t_4)$ (ions/s)	2.41×10^4	1.20×10^5	1.16×10^5	7.86×10^4	2.09×10^5	5.59×10^5	1.26×10^5	1.26×10^5
$r_d^u(\alpha_{cf}\|t_5)$ (ions/s)	3.81×10^4	2.86×10^4	3.18×10^4	4.04×10^4	4.83×10^4	5.73×10^4	3.86×10^4	3.79×10^4
$r_d^u(\alpha_{cf}\|t_6)$ (ions/s)	4046.8	2346.8	2660.9	3511.9	4333.6	4806.9	3035.7	3496.6
$r_d^u(\alpha_{cf}\|t_7)$ (ions/s)	135.62	335.68	182.11	0	221.73	578.85	288.1	317.49
$r_d^u(\alpha_{cf}\|t_8)$ (ions/s)	0	614.11	1.11	84.01	0	707.79	115.07	66.91

be near-linear, and therefore it required a nonlinear (i.e. ℓ^2-norm or higher) optimization scheme in order to compute the trade-off.

$$\min_{s,\Delta} \sqrt{\left(1 - \frac{\bar{t}_d - \bar{t}_{d,min}}{\bar{t}_{d,max} - \bar{t}_{d,min}}\right)^2 + \left(\frac{\sigma_{t_d}^2 - \sigma_{t_d,min}^2}{\sigma_{t_d,max}^2 - \sigma_{t_d,min}^2}\right)^2}, \tag{4.18}$$

Subject to:

Constraints, Eq. (4.8)-(4.12); Eq. (4.15)-(4.16)

In the above formulation, $\bar{t}_{d,min}$ and $\sigma_{t_d,min}^2$ denote the mean and variance of the dissolution time under the *minVar* scenario, whereas $\bar{t}_{d,max}$ and $\sigma_{t_d,max}^2$ denote the mean and variance of the dissolution time under *maxTime* (i.e. scenario II). The multi-objective optimization study was implemented for each crystal shape (Δ) and under the two different uncertainty confidence conditions scenarios, i.e. for $\alpha_{cf} = 31.8\%$ and $\alpha_{cf} = 2\%$ (84.1% and 99% confidence, respectively). The optimal trade-off results for both confidence scenarios are listed in Table 4.8. These results illustrate that the most optimal crystal shape under both scenarios is the

Table 4.8. ℓ^2-norm multi-objective optimization results for each of the considered $CaCO_3$ crystal shapes

Optimization Scenario	ℓ^2-Norm Multi-Objective Optimization: $\alpha_{cf} = 31.8\%$				ℓ^2-Norm Multi-Objective Optimization: $\alpha_{cf} = 2\%$			
Shape	*cube* **optimal**	*sphere*	*tetra* *infeasible*	*dode*	*cube* **optimal**	*sphere*	*tetra* *infeasible*	*dode* *infeasible*
Size	13824	15408	512	19961	13824	3544	512	451
$\bar{t}_d$ (s)	3.47	2.58	0.25	3.28	3.35	1.42	0.25	0.31
$\sigma_{t_d}^2$ (s^2)	84.55	42.44	0.06	80.72	78.92	14.54	0.06	0.56
$r_d^u(\alpha_{cf}\|t_1)$ (ions/s)	2.17×10^6	7.00×10^6	2.22×10^7 *infeasible*	3.85×10^6	2.21×10^6	6.97×10^6	4.73×10^7 *infeasible*	1.47×10^7 *infeasible*
$r_d^u(\alpha_{cf}\|t_2)$ (ions/s)	1.83×10^5	1.89×10^6	3.96×10^6	1.70×10^6	2.41×10^5	3.74×10^6	4.01×10^6	1.91×10^6
$r_d^u(\alpha_{cf}\|t_3)$ (ions/s)	4.62×10^4	8.59×10^5	6.74×10^5	3.44×10^5	4.06×10^5	4.88×10^6	5.04×10^6	1.74×10^6
$r_d^u(\alpha_{cf}\|t_4)$ (ions/s)	3.33×10^5	1.01×10^6	1.16×10^5	1.04×10^6	1.89×10^6	2.38×10^6	1.26×10^5	1.26×10^5
$r_d^u(\alpha_{cf}\|t_5)$ (ions/s)	3.40×10^5	4.29×10^5	3.18×10^4	6.18×10^5	1.17×10^6	2.83×10^5	3.86×10^4	3.79×10^4
$r_d^u(\alpha_{cf}\|t_6)$ (ions/s)	1.02×10^5	9.23×10^4	2660.9	1.25×10^5	1.03×10^5	2.50×10^4	3035.7	3496.6
$r_d^u(\alpha_{cf}\|t_7)$ (ions/s)	9196.4	6688.0	182.11	1.09	8971.8	1611.5	288.1	317.49
$r_d^u(\alpha_{cf}\|t_8)$ (ions/s)	0	0	1.11	0	0	79.03	115.07	66.91
L_{norm}*	0.57	0.62	----	0.59	0.59	0.85	----	----

*Normalized Distance from the Utopia Point (ℓ^2-Norm)

rhombohedral cubic shape. However, the dodecahedral crystal is able to achieve similarly optimal results under lower confidence, i.e. so long as its maximum dissolution rate could be guaranteed to fall below the desired threshold. Furthermore, the crystal size that best addresses the trade-off are medium-sized crystals, which have moderately high dissolution times and moderately low variability.

Fig. 4.11 showcases the results from each of the optimization studies compared to the utopia point for the two confidence intervals. For the sake of illustration, Fig. 4.11 also displays the optimal results determined for all of the eligible crystal shapes in addition to the optimal shape ($\measuredangle = cube$). Fig. 4.11 also highlights the Pareto frontier, i.e. the edge of the feasible search space between the optimal result points from both competing objectives. The Pareto frontier points were generated by solving the following ℓ^2-norm based optimization problem:

$$\min_{s}\left(w_{pareto}\left(1-\frac{\bar{t}_d-\bar{t}_{d,min}}{\bar{t}_{d,max}-\bar{t}_{d,min}}\right)^2+\left(1-w_{pareto}\right)\left(\frac{\sigma^2_{t_d}-\sigma^2_{t_d,min}}{\sigma^2_{t_d,max}-\sigma^2_{t_d,min}}\right)^2\right), \tag{4.19}$$

Subject to:

Constraints, Eq. (4.8)-(4.12); Eq. (4.15)-(4.16)

where $w_{pareto} = [0,0.1,0.2, \dots 0.9,1]$ is a weighted term that is adjusted between 0 and 1 to determine each of the Pareto points displayed in the figure. Note that the pareto front was generated only for the crystal shape that corresponds to the optimal solution, i.e. $\measuredangle = cube$. Additionally note that this pareto front addresses the trade-off between the *maxTime* optimization study ($\max_{s,\measuredangle} \bar{t}_d$) and the *minVar* optimization study ($\min_{s,\measuredangle} \sigma^2_{t_d}$) and therefore the optimal trade-off points indicate the best trade-off for each valid crystal shape that simultaneously maximize $\bar{t}_d$ and minimize $\sigma^2_{t_d}$. As in the previous scenarios, problem (4.19) was solved using *fmincon*'s built-in function available in MATLAB 2020a. Fig. 4.11 showcases that the ℓ^2-norm trade-off results for the rhombohedral cubic crystal represent the closest point within the feasible search space to the targeted utopia point. Furthermore, the figure showcases that the optimal dodecahedral crystal design is able to achieve results within the same proximity to the utopia point. This highlights that the slower-dissolving crystals are essential for achieving optimal dissolution behaviour for slow-release applications.

4.6 Summary

The crystal dissolution process is a vital process that plays a critical role in numerous biological applications such as nutrient and pharmaceutical drug delivery. As a result, it is important to develop process models to capture and study the crystal dissolution process and furthermore understand and control the impact of environmental uncertainty on the dissolution behaviour. In this chapter, 3D MFkMC and standard kMC models were created to capture the dissolution of an entire crystal system. These models were subsequently compared to showcase the computational strengths of MFkMC. The proposed frameworks were additionally used to analyze the dissolution process on crystals of different sizes and shapes, and to study the impact of fluctuations in the system temperature and pH (i.e., the key environmental parameters) on the crystal dissolution. These results highlighted that the expected fluctuations in the pH are substantial and must be taken into account, whereas the expected variability in the temperature had minimal effect on the system. PCE models and LPCMs were additionally constructed to efficiently propagate parametric uncertainty in the activation energy (i.e. the key parameter considered to be affected by the pH) through the crystal dissolution model for a crystal of given size and shape. The LPCMs were subsequently used to perform optimization on the crystal dissolution system through a trio of different case studies. These case studies sought to maximize the time required for the crystal to dissolve and minimize the variability due to uncertainty on the dissolution time while

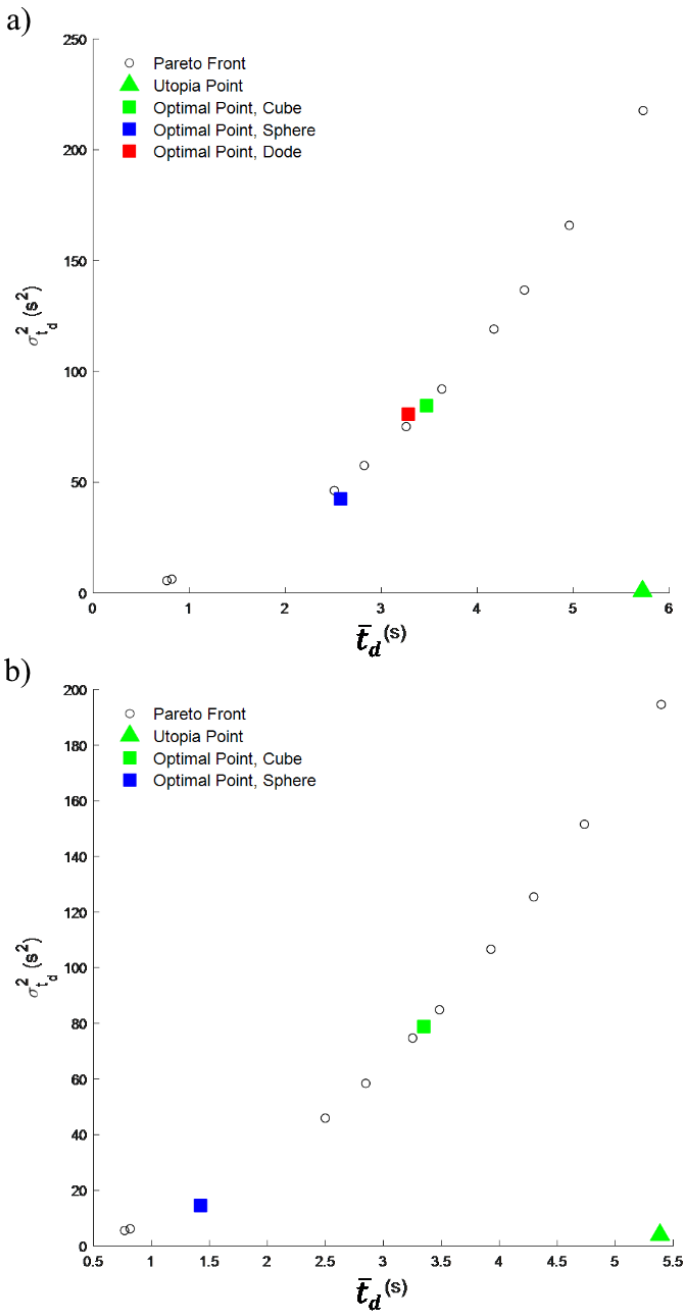

Figure 4.11: Location of the optimal trade-off points for the rhombohedral cubic crystal (green ×), spherical crystal (blue ×), and dodecahedral crystal (red ×), as well as the utopia point (green ▲), along the mean dissolution time ($\bar{t}_d$)/dissolution time variance ($\sigma^2_{t_d}$) Pareto front (black ○) under: a) 84.1% confidence ($\alpha_{cf} = 31.8\%$), b) 99% confidence ($\alpha_{cf} = 2\%$). Note that this pareto front addresses the trade-off between the *maxTime* optimization study ($\max_{s,\Delta} \bar{t}_d$) and the *minVar* optimization study ($\min_{s,\Delta} \sigma^2_{t_d}$) and therefore the optimal trade-off points indicate the best trade-off for each valid crystal shape that simultaneously maximize $\bar{t}_d$ and minimize $\sigma^2_{t_d}$

simultaneously limiting the maximum dissolution rate experienced by the system. These studies highlighted that moderate crystal sizes and simpler crystal structures with higher concentrations of low-reaction terrace sites are needed to achieve the desirable objectives. These findings overall demonstrate the importance of taking environmental variability into consideration when designing crystals for biological and pharmaceutical purposes.

Chapter 5 – MFkMC Model for Capillary Rise Systems‡

Capillary action-driven transport through small cavities plays a crucial role in numerous applications, ranging from oil extraction,[24,202] to capillary pumps in applications such as immunoassays,[25,203] to low-gravity fluid flow applications,[204] to fluid manipulation in heating systems.[26,205] Consequently, there has been significant interest in developing models to capture the behaviour of capillary action. Capillary action typically occurs in rough, nonuniform microscale capillaries that are often a few micrometers to millimeters in diameter and that frequently contain nanoscale asperities. However, capillary action can extend over distances that can theoretically range from a few micrometers to over a hundred kilometers.[28] Hence, it is desirable to implement modelling approaches such as kMC that can capture the nanoscale evolution of capillary action and extend it to the macroscale system over which it evolves. However, traditional kMC models are incapable of capturing the movement of the fluid-fluid based capillary action interface as highlighted in Section 2.1.2. Furthermore, although the MFkMC algorithm discussed in Chapter 3 has the potential to accurately capture the capillary action behaviour, this method is still limited by a lack of rate expression to capture the fluid-fluid interface movement based on its underlying physics.

Motivated by this, the objective of this section is to expand the MFkMC algorithm to capture fluid-fluid based moving interface systems based on the fundamental force balances affecting the interface. The developed force balance-based MFkMC (FB-MFkMC) model will be subsequently applied to simulate capillary rise (i.e., vertical capillary action) of water in stainless steel tubes of different shapes. The FB-MFkMC model will be initially used to simulate capillary rise in cylindrical tubes of different radii, and the results of these simulations will be compared against known analytical solutions. Subsequently, the FB-MFkMC model will be used to simulate a pair of models that cannot be described analytically. In the first model, FB-MFkMC will be used to simulate capillary rise in a capillary with irregular geometry. On the other hand, the second model will consider capillary rise in a cylindrical tube with nanoscale roughness asperities applied to its surface. Section 5.1 will describe the development of the FB-MFkMC algorithm to capture fluid-fluid based moving interfaces based on their force balances. This section will additionally discuss the implementation and development of the FB-MFkMC model for capillary rise. Subsequently, Section 5.2 will outline the three case studies and present the capillary rise model results for each scenario. A summary of this chapter will be provided in Section 5.3.

5.1 MFkMC Algorithm for Capillary Rise

The objective of this subsection is to provide a general MFkMC-based framework to simulate capillary rise of a fluid within a solid cavity. In order to implement MFkMC to capture capillary rise, it is first necessary

‡ The contents of this chapter were published in the Journal of Physical Chemistry B[23]

to determine rates that can describe the movement of the fluid interface as it rises up the wetting cavity. The key properties of the capillary-driven systems such as capillary rise are dictated by the movement of the triple contact line, and consequently it is only necessary to consider the rate equations governing the triple line's local movement when modelling capillary action applications.[10] Although kMC-based approaches have yet to be implemented for capillary action, there have been previous attempts at deriving kinetic rate equations that govern the movement of a triple contact line within a capillary-driven system. Most prominently, Blake and Haynes proposed the molecular-kinetic model, which predicts the local contact angle of the triple contact line on a flat surface based on energy dissipation from kinetic surface events.[206] Within this model, the local advancement or recession of the triple contact line is associated with dissipation of energy at the triple contact line due to molecular movements of the fluid molecules over a distance λ; this can be expressed as follows:

$$W_{adv,i,} = k' \, exp\left(\frac{f_i \lambda^2}{2k_b T}\right), \tag{5.1}$$

$$W_{rec,i} = k' \, exp\left(\frac{-f_i \lambda^2}{2k_b T}\right) \tag{5.2}$$

where $W_{adv,i}$ and $W_{rec,i}$ denote the local rate of advancing and receding respectively of the i^{th} interface site at the triple contact line over the incremental distance λ, and f_i denotes the force per unit length experienced locally by the contact line at an interface site i. In addition, k' is a rate constant that was originally defined to include the Arrhenius rate of liquid adsorption/desorption on the surface as per the Blake-Haynes model. The kinetic rate equations in Eqs. (5.1)-(5.2) can be combined to define the local velocity of the triple line as follows:[206]

$$v_i = \lambda\left(W_{adv,i} - W_{rec,i}\right) = 2\lambda k' \, sinh\left(\frac{f_i \lambda^2}{2k_b T}\right) \tag{5.3}$$

The force per unit length f_i is associated with the capillary force exerted on the contact line, and it was originally defined within the Blake-Haynes model as $f = \gamma_{sv} - \gamma_{sl} - \gamma_{lv}\cos(\theta)$ (i.e., re-defining Young's Equation for a dynamic contact angle θ). However, this approach is rudimentary as it fails to account for the remainder of the forces affecting the fluid rise, it relies on fitted model parameters, and it has been observed to deviate from experimental results. Their equations, however, do provide general kinetic rate expressions that can be readily coupled with an MFkMC-based algorithm to form the FB-MFkMC approach. As a result, Eqs. (5.1)-(5.2) were used as a general basis to couple the balance of the known forces acting on the triple contact line, i.e., the modified Lucas-Washburn equation in Eq. (2.9).

In order to couple Eq. (2.9) with Eqs. (5.1)-(5.2), it is necessary to determine the relationship between the kinetic rates $W_{adv,i}$ and $W_{rec,i}$, and the force experienced by each molecular site along the contact line. In order to accomplish this task, Eq. (5.3) can be re-arranged as a function of the force per unit length, f_i.

Subsequently, this expression can be substituted into Eqs. (5.1)-(5.2) to obtain the kinetic rates in the following form:

$$W_{adv,i} = k' \, exp\left(sinh^{-1}\left(\frac{v_i}{2\lambda k'}\right)\right) \tag{5.4}$$

$$W_{rec,i} = k' \, exp\left(-sinh^{-1}\left(\frac{v_i}{2\lambda k'}\right)\right) \tag{5.5}$$

Note that the value of k' was observed to have negligible effect on the system behaviour, and consequently its value was set to $k' = 1$ s^{-1} within this work.[23] These kinetic rate equations can now be coupled with the force balance in Eq. (2.9) via the local velocity of the triple line, i.e. by setting $v_i = v_{cr}$, which is the only parameter in common between the equations. By re-arranging Eq. (2.9) for v_{cr} and substituting it into Eqs. (5.4)-(5.5), the kinetic rates for the triple contact line to advance and recede can be defined as follows:

$$W_{adv,i} = k' \, exp\left(sinh^{-1}\left(\frac{2\gamma_{lv}R_{cr,i}\,sin(\beta_{s,i}-\theta_i)-\rho g h_i R_{cr,i}^2}{16\mu h_i \lambda k'}\right)\right), \tag{5.6}$$

$$W_{rec,i} = k' \, exp\left(-sinh^{-1}\left(\frac{2\gamma_{lv}R_{cr,i}\,sin(\beta_{s,i}-\theta_i)-\rho g h_i R_{cr,i}^2}{16\mu h_i \lambda k'}\right)\right) \tag{5.7}$$

where $R_{cr,i}$, $\beta_{s,i}$, θ_i, and h_i denote the cavity radius, cavity wall angle, local contact angle, and triple contact interface height at the i^{th} interface site along the triple contact line. Note that $R_{cr,i}$, $\beta_{s,i}$, and θ_i are functions of the fluid height in the capillary tube h_i. Furthermore, note that the FB-MFkMC rate equations proposed above are used to determine the probability that a localized section of the interface will displace by a distance λ based on the local velocity of the interface at that point. Therefore, this capillary-driven FB-MFkMC model discretizes the movement of the interface so that it can only move over distance λ at any given point in time. As a result, the parameter λ can be adjusted to fine-tune or coarse-grain the FB-MFkMC capillary action system and control the trade-off between model accuracy and computational efficiency. If λ is small (e.g., if λ is defined as the local intermolecular spacing between interfacial molecules), then the system will have very high accuracy and will be able to accommodate for extremely small spatial and temporal heterogeneities, however it will require high CPU times to reach completion. On the other hand, large values of λ (e.g., if λ is 5% of the total system size), then the system will be highly efficient and will have extremely small CPU times, however they will be noisy and will miss out on any fine-scale behaviour taking place. Consequently, λ must be chosen *a priori* in order to address the trade-off between the model accuracy and model efficiency. Additionally note that the proposed capillary action FB-MFkMC method shares several similarities with the level set method of interface movement, as it evolves the interface in space and time based on the local interface velocity profile. However, unlike the level set method, the FB-MFkMC approach to simulating fluid-fluid interfaces defines the interface explicitly based on the positions of the interfacial molecules. Specifically, when the FB-MFkMC interface is discretized on a molecular level, it uses the velocities of the interfacial molecules

themselves to advance the interface. Therefore, FB-MFkMC is capable of handling complicated interface geometries in a similar fashion to the implicit level set method.

The capillary rise case study considered within this work consists of a body of water interacting with vertical radially-symmetric stainless steel tubes of varying dimensions. This system was implemented using lattice-free FB-MFkMC to predict the height of water in the steel tubes over time. The system was considered to be axisymmetric for the sake of simplicity, and consequently the capillary rise system was modeled using a 1D FB-MFkMC model. In this system, the interface (i.e., the triple contact line) can be captured using FB-MFkMC through the use of a single fluid interface site and a single vapour interface site, which predicts the location and system properties at the fluid and vapour sides of the triple contact line, respectively. Note that in this case study, the location of the solid interface remained fixed in time; thus, it was not necessary to consider a solid interface site in the FB-MFkMC algorithm. Due to the 1D and lattice-free nature of the FB-MFkMC model considered in this study, the fluid and vapour-phase sites were captured using the list indexing approach discussed in Section 3.3.4, where the fluid and vapour site information was stored in an array that keeps track of their vertical location h_i, as well as the cavity radius $R_{cr,i}$, local cavity wall angle $\beta_{s,i}$, velocity $v_{cr,i}$, and contact angle θ_i at the triple contact line. Note that there was no need to keep track of the interface site "connectivity" (i.e., keeping track of each site's nearest neighbours). This is because the 1D model only considers a single interface site for each phase and these sites are continually adjacent as per MFkMC's definition of an interface. The FB-MFkMC algorithm assumes that fluid-phase molecules can advance and displace the vapour interface site according to the advancing rate $W_{adv,i}$ in Eq. (5.6). Similarly, the FB-MFkMC algorithm assumes that vapour-phase molecules can advance and displace the fluid interface site according to the inverse receding rate equation W_{rec} in Eq. (5.7). Note that the force balance accommodates for the behaviour of the solid, fluid, and vapour phases and therefore the derived rate equations account for both the advancing and receding events $\epsilon_{adv,i}$ and $\epsilon_{rec,i}$ required to move the interface as discussed in Chapter 3. Furthermore, note that since the kinetic rates of advancing in Eqs. (5.6) and (5.7) do not directly depend on the time t or the time increment δt, it does not matter where δt is calculated within the FB-MFkMC algorithm. However, the time increment δt was calculated before selecting a site in the algorithm above in order to mirror the general MFkMC structure presented in Section 3.2. The complete FB-MFkMC algorithm for capillary rise implemented within this study is summarized as follows:

1. Initialize the cavity by defining the variability in the cavity radius $R_{cr,i}$ as a function of the vertical position within the cavity h_i.
2. Define the initial positions of the fluid and vapor interface sites as well as the initial velocity $v_{cr,0,i}$ of the triple contact line. Calculate and store the cavity radius $R_{cr,i}$, the cavity wall angle $\beta_{s,i}$, and the contact angle θ_i.

3. Calculate and store the rates of advancement for the fluid and vapor interface sites, $W_{adv,i}$ and $W_{rec,i}$, according to Eqs. (5.6) and (5.7).
4. Calculate the kMC time increment, δt, according to Eq. (3.11) to determine the time $t + \delta t$ at which the next event will occur.
5. Apply MC sampling to select either the fluid or the vapor interface site according to Eq. (3.12). If the fluid interface site is selected, then the fluid will advance and displace the vapor interface site and the vertical location of both sites will be incremented by λ. On the other hand, if the vapor interface site is selected, then the vapor will advance and displace the fluid interface site and the vertical location of both sites will be decremented by λ.
6. Calculate the new cavity radius $R_{cr,i}$, cavity wall angle $\beta_{s,i}$, contact angle θ_i, and velocity v_i of the triple contact line.
7. Calculate the new rates of advancing for the fluid and vapor interface sites, $W_{adv,i}$ and $W_{rec,i}$, according to Eqs. (5.6)-(5.7).
8. Repeat Steps 4-7 until a final time t_f has been reached.

5.2 Capillary Rise Model Results, Validation, and Analysis

The objective of this section was to apply the FB-MFkMC algorithm discussed in the previous section to model the capillary-driven rise of water in radially-symmetric vertical stainless steel tubes of varying shapes. The proposed FB-MFkMC algorithm was used to simulate capillary rise under three different scenarios: capillary rise in perfectly smooth cylindrical tubes of uniform radii, capillary rise in an axisymmetric tube with complex geometry, and capillary rise in roughened cylindrical tubes. For each of these case studies, the capillary action FB-MFkMC algorithms were executed until a final time $t_f = 0.5$ ms was achieved. Furthermore, the fluid properties and relevant parameters for each of these systems are listed in Table 5.1.

Table 5.1. Capillary rise parameters for water rising up a stainless steel tube

Parameter	Symbol	Value
Equilibrium contact angle, water on stainless steel	θ_e	71°
Water-air surface tension at $T = 25$°C	γ_{lv}	72.28 mN/m
Dynamic viscosity of water at $T = 25$°C	μ	0.89 mPa/s
Density of water at $T = 25$°C	ρ	997 kg/m^3
Line tension of water	ς	20 pN ([43])
Rate constant, movement of the triple contact line	k'	1 s^{-1}
Step change considered by the MFkMC model	λ	7.07×10^{-9} m

5.2.1 Case Study 1: Capillary Rise in Perfectly Cylindrical Cavities

The first case study considered capillary rise in three perfectly cylindrical vertical tubes of constant radii $R_{cr.i} = R_{cr},\ R_{cr} = [3,4,5]$ mm in order to validate the FB-MFkMC model performance. The results of this analysis were compared against the known analytical solution to the Lucas-Washburn equation in a perfect cylinder, which predicts the height of the capillary as a function of time t:[207]

$$h = \frac{\mathcal{A}}{\mathcal{B}}\left(1 + \mathcal{W}\left(-e^{-1-\frac{B^2 t}{A}}\right)\right) \tag{5.8}$$

where $\mathcal{A} = \frac{R_{cr}\gamma_{lv}\cos(\theta_e)}{4\mu}$, $\mathcal{B} = \frac{R_{cr}^2 \rho g}{8\mu}$, and $\mathcal{W}$ denotes the Lambert W function. Furthermore, the FB-MFkMC algorithm was used to simulate the results for each cylinder radii over five independent simulations to showcase the effects of stochastic variability inherent to kMC methods on the capillary rise results.

The results of this study are illustrated in Fig. 5.1, where the solid lines denote the solution predicted by Eq. (5.8) and the dotted lines denote the solution to the FB-MFkMC equation. Note that the similarly-coloured dotted lines showcase the results from each of the independent FB-MFkMC simulations. Furthermore, the computational cost for this study as well as the percent relative root mean squared errors (PRMSE) between the capillary rise height predicted by FB-MFkMC and the height predicted using Eq. (5.8) are listed in Table 5.2. These results illustrate that the FB-MFkMC equations are in complete agreement with the analytical

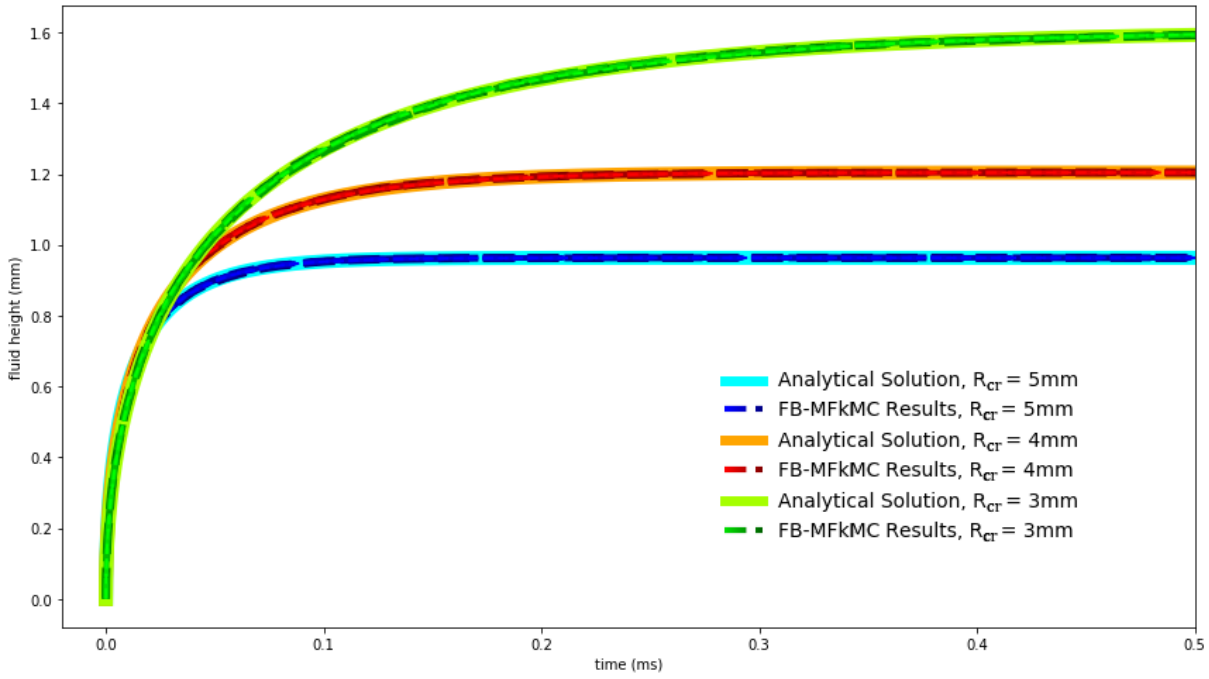

Figure 5.1: Capillary rise height profiles as a function of time for water in perfectly cylindrical tubes of varying radii

Table 5.2. FB-MFkMC computational costs and PRMSEs between the analytical and FB-MFkMC-predicted capillary rise heights for each of the three cylindrical tube studies

Size (mm)	FB-MFkMC Iteration	CPU time (s)	PRMSE (%)
$R_{cr} = 5$	1	3.363	4.296×10^{-3}
	2	3.611	3.004×10^{-3}
	3	3.343	2.221×10^{-1}
	4	3.464	5.293×10^{-3}
	5	3.504	4.251×10^{-3}
$R_{cr} = 4$	1	3.472	1.132×10^{-2}
	2	3.526	6.288×10^{-3}
	3	3.347	6.747×10^{-3}
	4	3.627	3.336×10^{-3}
	5	2.925	9.545×10^{-3}
$R_{cr} = 3$	1	3.052	4.867×10^{-1}
	2	3.018	7.951×10^{-3}
	3	2.909	8.623×10^{-3}
	4	3.229	2.415×10^{-2}
	5	2.988	1.100×10^{-1}

solutions listed in Eq. (5.8), as the PRMSE results remain below 0.3% and the majority of the errors are below 0.01%. Furthermore, they showcase that the kMC-induced stochastic fluctuations do not significantly affect the predicted capillary rise behaviour. Table 5.2 also demonstrates the efficiency of the FB-MFkMC algorithm, as the system only required 95 s on average to simulate capillary rise for a nanoscale λ; note that the computational time can be reduced even further by considering a larger step size λ. The results in Fig. 5.1 additionally demonstrate the different dynamics of capillary rise for cylinders of different diameters. In all three cases, the water begins to rapidly rise into the cylinder tubes before gradually decelerating until the water column height reaches steady state. This steady state level is established as the point where the capillary forces driving the water upward are completely balanced by the gravity forces pulling the column of water downwards. The results further highlight that the water rises higher in tubes with a narrower radius. This behaviour is due to the relationship between the capillary force and the tube radius, shown in the first term of the Lucas-

Washburn equation (i.e., Eqs. (2.5) and Eq. (2.9) in Chapter 2), which showcases that the capillary force term is inversely proportional to the radius of the capillary tube.

5.2.2 Case Study 2: Capillary Rise in Irregular Axisymmetric Cavities

The proposed FB-MFkMC model is not just restricted to considering relatively simple geometries but can also be applied to simulate capillary rise in any cavity irrespective of its shape. As a proof-of-concept to demonstrate the general applicability of the proposed FB-MFkMC algorithm, the framework outlined in Section 5.1 wa s applied to capture capillary rise in a radially-symmetric stainless steel tube with an irregular geometry, which is illustrated in Fig. 5.2. Note that FB-MFkMC is not just limited to simulating axisymmetric cavities and can be applied to capture capillary rise in non-symmetric cavities with any potential geometry. However, these non-symmetric systems would require use of a 2D FB-MFkMC model and therefore cannot be captured using the 1D FB-MFkMC algorithm proposed in this chapter. Further specifics about how to develop a triple contact interface system into 2D are provided in the next chapter. Therefore, non-symmetric cavities have not been considered in this study for brevity. The proposed tube geometry in Fig. 5.2 features a tube whose radius varies vertically; it initially consists of a spherical segment of radius $R_{sphere} = 0.5$ mm that has a lower cross-sectional radius $R_{sphere,low} = 0.48$ mm and an upper cross-sectional radius $R_{sphere,up} = 0.05$ mm, and it subsequently turns into a cone with a wall of slope $\beta_{s,cone} = 104.04°$. Note that the total height of the spherical segment, before it changes into a cone, is $H_{sphere} = 0.637$ mm. The cone rises for a height of $H_{cone} = 0.1$ mm before tapering off to a cylinder of constant radius $R_{cyl} = 25$ µm. The FB-MFkMC algorithm

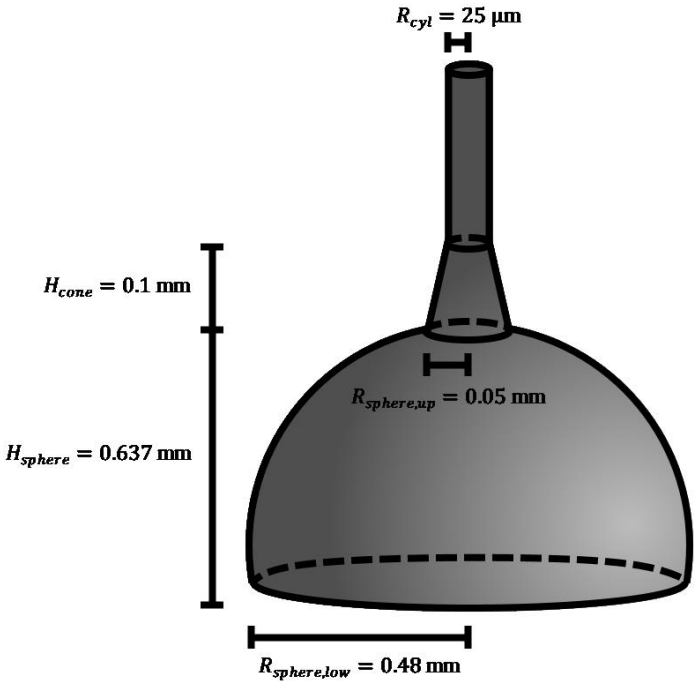

Figure 5.2: The irregularly-shaped stainless steel tube used to generate the results in Fig. 5.3

was used to simulate the results over five independent simulations in order to showcase the effects of the kMC-induced stochastic variability. The results of the capillary rise study are depicted in Fig. 5.3. Note that the differently-shaded lines in this figure showcase the results from independent FB-MFkMC runs. The results presented within the figure illustrate that the transient behaviour of the water inside the irregular tube is significantly different compared to the behaviour within a cylindrical tube. Most notably, the water rises rapidly through the spherical segment of the tube due to the rapidly-decreasing radius, as highlighted inside inlet A of the Fig. 5.3. Once the water reaches the transition point between the sphere and the cone (i.e., at $h_i = H_{sphere} = 0.637$ mm), it continues to increase but at a notably slower rate until it reaches the top of the cone, as illustrated by inlet B in Fig. 5.3. Once the droplet reaches the cylinder part of the tube (i.e., $h_i = H_{sphere} + H_{cone} = 0.737$ mm), the capillary force is not enough to overcome both the change in the tube angle and the gravitational force at this height. As a result, the triple contact line pins at the transition between the cone and the cylinder parts of the tube and the water column ceases to advance. The results in Fig. 5.3 additionally demonstrate that the inherent kMC variability has negligible effect on the capillary rise performance for tubes of irregular geometries, as each of the independent FB-MFkMC simulations produced similar results.

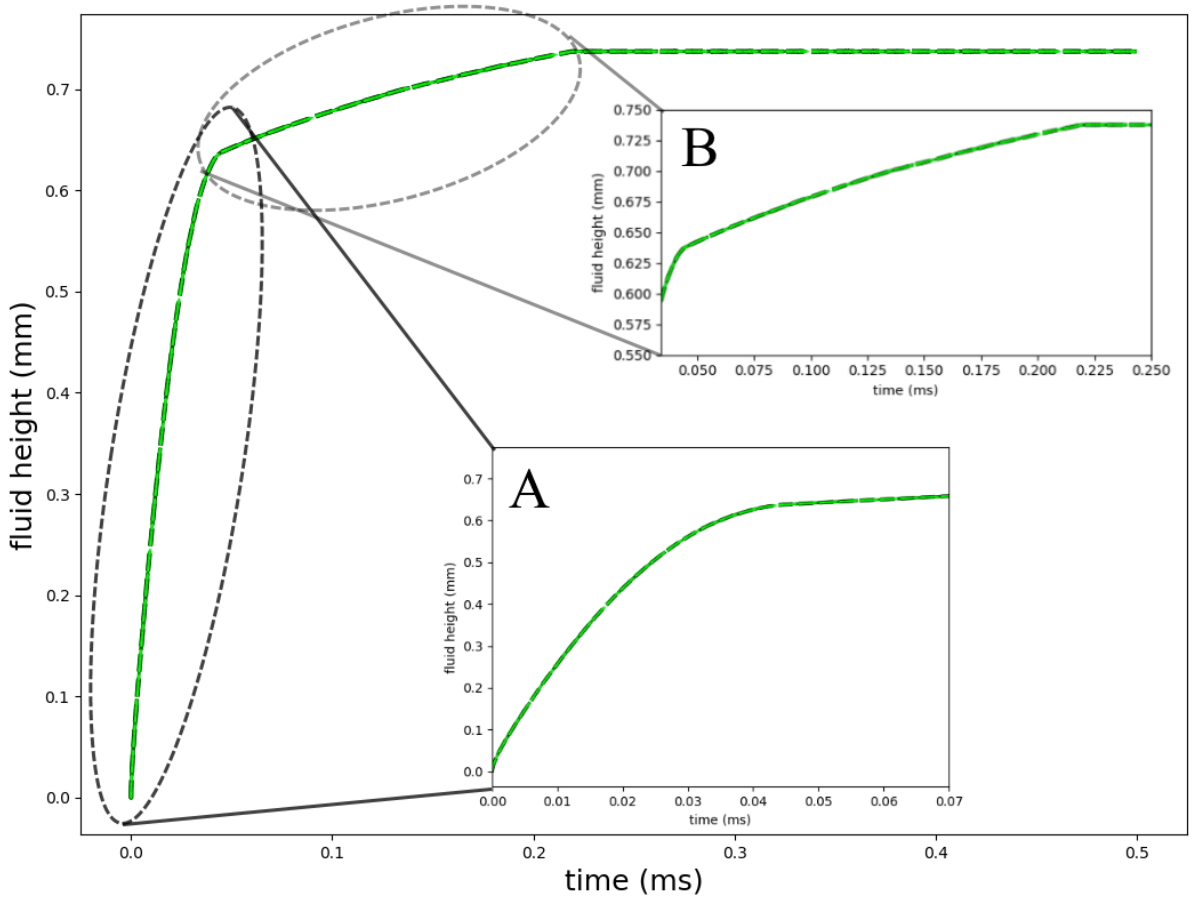

Figure 5.3: Capillary rise height profile inside the axisymmetric tube of irregular geometry in Fig. 5.2

5.2.3 Case Study 3: Capillary Rise in Roughened Cylindrical Cavities

The proposed FB-MFkMC model is also capable of capturing molecular-level roughness on the solid surface and gauging its effects on the overall macroscopic capillary rise behaviour. In order to evaluate this effect, the FB-MFkMC algorithm was used to simulate capillary rise on a cylindrical tube with nanoscale roughness added to its surface. In this procedure, the roughness was geometrically incorporated into the capillary tube profile by a molecular-level deviations δR to the droplet radius at stochastically-determined locations along the height of the cylinder. These geometric deviations in the droplet radius consequently affected the capillary rise behaviour based on the droplet radius variation conditions encoded in the rate equations (i.e., Eqs. (5.6)-(5.7)) according to Eqs. (2.7)-(2.8). The surface roughness δR was stochastically added using a normalized distribution $\mathcal{N}(\bar{\mathcal{N}}, \sigma_{\mathcal{N}}^2)$ with mean $\bar{\mathcal{N}}$ and variance $\sigma_{\mathcal{N}}^2$:

$$\delta R = q\left\lfloor \mathcal{N}(\bar{\mathcal{N}} = 0, \sigma_{\mathcal{N}}^2 = 0.25) \right\rceil \tag{5.9}$$

where the notation $\lfloor d \rceil$ is used to denote rounding the parameter d to the nearest integer value, and where q denotes the size of a single atom defect. Since the solid material considered in this case study (stainless steel) is an alloy, this simulation estimated the value of q based on the lattice length of AISI 316L stainless steel ($q = 0.3596$ nm).[208] The results from the normal distribution were rounded so that the simulation would only consider roughness asperities whose heights were multiples of q (i.e. roughness asperities consisting of an integer number of atoms.) The roughness variance ($\sigma_{\mathcal{N}}^2$) was selected so that the cylinder surface would have an asperity density of roughly one asperity per 22.3 nm (i.e., roughly one asperity every 62 surface atoms) in an attempt to capture the roughness metrics exhibited on practical AISI 316L stainless steel surfaces. Note that asperities of positive height represent roughness peaks, whereas asperities negative height correspond to roughness valleys (i.e., vacancies along the surface of the cylindrical tube). Furthermore, note that due to the radial symmetry assumption applied when deriving the 1D capillary rise model, each roughness asperity in this study is assumed to form a uniform ring around the cavity. This axisymmetric roughness profile is not expected to occur in reality, and therefore the 1D axisymmetric capillary rise model would have very limited predictive capabilities. As a result, this surface roughness case study represents a proof-of-concept case study that is only intended to showcase that the FB-MFkMC capillary rise model can accommodate for surface roughness. To this extent, the asperity density used in this case study was not chosen to reflect the real roughness profiles expected in stainless steel; rather, it was chosen to showcase that the capillary rise FB-MFkMC model captures the expected behaviour of roughness under the roughness profile considered in this work. Note that the FB-MFkMC model can be adapted to accommodate for realistic roughness profiles through expansion to a 2D model where the azimuthal axis cannot be disregarded; however, 2D models have not been considered in this work for the sake of brevity. Further details about how to model a triple contact interface system in 2D can be found in the next chapter. FB-MFkMC was used to simulate capillary rise on rough cylinders of radius $R_{cr} =$

[3,4,5] mm and the results are compared against the capillary rise behaviour inside an ideally-smooth cylindrical tube using the analytical solution presented in Eq. (5.8). The FB-MFkMC algorithm was used to simulate the results for each cylinder radii over five independent simulations. The results of this analysis are presented in Fig. 5.4. Note that in this figure, the solid lines indicate the expected behaviour inside an ideally-smooth cylindrical tube, whereas the dashed lines indicate the solutions predicted using FB-MFkMC for the rough cylindrical tubes. In addition, note that the similarly-coloured dashed lines denote the results from each of the independent FB-MFkMC simulations that were executed for each pore radius. These results indicate that there is substantial deviation between the expected results in a smooth cylinder and the predicted results in a rough cylinder. In particular, the results showcase that the column of water within the tube eventually becomes

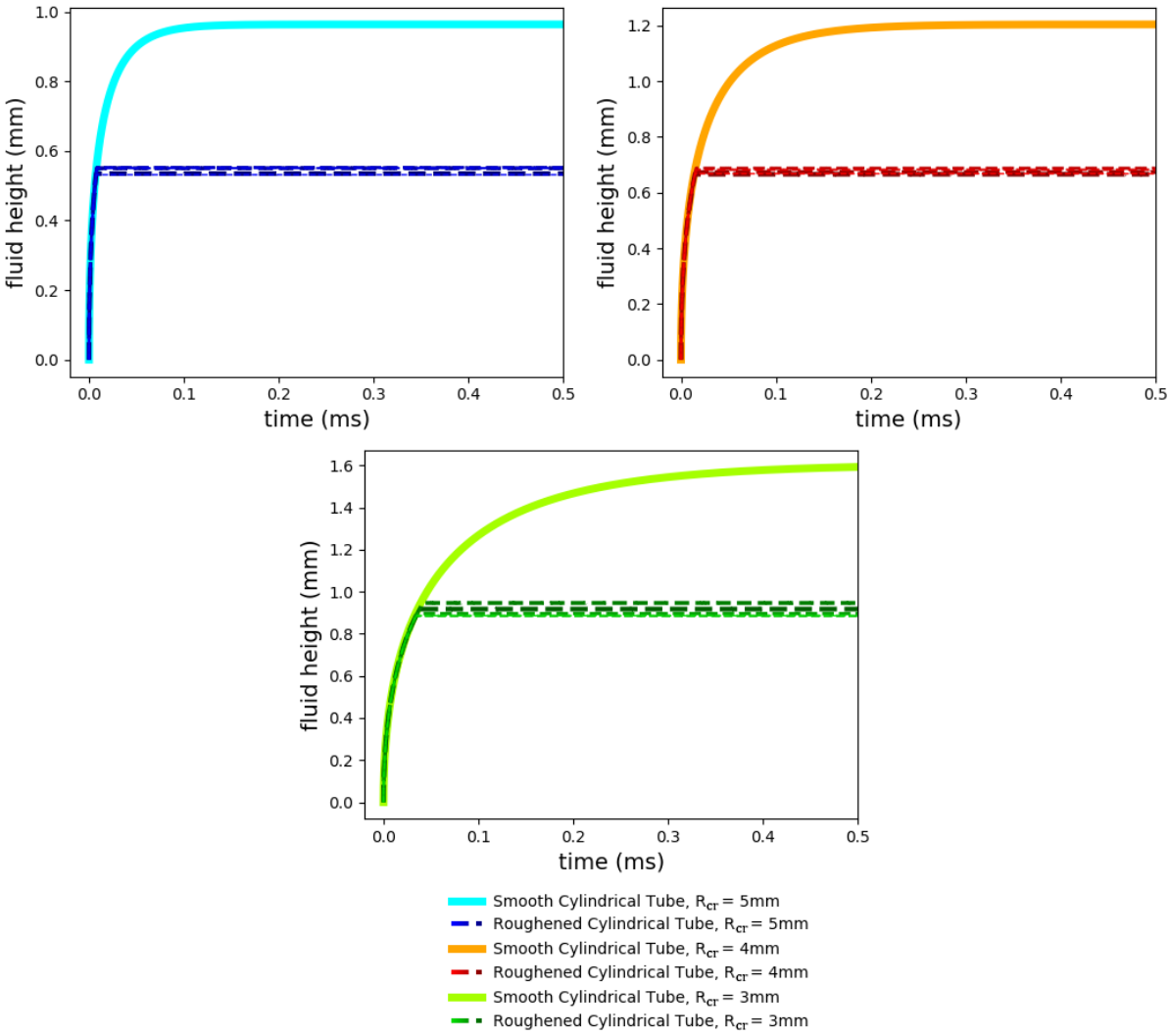

Figure 5.4: Capillary rise height inside roughened cylindrical tubes of varying radii: a) $R_c = 5$ mm; b) $R_c = 4$ mm; c) $R_c = 3$ mm. Note that the dashed lines indicate the FB-MFkMC results whereas the solid lines denote the results from the analytical solution to the Lucas-Washburn equation

pinned on roughness asperities, preventing the water from rising any further. Note that the water's triple contact line is expected to pin each time it encounters a roughness asperity.[27] However, the column of water does not remain trapped on the lower asperities within the tube because the capillary force is sufficient to overcome both the asperity pinning and the downward gravitational force. On the other hand, the water contact line remained pinned on asperities that are sufficiently high up within the tube, where the capillary force of the water column is too weak to overcome both the asperity and the increased gravitational force at that cavity height. The results in Fig. 5.4 additionally showcase the effects of stochastic variability on the FB-MFkMC results. Note that the variability in these results originate from the stochastic generation of the surface roughness asperities; they are not induced by the stochastic MFkMC algorithm behaviour. These results indicate that the stochastic variability has a noticeable effect on the capillary rise results and that it induces pinning at different heights depending on the surface roughness profiles. These results were expected since the surface roughness profiles were randomly generated and therefore the location of the pinning asperities were expected to vary. Furthermore, these randomized roughness profiles were intentionally included in the simulations to showcase that different roughness profiles result in different system behaviour. Note that the increase in surface area induced by the roughened surface is expected to affect the capillary force in addition to inducing pinning effects, as captured in the capillary action force balance modifications highlighted in Eq. (2.9). However, these capillary effects were not observed to have a significant effect in the FB-MFkMC-predicted model results. This is due the assumptions made in the attempt to replicate a practical roughened surface profile. Due to the axisymmetric assumptions applied to the FB-MFkMC capillary action model, the generated roughness profiles feature very few abrupt changes in the cavity radius and predominantly consist of large plateaus where the radius remains constant. Consequently, the overall surface area of the roughened capillary tubes does not significantly increase, resulting in minimal changes in the pre-pinning capillary rise dynamics within the cavity as showcased in Fig. 5.4. However, the sparse distribution of the sporadic changes in the cavity radius aid in emphasizing the role of roughness-induced pinning in capillary action. The pinning results mirror those predicted within the literature, where the fluid triple contact line interaction with individual roughness asperities was directly studied.[27] These results directly observed that the triple contact line will locally pin on asperities and cease to move until the local configuration of the neighbouring triple interface sites adopt a configuration suitable for inducing further capillary-driven advancement. The aforementioned work furthermore postulates that the strength of the pinning is proportional to how much of the triple line is affected by the roughness asperity, to the degree that should the asperity span the entire circumference of a cylindrical pore, that the fluid triple line would remain pinned indefinitely. The results in the aforementioned work furthermore validated this hypothesis through the use of another 1D capillary rise model. These results additionally can be used to showcase how the changes in capillary force are minimal for low surface asperity concentrations. Overall the results from this study further validate the performance of the FB-MFkMC capillary rise model and showcases its potential to capture real-world systems.

5.3 Summary

Capillary action is a crucial moving interface phenomena that plays an important role in the study and design of numerous fluid transport applications. These phenomena can span large spatial domains but their behaviour is sensitive to fluctuations on the molecular level, and consequently it is necessary to develop modelling algorithms that can capture their behaviour on all the relevant scales. This chapter developed a 1D FB-MFkMC model to capture capillary rise within axisymmetric vertical cavities. In particular, the FB-MFkMC algorithm was developed in order to capture the movement of fluid-fluid moving interfaces based solely on the balance of forces acting locally across the interface. The developed capillary rise FB-MFkMC model was highlighted to be able to accurately capture the expected sessile droplet behaviour in ideal cylindrical pores of different radii. However, the model also proved versatile in capturing capillary action behaviour in systems without a known analytical solution, such as in cavities with irregular axisymmetric geometry and in pores subject to molecular-level roughness. These studies showcased that the FB-MFkMC model was able to accommodate for this behaviour in a physically-reasonable manner and further highlighted the potential for MFkMC to capture moving interface systems in an accurate yet efficient manner.

Chapter 6 – MFkMC Model for Sessile Droplet Spreading on a Smooth Surface[§]

The impact and spreading of fluid droplets on a solid surface is an important process that occurs frequently in a wide variety of different natural, technological, and industrial operations.[144,209] Within these applications, it is important to understand the behaviour of how a droplet spreads, and thus there has been substantial interest and research devoted to studying sessile droplet behaviour on different surfaces, both experimental and theoretical, as highlighted in Chapter 2.[8,150] Sessile droplets are frequently large (>1mm) and evolve over relatively lengthy (>1s) time periods, however the surfaces in contact with the droplet are often rough and contain molecular-level asperities. As a result, there is a need for modelling techniques that can bridge the scales ansd capture the macroscale evolution of the droplet while still accounting for the molecular-level phenomena taking place, such as FB-MFkMC. This kMC-based modelling approach is reliant upon having a well-defined closed form expressions for the force or energy balances acting upon the interface for liquid-liquid interfaces. However, as highlighted in Section 2.2.2.2, analytical expressions have not been derived for all the forces affecting droplet spread on a solid surface, and consequently a complete description of this force balance is presently lacking within the literature. In order to resolve this issue, past sessile droplet models assumed that the force balance affecting the droplet movement could be described using a damped harmonic oscillator equation.[23] However, this approach oversimplifies the balance of forces acting upon the interface and cannot provide a detailed description of the underlying physics. Consequently, FB-MFkMC models presently lack the ability to provide detailed analyses on the effects of key droplet parameters on its overall spreading behaviour.

Motivated by the findings discussed above, the objective of this work is to develop a comprehensive semi-empirical force balance that can adequately describe the spreading behaviour of a capillary-driven droplet on a solid surface, while accommodating for the key capillary, inertial, and viscous damping forces. Due to the absence of pure analytical viscous damping models in the literature, this work developed a fitted semi-empirical expression for the viscous term that is not reliant upon any conditionally-specific assumptions and therefore can be applied to a droplet spreading system for most given fluids. The proposed force balance is coupled with the FB-MFkMC algorithm in order to model sessile droplet spread for a variety of different fluids and surface materials. The proposed framework was validated using droplet spreading data derived both from experiments and from previous studies within the literature. The FB-MFkMC model was additionally used to analyze the

[§] The contents of this chapter have been reproduced from D. Chaffart, et al., "A semi-empirical force balance-based model to capture sessile droplet spread on smooth surfaces: A moving front kinetic Monte Carlo study," Phys. Fluids **35**(3), 032109 (2023),[43] with the permission of AIP Publishing

effects of each force over the different regimes of droplet spreading. Section 6.1 will describe the implementation and development of the FB-MFkMC model for sessile droplets on smooth surfaces. Subsequently, Section 6.2 will discuss the proposed force balance and will provide particular attention to the derivation of the viscous damping force. Section 6.3 will then validate the full FB-MFkMC model against experimental results and provide further analysis on the effects of the forces on the droplet behaviour. A summary of this chapter will be provided in Section 6.4.

6.1 MFkMC Algorithm for Sessile Droplet Spread

The behaviour of sessile droplet spread is similar to the behaviour governing capillary rise, and consequently there are many similar aspects between the developed FB-MFkMC sessile droplet model and the FB-MFkMC capillary rise model considered in the previous chapter. The sessile droplet system considered in this work consisted of a fluid droplet spreading on an ideally-flat two dimensional surface. Under these conditions, the droplet expanded and contracted radially with respect to the droplet center, i.e., where the droplet first contacted the surface. This system was captured using a 2D square lattice-based FB-MFkMC algorithm that modelled the spreading of the droplet triple contact line. Much like the capillary rise model considered previously, the triple line consists of a fluid-fluid interface and consequently the contact line dynamics can be captured using the kinetic-like rate equations listed in Eqs. (5.4)-(5.5). However, unlike the capillary rise case study, there do not exist a series of closed form expressions that describe the force balance acting upon the sessile droplet triple line within the literature; this will be further discussed within Section 6.2.

On an ideally smooth surface, the triple contact interface of a sessile droplet will advance and recede radially with respect to the point in which the droplet first contacted the surface. As a result, the droplet contact line can be considered to be composed of an infinite number of independent, non-interactive damped harmonic oscillators advancing and receding relative to the center of the droplet/surface interface, as illustrated in Fig. 6.1a. Note that the behaviour of these theorized droplet oscillators are based on the balance of forces acting on the droplet, which will be discussed in Section 6.2. Consequently, this terminology has no affiliation with the empirical damped harmonic oscillator equations typically used to describe the dynamics of these systems. Furthermore note that due to the nature of a lattice-based FB-MFkMC algorithm, the triple contact line is discretely defined as the boundary between the interfacial atmosphere-phase and fluid droplet-phase lattice sites as depicted in Fig. 6.1b and 6.1c. Consequently, each droplet-phase interfacial lattice site can be viewed as an independent oscillator moving in a single direction relative to the droplet center. Additionally, each of the atmosphere-phase interfacial lattice sites can be viewed as a site that has the potential to be immediately occupied by a droplet oscillator on the other side of the triple interface. Note that much like the capillary rise FB-MFkMC model, the location of the solid interface does not move and therefore it is not necessary to consider any solid interface sites in the FB-MFkMC algorithm.

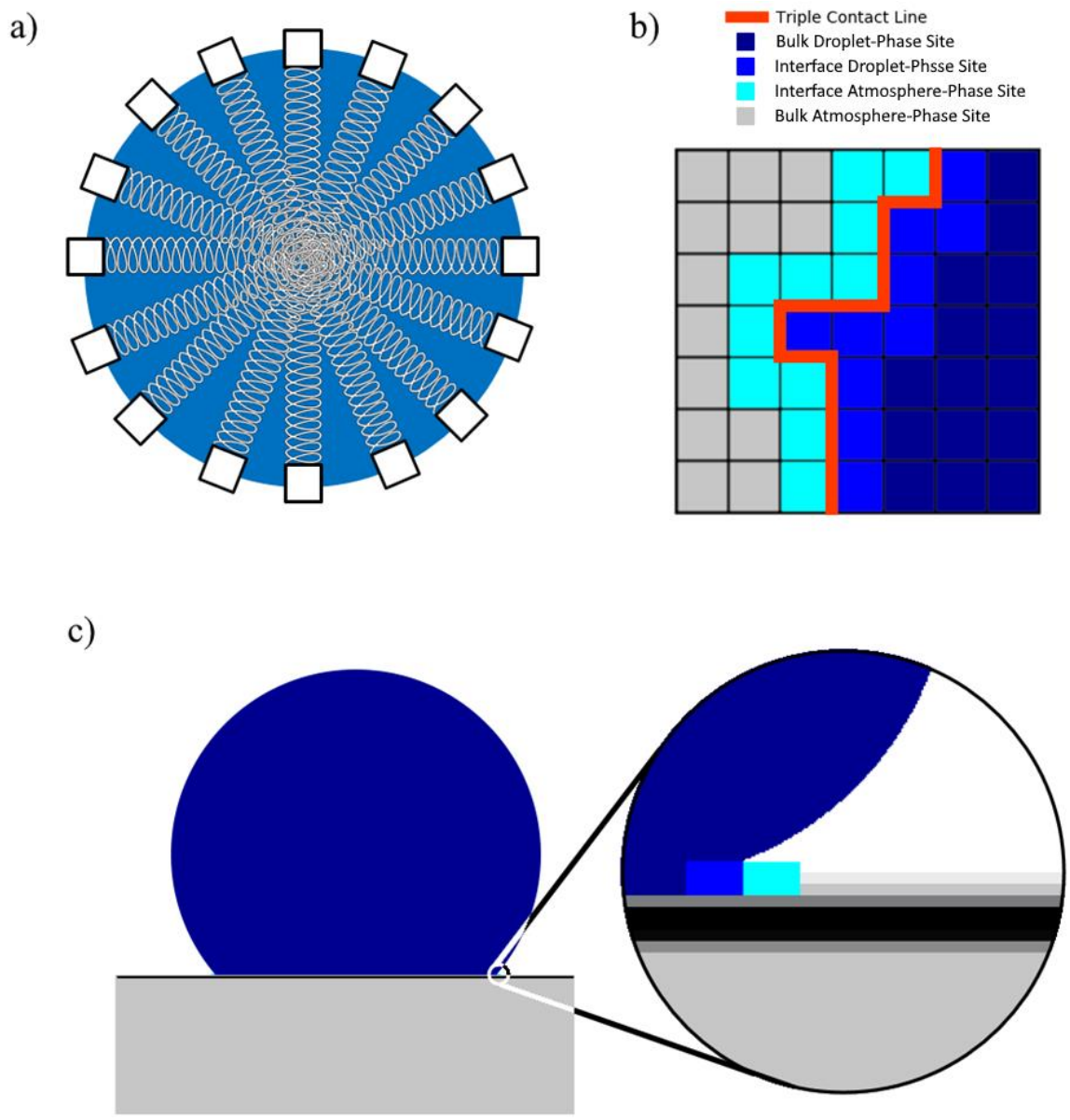

Figure 6.1: a) The droplet triple contact line can be considered as a series of infinite, independent damped harmonic oscillators; b) Triple contact line definition on a 2D lattice, note that both bulk phase sites are unmarked on the FB-MFkMC lattice; c) side view of the droplet represented by the 2D lattice in part b)

Based on these considerations, the proposed FB-MFkMC algorithm defines the events governing the interface movement based on the phase of the interfacial sites, as illustrated in Fig. 6.2. For each of the atmosphere-phase interfacial sites, the FB-MFkMC approach assumes that there is an oscillator located one lattice unit away in the direction of the droplet center that can advance into this site i according to the advancing rate $W_{adv,i}$ in Eq. (5.4), as depicted in Fig. 6.2a. Similarly, the FB-MFkMC approach assumes that each of the

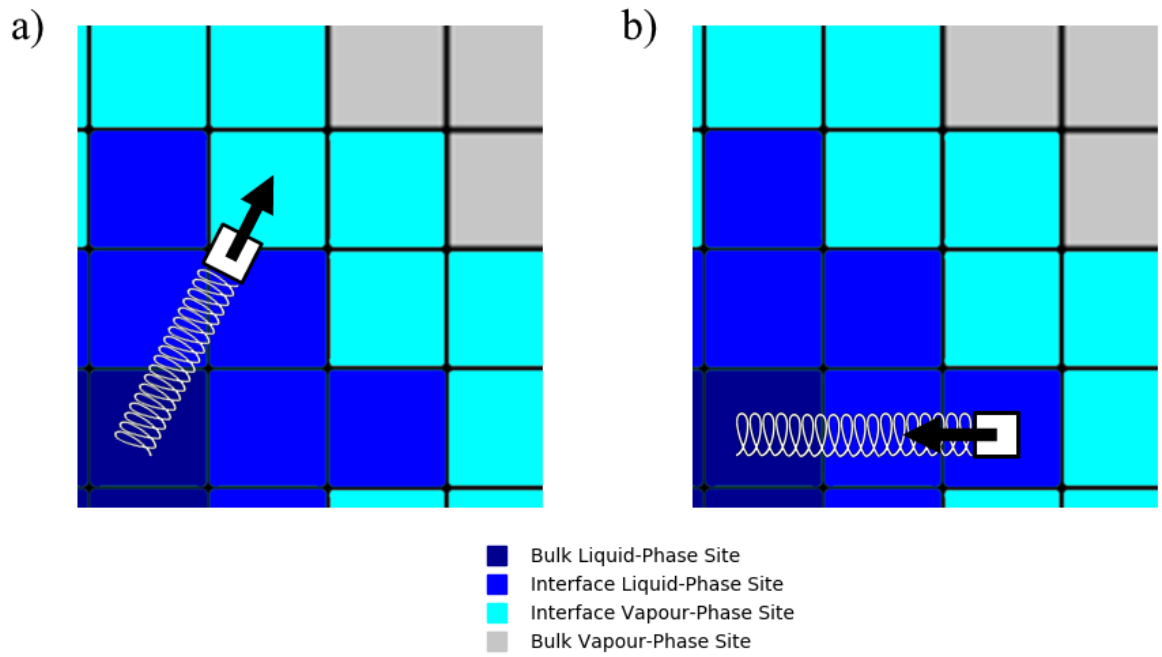

Figure 6.2: In the sessile droplet MFkMC algorithm, the event taking place is defined based on the type of interfacial site. a) interface atmosphere-phase sites keep track of the advancing rate of a droplet oscillator (local triple contact line site) located 1 lattice unit away; therefore they capture the receding rate of the atmosphere-phase site as it is displaced by the droplet-phase; b) interface droplet-phase sites keep track of the receding rate of a droplet oscillator located at that site; therefore they capture the receding rate of the droplet-phase site as it is displaced by the atmosphere-phase

i^{th} droplet-phase interfacial sites are occupied by droplet oscillators and it calculates the rates that these oscillators will recede toward the droplet center according to $W_{rec,i}$ in Eq. (5.5), as depicted in Fig. 6.2b. Therefore, the atmosphere-phase interface sites are assigned rates calculating the probability that the atmosphere-phase will recede away from these sites as they become occupied by the droplet-phase (triple contact line will advance away from the droplet center), whereas the droplet-phase interface sites are assigned rates determining the probability that the droplet-phase will recede away from these sites as they become occupied by the atmosphere-phase (triple line will recede towards the droplet center). Note that although the droplet oscillators depicted by the droplet-phase interfacial sites can also advance into the atmosphere phase, this behaviour is disregarded as it is already accounted for by the rates of droplet advancing assigned to the atmosphere-phase interfacial sites.

The lattice-based FB-MFkMC algorithm considered in this work restricts the positions of the droplet-phase and atmospheric-phase interface sites to a square lattice grid in order to significantly reduce computational costs. Consequently, it is necessary to implement additional rules in order to prevent any

unrealistic droplet behaviour that might occur due to approximating the radial spread of the spherical cap-shaped droplet using a cartesian grid (i.e., unrealistically large asymmetric deviations in the droplet radius, impossible droplet spreading in non-radial directions, and the formation of satellite droplets under unrealistic conditions),[23] as follows:

$$W_{\varepsilon,i,ord} = \begin{cases} k' \, exp\left(\left(\frac{\bar{R}_{drop}+\lambda}{R_{drop,i}+\lambda}\right) sinh^{-1}\left(\frac{v_{drop,i}}{2\lambda k'}\right)\right), & \varepsilon = adv \\ k' \, exp\left(-\left(\frac{\bar{R}_{drop}+\lambda}{R_{drop,i}-\lambda}\right)^{-1} sinh^{-1}\left(\frac{v_{drop,i}}{2\lambda k'}\right)\right), & \varepsilon = rec \end{cases} \tag{6.1}$$

$$W_{\varepsilon,i,fc}\left(x_{\mathcal{R}_i,\phi_i}, y_{\mathcal{R}_i,\phi_i}\right) =$$

$$\begin{cases} W_{adv,i,ord}, & \varepsilon = adv \; and \; (\lfloor (x_{\mathcal{R}_i-\lambda,\phi_i}, y_{\mathcal{R}_i-\lambda,\phi_i}) \rfloor \; or \; \lceil (x_{\mathcal{R}_i-\lambda,\phi_i}, y_{\mathcal{R}_i-\lambda,\phi_i}) \rceil \; are \; droplet \; sites) \\ W_{rec,i,ord}, & \varepsilon = rec \; and \; (\lfloor (x_{\mathcal{R}_i+\lambda,\phi_i}, y_{\mathcal{R}_i+\lambda,\phi_i}) \rfloor \; and \; \lceil (x_{\mathcal{R}_i+\lambda,\phi_i}, y_{\mathcal{R}_i+\lambda,\phi_i}) \rceil \; are \; atmosphere \\ & \quad sites) \; and \; (\lfloor (x_{\mathcal{R}_i-\lambda,\phi_i}, y_{\mathcal{R}_i-\lambda,\phi_i}) \rfloor \; or \; \lceil (x_{\mathcal{R}_i-\lambda,\phi_i}, y_{\mathcal{R}_i-\lambda,\phi_i}) \rceil \; are \; droplet \; sites) \\ 0, & otherwise \end{cases} \tag{6.2}$$

$$W_{\varepsilon,i}\left(x_{\mathcal{R}_i,\phi_i}, y_{\mathcal{R}_i,\phi_i}\right) = \begin{cases} \frac{W_{tot,nc}}{\sum_i (W_{adv,i,fc}+W_{rec,i,fc})} W_{\varepsilon,i,fc}\left(x_{\mathcal{R}_i,\phi_i}, y_{\mathcal{R}_i,\phi_i}\right), & \varepsilon = adv \\ \frac{W_{tot,nc}}{\sum_i (W_{adv,i,fc}+W_{rec,i,fc})} W_{\varepsilon,i,fc}\left(x_{\mathcal{R}_i,\phi_i}, y_{\mathcal{R}_i,\phi_i}\right), & \varepsilon = rec \end{cases} \tag{6.3}$$

where $W_{\varepsilon,i,ord} \in \boldsymbol{W_{i,ord}} = \left[W_{adv,i,ord}, W_{rec,i,ord}\right]$ and $W_{adv,i,ord}$ / $W_{rec,i,ord}$ denote the advancing/receding rates respectively for an interface site i accommodating only for the unrealistic droplet radius deviations; $W_{\varepsilon,i,fc} \in \boldsymbol{W_{i,fc}} = \left[W_{adv,i,fc}, W_{rec,i,fc}\right]$ and $W_{adv,i,fc}$ / $W_{rec,i,fc}$ denote the advancing/receding rates respectively for the i^{th} interface site that additionally accommodate for the impossible droplet spreading in non-radial directions and for the formation of unrealistic satellite droplets; $R_{drop,i}$ denotes the current local radius of the triple contact line at the i^{th} site; $\bar{R}_{drop}$ denotes the average contact radius of the entire droplet; $W_{tot,nc}$ denotes the total sum of all rates without accommodating for the unphysical droplet radius deviations; x and y are the Cartesian coordinates of a given lattice site i; and the subscripts R_i and ϕ_i denote the radial and azimuthal polar coordinates of the same i^{th} lattice site. Further details about these challenges and the derivations of Eqs. (6.1)-(6.3) above can be found in Section C.1. Furthermore, the complete step-by-step FB-MFkMC algorithm for the sessile droplet model implemented within this work is listed in Section C.2.

Note that the presented FB-MFkMC algorithm is dependent on the local velocity of the triple contact line v_i, as highlighted in the rate expressions in Eq. (6.1). This parameter cannot be determined from FB-MFkMC itself and therefore requires an additional means to determine its value at any point in time. This can be accomplished by analyzing the balance of forces acting upon the local droplet interface and recasting them to solve for the contact line's local velocity. Further details on this process will be provided in the next section.

6.2 Sessile Droplet Force Balance Model Development

When a droplet is placed on a solid surface, it will spread and recede until it minimizes the overall surface energy between the droplet, the surface, and the atmospheric phase surrounding them. This minimization of the interfacial energies exerts a continuous restoration force on the drop (i.e. the capillary force) that drives the droplet to spread so long as there is a surface energy imbalance. These capillary forces are opposed by inertial forces, which resist droplet deceleration and acceleration and can drive the droplet to expand or contract past the capillary equilibrium size. These driving forces, however, are countered largely by viscous damping forces that continuously dissipate energy from the system.

The dynamic behaviour of a sessile droplet is considered to be predominantly driven by the aforementioned forces (capillary, inertial, and viscous damping).[139,144] Therefore, it is necessary to have a detailed understanding of these forces in order to capture crucial droplet spreading behaviour and to simulate them using modelling approaches such as the FB-MFkMC algorithm described in the previous section. Note that for sufficiently large droplets (i.e., droplets larger than the capillary length of the fluid as depicted in Eq. (2.13)), the droplet behaviour is known to be additionally affected by gravity forces. However, the droplets considered in this study are all smaller than their capillary lengths and therefore gravity will not be included within the force balance.[144] This section aims to develop and assemble complete analytical and semi-empirical expressions for each of the key fundamental forces affecting sessile droplet spread. These force balances are derived through a combination of analytical equations proposed within the literature (i.e., the capillary and inertial forces listed in Eqs. (2.10) and (2.12) respectively) and coupled with a semi-empirical expression for the viscous damping force derived within this work. The following sub-sections provides a more detailed description into the derivation of the semi-empirical viscous damping force and will provide further analysis on the force balance assembly and its incorporation into the FB-MFkMC algorithm.

6.2.1 Derivation of the Viscous Damping Force

The dynamic behaviour of a spreading sessile droplet greatly depends on viscous damping. However, despite its overall significance, no concrete mechanistic models have yet been devised to represent the viscous damping force in these systems. This is a result of the nature of this force and how it is computed. According to Eq. (2.15), it is necessary to determine the fluid velocity at all points along the system surface in order to calculate the viscous damping force. However, this information necessitates determining the solution to the Navier-Stokes equations within a sessile droplet shape, which has yet to be achieved within the literature. Consequently, there have not been studies within the literature that have attempted to develop a purely-explicit mechanistic viscous force equation due to the challenges highlighted above. Over the course of this study, a few attempts were made to derive analytical expressions for the viscous damping force. These approaches included deriving analytical expressions for the fluid velocity profiles under Stokes flow conditions and solving

for the velocity profiles numerically using CFD-based techniques. These expressions were subsequently incorporated into the viscous stress tensor and integrated to yield the viscous damping force. Despite these efforts, the tested approaches failed to provide a realistic viscous damping force expression. Further details about these attempts are described in Appendix C. In addition, there have been a handful of attempts within the literature to derive a semi-empirical expression for the viscous damping force, such as the cylindrically-based viscous force expression in Eq. (2.16).[140] However, these methods thus far have failed to capture the full viscous damping behaviour within a general sessile droplet system.

In order to overcome these issues, this work proposed the development of a semi-empirical force model to capture viscous damping within a droplet on a solid surface. The proposed model takes the following form:

$$\vec{F}_v(\boldsymbol{x},t) = -2\pi\mu v_{drop}(\boldsymbol{x},t)V_{Rs}c \tag{6.4}$$

where $v_{drop}(\boldsymbol{x},t) = \frac{dR_{drop}(x,t)}{dt}$ denotes the velocity of the droplet's triple contact line at a given location $\boldsymbol{x}$ and time point t; $V_{Rs} = \sqrt[3]{\frac{3V}{4\pi}}$ is a term added to the expression to accommodate for the effects of the droplet volume V on the viscous force; and c is an empirically-derived dimensionless parameter. Note that the equation has a form resembling viscous damping formulations found in similar systems, such as the viscous force equations in capillary rise systems.[56] Consequently, Eq. (6.4) was given a linear dependence on both the viscosity μ and the velocity of the droplet interface v_{drop}. In addition, the 2π term was added to account for the axisymmetric nature of the droplet. The empirical parameter c was added to account for discrepancies observed in the droplet behaviour between the force balance-based model results and those observed experimentally. Note that in order for $\vec{F}_v$ to have the appropriate force units (i.e., N), the parameter c must be unitless. The value of c can be determined by applying model-fitting using data obtained both experimentally and from the literature. These fitted c values can be subsequently analyzed to determine their relationship with respect to the physical parameters governing sessile droplet spread such as the droplet Ohnesourge number Oh defined in Eq. (2.19). In this work, the value of c was fit using a wide variety of different functions using nonlinear regression to approximate the relationship between c and Oh, and it was observed that the system's behaviour was best represented according to a modified Hoerl relationship[210,211], i.e.,

$$c = a b^{1/Oh} Oh^{w} \tag{6.5}$$

where a, b, and w are empirically fitted via model fitting techniques based on a select set of experimental data. Furthermore note that Eq. (6.5) is an empirical expression and that other models could be similarly derived to correlate c with Oh or other sessile droplet metrics. Further details concerning this equation's derivation and the model fitting process are provided in Section 6.3. By combining Eqs. (6.4)-(6.5), the final form for the semi-empirical viscous damping force was determined to be:

$$\vec{F}_v(\boldsymbol{x},t) = -2\pi a\mu v_{drop}(\boldsymbol{x},t)V_{Rs}\mathscr{b}^{1/Oh}Oh^{w} \tag{6.6}$$

6.2.2 Force Balance Assembly and MFkMC Coupling

The semi-empirical force equation highlighted in the previous section was assembled alongside the analytical capillary and inertial force expressions listed in Section 2.2.2.2 of the second chapter in order to describe the balance of forces acting upon the droplet interface. The complete force balance is derived by adding the individual force terms shown in Eqs. (2.10), (2.12), and (6.6) together as follows:

$$\pi\rho {R_{drop}}^3\left(\frac{\cos\theta}{6\sin\theta}+\frac{\cos\theta}{4\sin^3\theta}-\frac{\theta}{4\sin^4\theta}\right)\frac{d^2R_{drop}}{dt^2} = 2\pi R_{drop}\gamma_{lv}(\cos\theta_e-\cos\theta) - 2\pi a\mu v_{drop}V_{Rs}\mathscr{b}^{1/Oh}Oh^{w} \tag{6.7}$$

Note that the above force balance expression seems to imply axisymmetry in the droplet spreading behaviour, as the force balance equation does not showcase any dependence on the azimuthal (ϕ) axis. However, droplet spreading is not completely axisymmetric even on a smooth surface and frequently experiences stochastic microscale fluctuations in the radius along the length of the interface.[212,213] This can be captured in the force balance by modifying Eq. (6.7) to accommodate for differences in the radius and the contact angle for different azimuthal positions along the droplet interface, as follows:

$$\pi\rho R_{drop}(\phi,t)^3\left(\frac{\cos\theta(\phi,t)}{6\sin\theta(\phi,t)}+\frac{\cos\theta(\phi,t)}{4\sin^3\theta(\phi,t)}-\frac{\theta(\phi,t)}{4\sin^4\theta(\phi,t)}\right)\frac{d^2R_{drop}(\phi,t)}{dt^2}$$
$$= 2\pi R_{drop}(\phi,t)\gamma_{lv}\big(\cos\theta_e-\cos\theta\,(\phi,t)\big) - 2\pi a\mu v_{drop}(\phi,t)V_{Rs}\mathscr{b}^{1/Oh}Oh^{w} \tag{6.8}$$

This equation can be further written in a discretized form as follows:

$$\pi\rho R_{drop,i}^3\left(\frac{\cos\theta_i}{6\sin\theta_i}+\frac{\cos\theta_i}{4\sin^3\theta_i}-\frac{\theta_i}{4\sin^4\theta_i}\right)\frac{d^2R_{drop,i}}{dt^2}$$
$$= 2\pi R_{drop,i}\gamma_{lv}(\cos\theta_e-\cos\theta_i) - 2\pi a\mu v_{drop,i}V_{Rs}\mathscr{b}^{1/Oh}Oh^{-w} \tag{6.9}$$

where $R_{drop,i} = R_{drop}(\phi_i,t)$, $\theta_i = \theta(\phi_i,t)$, and $v_{drop.i} = v_{drop}(\phi_i,t)$ denote the droplet contact radius, contact angle, and velocity for the i^{th} droplet interface site located at a position $(\mathcal{R}_i,\phi_i)$ in polar coordinates. Note that due to the stochastic nature of the microscale fluctuations in the contact line, it is difficult to solve the force balance on its own to determine the droplet contact radius or velocity. This expression presently has no defined closed-form stochastic differential equation representation. Furthermore, any derived closed-form equations would be highly nonlinear with respect to the stochastically-varying parameters $R_{drop}(\phi,t)$ and $\theta(\phi,t)$, and consequently it would be highly difficult to solve in an accurate and efficient manner. Consequently, this force balance benefits immensely from coupling with the sessile droplet FB-MFkMC model proposed in Section 6.1. Due to the inherently stochastic nature of the algorithm, FB-MFkMC can deal with the stochastic variability of the system in an accurate and efficient manner. Furthermore, FB-

MFkMC can provide microscale information to the force balance that it cannot otherwise accommodate for, such as surface roughness, however this is beyond the scope of this work. The sessile droplet FB-MFkMC model developed in this work has the capability of capturing the general stochastic spreading behaviour of droplets on solid surfaces. However, the rate equations governing the movement of the droplet interface require knowledge of the local velocity $v_{drop,i}$ along the length of the droplet triple contact interface, as highlighted in Eq. (6.1) of Section 6.1. This information can be readily determined by analyzing the balance of forces acting along the length of the interface and using them to predict the droplet velocity at any point in time. Therefore, in order to accurately capture sessile droplet spreading behaviour on a surface, the FB-MFkMC algorithm must be coupled with the force balance presented above. In order to couple these two approaches together, it is necessary to rearrange Eq. (6.9) in terms of the triple contact line velocity, $v_{drop,i}$. However, doing so requires knowledge of the triple contact line acceleration, $\frac{d^2R_{drop,i}}{dt^2}$, in order to analyze the inertia term. This can be accomplished by using the acceleration's definition as the derivative of velocity, and approximating this term using backwards finite difference over a finite time interval δt, i.e. $\frac{d^2R_{drop,i}}{dt^2} = \frac{dv_{drop,i}}{dt} \cong \frac{v_{drop,i} - v_{drop,prev,i}}{\delta t}$, where $v_{drop,prev,i} = v_{drop,i}(t - \delta t)$ denotes the velocity of the i^{th} triple contact line site at the previous time point. By substituting this approximation into Eq. (6.9), the force balance can be rearranged in terms of $v_{drop,i}$ as follows:

$$v_{drop,i} = \frac{\frac{\mathcal{F}_i}{\delta t} v_{drop,prev,i} + 2\pi R_{drop,i}\gamma_{lv}(\cos\theta_e - \cos\theta_i)}{\frac{\mathcal{F}_i}{\delta t} + 2\pi a \mu V_{Rs} b^{1/Oh} Oh^{-w}} \tag{6.10}$$

where $\mathcal{F}_i$ is the discretized form of $\mathcal{F}$ and is a function of both $R_{drop,i}$ and θ_i. Eq. (6.10) can be subsequently substituted into Eq. (6.1) to determine the rate expressions necessary to propagate the droplet movement according to FB-MFkMC. Note that the finite difference time interval δt in Eq. (6.10) is the same as the MFkMC sample time δt presented in Eq. (3.11). This interval is typically miniscule as compared to the overall simulation time, and therefore the truncation error associated with finite difference approximations is negligible. The proposed FB-MFkMC method combines the features of the MFkMC algorithm with the fundamental physical principles captured by the force balance, and therefore it has the potential to yield accuracy in its predictions while efficiently capturing sessile droplet systems over realistically-long timescales. Furthermore, the framework can be readily expanded to include microscale features such as surface roughness and etched surface structures, and therefore improving its capabilities of capturing a physical droplet system. However, the proposed framework is still dependent on an empirically-fitted parameter c, and therefore it is still missing additional information in order to provide a purely physical approach to capturing sessile droplet spread. Consequently, further studies are required in the future to determine a purely mechanistic expression for the viscous damping force and thus improve the physical prediction capabilities of the FB-MFkMC model.

6.3 Model Validation and Analysis

The previous sections have discussed the development of a FB-MFkMC model to capture sessile droplet spread on an ideally flat surface. This model is based upon the semi-empirical force balance shown in Eq. (6.10), which contains empirical parameters (a, b, and w) derived from model-fitting. The objective of this section is to showcase the fitting of the model to data derived both experimentally and from within the literature. This section additionally validates the model using experimental data not previously used in the model fitting, and further investigates the model results to highlight its ability to universally capture sessile droplet spreading on an ideally flat surface under any droplet spreading regime.

6.3.1 Experimental Setup & Model Fitting

The semi-empirical FB-MFkMC sessile droplet algorithm implemented within this work was fit and subsequently validated using data obtained experimentally and from the literature. The experiments were performed by releasing deionized water droplets from syringes onto various smooth perfluorodecyltrichlorosilane (FDTS), polytetrafluoroethylene (PTFE), and pure silicon (Si) surfaces using the experimental setup showcased in Fig. 6.3a. Note that the FDTS and PTFE surfaces were prepared by depositing the respective coatings onto pure Si wafers via molecular vapour deposition. The volume of the water droplets considered in this study were controlled using a syringe pump and were allowed to vary between 0.46-9.8 μL. Furthermore, as shown in Fig. 6.3, the initial impact velocities v_{impact} and spreading velocities $v_{drop,0}$ of the droplets were controlled by varying the droplet release height h (i.e., the distance between the syringe tip and the solid surface) using a custom homemade stage (Fig. 6.3b). The impact and subsequent spreading of the droplets on the solid surfaces were recorded using a FASTCAM Mini UX 100 high-speed CCD camera at 2,000 frames per second (fps) (0.5 ms per frame). The recorded video files were subsequently analyzed frame-by-frame using ImageJ to extract the relevant droplet information (i.e., the contact radius $R_{drop,exp}(t)$) as a function of time t (Fig. 6.3c). The experimental setup was utilized to record the spreading behaviour of nine different droplets of various sizes and impact velocities impacting solid surfaces of different materials. The details for each experiment are listed in Table 6.1. In addition to the experiments performed in this study, this work additionally analyzed and validated the developed sessile droplet FB-MFkMC model using droplet spreading data reported within the literature.[214–216] The selected literature data was chosen to represent the spreading behaviour of different fluids over different solid surfaces that were not tested in the aforementioned experiments, and the information for each considered dataset is listed in Table 6.1.

Following the accumulation of the experimental and literature results, this data was used to determine the empirical parameter c for each sample via model fitting. This process was accomplished by coupling the force balance with the MFkMC algorithm to form the FB-MFkMC approach, as highlighted in Section 6.2.2, to provide measurable metrics so that the parameter c within the viscous damping term could be compared to

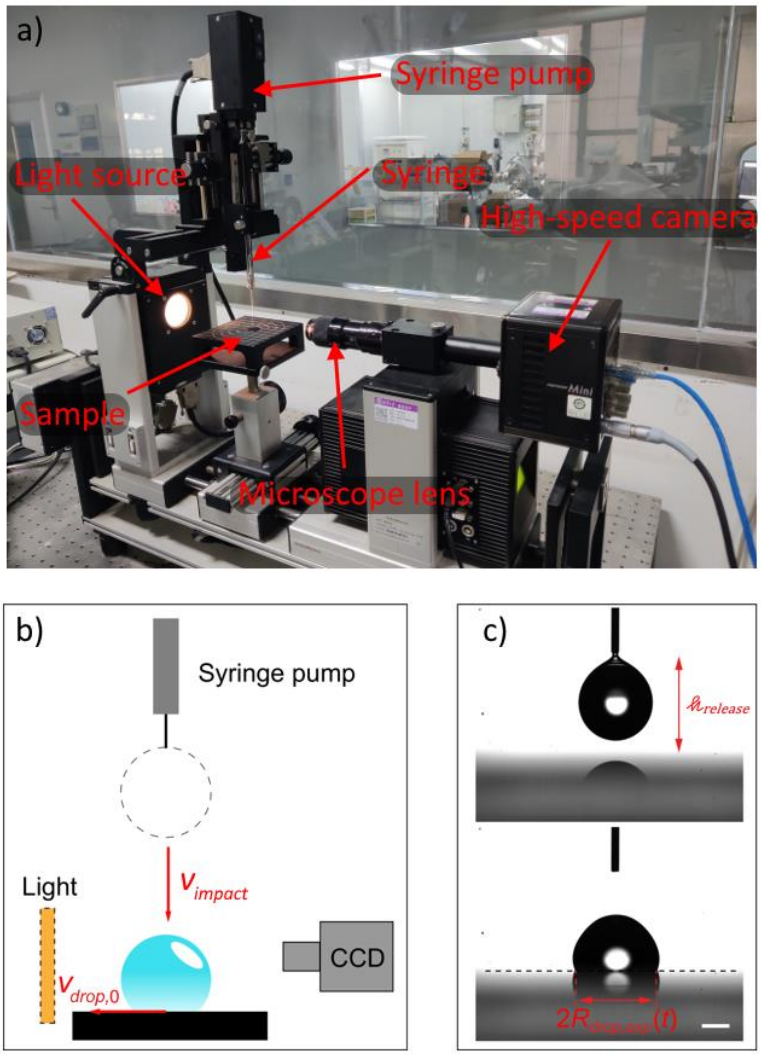

Figure 6.3: Dynamic process of drop spreading: a) Experimental setup; b) Schematic of the experimental setup (not drawn to scale); c) Two snapshots showing before (upper panel) and after (lower panel) the drop contacts the sample surface (Si surface). The contact diameter at time t is labeled as $2R_{drop,exp}(t)$. The scale bar is 1 mm

the available data. The FB-MFkMC sessile droplet model results were subsequently fit to the obtained droplet results using least squares nonlinear regression. For each iteration of the least squares fitting, the FB-MFkMC sessile droplet model results were interpolated to determine the sessile droplet spreading information at the same timepoints available from the experimental data. Furthermore, the optimal solution of c was determined by minimizing the percent relative root mean squared error between the interpolated model-predicted and experimental results as follows:

$$PRMSE = 100\% \cdot \sqrt{\frac{\frac{1}{n}\sum_j^n \left(R_{drop,exp}(t_j) - R_{drop,int}(t_j)\right)^2}{\sum_j^n R_{drop,int}^2(t_j)}} \tag{6.11}$$

Table 6.1: Properties and parameters for the sessile droplet experimental (Exp) and literature-derived (refs) sample data considered in this work

Sample Name	Liquid Material	Solid Surface	V (μL)	$v_{drop,0}$ (m/s)	ρ (kg/m^3)	μ (Pa·s)	γ_{lv} (N/m)	θ_e (°)	κ^{-1} (mm)
Sample A (Exp)	Water	PTFE	0.46	0.27	997	8.90×10^{-4}	7.28×10^{-2}	107	2.727
Sample B (Exp)	Water	FDTS	6.2	0.29	997	8.90×10^{-4}	7.28×10^{-2}	103.1	2.727
Sample C (Exp)	Water	FDTS	6.2	0.259	997	8.90×10^{-4}	7.28×10^{-2}	103.1	2.727
Sample D (Exp)	Water	FDTS	6.2	0.22	997	8.90×10^{-4}	7.28×10^{-2}	103.1	2.727
Sample E (Exp)	Water	FDTS	9.8	0.359	997	8.90×10^{-4}	7.28×10^{-2}	103.1	2.727
Sample F (Exp)	Water	FDTS	9.8	0.259	997	8.90×10^{-4}	7.28×10^{-2}	103.1	2.727
Sample G (Exp)	Water	FDTS	9.8	0.19	997	8.90×10^{-4}	7.28×10^{-2}	103.1	2.727
Sample H (Exp)	Water	PTFE	2.57	0.14	997	8.90×10^{-4}	7.28×10^{-2}	107	2.727
Sample I (Exp)	Water	Si	3.5	0.245	997	8.90×10^{-4}	7.28×10^{-2}	64	2.727
Sample J ([214])	Water	Wax	27	1.3	997	8.90×10^{-4}	7.28×10^{-2}	76	2.727
Sample K ([215])	10% Glycerol	Stainless Steel	8.38	1.7	1025.9	1.22×10^{-3}	7.0×10^{-2}	4.0	2.637
Sample L ([215])	30% Glycerol	Stainless Steel	7.99	2.55	1083.9	2.57×10^{-3}	6.7×10^{-2}	7.1	2.51
Sample M ([215])	70% Glycerol	Stainless Steel	9.49	2.62	1190.4	2.68×10^{-2}	5.8×10^{-2}	26.1	2.229
Sample N ([216])	100% Glycerol	Wax	7.7	2.7	1220	0.116	6.3×10^{-2}	53.4	2.294

where t_j denotes the jth time point from the experimental results; $R_{drop,exp}(t_j)$ and $R_{drop,int}(t_j)$ denote the droplet contact radius from the experimental results and from the interpolated FB-MFkMC-predicted results at time t_j, respectively; and n denotes the total number of measurements for a given droplet experiment.

6.3.2 Model Validation

The model fitting approach discussed above was used to determine the values of c for each experimental study considered in this work. The fitted values c are listed in Table 6.2 for each of the experimental studies considered in this work, along with their reported normalized root mean squared errors. Table 6.2 additionally lists the computational time required to simulate each result using the sessile droplet FB-MFkMC algorithm. Note that all the FB-MFkMC results simulated in this work were operated using the lattice spacing parameters λ listed in Table 6.2. These spacing parameters were chosen based on the size of the droplet being simulated via FB-MFkMC and their values were determined *a priori* to be the largest spacing parameter that did not significantly affect the accuracy of the results, i.e., all smaller values of λ would output similar results. Furthermore, the FB-MFkMC results were generated using a pre-exponential constant value of $k' = 1$ s^{-1} in

Table 6.2: FB-MFkMC sessile droplet model and c fitting results

Sample Name	Oh	λ (m)	Fitted c values	PRMSE	Computation Time (s)
Sample A (Exp)	2.001×10^{-3}	5×10^{-5}	196.2656	0.729673	13.67
Sample B (Exp)	2.001×10^{-3}	5×10^{-5}	207.3654	0.586961	103.96
Sample C (Exp)	2.001×10^{-3}	5×10^{-5}	182.6875	0.586318	130.25
Sample D (Exp)	2.001×10^{-3}	5×10^{-5}	202.8232	0.786432	164.77
Sample E (Exp)	2.001×10^{-3}	5×10^{-5}	219.3137	0.434094	72.59
Sample F (Exp)	2.001×10^{-3}	5×10^{-5}	191.3227	0.429289	83.58
Sample G (Exp)	2.001×10^{-3}	5×10^{-5}	186.3903	0.558511	88.59
Sample H (Exp)	2.001×10^{-3}	5×10^{-5}	177.78	0.813364	33.19
Sample I (Exp)	2.001×10^{-3}	5×10^{-5}	208.1464	0.888258	103.43
Sample J ([214])	2.001×10^{-3}	1×10^{-4}	204.9014	4.170475	1064.53
Sample K ([215])	2.801×10^{-3}	1×10^{-4}	250.0	2.563906	264.92
Sample L ([215])	6.018×10^{-3}	1×10^{-4}	182.479	1.646412	175.26
Sample M ([215])	6.844×10^{-2}	1×10^{-4}	44.04654	0.918891	84.70
Sample N ([216])	0.2762	1×10^{-4}	11.39	0.957991	50.21

Eq. (6.1). Note that a sensitivity analysis (not shown for brevity) was performed on k' to observe its effects on the MFkMC predictions. This analysis revealed that this parameter has a negligible effect on the system behaviour, and consequently its value was set to $k' = 1$ s^{-1} within this work.[23] The results in Table 6.2 highlight that the FB-MFkMC sessile droplet model requires only 170 s of CPU time on average to simulate the sessile droplet behaviour, thus demonstrating its computational efficiency over other molecular-level modelling techniques.[23] Note that the observed computational times varied depending on simulation parameters such as the spacing constant λ, the maximum achieved droplet radius, and the simulation time; consequently, the computational cost was much larger for simulations such as Sample J that experienced significant droplet spreading over larger timescales, whereas it was orders of magnitude smaller for Sample A due to its small size. Furthermore, these results highlight that the FB-MFkMC sessile droplet model can adequately capture the sessile droplet spread once the empirical viscous parameter c is known, due to the fact that the reported errors are below 5%, and most of the errors are below 1%. Furthermore, the largest error was observed for Sample J, whose surface was reported to be rough, and therefore more significant deviations are expected due to surface non-idealities.[214] This highlights that the MFkMC model is capable of both accurately and efficiently capturing the sessile droplet spread. In addition to the above analysis, Fig. 6.4 compares the sessile droplet spreading

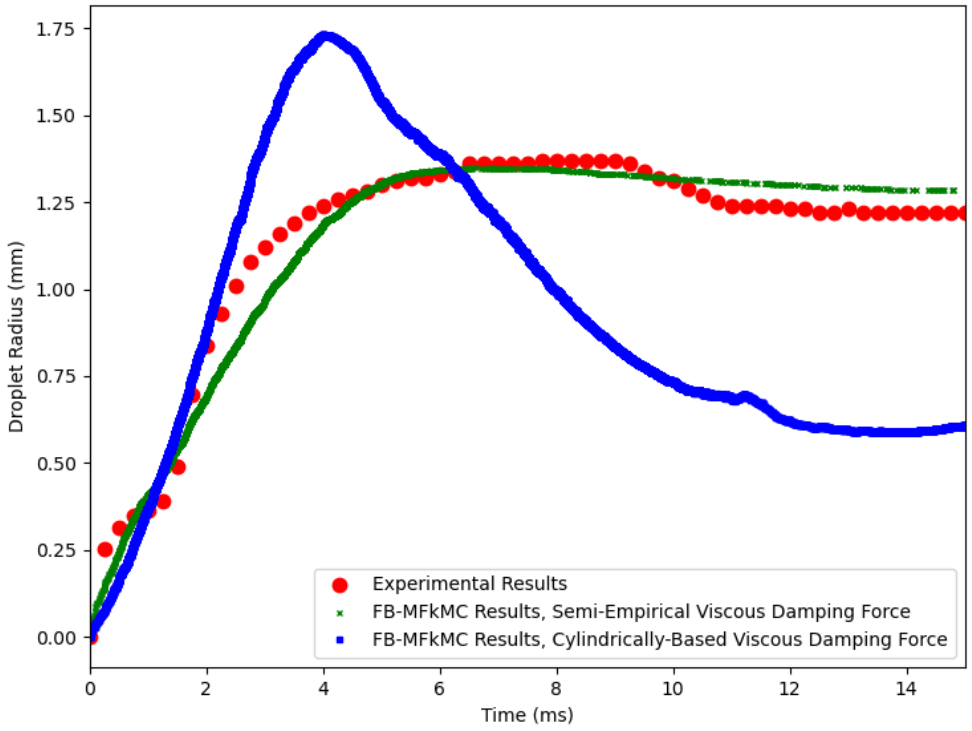

Figure 6.4: Comparison of the experimental sessile droplet spreading behaviour observed for Sample D (red •) to the FB-MFkMC results generated using the full semi-empirical force balance (green x) and the FB-MFkMC results generated using the cylindrically-based viscous damping force proposed in the literature[140] (blue ■)

behaviour of Sample E generated using FB- MFkMC (green xs) to the experimentally-observed data (red dot) and to results generated using a modified FB-MFkMC sessile droplet algorithm where the viscous damping force is calculated using the cylindrically-based simplified viscous damping force proposed within the literature and showcased in Eq. (2.16) (blue squares).[140] This semi-empirical simplified viscous model relies on numerous assumptions as highlighted in Section 2.2.2.2, and is therefore only able to adequately capture the viscous damping behaviour of a sessile droplet under special circumstances. The results in Fig. 6.4 highlight that for the sessile water droplet system considered in Sample D, the cylindrical viscous model is unable to adequately reflect the droplet spreading behaviour. The observed behaviour highlights that the predicted viscous force using this method is negligibly small compared to the inertial and capillary forces, and therefore the predicted droplet behaviour behaves notably more underdamped than the observed droplet behaviour. This is in contrast to the semi-empirical viscous damping model proposed in this work, which was observed to sufficiently capture the energy dissipation within the sessile droplet system and therefore it was able to accurately replicate the sessile droplet behaviour observed experimentally. These results further highlight the capacity of the semi-empirical viscous damping force-based FB-MFkMC model proposed in this work to capture sessile droplet spreading behaviour.

The results in Tables 6.1 and 6.2 can be additionally used to determine the relationship between c and the sessile droplet system parameters. Fig. 6.5a provides a plot of the relationship between c and the intrinsic contact angle θ_i, the droplet volume V, and the impact velocity v_0 for the results gathered from experiments, i.e., for the water droplet results. Note that in Fig. 6.5, the values of c are illustrated through the colours of the points; furthermore, the size of the points are used to convey their depth in the 3D plot space. The results from the figure and tables highlight that the value of c remains constant at around $c = 197.5$ for a droplet of water, regardless of the physical droplet parameters or the surface materials. These results can be seen from the minimal variance in the point colours in Fig. 6.5a, as well in the low deviations in the reported c values within Table 6.2. Furthermore, Fig. 6.5b illustrates the relationship for droplets of different fluids between c and the fluid density ρ, the fluid viscosity μ, and the liquid-vapour surface tension γ_{lv}. Note that the information within Fig. 6.5b is communicated in the same manner as within 6.6a, i.e., the values of c are communicated through the sample point colours, and the point sizes are used to simulate depth perception. The results from this figure highlight that the value of c is highly sensitive to the droplet liquid, as there are significant deviations in the observed point colours, and that c has a nonlinear relationship with the fluid's viscosity, density, and surface tension. Based on these observations, the value of c was proposed to depend on the dimensionless Ohnesorge number, which depicts the ratio between the viscous force and the inertial and capillary forces as depicted in Eq. (2.19). Note that unlike other commonly-used dimensionless quantities (i.e. the Reynolds, Capillary, and Weber numbers Re, Ca, and We), Oh does not depend on a characteristic velocity. As a result, it is ideal for fitting the parameter c whose value was observed to be velocity-independent as highlighted in Fig. 6.5a. Furthermore, the results in Tables 6.1-6.2 and Fig. 6.5a highlight that the value of c was observed to be independent of the droplet size and its physical dimensions. As a result, the characteristic length ℓ in Eq. (2.19) was selected to be the fluid capillary length κ^{-1}, as depicted in Eq. (2.13). The capillary length has units of length but its value depends on the fluid properties (i.e., γ_{lv} and ρ) rather than the droplet dimensions, and therefore it is the perfect characteristic length to approximate the value of c. The Ohnesorge numbers and capillary lengths for each of the experimental samples are listed in Table 6.2. Furthermore, Fig. 6.6 illustrates the relationship between Oh and the fitted c values, which highlights that the affiliation between these parameters, for the most part, collapse onto a single curve. Based on these results, an empirical expression for the observed curve was determined by fitting the available data to a wide variety of different curve models using CurveExpert Professional 2.7.3. Note that the model fitting was only performed using the water, pure glycerol, and 70% glycerol data so that the remaining data could be used for validation (marked as 'fitting data' and 'validation data', respectively, in Table 6.3). According to this analysis, the variation in c is most readily captured using the Hoerl model (i.e., Eq. (6.5)), with fitted model coefficients $a = 8.0720$, $b = 0.9975$, and $w = -0.8314$, such that the full expression for c can be denoted as follows:

$$c = 8.0720 \cdot 0.9975^{1/Oh} Oh^{-0.8314} \tag{6.12}$$

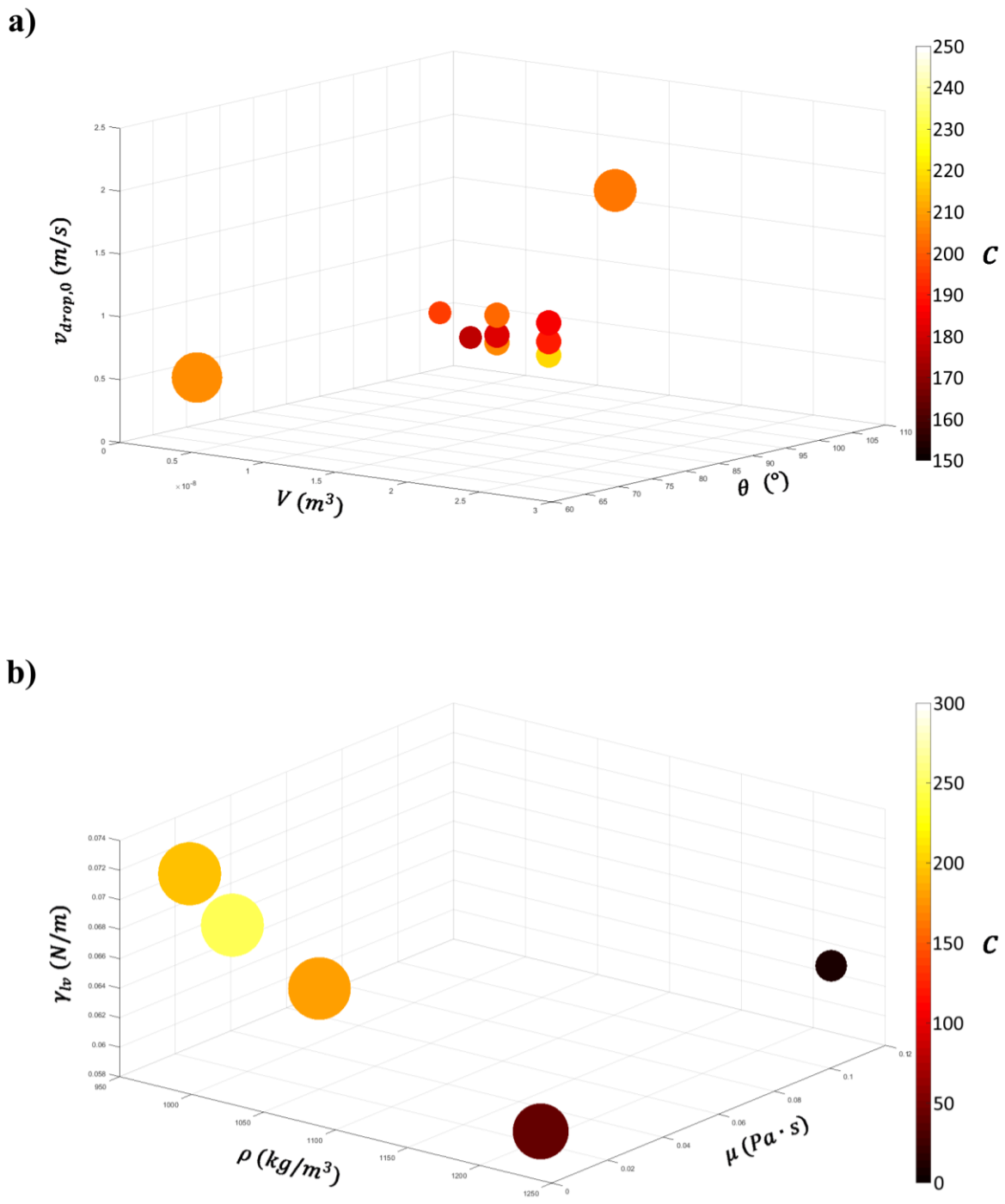

Figure 6.5: Variation in the fitted values of c for: a) water droplets, as a function of the droplet volume V, the initial velocity $v_{drop,0}$, and the contact angle θ; b) droplets of different liquids, as a function of their density ρ, dynamic viscosity μ, and surface tension γ_{lv}. Note that the value of c is communicated through the colour of the points. Furthermore, the point sizes indicate the depth of the points along the z axis

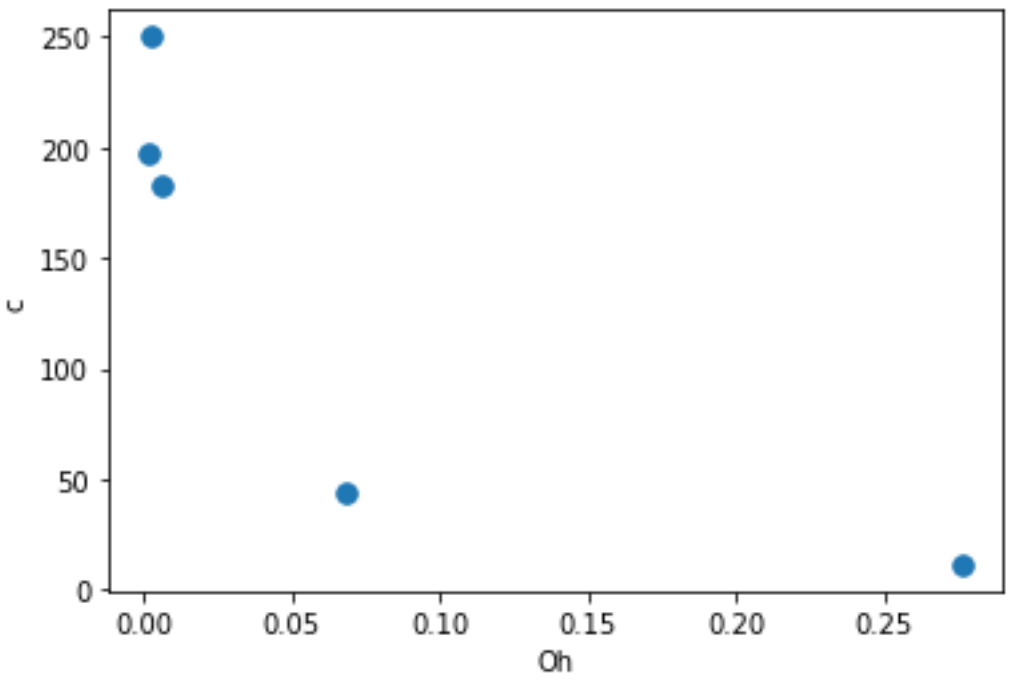

Figure 6.6: Variation in the empirical parameter c as a function of the Ohnesorge number Oh

Table 6.3. Dimensionless metrics of the sessile droplet samples and model results for predicting c as a function of Oh

Sample Name	Fitting or Validation to determine $c = f(Oh)$	PRMSE, $c = f(Oh)$	Re	Ca
Sample A (Exp)	Fitting	0.877935	144.84	3.303×10^{-3}
Sample B (Exp)	Validation	0.655293	242.56	2.324×10^{-3}
Sample C (Exp)	Fitting	0.590828	330.65	3.169×10^{-3}
Sample D (Exp)	Validation	0.845269	458.32	4.392×10^{-3}
Sample E (Exp)	Validation	0.439924	327.17	2.691×10^{-3}
Sample F (Exp)	Fitting	0.519011	385.17	3.169×10^{-3}
Sample G (Exp)	Validation	0.582917	431.27	3.548×10^{-3}
Sample H (Exp)	Validation	0.81984	133.26	1.713×10^{-3}
Sample I (Exp)	Validation	0.89692	258.50	2.997×10^{-3}
Sample J ([214])	Validation	4.741425	2710.2	1.590×10^{-2}
Sample K ([215])	Validation	4.443706	1802.8	2.960×10^{-2}
Sample L ([215])	Fitting	1.76496	1333.9	9.779×10^{-2}
Sample M ([215])	Validation	2.62018	152.59	1.212699
Sample N ([216])	Fitting	1.02	34.79	4.971429

Note that the Hoerl equation was selected for its ability to fit the fitting data for c to their corresponding Oh values. The full semi-empirical force balance can be expressed as follows:

$$\pi\rho R_{drop,i}^3\left(\frac{\cos\theta_i}{6\sin\theta_i}+\frac{\cos\theta_i}{4\sin^3\theta_i}-\frac{\theta_i}{4\sin^4\theta_i}\right)\frac{d^2R_{drop,i}}{dt^2}$$

$$=2\pi R_{drop,i}\gamma_{lv}(\cos\theta_e-\cos\theta_i)-16.1439\pi\mu v_{drop,i}V_{Rs}0.9975^{1/Oh}Oh^{-0.8314} \quad (6.13)$$

In order to validate the equation for c (i.e., Eq. (6.12)), the full FB-MFkMC sessile droplet model was used to capture the droplet spread for each of the experimental conditions outlined in Table 6.1. The results of this study are depicted in Fig. 6.7, where the dotted green lines denote the average contact radius of the droplets as predicted by the FB-MFkMC simulations and the red xs depict the droplet data recorded from experiments and from the literature. Note that the FB-MFkMC simulations were performed three times each in order to analyze the effects of the kMC stochasticity on the model results. However, the results for each FB-MFkMC simulation were observed to be identical, as showcased in the figure. This is because the droplet radii reported in the figure are calculated by averaging the radius of each droplet as they vary azimuthally, and therefore the 3D FB-MFkMC sessile droplet model innately accommodates for the average system behaviour without requiring additional simulations. In addition, Fig. 6.8 illustrates a top-down view of Sample C at different time intervals for a single FB-MFkMC simulation. Furthermore, Table 6.3 highlights the percent relative root mean squared error between the FB-MFkMC and experimental results calculated using Eq. (6.11). Note that in addition to the validation data, the PRMSE values are also listed for the fitting data in order to provide a benchmark of comparison for the validation data. These results highlight that the semi-empirical force balance is able to sufficiently predict the observed sessile droplet spreading, as the percent relative root mean squared errors predominantly remain below 5%. Furthermore, the predicted PRMSE values predominantly do not deviate significantly from the predicted PRMSE errors generated for the purely fit c values denoted in Table 6.2. Fig. 6.7 also illustrates that the FB-MFkMC sessile droplet model results do not deviate significantly from the experimental data and therefore they are able to accurately predict the sessile droplet behaviour. Note that although there are some deviations between the model and experiments particularly in Figs. 6.7d and 6.7j, these results can be attributed to surface roughness and other non-idealities on the experimental surface that are not accounted for by the present sessile droplet FB-MFkMC model, e.g., the rough wax surface in Sample J. These non-idealities can be readily integrated into the FB-MFkMC sessile droplet model through a series of modifications, however this is beyond the scope of this work. The results in Figs. 6.7-6.8 additionally demonstrate that the droplet advanced and receded uniformly, as the angular variation in the contact radius was observed to remain small.

The sessile droplet behaviour showcased above exhibited large variability in the ratio between the viscous, inertial, and capillary forces, as highlighted by the diverse values observed in Oh. In order to provide a deeper

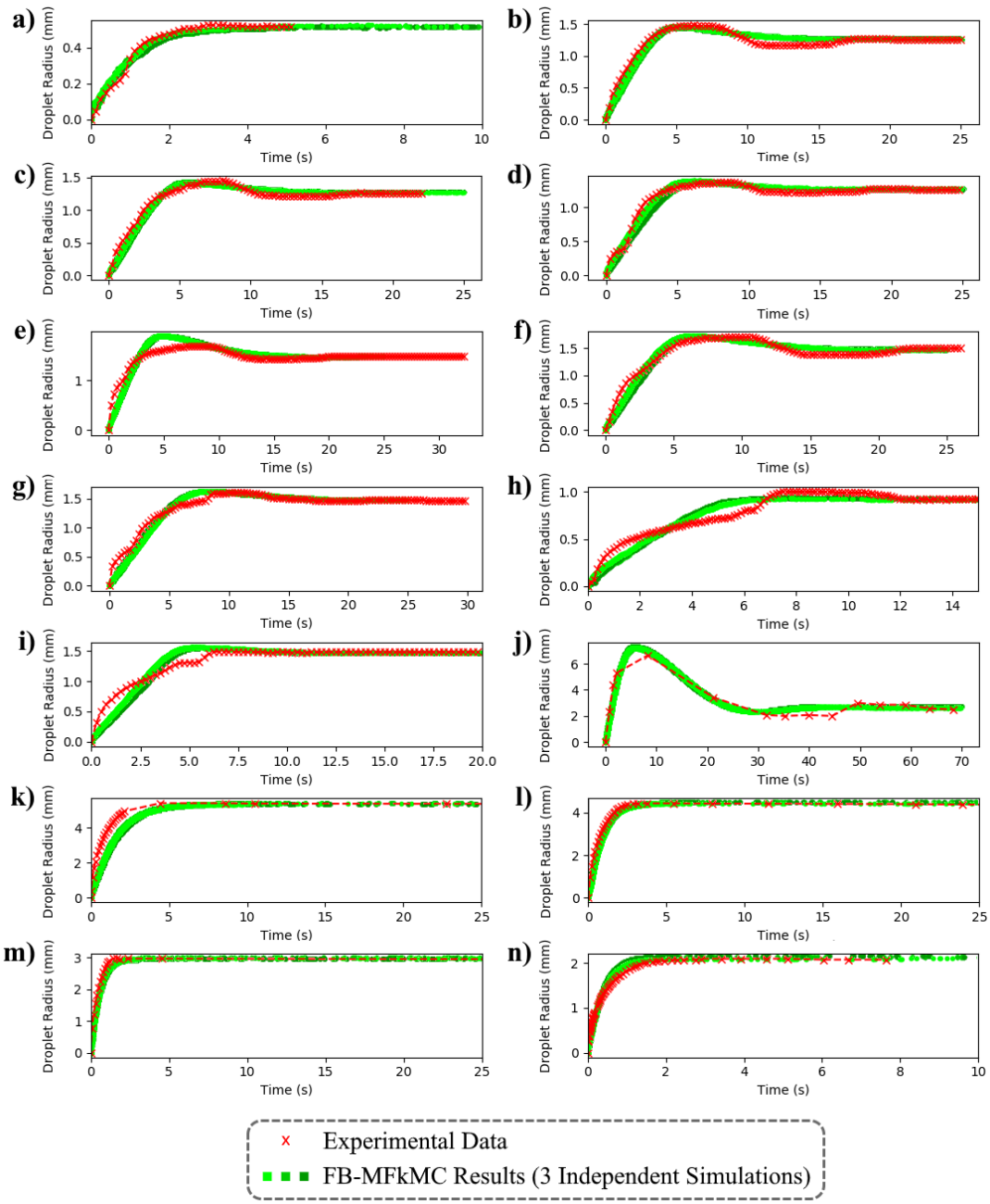

Figure 6.7: Comparison between the experimental/literature data (red x) and MFkMC-predicted results (green •) for sessile droplet spread: a) Sample A, water droplet on PTFE; b) Sample B, water droplet on FDTS; c) Sample C, water droplet on FDTS; d) Sample D, water droplet on FDTS; e) Sample E, water droplet on FDTS; f) Sample F, water droplet on FDTS; g) Sample G, water droplet on FDTS; h) Sample H, water droplet on PTFE; i) Sample I, water droplet on Si; j) Sample J, water droplet on wax; k) Sample K, 10% glycerol solution droplet on stainless steel; l) Sample L, 30% glycerol solution droplet on stainless steel; m) Sample M, 70% glycerol solution droplet on stainless steel; n) Sample N, pure glycerol droplet on wax

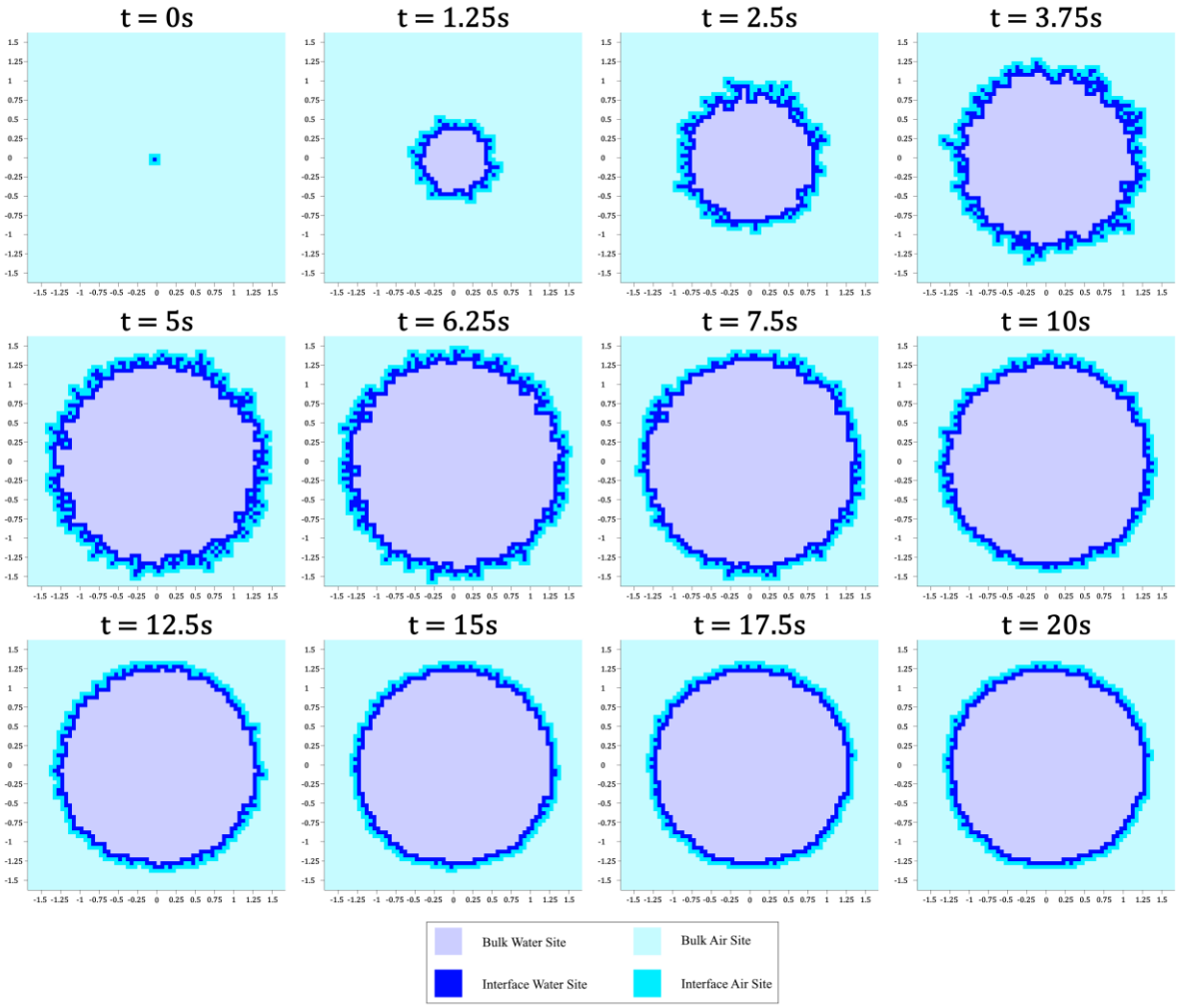

Figure 6.8: Top-down view of the radial variation in the spreading of a sessile water droplet ($V = 9.8$ µL, $v_{drop,0} = 0.22$ m/s, $\kappa^{-1} = 2.727$, $Oh = 2.001 \times 10^{-3}$) at different points in time along the droplet evolution. Note that the horizontal and vertical axes of each plot denote the distance to the droplet center in mm

analysis of the different droplet performances, Table 6.3 additionally lists the Reynolds and Capillary numbers calculated for each of the experimental data sets according to Eqs. (2.17) and (2.18) respectively. These dimensionless quantities denote the ratios of inertial to viscous damping forces (Re) and of viscous damping to capillary forces (Ca) at any point in time for each droplet. For each of the Re and Ca values calculated in this study, the characteristic length ℓ was selected to be V_{Rs} (which can be defined as the radius of the droplet as a perfect sphere) for each sample, whereas v was selected to be the horizontal component of the impact velocity $v_{drop,0}$. Note that unlike the Ohnesorge number, the characteristic length ℓ was selected to be V_{Rs} rather than the capillary length κ^{-1}. This decision was implemented to accommodate for both the droplet volume and its impact velocity when calculating Re and Ca, as these parameters are known to affect the sessile

droplet behaviour. Overall, the values listed in Table 6.3 indicate that the data used to fit and validate the semi-empirical viscous damping force expression span a wide range of both large and small Re and Ca values, therefore showcasing that the predicted model expression can adequately capture droplet behaviour under each of the possible force balance regimes (under inertial-driven, capillary-driven, and viscous-driven regimes). Additionally, the droplet data spans fluids of both low viscosity (water) and high viscosity (pure glycerol), which further illustrates that the semi-empirical viscous damping force expression can capture this force for both viscid and inviscid droplets, thus showcasing its overall generality.

In addition to showcasing the widespread applicability of the proposed sessile droplet model, the dimensionless quantities Ca and Re can also be used to provide analysis on the sessile droplet properties as it varies from system to system. As illustrated by the results in Table 6.3, all of the water droplet samples and many of the glycerol mixture samples have a large Reynolds number and a small Capillary number, indicating that the viscous damping force experienced by these samples is small compared to the inertial and capillary forces. Consequently, if the droplet is underdamped, it is expected these droplets would experience a large number of oscillations and a small oscillation period due to the low viscosity and the high inertial forces, respectively.[144,217] This is in alignment with the observed results in Figs. 6.7b-g, which showcase that the sessile water droplets experience 2-3 oscillations with periods smaller than 10 ms. Furthermore, if the droplet is overdamped, the small Capillary and large Reynolds numbers indicate that the drop will approach its equilibrium at a faster rate compared to droplets with a higher viscosity contribution. In order to illustrate this behaviour, the Reynolds and Capillary numbers for the 0.46 μL water droplet (i.e., Sample A) were artificially increased and decreased, respectively, by decreasing the impact velocity $v_{drop,0}$, decreasing the density ρ, decreasing the surface tension γ_{lv}, and increasing the viscosity μ, using the FB-MFkMC sessile droplet model as showcased in Fig. 6.9. The results from these analyses are illustrated alongside the unmodified droplet behaviour determined from the experimental data. These results highlight that the weaker the viscous force, the more rapidly the droplet will approach its equilibrium state when overdamped.

On the other hand, the viscid glycerol samples have significantly smaller Re and larger Ca as compared to the water samples, indicating that the viscous force dominates for these droplets. Consequently, these droplets are unlikely to experience oscillations and any that do occur are expected to have a large period. These results can be observed in the plots showcased in Figs. 6.7k-n, which highlight the overdamped nature of the viscid glycerol-based drops. In order to further highlight this behaviour, the sessile droplet FB-MFkMC model was used to simulate the pure glycerol droplet on a PTFE surface ($\theta_i = 116°$),[218] as shown in Fig. 6.10. Note that the presence or absence of oscillations within a droplet is influenced by the intrinsic contact angle in addition to the parameters within Re and Ca, and consequently a fluid droplet of fixed volume and impact velocity can experience both overdamped and underdamped behaviour depending on the solid surface material. The results in Fig. 6.10 showcases that when oscillating, the period of oscillation remains large (~100 ms) and

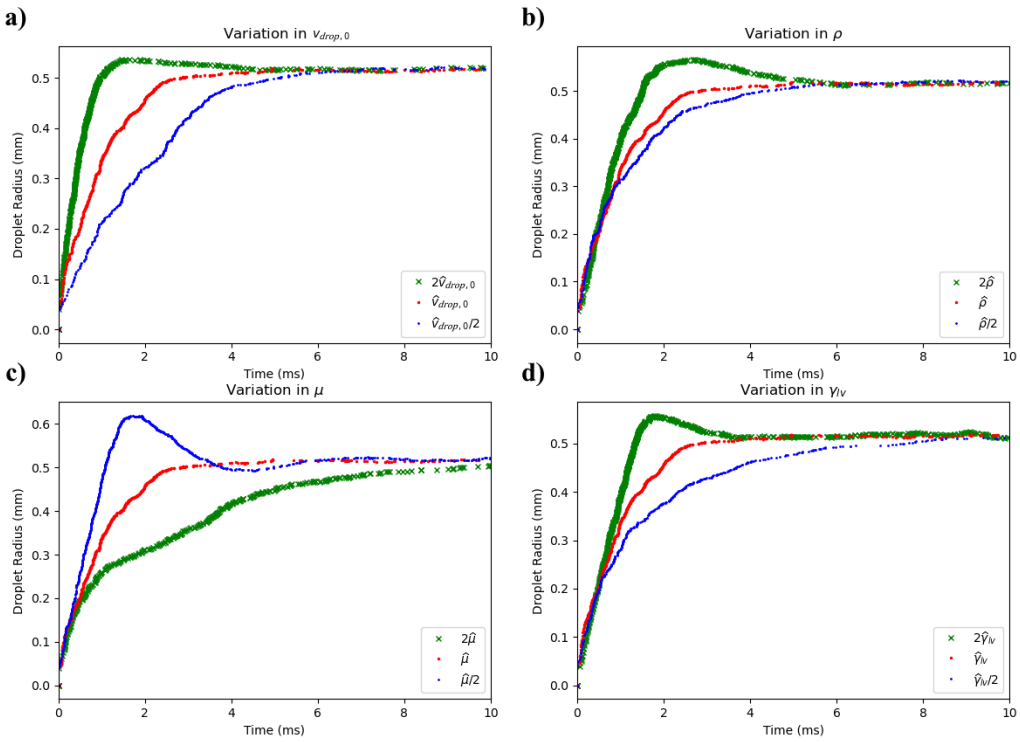

Figure 6.9: Variation in the spreading behaviour of water under Sample A conditions, according to: a) variations in $v_{drop,0}$; b) variations in ρ; c) variations in μ; d) variations in γ_{lv}

there is only a single oscillation before the droplet attains steady state, as predicted based on the dimensionless numbers. In order to further analyze the behaviour of high viscosity droplets, Fig. 6.11 depicts the behaviour of the glycerol droplet when μ, ρ, γ_{lv}, v_o, and the volume V are artificially modified. These results, which are generated using the FB-MFkMC sessile droplet model, further illustrate the trends mentioned above, i.e., larger Re and smaller Ca lead to larger oscillations with smaller periods, whereas smaller Re and larger Ca result in increased droplet damping.

6.4 Summary

The spreading of sessile droplets plays a crucial role in a wide range of different applications in surface science and engineering, and consequently there is significant demand to model and study droplet spread. The droplet spreading process in sufficiently small droplets is governed by the inertial, capillary, and viscous damping forces acting upon the droplet triple contact line. However, the complete expressions for these forces were not completely known within the literature. This chapter developed a comprehensive semi-empirical force balance to capture the fundamental physics governing sessile droplet spread on an ideally flat surface. The proposed balance was derived based on analytical expressions previously derived to calculate the inertial and capillary forces, coupled with a semi-empirical expression to accommodate for the viscous damping force. The

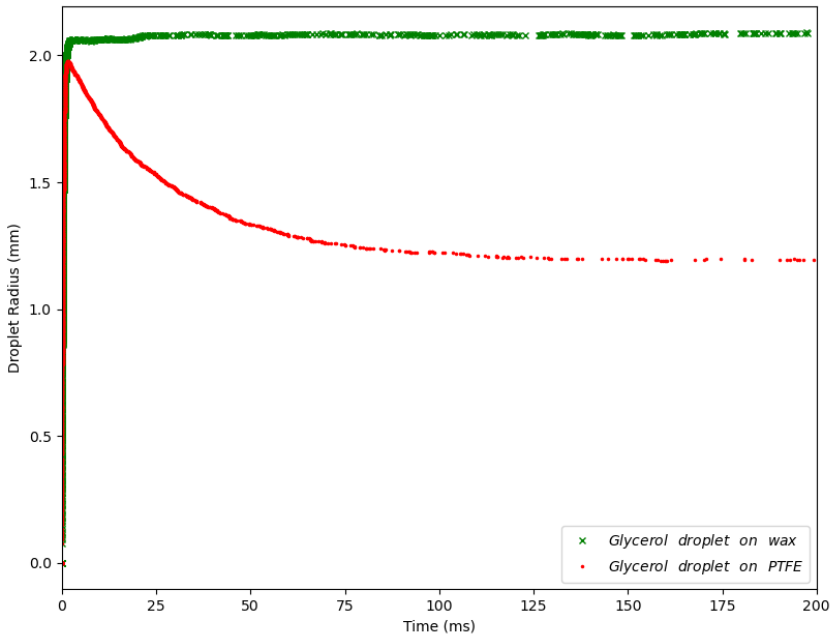

Figure 6.10: Spreading behaviour of the pure glycerol droplet on wax (green x) and on PTFE (red •)

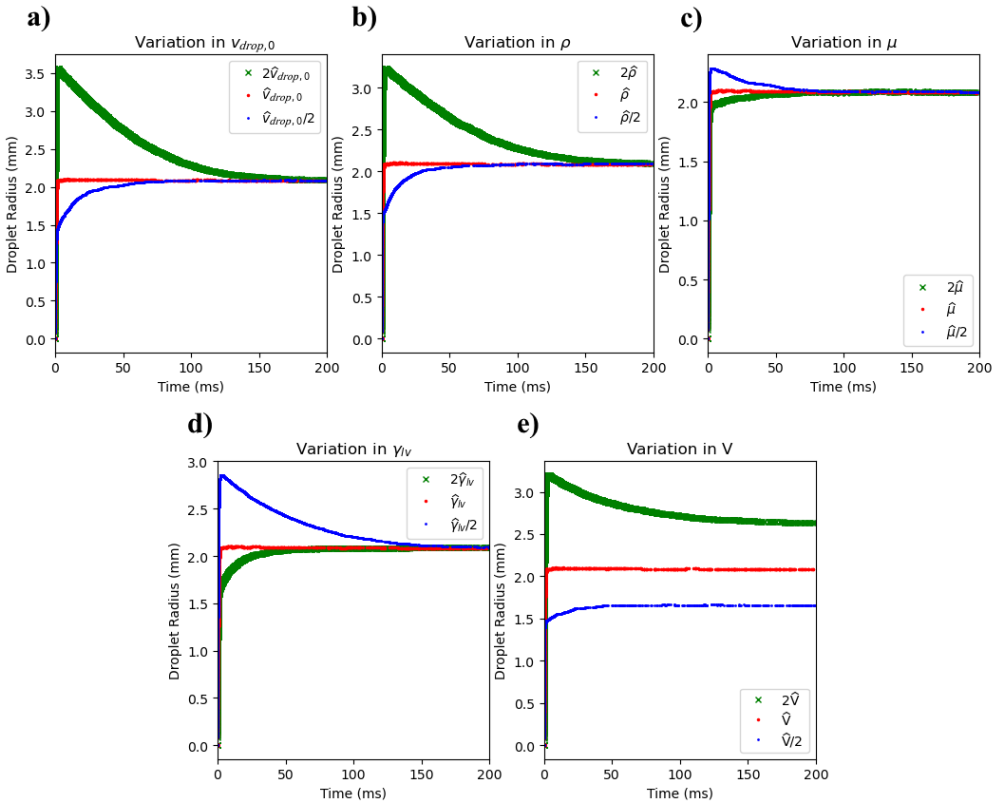

Figure 6.11: Variation in the spreading behaviour of pure glycerol under Sample N conditions, according to: a) variations in $v_{drop,0}$; b) variations in ρ; c) variations in μ; d) variations in γ_{lv}; e) variations in V

viscous damping behaviour was subject to a fitted empirical parameter whose value was determined to be dependent on the liquid material and its properties. Low-order expressions were proposed to predict the values of the parameter as a function of the droplet liquid's Ohnesorge number. The full force balance was coupled with the FB-MFkMC algorithm to form the sessile droplet FB-MFkMC model, which was subsequently used to simulate the spread of sessile droplets on smooth surfaces. This modelling approach was validated using droplet data derived from experiments and from results reported previously within the literature. The proposed model was observed to provide acceptable predictions of sessile droplet spreading regardless of the droplet size, shape, composition, and the solid surface material. Furthermore, the model results were observed to reflect the expected droplet behaviour under a variety of different Reynolds and Capillary number values.

Chapter 7 – MFkMC Model for Sessile Droplet Spreading on Superhydrophobic Surfaces

Solid surfaces are prone to contamination and fouling that have been demonstrated to cause adverse effects in applications such as hospital sanitation, window fogging, and biocontamination. Consequently, there is a crucial need to develop anti-wetting superhydrophobic surfaces (SHSs) in order to minimize and eliminate surface contamination.[34,35,219] The superhydrophobic behaviour of these surfaces can be attributed to hierarchical or nanoscale surface asperities and roughness structures, as highlighted in Section 2.2.2.4.[174,220] The study of SHSs is fairly mature, and there have been many proposed surfaces that have demonstrated excellent water repellency.[160,221] However, there still remain a number of challenges that inhibit the performance and wide-scale application of SHSs. Most notably, SHSs are prone to deactivation due to Cassie-to-Wenzel (C2W) transitions, which has resulted in a significant amount of research into preventing and reversing C2W deactivation.[37–39] Another key challenge is the difficulty in developing models to capture superhydrophobic surface behaviour. Many of these challenges can be likewise overcome through the use of the aforementioned FB-MFkMC algorithm discussed within the previous chapter. Nevertheless, there still remain key issues on how to implement FB-MFkMC to capture droplet spread on an SHS. Unlike ideally flat surfaces, the textured surface of an SHS changes as a function of space and therefore it is necessary to map the solid surface structure itself within the MFkMC model rather than assume it to remain spatially homogeneous. Furthermore, the droplet spreading behaviour changes between the gaps of an SHS's roughness asperities and therefore it is necessary to accommodate for the additional physics and model considerations that occur due to the surface heterogeneity. In addition, the model must be adapted to accommodate for C2W transitions.

To address the challenges outlined above, the aim of this chapter is to expand the FB-MFkMC model to capture sessile droplet spread on SHSs. The proposed SHS-based MFkMC (SHS-MFkMC) model will be modified using a Periodic Unit (PU) grid mechanism developed to accommodate for the spatial heterogeneities in the SHS. Furthermore, it will analyze the conditions and underlying physics necessary to capture Cassie mode droplet spreading and to predict the C2W transition. These results will be subsequently validated against experimental results from the literature and assessed via sensitivity analysis. Section 7.1 will describe the PU method used to model an SHS and it will furthermore describe the modifications made to the MFkMC model to capture both superhydrophobic droplet spreading and C2W transitions. Section 7.2 will subsequently validate the model with regards to both Cassie regime spreading and C2W. This section will additionally provide further analysis on the effects of the SHS structure on the droplet behaviour and whether it undergoes C2W. Concluding remarks will be provided in Section 7.3.

7.1 MFkMC Algorithm for Superhydrophobic Droplet Spread

In order to capture sessile droplet spread on an SHS using SHS-MFkMC, it is necessary to modify this modelling approach in order to accommodate for the different solid surface structure and new physics that take place as a result of the solid surface spatial heterogeneities. This section will therefore outline each of the modifications that were made to capture the superhydrophobic behaviour. This section will initially provide an overview of the Periodic Unit (PU) technique developed to efficiently model the structure of the superhydrophobic surface. Subsequently, it will present the modifications made to the triple contact line force balance equations and to the SHS-MFkMC algorithm to accommodate for Cassie droplet spreading on an SHS. In addition, this section will also provide an overview of the different methods that were incorporated to predict C2W occurrences. Note that this chapter is predominantly focused on capturing the Cassie spreading regime of a droplet on an SHS and determining whether it would undergo C2W transitions.

7.1.1 Superhydrophobic Surface Representation using the Periodic Unit Method

One of the most defining physical features of SHSs are the roughness asperities that are responsible for the surfaces' superhydrophobic properties. In an artificial SHS, these asperities frequently take the form of periodically-spaced near-identical pillars separated by gaps, as illustrated in Fig. 7.1a. These pillars can be manufactured in a variety of different shapes, and each different pillar design affects the superhydrophobic properties of the surface. Note that although there are a wide variety of different pillar structures available to study, this work only considers SHSs that have trapezoidal pillar designs, where the tops of the pillars are squares of length $a_{p,t}$, the bottoms of the pillars have lengths of $a_{p,b}$, and the pillar heights are H_p, as illustrated in Figs. 7.1b-c. Furthermore, the pillar walls intersect the surface below it at an angle of φ_p, as highlighted in Fig 7.1b. Note that φ_p is measured with respect to the surface normal vector (i.e., the vector orthogonal to the bottom surface of the SHS), such that $\varphi_p = 0$ when $a_{p,t} = a_{p,b}$ and $b_{p,t} = b_{p,b}$. Consequently, the angle showcased in Fig. 7.1b corresponds to $\varphi_p + 90°$ for the sake of viewability. Finally, the pillars are separated by a gap of $b_{p,t}$ and $b_{p,b}$ between the tops and bases of the pillars, respectively. Note that the majority of SHS pillar designs considered in this work will have a rectangular prism shape (i.e., $\varphi_p = 0$, $a_{p,t} = a_{p,b}$, $b_{p,t} = b_{p,b}$), as illustrated in Fig. 7.1.

The SHS-MFkMC model presented in Chapter 6 was designed to capture sessile droplet spread on an ideally flat, spatially homogeneous solid surface. As a result, the model had no need to accommodate for any spatial variations in the surface height and therefore the surface could be represented by a flat 2D plane to minimize computational costs. However, in the case of a pillared SHS, these assumptions cannot be applied and therefore it is necessary to map out the surface height at every point in space. Nonetheless, mapping the

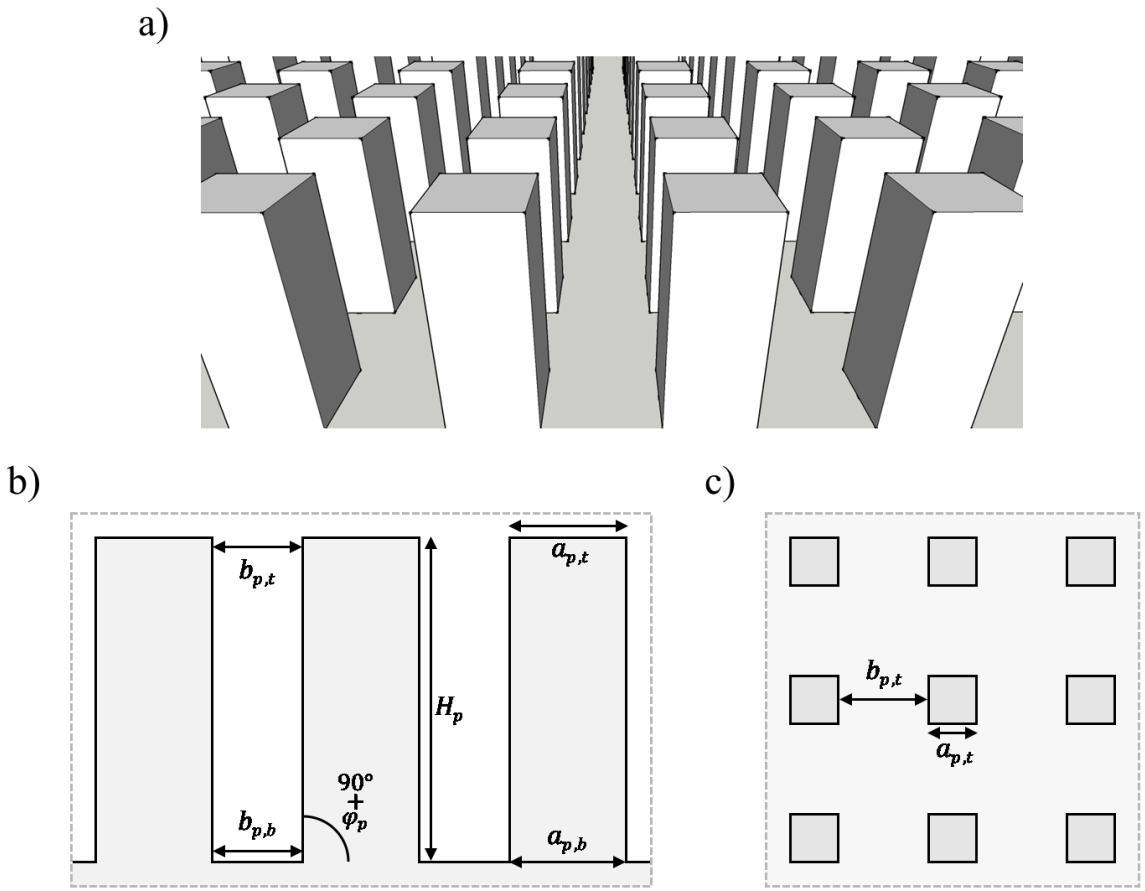

Figure 7.1: a) Superhydrophobic surface structure consisting of periodic pillars; b) side view of the trapezoidal (rectangular) pillars considered in this study; c) top-down view of the trapezoidal (rectangular) pillars considered in this study. Note that the angle showcased in this figure corresponds to $\varphi_p + 90°$ since φ_p is measured with respect to the surface normal vector

geometry of the entire solid surface would be computationally and memory intensive, and it would eliminate one of the key computational advantages of using MFkMC (i.e., that sites not directly on a moving interface can be ignored). As a result, it is necessary to develop an alternative method to efficiently capture the shape of an SHS so that it is not necessary to store the entire solid surface structure. This goal can be accomplished through the use of the Periodic Unit method, which decomposes the solid surface into single periodic units (PUs), that each consisting of a single solid pillar as illustrated in Fig. 7.2. These PUs are defined such that on a periodically-repeating pillared surface, each PU is identical and therefore they can be tiled together to represent the entirety of the solid surface. Furthermore, because each PU is assumed to be identical, it is only necessary to have a detailed model for a single PU, and therefore this method can represent the complete solid surface in a memory-efficient manner.

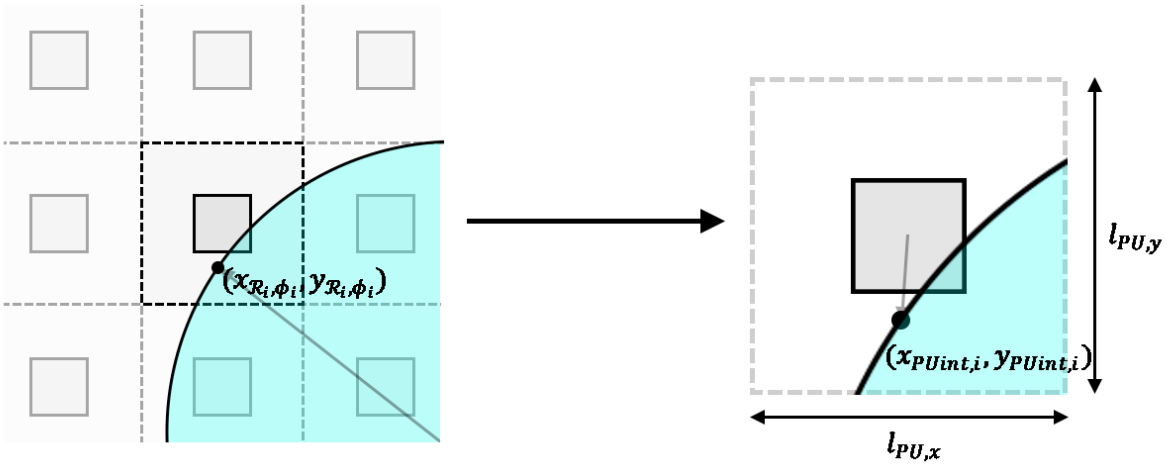

Figure 7.2: Top-down view of the decomposition of a periodically-spaced pillared SHS into PUs

The PU method can be readily coupled together with SHS-MFkMC to efficiently determine the height of the solid surface at any point in space along the droplet triple contact interface. In this manner, whenever a new interface site is created within the MFkMC framework (i.e., according to Step 6 of the MFkMC algorithm as presented in Section 3.2), the SHS-MFkMC model will determine the location of the new interface site and share this information with the PU method. Upon receiving the interface location, the PU method will determine where within its respective PU that the site is located, as follows:

$$x_{PUint,i} = mod\left(x_{\mathcal{R}_i,\phi_i} + \frac{l_{PU,x}}{2}, l_{PU,x}\right) - \frac{l_{PU,x}}{2} \tag{7.1}$$

$$y_{PUint,i} = mod\left(y_{\mathcal{R}_i,\phi_i} + \frac{l_{PU,y}}{2}, l_{PU,y}\right) - \frac{l_{PU,y}}{2} \tag{7.2}$$

where $x_{PUint,i}$ and $y_{PUint,i}$ denote the cartesian x- and y-axis coordinates respectively of the interface i location within its own PU relative to the PU center; $x_{\mathcal{R}_i,\phi_i}$ and $y_{\mathcal{R}_i,\phi_i}$ denote the cartesian x- and y-axis coordinates respectively of the interface i location on the complete droplet surface relative to the droplet center; $l_{PU,x}$ and $l_{PU,y}$ denote the length (along the x-axis) and width (along the y-axis) respectively of the PU; and the mod function outputs the remainder of division between two numbers d_1 and d_2 (i.e., the remainder of d_1/d_2) as follows:

$$mod(d_1, d_2) = d_1 - d_2\lfloor d_1/d_2 \rfloor \tag{7.3}$$

Fig. 7.2 additionally provides a visual representation of how an interface's location is mapped to PU coordinates according to the PU method. Once the interface site's coordinates within the PU have been determined, the PU method will check the solid surface height beneath the interface site and return this information to the FB-MCkMC algorithm. This information will be subsequently used to determine whether

the newly-formed interface site is on top of a pillar or overtop of a pillar gap. Note that when using the PU method, it is ideal to select the MFkMC spatial discretization parameter λ such that $l_{PU,x}$ and $l_{PU,y}$, as well as the pillar width $a_{p,t}$ and interpillar gap $b_{p,t}$, are integer multiples of λ.

The proposed PU method discussed above is ideal for capturing smooth SHSs consisting of identical repeating pillar structures in the absence of surface roughness. However, this method can be modified to pseudo-randomly accommodate for potential surface roughness, individual irregularities in the pillar structure, or other differences between various PUs. This can be accomplished using a pseudo-random number generator to assign molecular-level roughness structures and other surface aberrations to an individual PU based on the PU's coordinates (x_{PU}, y_{PU}) along the PU grid. When a solid surface is decomposed into individual PUs using the PU method, the surface is interpreted as a grid of repeating PUs. As a result, each individual PU can be assigned its own integer index value that denotes its location on the solid surface, as illustrated in Fig. 7.3a. This index can be subsequently used to generate a unique seed for a pseudo-random number generator that can then be used to describe where surface irregularities would occur for that given PU, as illustrated in Fig. 7.3b. Since the surface aberrations are pseudo-randomly generated in a manner that is uniquely linked to the coordinates of an individual PU along the PU grid, it will guarantee that the same features will be generated every time for the same PU without having to store the entire solid surface. Note that when this surface roughness variant of the PU method is combined with a stochastic modelling approach such as SHS-MFkMC,

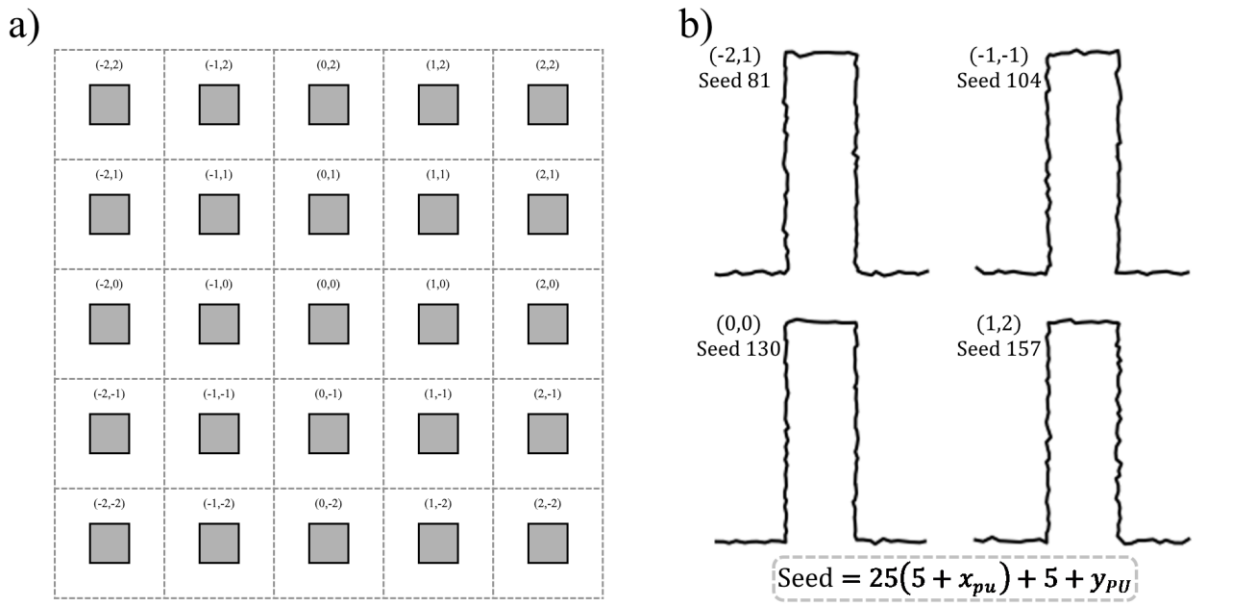

Figure 7.3: a) When mapping an SHS using the PU method, the surface is sub-divided into a grid of individual PUs, which each have their own unique integer coordinates on the PU grid; b) theorized roughness profiles for different PU pillars generated pseudo-randomly based on their PU grid coordinates (x_{PU}, y_{PU})

it is necessary to use a second random number generator for the PU surface generation that is completely independent from the generator used for the stochastic method in order to prevent biasing of the MFkMC event selection.

7.1.2 Force Balance and MFkMC Algorithm Modifications

When a droplet undergoes Cassie spreading overtop of an SHS, it will showcase different behaviour depending on whether the droplet triple interface is advancing on top of a pillar or overtop of the gap between pillars, as illustrated in Fig. 7.4. While crossing the inter-pillar gaps, the droplet's local advancing front is no longer defined by the local solid/liquid/vapour contact line but by the local droplet-vapour interface due to the absence of a solid surface. However, upon reaching the next pillar, the droplet will subsequently create a new local triple contact line as depicted in the figure. In order to account for this lateral inter-pillar droplet spreading, the SHS-MFkMC algorithm defines a second type of interface that is used to advance/recede the droplet across the gaps, which is referred to as the vapour/liquid/vapour (VLV) interface. Accordingly, the VLV is used to advance/recede the droplet until it reaches the next pillar surface, where it will create a new triple contact line (TCL) that will continue to advance or recede. Consequently, the VLV can be seen as an extension of the droplet's line of advancement (i.e. an extension of the real triple contact line, along with the droplet TCL on the surface pillar tops) specifically defined for crossing gaps in the absence of a triple interface.

When a droplet is moving across the gap between two pillars, it will experience different forces compared to when it is advancing on top of a pillar surface (i.e., VLV and TCL droplet interface sites will have a different force balance acting upon them). As a result, it is necessary to modify the balance of forces for VLV and TCL

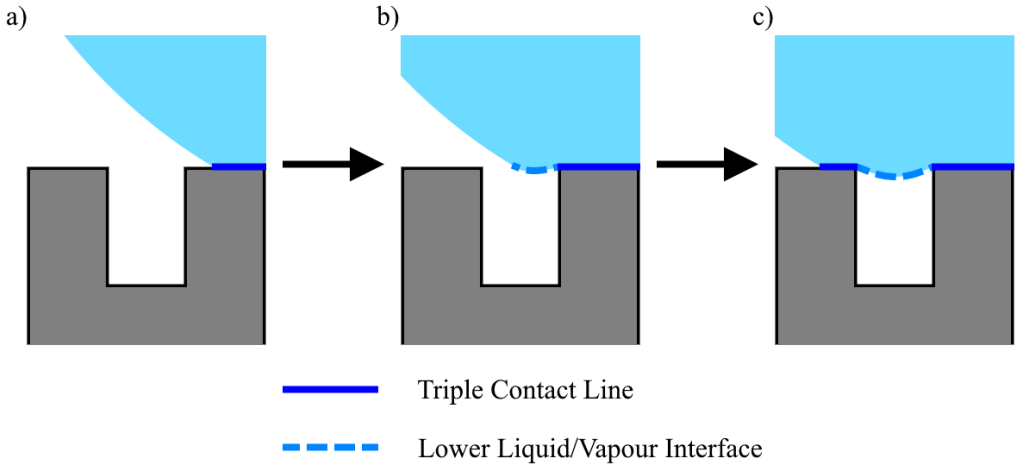

Figure 7.4: a) The advancing front of the sessile droplet is defined using the triple contact line (TCL) when in contact with the solid surface. b) When the advancing front is located over the gap between two SHS pillars, it cannot be described using the triple contact line; it must be instead described using the vapour/liquid/vapour interface (VLV) between the pillars. c) Once the advancing front reaches another pillar, it can once again be described using the TCL

sites in order to accommodate for these differences. In addition, the SHS-MFkMC algorithm method is observed to induce phantom pinning of the droplet interface along the edges of pillars when the movement of the droplet interface changes direction (i.e., SHS-MFkMC falsely predicts that the droplet will pin on the edges of pillars when the droplet stops advancing and starts to recede). This phantom pinning is due to the method used by SHS-MFkMC to define the interface, and consequently it is necessary to implement additional rules to prevent this unrealistic behaviour. The SHS-MFkMC force balance equations can be modified in order to accommodate for both the differences in physics between VLV and TCL sites, and to prevent phantom pinning, as follows:

$$w_{SHS} = \frac{A_{sdbi}}{A_{db}} \tag{7.4}$$

$$v_{drop,i,na} = \begin{cases} \frac{\left(2\pi(2-w_{SHS})R_{drop,i}\gamma_{lv}(\cos\theta_e - \sin(\beta_{s,i}-\theta_i)) + \frac{\mathcal{F}_i}{\delta t}v_{drop,prev,i}\right)}{\left(\frac{\mathcal{F}_i}{dt} + 16.1439\pi w_{SHS}\mu V_{Rs}0.9975^{\frac{1}{Oh}}Oh^{-0.8314}\right)}, & pillar\ edge\ and\ receding, i\ is\ TCL \\ \frac{\left(2\pi(2-w_{SHS})R_{drop,i}\gamma_{lv}(-1-\sin(\beta_{s,i}-\theta_i)) + \frac{\mathcal{F}_i}{\delta t}v_{drop,prev,i}\right)}{\left(\frac{\mathcal{F}_i}{dt} + 16.1439\pi w_{SHS}\mu V_{Rs}0.9975^{\frac{1}{Oh}}Oh^{-0.8314}\right)}, & pillar\ edge\ and\ receding, i\ is\ VLV \\ \frac{\left(2\pi(2-w_{SHS})R_{drop,i}\gamma_{lv}(\cos\theta_e - \cos\theta_i) + \frac{\mathcal{F}_i}{\delta t}v_{drop,prev,i}\right)}{\left(\frac{\mathcal{F}_i}{dt} + 16.1439\pi w_{SHS}\mu V_{Rs}0.9975^{\frac{1}{Oh}}Oh^{-0.8314}\right)}, & otherwise, i\ is\ TCL \\ \frac{\left(2\pi(2-w_{SHS})R_{drop,i}\gamma_{lv}(-1-\cos\theta_i) + \frac{\mathcal{F}_i}{\delta t}v_{drop,prev,i}\right)}{\left(\frac{\mathcal{F}_i}{dt} + 16.1439\pi w_{SHS}\mu V_{Rs}0.9975^{\frac{1}{Oh}}Oh^{-0.8314}\right)}, & otherwise, i\ is\ VLV \end{cases} \tag{7.5}$$

$$v_{drop,i,tvf} = \begin{cases} v_{drop,i,na}(i\ is\ VLV), & i\ is\ TCL \\ v_{drop,i,na}(i\ is\ TCL), & i\ is\ VLV \end{cases} \tag{7.6}$$

$$v_{drop,i} = \begin{cases} v_{drop,i,na}, & interface\ not\ on\ pillar\ edge \\ \frac{v_{drop,i,na} + v_{drop,i,tvf}}{2}, & interface\ on\ pillar\ edge \end{cases} \tag{7.7}$$

where w_{SHS} denotes the ratio of the underside of the droplet in contact with the solid surface pillar tops; A_{db} denotes the surface area on the bottom of the droplet (i.e., the part of the droplet that would be contacting the solid surface on an ideally-smooth surface); A_{sdbi} denotes the surface area of the droplet in direct contact with the pillar tops; $v_{drop,i,na}$ and $v_{drop,i}$ denotes the velocity of the ith interface site before and after it is modified to accommodate for the phantom pinning, respectively; $v_{drop,i,tvf}$ is the predicted velocity of the i^{th} interface site if it had the opposite surface designation (i.e., if site i was a VLV site ($\theta_{e,i} = \pi$) instead of a TCL site ($\theta_{e,i} = \theta_e$), and vice versa); $\beta_{s,i}$ denotes the energy barrier angle for a receding interface site i experiencing genuine pinning along the pillar edges; and $v_{drop,i}(\theta)$ denotes the velocity for site i calculated using an equilibrium contact angle $\theta_{e,i} = \theta$. In these equations, the term w_{SHS} in Eqs. (7.4) and (7.5) is used to

accommodate how the solid-air ratio beneath the droplet affects both the viscous damping and capillary forces. Furthermore, Eq. (7.5) accommodates for the differing physics experienced by the VLV sites as well as the effects of droplet pinning on the pillar edges while receding. In addition, Eqs. (7.6)-(7.7) are implemented to prevent unrealistic phantom pinning that was observed to occur on the SHS due to the underlying assumptions behind MFkMC. In particular, Eq. (7.6) calculates the velocity of a TCL interface site as if it was a VLV interface site, and vice versa. Subsequently, Eq. (7.7) assesses whether or not the interface site is on a pillar edge. If the interface is on an edge, then this equation averages the expected interface velocity calculated using Eq. (7.5) with the modified velocity calculated using Eq. (7.6) if the interface is on a pillar edge. However, if the interface is not on a pillar edge, this equation sets the velocity to be the expected velocity predicted using Eq. (7.5). Further information about each of the aforementioned complications and the derivation of Eqs. (7.4)-(7.7) can be found in Appendix D.

7.1.3 Cassie-to-Wenzel Transitions

One of the most crucial challenges affecting SHS design is that the surfaces are prone to deactivation due to surface fowling via Cassie-to-Wenzel transitions, where sessile droplets become pinned via Wenzel wetting mechanisms within the roughness asperities as discussed in Section 2.2.2.3. Consequently, it is important to accommodate for these phenomena when modelling SHSs using a method such as SHS-MFkMC. This section will predominantly focus on the fundamental processes necessary for SHS-MFkMC to accommodate spontaneous C2W transitions on an SHS. Note that this process can be modified to accommodate for induced C2W transitions (e.g., through the application of external pressure or vibration to a sessile drop) or C2W via evaporation, however these transitions were not considered within this work for the sake of time. C2W transitions are known to spontaneously occur on an SHS via two different mechanisms, i.e., via droplet sag and via spontaneous de-pinning. In order to accommodate for these transition mechanisms, it is important to understand the behaviour of the droplet as it crosses inter-pillar gaps. When a sessile droplet advances across a gap between two roughness asperities, it will experience curvature and sag downwards due to capillarity. If the height of the pillars does not exceed the height of the droplet sag, then the droplet will contact the bottom surface of the gap and spread, transitioning the droplet into the Wenzel state, as illustrated in Fig. 7.5a. Consequently, it is necessary to incorporate the droplet sag height into the SHS-MFkMC model to predict when C2W transitions will begin to occur. Note that the MFkMC algorithm itself does not directly simulate the entire curvature of the droplet sag as it crosses a gap, but rather it captures the horizontal droplet advancement using the VLV approach discussed in the previous section in order to reduce the computational costs. However, the VLV approach can still be modified to accommodate for sag height. In general, the height of droplet sag $\hbar_{sag,i}$ at a given point i along the droplet advancing interface depends on the distance from site i to the nearest pillar that the droplet is in contact with ($d_{VLV,i}$) and the intrinsic contact angle (θ_e), and can be depicted according to the following equation:[222]

$$\hbar_{sag,i} = d_{VLV,i} \frac{1-\sin\theta_e}{-\cos\theta_e} \tag{7.8}$$

In order to accommodate for C2W via droplet sag, the SHS-MFkMC model was modified to calculate the sag height for every VLV interface site. Each time that the droplet would advance over the gap, the SHS-MFkMC algorithm would calculate the distance $d_{VLV,i}$ between the new site i and the nearest droplet-contacted pillar edges and use it to calculate the local sag height according to Eq. (7.8), as illustrated in Fig. 7.6. However, calculating $d_{VLV,i}$ can be computationally difficult for a stochastically-advancing droplet whose interface is continuously evolving on a molecular level. In order to overcome this issue, this work approximated the radial spread of the droplet as a perfect circle when calculating the distance $d_{VLV,i}$. Note that this assumption is only applied for the sake of calculating the drop sag, and that it is not used when simulating the radial droplet spread across the SHS using SHS-MFkMC. In addition, the droplet sag implementation in this work sub-divides the gap space within a PU into two regimes, the previous PU contact regime (Regime 1) and the current PU contact regime (Regime 2), as depicted in Fig. 7.7a. According to this method, Regime 1 is used when the droplet is not considered to be in contact with the pillar within its own PU; in this method, the distances are calculated between the selected droplet site and the pillars in each adjacent PU, and the shortest distance is selected to be $d_{VLV,i}$. On the other hand, Regime 2 is used when the droplet contacts its own PU's pillar using the uniform radius assumption; under this assumption, the closest pillar to the selected droplet site is the pillar within its

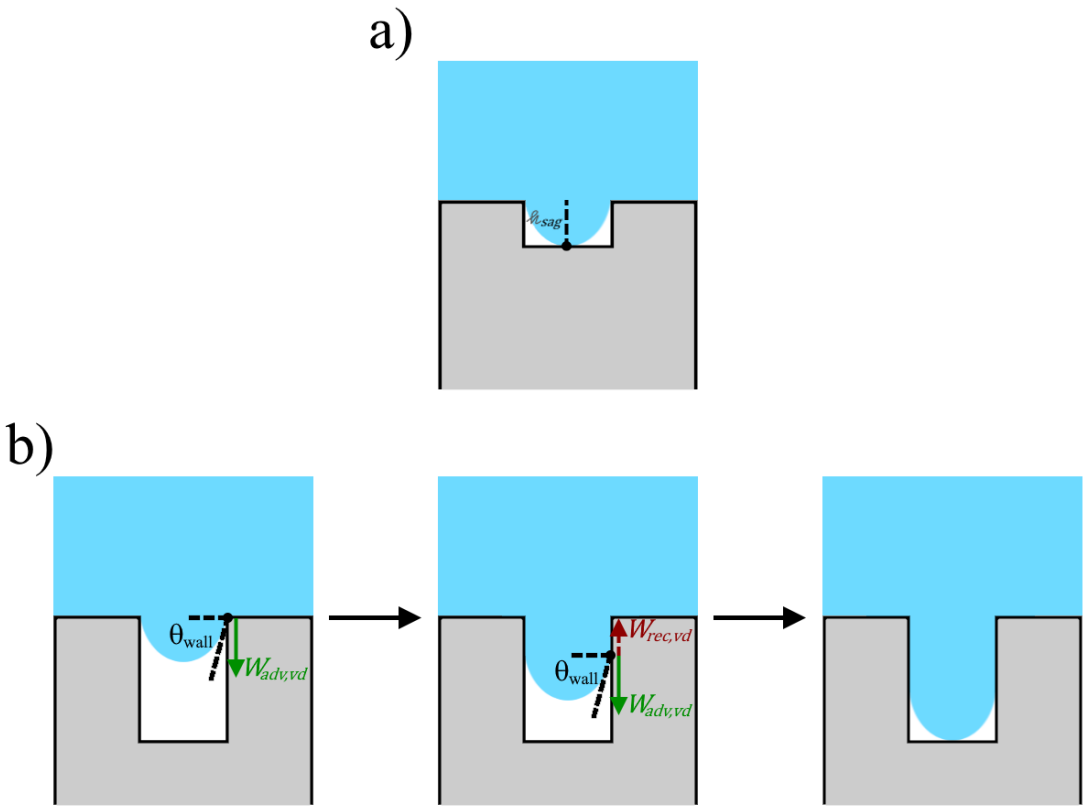

Figure 7.5: Mechanisms of C2W transitions via: a) Sag impalement; b) Sidewall depinning

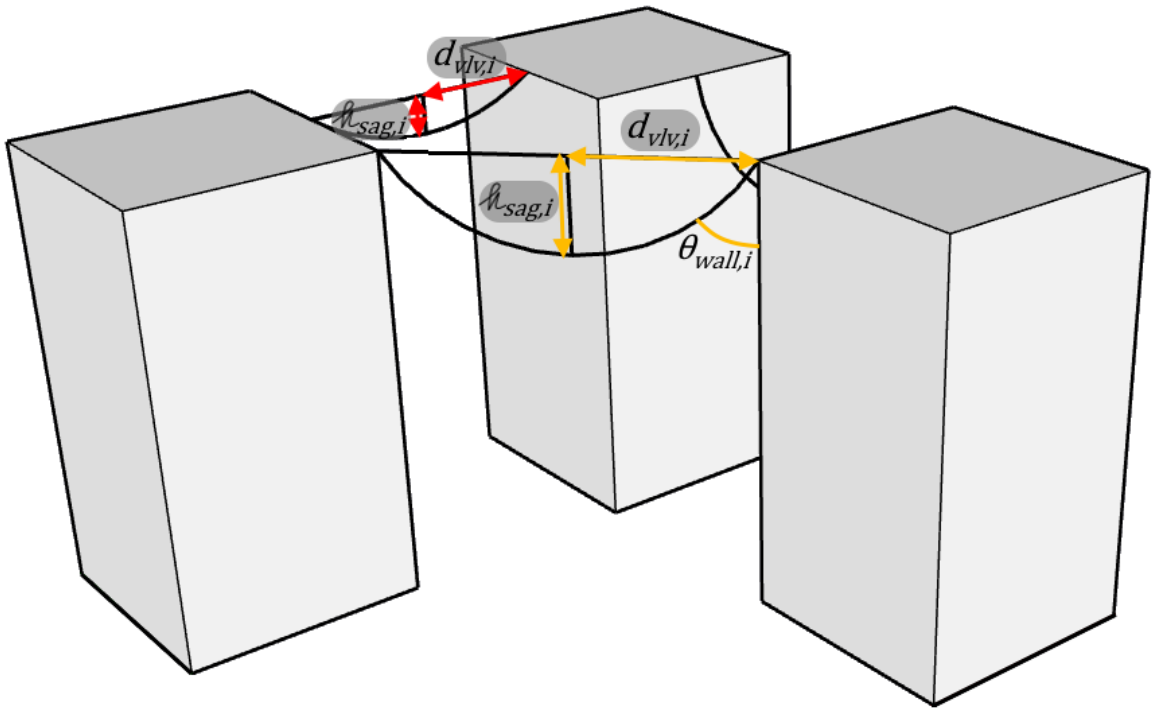

Figure 7.6: Calculation of droplet sag height based on its distance from the nearest pillar

own PU and therefore this distance is used to calculate $d_{VLV,i}$. The method implemented in this work further sub-divided each of these regimes into two different sub-regimes that describe whether $d_{VLV,i}$ for a given site i should be calculated based on how the minimum distance to the closest pillar should be calculated. The sag of a droplet at an interface site i depends on the distance $d_{VLV,i}$ between the site and the nearest point on the pillar edge that is also in contact with the droplet, i.e., the nearest point on the pillar edge that is wetted by the droplet. When the droplet first advances into a new PU (Regime 1) or first contacts a new pillar within its own PU (Regime 2), the minimum closest point of contact on the nearest pillar will not be wetted by the droplet (according to the circular droplet approximation), and consequently $d_{VLV,i}$ will need to be calculated by following the outer circumference of the droplet interface until it contacts the nearest pillar, as illustrated by Regimes 1a and 2a in Fig. 7.7b. However, as the droplet advances, the closest pillar edge site to the i^{th} interface site will eventually wet (i.e., it will eventually be in contact with the droplet). Once this occurs, the minimum distance $d_{VLV,i}$ will be equal to the minimum distance between the i^{th} site and the closest pillar edge site, as illustrated by Regimes 1b and 2b in Fig. 7.7b. Each sub-regime determines the closest wetted point along the edge of the nearest droplet-contacted pillar to the chosen site i, and then calculates the difference between the two points (i.e., the distance $d_{VLV,i}$). The SHS-MFkMC algorithm then calculates the sag height and compares it to the surface pillar height to determine whether or not the droplet will undergo C2W via droplet sag, as highlighted within the SHS-MFkMC algorithm in Section 7.1.4.

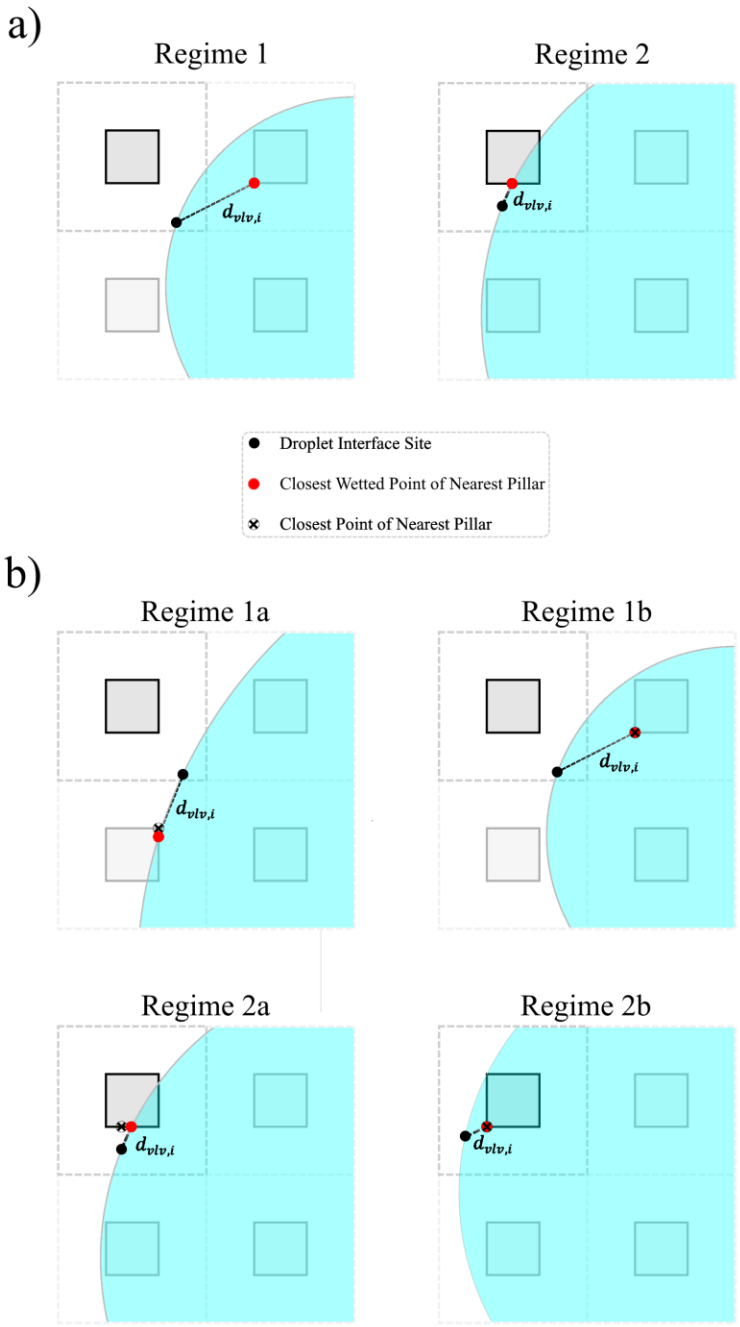

Figure 7.7: Calculation of the distance from the interface to the nearest pillar: a) The method in which $d_{vlv,i}$ is calculated depends on whether the droplet (via the circular droplet approximation) is not in contact with the pillar within its own PU (Regime 1) or whether it does contact the pillar within its own PU (Regime 2); b) Each regime can be further sub-divided into two sub-regimes depending on whether the closest point of contact on the nearest pillar should be determined by following the circumference of the assumed perfect circle from the i^{th} droplet site to the nearest pillar (Regimes 1a, 2a) or whether the distance can be calculated directly between the i^{th} site and the point on the pillar (Regimes 1b, 2b)

When a Cassie regime sessile droplet begins to spread across an inter-pillar gap on an SHS, the droplet sag will form a triple contact interface with the vertical pillar walls at the pillar edge, which can be categorized by the contact angle θ_{wall}, as illustrated in Fig. 7.5b. This triple contact interface will typically remain pinned along the pillar edge for SHSs not prone to spontaneous C2W. However, this interface can also depin and advance or recede vertically along the pillar wall if the vertical forces acting upon the interface (e.g., the gravity force, vertical inertia, etc.) are sufficiently large enough to overcome the capillary-driven pinning. This behaviour can furthermore result in spontaneous C2W if the interface advances far enough along the pillar walls that it contacts the bottom solid surface, as shown in Fig. 7.5b. When the droplet's vertical triple interface is moving, it will advance or recede along the pillar wall according to vertical advancing and receding rates $W_{adv,vd}$ and $W_{rec,vd}$, which are captured according to the moving interface rates presented in Eqs. (5.4)-(5.5). These rates are influenced by the vertical balance of capillary, inertial, viscous damping, and gravity forces acting on the interface, and can be described using the following force balance:

$$\rho h_{vd,i}\frac{dv_{vd,i}}{dt}+\rho v_{vd,i}^2=\frac{3\mu h_{vd,i}v_{vd,i}}{d_{VLV,i}^2}+\rho g h_{vd,i}-\frac{\gamma_{lv}}{d_{VLV,i}}cos\,\theta_{wall,i} \tag{7.9}$$

where $h_{vd,i}$ denotes the distance the i^{th} droplet sag site has travelled vertically along the pillar wall; $v_{vd,i}$ denotes the vertical velocity of the droplet sag; and $\theta_{wall,i}$ denotes the contact angle between the droplet sag and the pillar wall at a TCL site i. Note that when the droplet has finished advancing over the gap between two pillars, $d_{VLV,i}$ can be replaced by half of the interpillar gap distance at the top of the pillar $\frac{b_{p,t}}{2}$. Furthermore note that Eq. (7.9) is the same equation as the force balance for capillary action between two parallel plates. In order to accommodate for spontaneous C2W via depinning, the SHS-MFkMC algorithm was modified to incorporate the advancing and receding movement of the vertical droplet sag TCL. This vertical droplet movement was integrated by re-arranging Eq. (7.9) with respect to the velocity, as follows:

$$v_{vd,i}=\frac{h_{vd,i}}{2\delta t}-\frac{3\mu h_{vd,i}}{2\rho d_{VLV,i}^2}-\sqrt{\left(-\frac{h_{vd,i}}{2\delta t}+\frac{3\mu h_{vd,i}}{2\rho d_{VLV,i}^2}\right)^2-2\frac{\rho h_{vd,i}v_{vd,prev,i}}{\delta t}-2\rho g h_{vd,i}+2\frac{\gamma_{Lv}}{d_{VLV,i}}cos\,\theta_{wall,i}} \tag{7.10}$$

Subsequently, this equation is substituted into Eqs. (5.4)-(5.5) to derive the rate equations for vertical droplet movement $W_{adv,vd,i}$ and $W_{rec,vd,i}$ in the same manner discussed in Chapters 5 and 6. The vertical rates of movement were incorporated into the pool of possible events within the SHS-MFkMC model such that they would be randomly selected to occur. If the droplet interface began to advance, the algorithm would keep track of its position and would double check to see if the sag height would come in contact with the bottom solid surface. If this contact were to occur, then the droplet would be considered to have transitioned into the Wenzel state. Note that in order to reduce the overall computational cost and memory requirements, it was assumed that once the droplet VLV had completely advanced over the gap between two pillars, the vertical TCL would

not experience any significant depinning or movement if it had not already done so, as the VLV distance $d_{VLV,i}$ and therefore the sag contact angle $\theta_{wall,i}$ would remain constant. As a result, this model only considered the droplet sag TCLs adjacent to gaps along the edge of the droplet or those that were still experiencing movement so that all TCLs towards the center of the droplet bottom could be disregarded.

7.1.4 SHS-MFkMC Algorithm for Sessile Droplet Spread on an SHS

Cassie wetting sessile droplet spreading on an SHS is an intricate and complicated process that features significantly altered physics compared to droplet spreading on a smooth surface. Consequently, in order to capture this behaviour using SHS-MFkMC, the FB-MFkMC algorithm has been substantially modified in order to accommodate for the new physics and additional challenges highlighted in Sections 7.1.1-7.1.3. Accordingly, the complete SHS-MFkMC algorithm to capture sessile droplet spread on an SHS is illustrated in Fig. 7.8 and can be described as follows:

1. Initialize the SHS using the PU method according to the *PUinit* sub-algorithm shown in Table 7.1
2. Set the initial time to $t = 0$s
3. Initialize the system to depict the droplet on the surface
    3.1. Initialize the MFkMC lattice to depict when the droplet contacts the surface by marking the droplet and atmosphere interface sites according to Fig. 7.9
    3.2. Calculate the initial properties of each interface site i using the *SiteInit* sub-algorithm presented in Table 7.2.
    3.3. Set $v_{drop,i} = v_{drop,0}$ for each interface site i
4. Determine the time $t + \delta t$ when the droplet interface will move according to Eq. (3.11)
5. Update the time-dependent event rates
    5.1. Update $v_{drop,i}$ according to Eqs. (7.5)-(7.7) and (7.10)
    5.2. Update $W_{tot,nc}$ and calculate $W_{adv,i}$ and $W_{rec,i}$ according to Eqs. (6.1)-(6.3) and (5.4)-(5.5)
6. Apply MC sampling to select a random interface event at a site i according to Eq. (3.12)
    6.1. If the selected event is a vertical droplet spreading event:
        6.1.1. Execute the event at site i according to the *VertEvent* sub-algorithm in Table 7.4
        6.1.2. If site i is now a droplet site and $h_{vd,i} \geq H_p$, then the droplet has undergone C2W via spontaneous depinning
    6.2. If the selected event is a horizontal droplet spreading event:
        6.2.1. Execute the event at site i according to the *HorizEvent* sub-algorithm in Table 7.5
        6.2.2. If site i is now a droplet site and $h_{sag,i} \geq H_p$, the droplet has undergone C2W via droplet sag
7. Repeat Steps 4-6 until either the droplet has undergone C2W or the final time $t = t_f$ has been reached

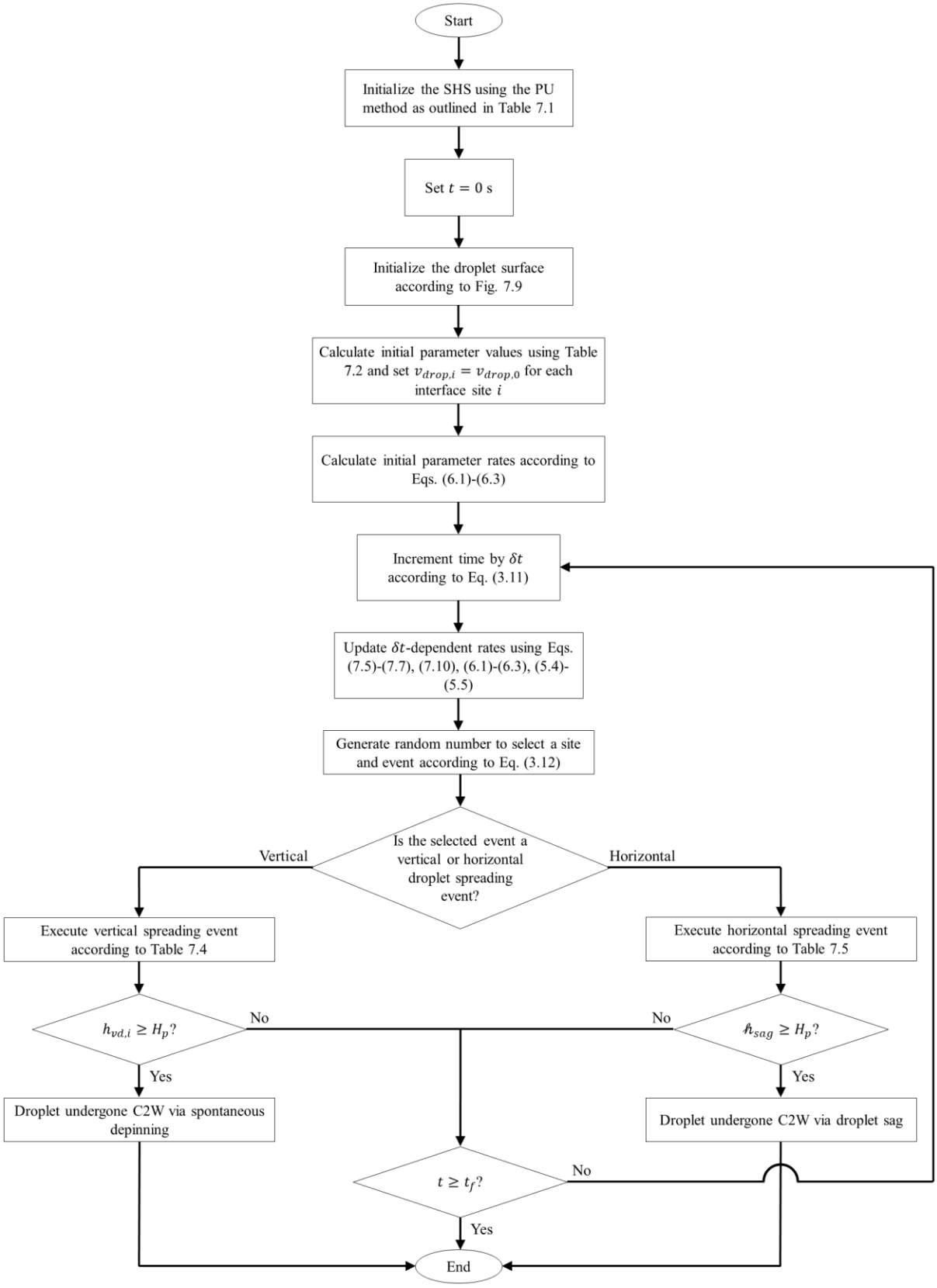

Figure 7.8: Flowchart of the SHS-MFkMC algorithm

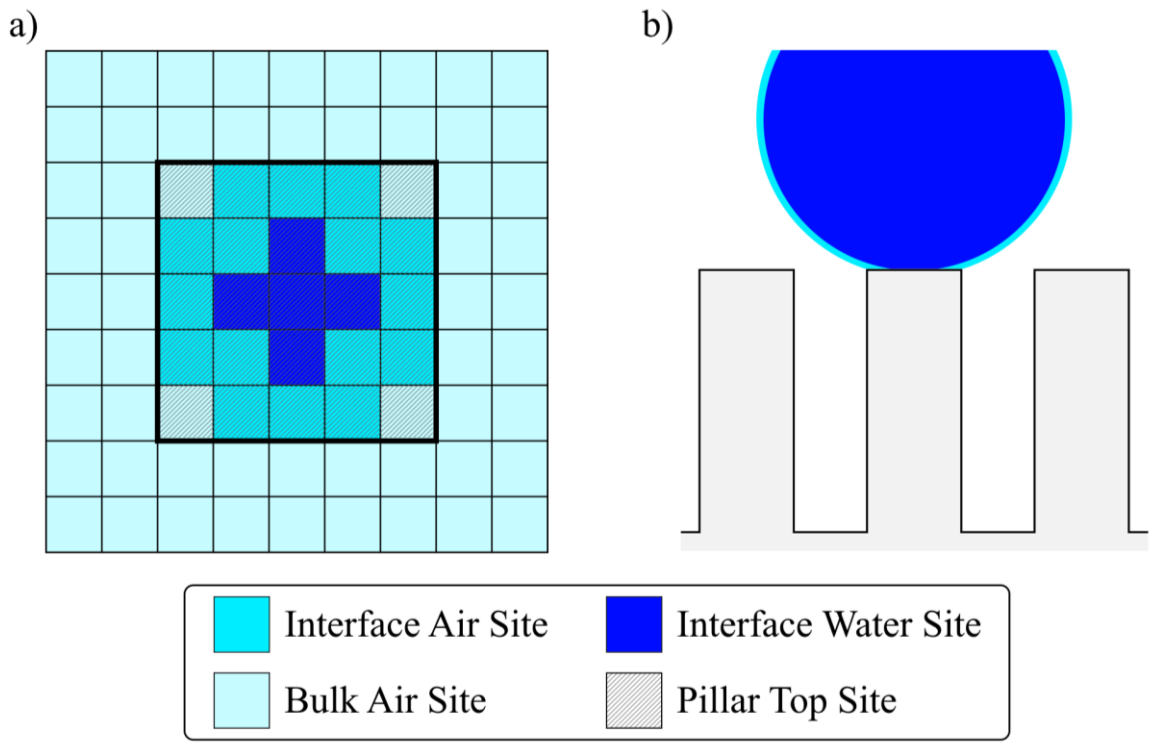

Figure 7.9: a) Initial configuration on the MFkMC lattice for the moment when the droplet first impacts the solid surface; b) Side view of the droplet when it first impacts the solid surface of an SHS

The above algorithm highlights how the PU method, vertical droplet movement along the pillar walls, C2W detection, and pillar edge detection are accommodated into the FB-MFkMC algorithm to built the SHS-MFkMC process. Through the inclusion of these processes, the algorithm is able to accommodate the specific features associated with sessile droplet spread on an SHS. However, the SHS-MFkMC algorithm is based on the MFkMC algorithm outlined in Section 3.2, and therefore it is subject to the same MFkMC challenges and limitations outlined in Chapter 3. Furthermore, the additional physics and features incorporated into the SHS-MFkMC model impacts the computational efficiency of the model and consequently, the model is computationally slow compared to the FB-MFkMC model used to capture sessile droplet spread on a smooth surface. In particular, the formation of vertical triple contact interface sites along the edges of each pillar significantly increases the total number of interface sites considered within the model, thus increasing its overall

Table 7.1: The *PUinit* sub-algorithm

1. Initialize a $l_{PU,x} \times l_{PU,y}$ rectangular space to represent a single PU
2. Discretize the PU interior space according to λ
3. Determine and store the surface height H_i at each discretized point based on the pillar physical structure (i.e. $a_{p,t}$, $a_{p,b}$, $b_{p,t}$, and $b_{p,b}$), as illustrated in Fig. 7.10

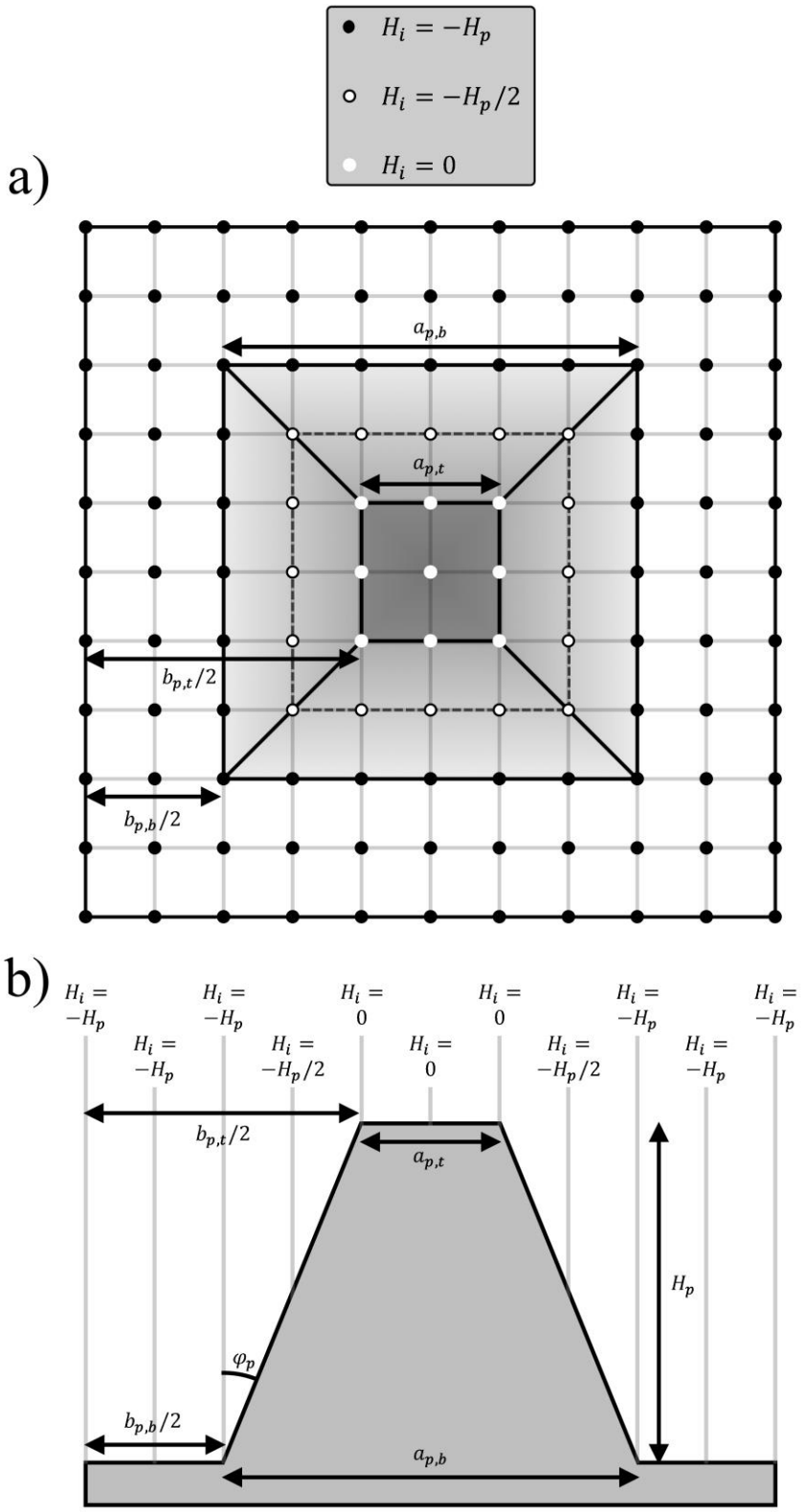

Figure 7.10: Determining the height H_i of the SHS relative to the pillar top while initializing the PU method for a sample pillar geometry: a) top view; b) Side view

Table 7.2: The *SiteInit* sub-algorithm

1. Set $R_{drop,i} = \mathcal{R}_i$ based on the polar coordinates $(\mathcal{R}_i, \phi_i)$ for site i
2. Determine the surface height H_i below site i
   - 2.1. Determine $x_{PUint,i}$ and $y_{PUint,i}$ according to $(x_{\mathcal{R}_i,\phi_i}, y_{\mathcal{R}_i,\phi_i})$ using Eqs. (7.1)-(7.2)
   - 2.2. Determine and output H_i at the point $(x_{PUint,i}, y_{PUint,i})$ within the PU
   - 2.3. If $H_i = 0$, (i.e., on top of the pillar), mark site i as a TCL site
   - 2.4. If $H_i < 0$, calculate $d_{VLV,i}$ using Regime 2b and calculate $\hbar_{sag,i}$ according to Eq. (7.8)
     - 2.4.1. If $\hbar_{sag,i} > H_i$, mark site i as a TCL site
     - 2.4.2. If $\hbar_{sag,i} < H_i$, mark the site as a VLV site
3. Record how many nearest neighbour sites at $\lfloor (x_{\mathcal{R}_i-\lambda,\phi_i}, y_{\mathcal{R}_i-\lambda,\phi_i}) \rfloor$ and $\lceil (x_{\mathcal{R}_i-\lambda,\phi_i}, y_{\mathcal{R}_i-\lambda,\phi_i}) \rceil$ are droplet sites
4. Record how many nearest neighbour sites at $\lfloor (x_{\mathcal{R}_i+\lambda,\phi_i}, y_{\mathcal{R}_i+\lambda,\phi_i}) \rfloor$ and $\lceil (x_{\mathcal{R}_i+\lambda,\phi_i}, y_{\mathcal{R}_i+\lambda,\phi_i}) \rceil$ are droplet sites
5. Determine if site i or one of its nearest neighbour sites j_i border a pillar edge according to the *EdgePillar* sub-algorithm in Table 7.3.
6. Calculate θ_i using Eq. (2.11)
7. Update $\bar{R}_{drop}$, $W_{tot,nc}$, A_{sdbi} and A_{db}
8. Calculate w_{SHS}, $W_{adv,i}$ and $W_{rec,i}$ according to Eq. (7.4) and Eqs. (6.1)-(6.3)

computational cost. However, this challenge can be overcome by excluding the vertical TCL sites around a pillar once the droplet had completely crossed the gap to the adjacent pillars in order to minimize the considered number of interface sites, as highlighted at the end of Section 7.1.3.

7.2 Model Validation and Analysis

The objective of this section is to validate the proposed SHS SHS-MFkMC algorithm against data available from the literature. These studies validate the model's ability to both capture sessile droplet spreading on an SHS, and its ability to predict C2W transitions. This section additionally investigates the model predictions and highlights its general ability to capture sessile droplet spread on an SHS. These results are furthermore used to analyze the behaviour of sessile droplet spreading on SHSs, and to determine the surface structure criteria necessary to prevent spontaneous C2W.

Table 7.3: The *EdgePillar* sub-algorithm

1. Analyze the state of site i and each its nearest neighbours j_i
    1.1. If site i is both a droplet interface site and a TCL site:
        1.1.1. If any nearest neighbour j_i is both an atmosphere interface site and a VLV site:
            1.1.1.1. Mark site i as a pillar edge droplet site
            1.1.1.2. Calculate $\beta_{s,i}$ according to Eq. (2.7)
            1.1.1.3. Initialize $v_{vd,i} = v_{impact}$ and set $h_{vd,i} = 0$
            1.1.1.4. Calculate $W_{adv,vd,i}$ and $W_{rec,vd,i}$ by coupling $v_{vd,i}$ with Eqs. (5.4)-(5.5)
        1.1.2. Else:
            1.1.2.1. Mark site i as not a pillar edge droplet site
            1.1.2.2. Set $\beta_{s,i} = \frac{\pi}{2}$ radians
    1.2. If site i is both an atmosphere interface site and a VLV site:
        1.2.1. Mark site i as not a pillar edge droplet site
        1.2.2. Set $\beta_{s,i} = \frac{\pi}{2}$ radians
        1.2.3. If any nearest neighbour site j_i is both a droplet interface site, a TCL site, and is not currently a pillar edge site:
            1.2.3.1. Mark site j_i as a pillar edge droplet site
            1.2.3.2. Calculate β_{s,j_i} according to Eq. (2.7)
            1.2.3.3. Initialize $v_{vd,j_i} = v_{impact}$ and set $h_{vd,j_i} = 0$
            1.2.3.4. Calculate W_{adv,vd,j_i} and W_{rec,vd,j_i} by coupling v_{vd,j_i} with Eqs. (5.4)-(5.5)
    1.3. Else:
        1.3.1. Mark site i as not a pillar edge droplet site
        1.3.2. Set $\beta_{s,i} = \frac{\pi}{2}$ radians

The SHS SHS-MFkMC algorithm implemented within this work was validated using experimental data obtained from the literature in order to assess its capabilities of capturing both Cassie-state sessile droplet spreading and spontaneous C2W transitions. In order to conduct these validation studies, the SHS-MFkMC model was used to capture the spreading behaviour of droplets of water dropped onto various SHSs consisting

Table 7.4: The *VertEvent* sub-algorithm

1. If site i is an atmosphere site:
    1.1. Change site i into a droplet interface site
    1.2. Remove the droplet interface site above site i
    1.3. Create a new atmosphere interface site ji below site i
        1.3.1. Initialize $v_{vd,j_i} = v_{vd,i}$
        1.3.2. Calculate $h_{vd,j_i} = h_{vd,i} - \lambda$
        1.3.3. Calculate W_{adv,vd,j_i} by coupling v_{vd,j_i} with Eq. (5.4)
2. If site i is a droplet site:
    2.1. Change site i into an atmosphere interface site
    2.2. Remove the atmosphere interface site below site i
    2.3. Create a new droplet interface site j_i above site i
        2.3.1. Initialize $v_{vd,j_i} = v_{vd,i}$
        2.3.2. Calculate $h_{vd,j_i} = h_{vd,i} + \lambda$
        2.3.3. Calculate W_{rec,vd,j_i} by coupling v_{vd,j_i} with Eq. (5.5)

of rectangular pillars manufactured with different dimensions as outlined in Table 7.6. This table also shows the values of λ used to perform the SHS-MFkMC simulations. Furthermore, each of the SHS-MFkMC simulations were performed according to the algorithm outlined in Section 7.1.4. Subsequently, the average droplet radius for each study was calculated and compared to the average droplet radii reported within the literature.[33,167] Note that the SHS case studies considered in this study were selected to highlight different expected droplet spreading phenomena. In particular, the droplets in studies 1a and 1c were experimentally observed to bounce on the SHSs due to the high impact velocities v_{impact} and the large inter-pillar gaps $b_{p,t}$. In general, SHSs with large gap-to-pillar top surface area ratios tend to have lower wetting and therefore are more prone to promote droplet bouncing. Additionally, study 1d showcases the behaviour of the droplet in study 1c once it re-impacts on the same SHS after bouncing. In the 1d case study, the droplet has a much smaller v_{impact} and therefore undergoes very little oscillation before reaching steady state. Finally, the SHS in study 1b was selected due to its smaller gap-to-pillar top surface area ratio, where the impacting droplet was experimentally observed to oscillate on the surface before reaching steady state. Note that each of these validation studies were only conducted using droplets of water, and that no other droplet fluid was used to test

Table 7.5: The *HorizEvent* sub-algorithm

1. Update A_{sdbi} and A_{db} and calculate w_{SHS} according to Eq. (7.4)
2. If site i is an atmosphere site:
   2.1. Change site i into a droplet interface site
   2.2. Calculate $W_{rec,i}$ according to Eqs. (6.1)-(6.3)
   2.3. If $\hbar_{sag,i} \geq H_p$, the droplet has undergone C2W via droplet sag
3. If site i is a droplet site:
   3.1. Change site i into an atmosphere interface site
   3.2. Calculate $W_{adv,i}$ according to Eqs. (6.1)-(6.3)
4. Check to see if any interface sites have become bulk sites due to the executed event; remove any newly formed bulk sites.
5. Check to see if any new interface sites j_i are created from former bulk phase sites due to the executed event
   5.1. Initialize the new interface sites according to the *SiteInit* sub-algorithm in Table 7.2
   5.2. Initialize $v_{drop,j_i} = v_{drop,i}$
6. Determine if site i borders a pillar edge according to the *EdgePillar* sub-algorithm in Table 7.3
7. Update $\bar{R}_{drop}$ and $W_{tot,nc}$

the SHS model. This was due to the availability of sessile droplet spreading data on SHSs within the literature that could be used to validate the model, as the majority of the data available was conducted for water droplets. Furthermore, the modifications required to accommodate for SHSs within the SHS-MFkMC algorithm do not rely on the droplet fluid physical parameters as highlighted in Eqs. (7.4)-(7.7) and therefore it can be assumed that these parameters only affect droplet spreading on an SHS in the same manner that they affect spreading on a smooth surface. The results of this study are depicted in Fig. 7.11, where the solid green lines denote the average contact radius of the droplets as predicted by the SHS-MFkMC simulations and the dashed red lines depict the droplet data from the literature. Note that the SHS-MFkMC simulations were repeated three times for each case study in order to accommodate for the inherent stochasticity of the SHS-MFkMC algorithm. However, there were no notable deviations between the individual SHS-MFkMC simulations since the 3D SHS-MFkMC model innately accommodates for the average system behaviour by reporting the average droplet contact radius, as discussed previously in Section 6.3.2. The SHS-MFkMC results showcased in Fig. 7.11 were

Table 7.6: Properties and parameters for the SHS sessile droplet spreading data considered to validate the radial spreading predictions of the SHS-MFkMC model

Study Name	Study 1a ([33])	Study 1b ([167])	Study 1c ([167])	Study 1d ([167])
Liquid	Water	Water	Water	Water
Solid Surface	FDTS	Platinum	Platinum	Platinum
θ_e	104	95	95	95
V (uL)	3.59	2.57	2.57	2.57
$v_{drop,0}$ (m/s)	0.27	0.28	0.28	0.08
H_p (μm)	100	27	27	27
$a_{p,t}$, $a_{p,b}$ (μm)	25	20	20	20
$b_{p,t}$, $b_{p,b}$ (μm)	75	10	20	20
λ (μm)	25	10	10	10
ρ (kg/m^3)	997	997	997	997
μ (Pa·s)	8.90×10^{-4}	8.90×10^{-4}	8.90×10^{-4}	8.90×10^{-4}
γ_{lv} (N/m)	7.28×10^{-2}	7.28×10^{-2}	7.28×10^{-2}	7.28×10^{-2}
Computational Time (min)	33.7	333.4	45.9	143.1

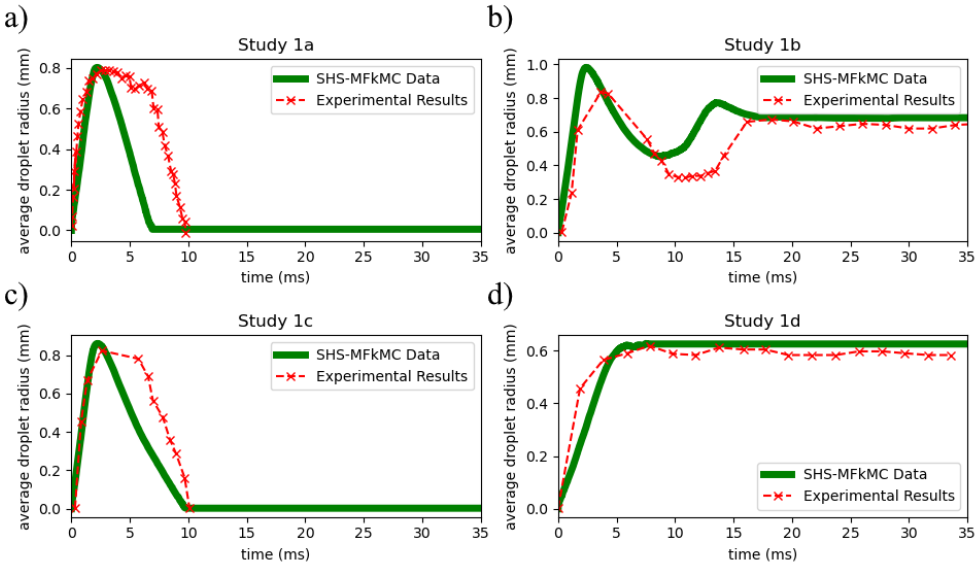

Figure 7.11: Comparison between the experimental/literature data (red --) and the averaged SHS-MFkMC-predicted results (green x) for sessile droplet spread on SHSs: a) Study 1a, droplet spread on an SHS with $H_p = 100$ μm, $a_{p,t} = 25$ μm, $b_{p,t} = 75$ μm, $v_{drop,0} = 0.27$ m/s; b) Study 1b, droplet spread on an SHS with $H_p = 27$ μm, $a_{p,t} = 20$ μm, $b_{p,t} = 10$ μm, $v_{drop,0} = 0.28$ m/s; c) Study 1c, droplet spread on an SHS with $H_p = 27$ μm, $a_{p,t} = 20$ μm, $b_{p,t} = 20$ μm, $v_{drop,0} = 0.28$ m/s; d) Study 1d, droplet spread on an SHS with $H_p = 27$ μm, $a_{p,t} = 20$ μm, $b_{p,t} = 20$ μm, $v_{drop,0} = 0.08$ m/s

accordingly determined by averaging the results from the three independent SHS-MFkMC runs. The results in this figure highlight that the SHS SHS-MFkMC algorithm is capable of qualitatively capturing the overall radial spread of sessile droplets on an SHS. For studies 1a and 1c, the SHS-MFkMC model was able to capture the droplet bouncing behaviour predicted from the experimental results. In both case studies, the droplet achieved a maximum spreading similar to the experimental data. Specifically, the maximum droplet radius in study 1a was observed to be 0.788 μm and 0.803 μm for the experimental and SHS-MFkMC models respectively, whereas in study 1c it was observed to be 0.823 μm and 0.860 μm for the experimental and SHS-MFkMC models, respectively. However, the SHS-MFkMC-predicted droplet receding behaviour in both studies differed from that of the experimental data and tended to predict that the droplet would bounce sooner than was observed experimentally. These notable deviations can be attributed to the effects of molecular-level surface irregularities on the sessile droplet spread. The surfaces of textured SHSs are known to experience significant nanoscale roughness and deviations from the expected pillar shapes due to the etching process used to manufacture the SHS.[223] These surface irregularities play a significant role in the sessile droplet spread and therefore such deviations between the model results and experiments is to be expected. The manufacturing of an SHS is most notably expected to affect the sharpness of the pillar edges, and produce pillars with a more rounded edge.[223] These rounded pillar edges are not expected to experience as sharp of pinning along the pillar edges compared to a perfect rectangular pillar structure. Since pinning is only expected to significantly affect the receding droplet behaviour, these manufacturing errors can explain the notably larger deviations in the droplet receding behaviour compared to its advancing behaviour. Similarly, large deviations can be observed in the droplet receding behaviour of study 1b. In this study, the SHS-MFkMC results are able to predict the amount of oscillations that the droplet will undergo before reaching steady state. In addition, the model predicts the final equilibrium contact radius of the droplet on the SHS. However, there are still significant deviations in both advancing and receding behaviour between the modelling and experimental results. These deviations are similar in behaviour to those observed in the ideally flat surface sessile droplet studies conducted in Chapter 6, although they are overall larger for the SHS surfaces. In particular, the SHS-MFkMC models for both SHSs and smooth surfaces tended to predict that the droplet would attain larger spreading radii when advancing and would similarly stop receding at larger contact radii before attaining steady state. This behaviour in both cases can be attributed due to surface roughness. In addition to the effects on the receding behaviour mentioned above, roughness is additionally expected to affect the predicted advancing behaviour, as discussed in Chapter 6. In particular, molecular-level surface irregularities are expected to inhibit droplet advancing and stop the droplet movement before it is able to attain its maximum spreading radius. This behaviour is the basis of Wenzel-based wetting on a roughened surface, where the increase in surface area due to the roughness is predicted to cause the hydrophobic surface to appear more hydrophobic and therefore cause a droplet to undergo a smaller maximum spreading radius than it would on an ideally smooth surface.[153] In comparison to studies 1a-1c, the SHS-MFkMC model results accurately predicted the sessile droplet spreading behaviour on

an SHS in study 1d. This is because the droplet in this study was expected to be overdamped and not experience any significant oscillations. As a result, it was not predicted to experience as significant effects due to surface roughness compared to the other studies. Most notably, the model was able to predict the final droplet spreading radius under Cassie wetting conditions on an SHS for both studies 1b and 1d, despite the changes in the surface geometry due to the pillars. This showcases that the SHS-MFkMC model can predict the superhydrophobicity of a given surface design, since the droplet spreading radius is directly correlated to the droplet contact angle as shown in Eq. (2.11). Overall, the model reasonably predicts the sessile droplet spreading behaviour on an SHS behaviour. There are still visible deviations between the SHS-MFkMC-predicted results and those observed from experiments, and these deviations are more notable than those observed on the ideally smooth surfaces studied in Chapter 6. However, as described above, these large deviations can be attributed to the effects of molecular-level surface irregularities on the sessile droplet spread. Although surface roughness is neglected in the present model, the model can be readily modified to accommodate for unique surface roughness profiles for each individual pillar as mentioned in Section 7.1.1. The integration of these methods into the SHS SHS-MFkMC algorithm will be the focus of future work. In addition to the above results, Table 7.6 listed the computational cost for each study. Note that the computational costs for the SHS-MFkMC model are significantly larger (i.e., one to two orders of magnitude larger) than those for the FB-MFkMC model discussed in Chapter 6. This is due to the increased number of processes accommodated by the SHS-MFkMC algorithm in order to capture droplet spreading on an SHS, as discussed in Section 7.1.4. Additionally, the studies in Table 7.6 required significantly smaller λ values to simulate in order to accurately capture the SHS geometry, resulting in increased computational costs. These changes were most significant for Study 1c. This study required a significantly larger number of MFkMC events to capture its underdamped behaviour compared to the other studies, and the majority of these events were executed when the model was storing a large number of interface sites, resulting in significantly increased computational costs.

Studies 1a-1d showcased above in Fig. 7.11 illustrated the radial Cassie wetting spread of a sessile droplet on an SHS where the droplet was not subjected to spontaneous C2W transitions. However, the SHS-MFkMC model is also capable of capturing the C2W transition regime as discussed in Section 7.1.3. In order to illustrate and validate this behaviour, the MFkMC-based model was used to simulate the spreading behaviour of droplets on different rectangular pillar-based SHS designs as listed in Table 7.7, where half the surface designs have been experimentally demonstrated to undergo spontaneous C2W. Note that the likelihood of the droplet undergoing spontaneous C2W transitions is highest during the initial stages of the droplet radial (Cassie regime) spreading, when the droplet is in contact with the fewest number of pillars.[224] Therefore, in order to reduce the computational cost, the SHS-MFkMC simulations of the SHSs were performed until the droplet either experienced a C2W transition or the droplet fully contacted the top surface of each of the pillars adjacent to the pillar that the droplet first contacted. Table 7.7 displays whether or not the SHS-MFkMC models

Table 7.7: Properties and parameters for the SHS sessile droplet spreading data considered to validate C2W transition predictions of the SHS-MFkMC model

Study Name	**Study 2a ([167])**	**Study 2b ([167])**	**Study 2c ([225])**	**Study 2d ([33])**
Liquid	Water	Water	Water/Glycerol	Water
Solid Surface	Platinum	Platinum	PDMS	FDTS
θ_e	95	95	71	104
V (uL)	2.57	2.57	4	3.59
v_{impact} (m/s)	0.36	0.28	0	1.02
H_p (μm)	27	27	45	100
$a_{p,t}$, $a_{p,b}$ (μm)	20	20	30	25
$b_{p,t}$, $b_{p,b}$ (μm)	20	56	30	75
C2W Observed Experimentally?	No	Yes	Yes	No
C2W Predicted by SHS-MFkMC?	No	Yes	Yes	No

underwent spontaneous C2W for each considered surface design. Table 7.7 furthermore lists the expected maximum sag height for each study as well as whether the surfaces were observed to undergo spontaneous C2W through experiments conducted in the literature.[33,167,225] Note that the maximum sag height between each of the pillars was measured along the gap between two diagonal pillars,[226] as illustrated in Fig. 7.6. In addition, Fig. 7.12 showcases the vertical droplet movement profiles for each of the studies as predicted using the SHS-MFkMC models. Note that all of the aforementioned surfaces experienced C2W transitions via depinning. This is because the maximum droplet sag height is typically small compared to the pillar heights fabricated experimentally. Consequently, to the author's knowledge, none of the experimental SHSs described within the literature reported spontaneous C2W via droplet sag. However, the SHS-MFkMC model will still analyze whether a droplet will undergo C2W via droplet sag through the sag height equation reported in Eq. (7.8), which has already been validated within the literature.[226,227] Furthermore note that all of the experimental results observed within the literature did not report the transient droplet behaviour as it advanced along the vertical pillar walls. These studies instead only reported whether the droplets underwent spontaneous C2W transitions, as reported in Table 7.7. As a result, Fig. 7.12 only illustrates the vertical droplet spreading behaviour predicted by the SHS-MFkMC simulations. The results from this figure demonstrate that the SHS-MFkMC model can predict whether or not an SHS will undergo spontaneous C2W transitions. Furthermore, the results in Fig. 7.12 demonstrate that once the droplet depins vertically from the pillar tops, it rapidly accelerates down the pillar sidewalls until it contacts the base and undergoes C2W. Fig. 7.12a furthermore showcases that in the face of

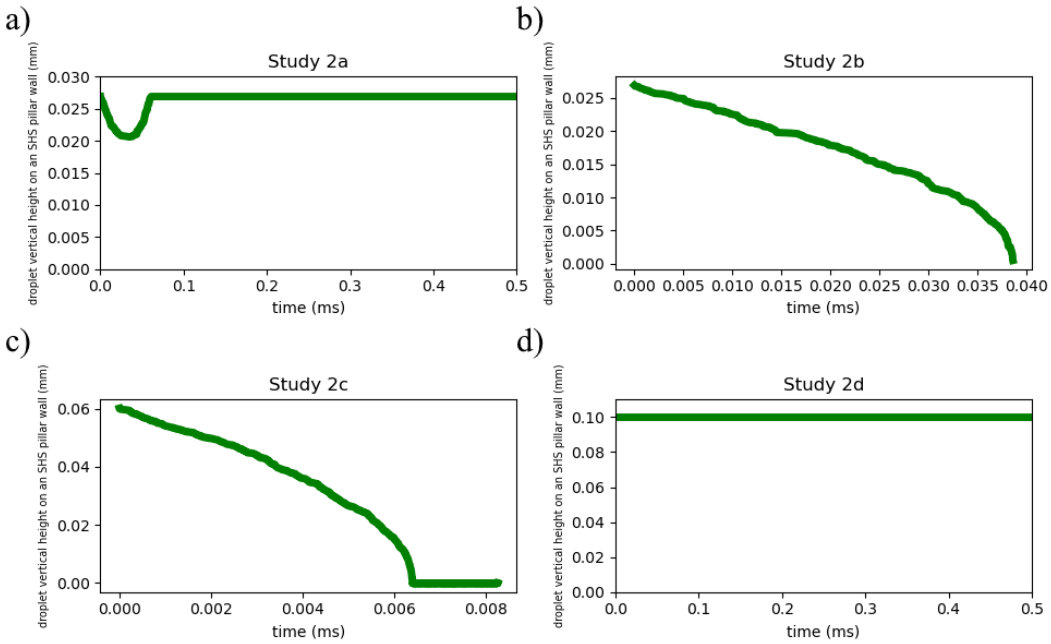

Figure 7.12: Droplet triple contact line vertical position along the pillar walls as a function of time for four different SHSs: a) Study 2a, $H_p = 27$ μm, $a_{p,t} = 20$ μm, $b_{p,t} = 20$ μm; b) Study 2b, $H_p = 27$ μm, $a_{p,t} = 20$ μm, $b_{p,t} = 56$ μm; c) Study 2c, $H_p = 45$ μm, $a_{p,t} = 30$ μm, $b_{p,t} = 30$ μm; d) Study 2d, $H_p = 100$ μm, $a_{p,t} = 25$ μm, $b_{p,t} = 75$ μm. These studies illustrate whether a sessile droplet will undergo spontaneous C2W transitions on the superhydrophobic surface

sufficient impact velocity, the droplet can depin from the pillar edges and momentarily advance down along the pillar walls. This behaviour is due to the vertical inertia force as depicted in Eq. (7.9). As a result, the observed movement along the pillar wall is temporary and the droplet sag readily retreats back to the pillar edge once the droplet has sufficiently decelerated due to the capillary and viscous damping forces. However, note that inertia can still induce a C2W transition on the SHS if the impact velocity is sufficiently large such that the droplet sag contacts the bottom surface of the SHS before the inertial force is overcome. This behaviour is expected and will be further explored later in this section.

To further validate C2W transitions using the SHS-MFkMC model, the model was used to replicate data derived from the literature to predict what intrinsic contact angles would cause an SHS to have an unstable Cassie regime, i.e., for what contact angles would a given SHS spontaneously undergo C2W.[224] This data from the literature was obtained for water droplets placed on a variety of different trapezoidal pillar structures where the width of the top of the pillar was modified while the pillar base dimensions remained constant, according to the parameters listed in Table 7.8. These different pillar shapes were categorized based on the solid fraction at the tops of the pillars according to the following dimensionless parameter:

$$\phi_{SHS} = \frac{a_{p,t}}{a_{p,b}+b_{p,b}} \tag{7.11}$$

Table 7.8: Properties and parameters for the SHS sessile droplet spreading data considered to validate C2W transition predictions of the SHS-MFkMC model for SHSs of varying ϕ_{SHS} and θ_e

Property	Value
Liquid	Water
θ_e	80-110°
V	2.57 uL
v_{impact}	0 m/s
H_p	50 μm
$a_{p,t}$	0-20 μm
$a_{p,b}$	20 μm
$b_{p,t}$	40-20 μm
$b_{p,b}$	20 μm
φ_p	11.31-0°
ϕ_{SHS}	0-0.5

This study was conducted by using the SHS-MFkMC model to capture whether or not a droplet of water on a given surface would transition to the Wenzel state for 49 different intrinsic contact angles between $70° \leq \theta_e \leq 130°$ for each of 25 different pillar surface structures categorized by $0\ \mu m \leq a_{p,t} \leq 20\ \mu m$ such that $0 \leq \phi_{SHS} \leq 0.5$. Note that the range of θ_e was chosen such that it captures the boundary between the metastable and unstable Cassie regimes for each surface pillar design. For each of these simulations, the SHS structure was initialized using the PU method according to the parameters listed in Table 7.8, as discussed in Section 7.1.4. Subsequently, SHS-MFkMC was used to evolve the surface behaviour over five independent simulations, and the vertical droplet spreading behaviour was recorded for each simulation. The results from these simulations where used to compute the average transition tendencies, i.e., whether or not the model predicted a C2W transition on average for each value of φ_p and θ_e. The results of this comparison are illustrated in Fig. 7.13, where the black line denote the transition region between surfaces that will undergo spontaneous C2W (in cyan) and those where the Cassie regime is stable (in dark blue). This figure illustrates that the SHS-MFkMC accurately predicts whether an SHS design will undergo spontaneous C2W, as it is able to accurately replicate the unstable Cassie regime boundary from the literature. Furthermore, the results from each of the aforementioned studies within this chapter highlight the strengths of the SHS-MFkMC algorithm compared to the other modelling methods commonly used to capture SHS behaviour. In particular, they highlight how the model can both depict the small-scale fluctuations in the interface and accommodate for microscale surface structures while still capturing the general macroscopic droplet spreading behaviour. Furthermore, they

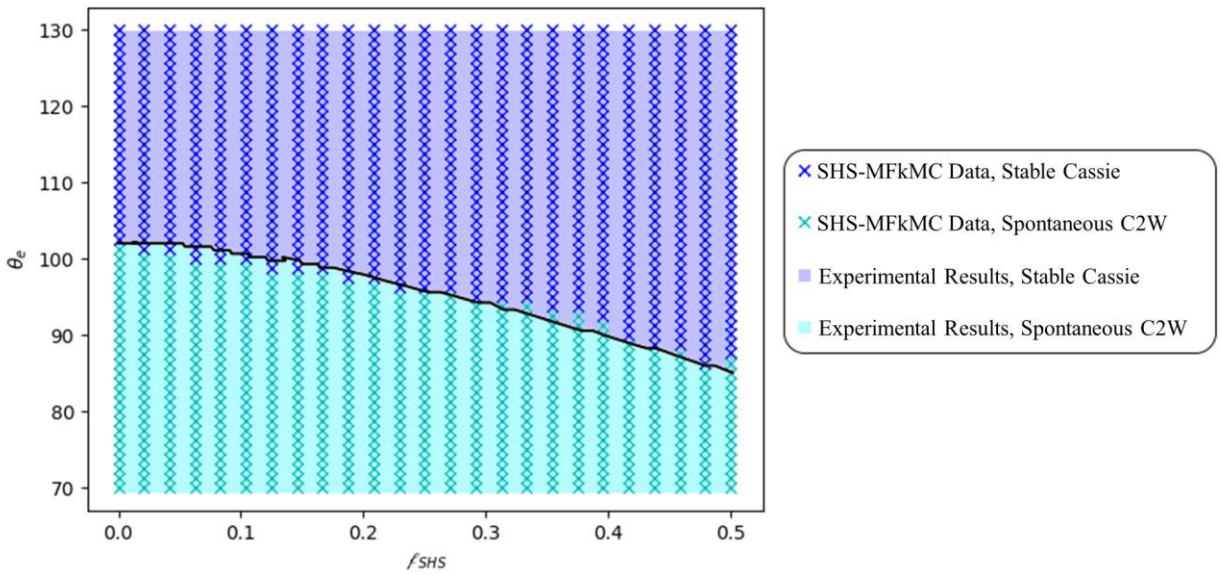

Figure 7.13: Spontaneous C2W transitions for pillars of different base angles φ_p (quantified based on the solid fraction parameter f_{SHS}) as a function of different intrinsic contact angles

illustrate the ability of the SHS-MFkMC to provide a force-based approach to assess the droplet behaviour on an SHS that is not prone to spurious interfacial force imbalances, unlike LB. Overall, these studies demonstrate the capability of the SHS-MFkMC model to capture sessile droplet spread and C2W transitions on a superhydrophobic surface.

One of the key strengths of developing a model to capture sessile droplet spread on an SHS is that the model can be readily used to assess the viability of different anti-wetting surface structures. As a result, the developed SHS-MFkMC model was used to provide analysis on the effects of the various SHS design parameters (i.e., H_p, $a_{p,t}$, φ_p, and $b_{p,t}$) on the sessile droplet behaviour. Furthermore, the model was used to evaluate the effects of the volume V and initial spreading velocity $v_{drop,0}$ of the droplet on its spreading and potential C2W transition behaviour. These studies were conducted by varying each of these parameters individually around a set of nominal conditions, as listed in Table 7.9. For each set of conditions, the SHS-MFkMC model was used to capture the transient spreading behaviour of each droplet as well as whether or not the droplet underwent C2W. The transient profiles obtained for each parameter are illustrated in Fig. 7.14. In addition, Table 7.10 lists each of the considered studies and showcases whether the system was predicted to undergo spontaneous C2W. Note that the current SHS-MFkMC model does not currently accommodate for Wenzel type wetting along the droplet surface. As a result, droplets that experience C2W in Fig. 7.14 are showcased as pinning at very low droplet radius values. This behaviour is not expected to occur in reality since the droplets are expected to continue spreading in the Wenzel state. However, the current focus of this study is not on the Wenzel regime but rather on the Cassie regime and on C2W transitions, and therefore Wenzel wetting

Table 7.9: Nominal SHS structure parameter and droplet property values used to assess the effects of each parameter on the sessile droplet behaviour

Parameter	Value
V	2.57 μL
$v_{drop,0}$	0.14 m/s
θ_e	95˚
H_p	27 μm
$a_{p,t}$, $a_{p,b}$	40 μm
$b_{p,t}$, $b_{p,b}$	40 μm
φ_p	0˚
v_{impact}	0.19 m/s

was not considered due to time restrictions and is left for future work. The results in Fig. 7.14 and Table 7.10 illustrate the importance that each of these parameters have on the SHS behaviour. As highlighted in Fig. 7.14a, the initial spreading velocity of the sessile droplet plays a critical role in designating whether the droplet will rebound off of the surface or will oscillate. As is expected, faster velocities lead to faster rebounding droplets that achieve larger maximum spreading before recoiling due to the larger Reynolds number Re, whereas slower velocities (i.e., smaller Re values) lead to smaller amplitude oscillations.[228] In addition, the droplet volume also impacts the oscillatory behaviour of a droplet on an SHS, as illustrated in Fig. 7.14b. In this figure, it is observed that larger droplets experience greater viscous damping (larger capillary number Ca values, smaller Re values), which when coupled with the increased size, leads to larger periods of oscillation as previously highlighted in Chapter 6. Larger droplets furthermore experience a larger maximum spreading amplitude due to their increased size, as would be expected. Fig. 7.14c illustrates that θ_e impacts the dynamic spreading behaviour of the surface. These results highlight that lower intrinsic contact angles result in fewer oscillations and less chances of the droplet rebounding off of the surface due to the more-hydrophilic nature of the pillar tops, as is expected. θ_e is additionally observed to impact whether or not a droplet will undergo spontaneous C2W for a given surface structure, with larger contact angles resulting in greater SHS stability, as previously illustrated in Fig. 7.13.[224]

Some of the most interesting sessile droplet behaviour can be observed by varying the dimensions of the SHS pillars. As illustrated in Fig. 7.14d, modifying the height of the pillars has minimal effect on the droplet average spreading behaviour. However, the height affects the likelihood that the droplet will undergo C2W transitions.[226] These results highlight that the droplet is expected to undergo C2W due to droplet sag when the

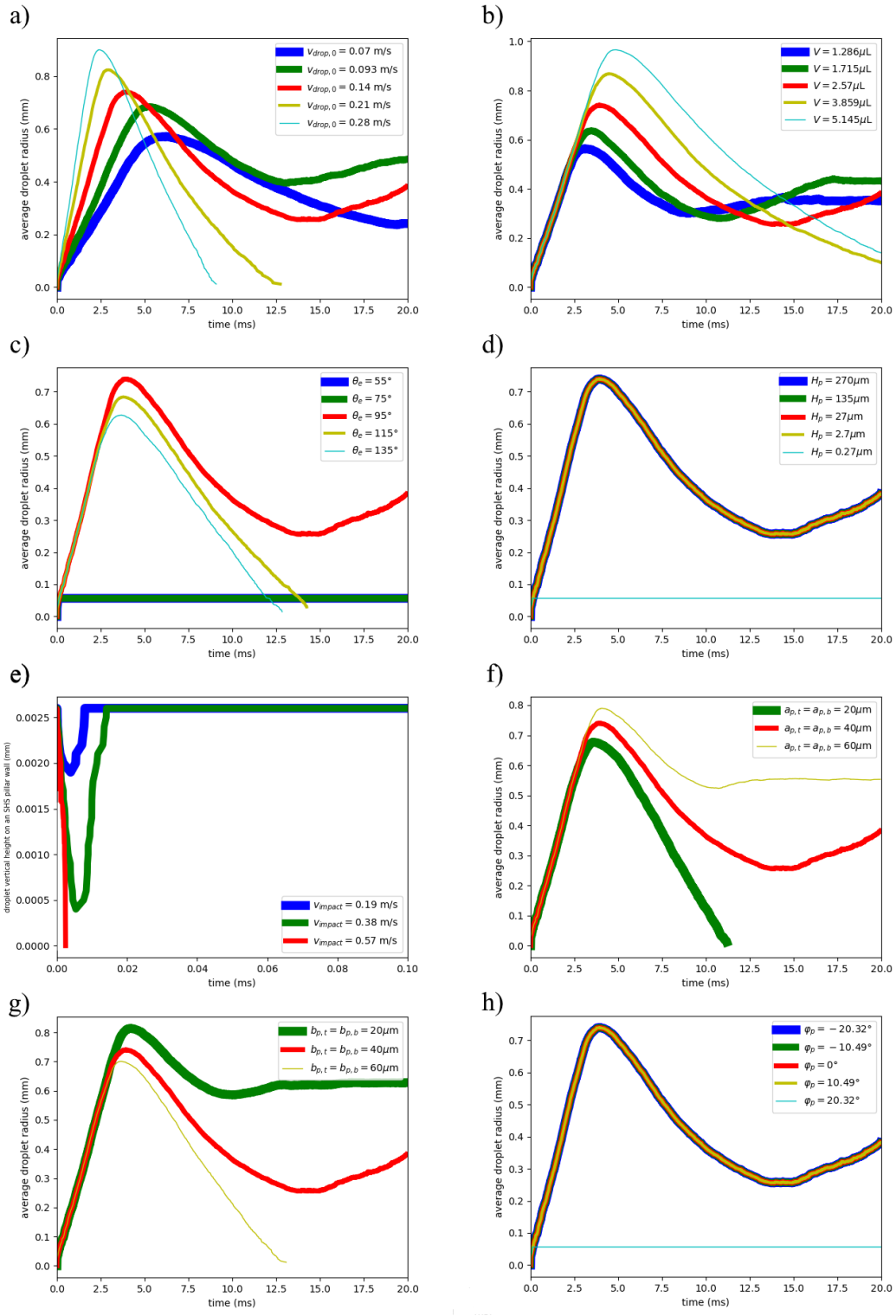

Figure 7.14: Variation in the spreading behaviour of water on various SHSs, according to variations: a) in $v_{drop,0}$; b) in V; c) in θ_e; d) in H_p; f) in $a_{p,t}$; g) in $b_{p,t}$; h) in φ_p; e) Vertical droplet height on the SHS wall for droplets of various v_{impact} and $H_p = 2.7$ μm

Table 7.10: Effects of SHS structure parameters and droplet property values on whether or not the SHS will undergo spontaneous C2W

Study		Spontaneous C2W?
Nominal		No
3a	$v_{drop,0} = 0.07$ m/s	No
	$v_{drop,0} = 0.093$ m/s	No
	$v_{drop,0} = 0.21$ m/s	No
	$v_{drop,0} = 0.28$ m/s	No
3b	$V = 1.286$ μL	No
	$V = 1.715$ μL	No
	$V = 3.859$ μL	No
	$V = 5.145$ μL	No
3c	$\theta_e = 55°$	Yes
	$\theta_e = 75°$	Yes
	$\theta_e = 115°$	No
	$\theta_e = 135°$	No
3d	$H_p = 270$ μm	No
	$H_p = 135$ μm	No
	$H_p = 2.7$ μm	No
	$H_p = 0.27$ μm	Yes
3e	$H_p = 2.7$ μm, $v_{impact} = 0.19$ m/s	No
	$H_p = 2.7$ μm, $v_{impact} = 0.38$ m/s	No
	$H_p = 2.7$ μm, $v_{impact} = 0.57$ m/s	Yes
3f	$a_{p,t} = 20$ μm	No
	$a_{p,t} = 60$ μm	No
3g	$b_{p,t} = 20$ μm	No
	$b_{p,t} = 60$ μm	No
3h	$\varphi_p = -20.32°$	No
	$\varphi_p = -10.49°$	No
	$\varphi_p = 10.49°$	No
	$\varphi_p = 20.32°$	Yes

pillar height is sufficiently small, i.e. $H_p = 0.27$ μm. Furthermore, the droplets are more likely to undergo C2W under sufficiently large inertial effects, as discussed previously. In order to illustrate this observation, Fig. 7.14e showcases the vertical droplet behaviour along the pillar walls for the $H_p = 2.7$ μm pillars subject to two different droplet impact velocities v_{impact}, as listed in Table 7.10. These results illustrate that the droplet will undergo spontaneous C2W due to the high inertia forces on pillars of sufficiently small height, as confirmed in previous studies.[229] Fig. 7.14f-g showcase the effects of the pillar width and the gap width on the sessile droplet spreading behaviour. Note that for the study in Fig. 7.14f, the pillar widths were modified by adjusting both $a_{p,t}$ and $a_{p,b}$ equally such that the pillar maintained a rectangular prism shape. Similarly, the gap width study in Fig. 7.14g was conducted by adjusting both $b_{p,t}$ and $b_{p,b}$ equally to prevent the formation of trapezoidal pillars. These figures highlight that modifying the width of the pillars and the gaps has a significant effect on the wettability of the SHS. In particular, larger width pillars and smaller gap widths lead to decreased superhydrophobic surface tendencies, as observed in the larger final contact radii within the figures. On the other hand, smaller pillar widths and larger pillar gaps significantly increase the superhydrophobicity and result in droplet rebound. These observations are in agreement with those found within the literature.[37,230] Additionally, Fig. 7.14h investigated the effects of the pillar side wall angle φ_p on the SHS behaviour. Note that these studies were conducted by modifying the base width of the pillars $a_{p,b}$, and therefore the widths of the pillar tops and their adjacent gaps remained the same for each case study. Consequently, the variation in φ_p did not significantly impact the Cassie regime spreading of the droplets. However, large positive φ_p angles were observed to significantly impact the likelihood of C2W due to the decreased apparent contact angle between the droplet sag and the pillar wall, as observed within the literature.[224] As a result, droplets on the surface with $\varphi_b = 20.32°$ were observed to undergo spontaneous C2W. These results overall illustrate the impact that a well-designed SHS can have on its superhydrophobic properties. Furthermore, this demonstrates the capacity of the SHS-MFkMC model to evaluate the wetting abilities of different surface designs. Consequently, this model has the potential to be readily used to determine the surface designs that maximize its superhydrophobic tendencies while preventing C2W transitions from occurring.

7.3 Summary

Superhydrophobic surfaces are important sessile droplet spreading applications responsible for creating self-cleaning and anti-fouling surface designs that are important for a variety of different engineering and materials applications. Furthermore, these surfaces are prone to deactivation by the detrimental C2W transition process and consequently there is significant demand to model and study droplet spread on these challenging textured surfaces. This chapter extended the previously-developed SHS-MFkMC algorithm to allow it to accommodate for SHS behaviour on surfaces containing periodic etched rectangular pillar structures. The proposed model was designed to accommodate for the repeating pillar structures using the proposed PU

method. Furthermore, it was modified to accommodate for the novel challenges and changes in the force balance necessary to capture Cassie mode droplet spreading. The model was additionally adjusted to accommodate for spontaneous C2W transitions due to vertical wall depinning and due to droplet sag. The model overall showcased that it was able to qualitatively replicate the Cassie droplet spreading behaviour observed within the literature on different SHS structures. The model additionally exhibited an excellent ability to predict whether a droplet would undergo spontaneous C2W. Furthermore, the model was used to evaluate the effects of various surface design parameters, as well as the droplet velocity and volume, on the sessile droplet spreading behaviour on an SHS. Overall, these results illustrated that the proposed SHS SHS-MFkMC model has the potential to serve as a highly predictive modelling tool for capturing droplet spread on an SHS. However, the model is still in need of further adjustments and modifications to allow it to quantitatively capture these systems as well as to accommodate for more advanced surface geometries. In addition, further work is necessary to allow the model to accommodate for other crucial droplet spreading and wetting transition phenomena such as hysteresis, Wenzel-state wetting, and the highly-desired W2C transitions. However, this chapter demonstrates the overall potential of SHS-MFkMC for capturing SHS wetting behaviour.

Chapter 8 – Conclusions & Future Work

8.1 Conclusions

This PhD thesis presented the development of the novel MFkMC method to capture the general behaviour of moving interface systems. This kMC-based methodology was particularly developed to provide a unique approach to capturing these dynamic interfaces that is not subject to the same disadvantages as the existing moving interface modelling methodologies. Although it has its own drawbacks, this method has overall showcased its competitive ability to mesoscopically capture moving interface behaviour and its capacity to incorporate additional important moving interface phenomena such as surface roughness. The newly developed MFkMC algorithm was used to analyze and study the dynamic interface behaviour within key systems in solids dissolution, axisymmetric capillary action, and sessile droplet spreading on both smooth and superhydrophobic surfaces. These studies showcased that MFkMC was able to macroscopically predict the expected application behaviour while simultaneously accommodating for the microscale phenomena. Furthermore, they highlighted how MFkMC was able to directly accommodate for the fundamental physics acting on the interface and can overcome any fictitious behaviour that occurred. The applications of MFkMC in all the studies below outlined the extensive utilization of this novel method to capture a wide variety of different solid- and fluid-based moving interface systems. Additionally, the case studies highlighted key insights into each of their individual processes that are outlined next.

The MFkMC algorithm was first-most adapted in Chapter 4 to capture the complete dissolution of 3D crystals within the human body. This study showcased that MFkMC can provide significant computational and memory advantages over standard kMC for sufficiently-large solid-based moving interface systems. Furthermore, the models were used to propagate uncertainty and perform robust optimization on the crystal dissolution behaviour due to uncertainties in key environmental system parameters. From these studies, it was observed that the expected changes in the system temperature only minimally impacted the dissolution behaviour. The variability in the pH, however, was predicted to induce significant deviations in the crystal dissolution process. These deviations were particularly observed to induce fluctuations over several orders of magnitude in the expected crystal dissolution behaviour. Furthermore, they were observed to introduce uncertainty as to whether the crystal would be completely dissolved, remain undissolved, or lie in a semi-dissolved state at a given point in time. The results from the robust optimization studies furthermore showcased that in order to maximize the crystal dissolution time while simultaneously minimizing the effects of uncertainty, it is necessary to use moderate-sized crystals of simple shapes containing lower ratios of the highly reactive kink and ledge sites. Overall, these results highlighted the need to account for environmental uncertainty when designing crystals for biological and drug delivery applications.

In order to further expand the applicability of the MFkMC approach, a method was developed to accommodate for the movement of fluid-fluid interfaces within the MFkMC framework in Chapter 5 based on the balance of forces acting upon the local interface. Subsequently, the developed FB-MFkMC framework was implemented to capture capillary rise within axisymmetric cavities of various shapes for both smooth and rough surfaces. These studies highlighted that the MFkMC approach provides a robust framework that can be readily modified to capture capillary action within cavities of any general shape. Furthermore, these results showcased that surface roughness critically impacts the movement of fluid-fluid interfaces along a solid surface. They furthermore showcased that roughened surfaces can cause a rising fluid undergoing capillary action to prematurely halt its ascent due to not having enough energy to overcome both gravitational forces and roughness asperities. These results demonstrated the importance of accommodating for molecular-level irregularities when designing systems subject to capillary action-driven transport. Furthermore, these analyses can be extended to discuss how surface roughness can critically affect the movement of any fluid-fluid interface along a solid surface.

In Chapter 6, the FB-MFkMC algorithm previously developed for capillary rise was modified to capture sessile droplet spread on an ideally flat surface. This model utilized a comprehensive semi-empirical force balance equation developed specifically to capture the fundamental balance of forces governing the droplet spreading process. The proposed balance consisted of a semi-empirical expression to accommodate for the viscous damping force that is subject to a fitted empirical parameter whose value is determined based on the droplet liquid's Ohnesorge number. The results from this study highlighted that the viscous damping force affecting a sessile droplet is dependent on the droplet fluid properties as well as the droplet interface velocity. The fully-assembled FB-MFkMC model was additionally observed to predict the sessile droplet spreading behaviour regardless of the droplet size, shape, composition, solid surface material, or Reynolds and Capillary number values. Overall, this study highlighted the dependence of the droplet spread on the different forces acting upon its interface. Furthermore, the study highlighted the necessity to try and capture these underlying forces as accurately as possible not just for MFkMC simulations but to better understand the general droplet spreading behaviour.

In Chapter 7, the newly established FB-MFkMC algorithm was extended into the SHS-MFkMC method in order to capture Cassie regime droplet spreading and spontaneous C2W transitions on superhydrophobic surfaces. This model was furthermore used to demonstrate the significant effects that surface roughness structures play on the wettability of a surface. These results highlighted that the hydrophobicity of a surface can be increased by using smaller pillars surrounded by larger air gaps. However, too large a gap was also observed to result in C2W transitions. These transitions could be mitigated by using sharper-angled pillar walls and by using taller pillar structures. The SHS-MFkMC model furthermore demonstrated its capability to predict the wetting and superhydrophobicity properties of a given surface design. This model additionally has the

capacity to be upgraded to accommodate for molecular-level asperities such as surface roughness and can therefore serve as a unique tool for capturing the entire wetting and dynamic spreading abilities of a sessile droplet on a realistically-rough SHS. However, further work is required to allow for the model to attain this ambition. Overall, these results highlighted the importance of SHS design on their wettability and showcased the general structure designs necessary to achieve ideal wetting properties.

In summary, the studies conducted in this work overall showcased the potential of the MFkMC algorithm and its ability to capture moving interface system behaviour. In addition, the results presented herein demonstrated that with proper model design, MFkMC has the potential to efficiently evolve moving interface systems on the molecular and microscale levels over the large-scale length and timescales associated with moving interfaces. Consequently, this method offers a bridge between computationally-expensive microscale simulations such as Molecular Dynamics and the continuum-based modelling techniques that struggle to accommodate for molecular-level behaviour. Furthermore, the studies highlighted how MFkMC can be readily modified and customized to accommodate for additional system features, such as surface roughness and non-flat surface geometries. Overall, the case study results demonstrated the general ability of MFkMC to capture the behaviour of moving interface systems.

8.2 Future Work

The results and interpretations drawn from this study can serve as a foundation for developing future research in this critical field of research. As a result, this work suggests the following avenues to further extend this research in the future.

- *Incorporate Surface Roughness into Sessile Droplet Models for both Smooth and Superhydrophobic Surfaces.* Both sessile droplet MFkMC models developed in this work assumed that the surfaces were molecularly smooth and not subject to any nanoscale roughness. As a result, both models were observed to deviate from the experimentally-predicted sessile droplet behaviour. This assumption is particularly detrimental to capturing droplet spread on an SHS, since the manufactured pillars are expected to contain significant aberrations that can significantly impact the observed spreading behaviour.[223] Furthermore, the addition of surface roughness is furthermore expected to impact the apparent (macroscopic) contact angle of a droplet, giving rise to the advancing and receding contact angles observed experimentally. Therefore, spatially-varying roughness should be integrated into both models based on real surface roughness profiles and pillar shape aberrations to allow for more realistic simulations of droplet spreading, including measurements for the advancing and receding contact angles, on both ideal surfaces and SHSs.
- *Expand the SHS Model to Accommodate for Wenzel-state Wetting and W2C Transitions*. The present MFkMC-based SHS droplet spread model does not accommodate for the continued droplet dynamics

once the droplet enters a Wenzel wetting state, and therefore it cannot accommodate for the inverse Wenzel-to-Cassie transition. Therefore, in order to capture the full range of expected sessile droplet spreading behaviour on an SHS, the SHS-MFkMC model should be extended to incorporate for Wenzel wetting and simulate the droplet spreading behaviour after undergoing W2C. These models can be subsequently used to determine the SHS structures that are unstable in the Wenzel regime and therefore will spontaneously undergo W2C.

- *Expand the SHS Model to Accommodate for Different Pillar Shapes.* There are a wide variety of different pillar shapes, in addition to rectangular pillars, that are used in the design of SHSs. These include SHSs designed with cylindrical and mushroom-shaped (double re-entrant) pillars, as well as other types of roughness asperities such as nanowires or spherical particles. In order to better accommodate for a wider variety of SHS designs, the SHS MFkMC method should be updated to be customizable for any specified pillar shape. In particular, the PU and droplet sag calculation methods should be generalized so that they can be readily adapted to any given pillar shape.
- *Development of a Non-Axisymmetric Rough Capillary Action MFkMC Model*. The capillary rise applications considered within this work were performed using an axisymmetric model, where it was assumed that the cavity and the fluid behaviour within the cavity would be radially uniform. However, this assumption is not always applicable. Capillary action frequently occurs in non-axisymmetric cavities, as illustrated while accommodating for C2W transitions in the SHS MFkMC model in Chapter 7. Furthermore, it is unlikely that the roughness profiles within a cavity would be radially uniform. In order to showcase the widespread applicability of the capillary action MFkMC algorithm, this model should be extended into a full 3D model to accommodate for capillary rise/fall in cavities of any shape. This model should be furthermore coupled together with spatially-varying roughness profiles based on real cavity roughness data in order to provide a superior representation of the effects of surface roughness on the capillary action process.
- *Development of Machine Learning-based Models to Efficiently Capture SHS Sessile Droplet Spreading.* One of the key objectives in studying SHS design is to determine surface structures that are capable of minimizing droplet wettability. This can be readily achieved through the use of rigorous model-based optimization studies as long as there is a detailed system model such as the SHS-MFkMC model. However, these optimization studies often require extensive model sampling, and thus can be computationally-intensive for detailed mechanistic models. This issue can be overcome through the use of machine learning techniques such as artificial neural networks. These processes have emerged as an efficient yet accurate means of predicting the relationship between a system's key observables and its inputs, regardless of noise or non-linearity. Consequently, they could provide an excellent means to optimize SHS surface designs. Therefore, the SHS-MFkMC model should be used to train deep neural

networks to capture key characteristic wetting parameters for a given SHS (e.g., its maximum contact radius, contact angle, and Cassie state stability) as a function of the surface structures that may emerge in novel anti-wetting, anti-biocontamination, and environmentally-friendly applications.[34,35,231] These trained networks can be subsequently used to perform rapid and efficient model-based optimization to predict the SHS designs that maximize its hydrophobicity and that prevent C2W transitions.

- *Integration of FB-MFkMC Model into Multiscale Frameworks for Extended Applications.* The proposed FB-MFkMC algorithm was developed to capture sessile droplet spread under ideal conditions and in the absence of external forces or additional phenomena taking place. However, the model can be readily adapted to accommodate for these kinds of processes by coupling it with additional modelling methods, such as CFD, that capture the additional phenomena. When FB-MFkMC is coupled with CFD models, the location of the CFD boundary conditions can be continuously modified based on the droplet shape and size as captured by the FB-MFkMC formulation. Furthermore, the influence of the CFD models on the droplet interface would be accommodated through the force balance term. This FB-MFkMC-based multiscale modelling approach could be used to solve for a wide variety of different advanced moving interface applications, such as solid particulate deposition on a surface via evaporating sessile droplet. The latter approach could also be used to study advanced deposition challenges such as the coffee ring effect.
- *Development of Crystal Dissolution MFkMC Model to Study the Dissolution of Commonly-Manufactured Crystal Shapes and to Capture Practical Pharmaceutical Drug Delivery Applications.* Calcium Carbonate nanoparticles have been increasingly studied as a biocompatible carrier for pharmaceutical drug delivery. In these applications, the desired objective is to achieve controlled release of a given active substance within the human body by controlling the dissolution of the $CaCO_3$. In a practical pharmaceutical drug delivery scenario, the desired $CaCO_3$ nanoparticles should have a highly porous vaterite structure in order to maximize the amount of substance loaded within the crystal.[232] Furthermore, typical fabrication processes for a given crystal material do not produce a wide variety of different geometric shapes but rather produce solids whose shape is best quantified based on the ratio of heights of the individual crystal faces.[98,102] Therefore, the method should be extended to capture the dissolution of porous vaterite $CaCO_3$ nanoparticles loaded with the desired active materials. Furthermore, it is recommended to adapt the MFkMC crystal dissolution model to accommodate for the expected manufactured crystal shapes. Finally, it is recommended to adapt the uncertainty propagation study to include uncertainty and variability in both the crystal shape and size and analyze how these will affect the dissolution performance for drug delivery applications.

Letter of Copyright Permission

Reprinted and adapted with permission from (Chaffart, D. et al. "A Moving Front Kinetic Monte Carlo Algorithm for Moving Interface Systems." The Journal of Physical Chemistry B (2022)). Copyright (2022) American Chemical Society.

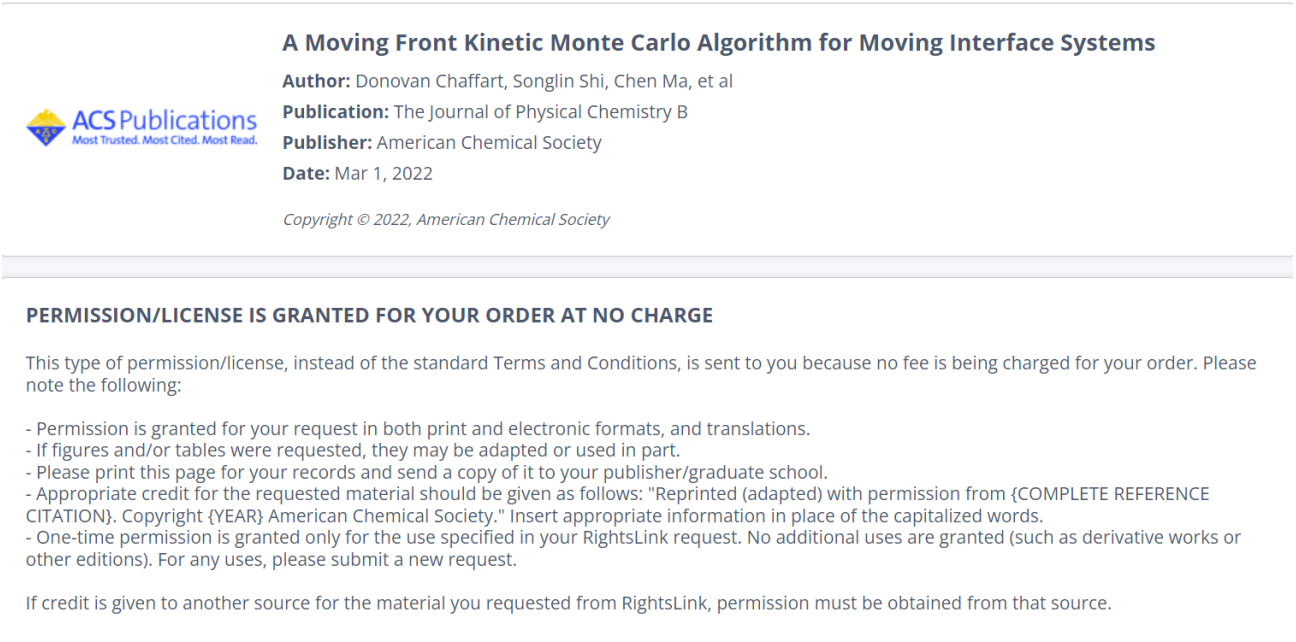

A Moving Front Kinetic Monte Carlo Algorithm for Moving Interface Systems

Author: Donovan Chaffart, Songlin Shi, Chen Ma, et al
Publication: The Journal of Physical Chemistry B
Publisher: American Chemical Society
Date: Mar 1, 2022

Copyright © 2022, American Chemical Society

PERMISSION/LICENSE IS GRANTED FOR YOUR ORDER AT NO CHARGE

This type of permission/license, instead of the standard Terms and Conditions, is sent to you because no fee is being charged for your order. Please note the following:

- Permission is granted for your request in both print and electronic formats, and translations.
- If figures and/or tables were requested, they may be adapted or used in part.
- Please print this page for your records and send a copy of it to your publisher/graduate school.
- Appropriate credit for the requested material should be given as follows: "Reprinted (adapted) with permission from {COMPLETE REFERENCE CITATION}. Copyright {YEAR} American Chemical Society." Insert appropriate information in place of the capitalized words.
- One-time permission is granted only for the use specified in your RightsLink request. No additional uses are granted (such as derivative works or other editions). For any uses, please submit a new request.

If credit is given to another source for the material you requested from RightsLink, permission must be obtained from that source.

References

[1] J.T. Davies, *Interfacial Phenomena* (Elsevier, 2012).

[2] R.C. Brower, D.A. Kessler, J. Koplik, and H. Levine, "Geometrical approach to moving-interface dynamics," Phys. Rev. Lett. **51**(13), 1111–1114 (1983).

[3] S. Adjerid, N. Chaabane, T. Lin, and P. Yue, "An immersed discontinuous finite element method for the Stokes problem with a moving interface," J. Comput. Appl. Math. **362**, 540–559 (2019).

[4] T.Y. Hou, Z. Li, S. Osher, and H. Zhao, "A hybrid method for moving interface problems with application to the Hele–Shaw flow," J. Comput. Phys. **134**(2), 236–252 (1997).

[5] M. Moog, R. Keck, and A. Zemitis, "SOME NUMERICAL ASPECTS OF THE LEVEL SET METHOD," Math. Model. Anal. **3**(1), 140–151 (1998).

[6] F.S. de Sousa, N. Mangiavacchi, L.G. Nonato, A. Castelo, M.F. Tomé, V.G. Ferreira, J.A. Cuminato, and S. McKee, "A front-tracking/front-capturing method for the simulation of 3D multi-fluid flows with free surfaces," J. Comput. Phys. **198**(2), 469–499 (2004).

[7] A.F. Voter, in *Radiat. Eff. Solids* (Springer, Dordrecht, Netherlands, 2007), pp. 1–23.

[8] A. Dupuis, and J.M. Yeomans, "Modeling Droplets on Superhydrophobic Surfaces: Equilibrium States and Transitions," Langmuir **21**(6), 2624–2629 (2005).

[9] Z. Guo, C. Zheng, and B. Shi, "Force imbalance in lattice Boltzmann equation for two-phase flows," Phys. Rev. E **83**(3), 036707 (2011).

[10] C.W. Extrand, "Contact Angles and Hysteresis on Surfaces with Chemically Heterogeneous Islands," Langmuir **19**(9), 3793–3796 (2003).

[11] J. Sang-Il Kwon, M. Nayhouse, G. Orkoulas, and P.D. Christofides, "Crystal shape and size control using a plug flow crystallization configuration," Chem. Eng. Sci. **119**, 30–39 (2014).

[12] I. Kurganskaya, and A. Lüttge, "Kinetic Monte Carlo approach to study carbonate dissolution," J. Phys. Chem. C **120**(12), 6482–6492 (2016).

[13] S. Rasoulian, and L.A. Ricardez-Sandoval, "Uncertainty analysis and robust optimization of multiscale process systems with application to epitaxial thin film growth," Chem. Eng. Sci. **116**, 590–600 (2014).

[14] V. Alvarez, and M. Paulis, "Effect of acrylic binder type and calcium carbonate filler amount on the properties of paint-like blends," Prog. Org. Coat. **112**, 210–218 (2017).

[15] T. Matschei, B. Lothenbach, and F.P. Glasser, "The role of calcium carbonate in cement hydration," Cem. Concr. Res. **37**(4), 551–558 (2007).

[16] B.B. Hanshaw, and W. Back, "Chemical mass-wasting of the northern Yucatan Peninsula by groundwater dissolution," Geology **8**(5), 222–224 (1980).

[17] G. Tanski, N. Couture, H. Lantuit, A. Eulenburg, and M. Fritz, "Eroding permafrost coasts release low amounts of dissolved organic carbon (DOC) from ground ice into the nearshore zone of the Arctic Ocean," Glob. Biogeochem. Cycles **30**(7), 1054–1068 (2016).

[18] G. Daculsi, R.Z. LeGeros, and D. Mitre, "Crystal dissolution of biological and ceramic apatites," Calcif. Tissue Int. **45**(2), 95–103 (1989).

[19] G. Daculsi, "Biphasic calcium phosphate concept applied to artificial bone, implant coating and injectable bone substitute," Biomaterials **19**(16), 1473–1478 (1998).

[20] U.S. Department of Health and Human Services Food and Drug Administration, *Q8(R2) Pharmaceutical Development* (Silver Spring, MD, 2009).

[21] Y. Zhang, and Z. Xu, "Kinetics of convective crystal dissolution and melting, with applications to methane hydrate dissolution and dissociation in seawater," Earth Planet. Sci. Lett. **213**(1), 133–148 (2003).
[22] L.N. PLUMMER, D.L. PARKHURST, and T.M.L. WIGLEY, in *Chem. Model. Aqueous Syst.* (AMERICAN CHEMICAL SOCIETY, 1979), pp. 537–573.
[23] D. Chaffart, S. Shi, C. Ma, C. Lv, and L.A. Ricardez-Sandoval, "A Moving Front Kinetic Monte Carlo Algorithm for Moving Interface Systems," J. Phys. Chem. B **126**(9), 2040–2059 (2022).
[24] N.R. Morrow, and X. Xie, "Oil recovery by spontaneous imbibition from weakly water-wet rocks," Petrophysics - SPWLA J. Form. Eval. Reserv. Descr. **42**(04), (2001).
[25] L. Gervais, M. Hitzbleck, and E. Delamarche, "Capillary-driven multiparametric microfluidic chips for one-step immunoassays," Biosens. Bioelectron. **27**(1), 64–70 (2011).
[26] S.W. Chi, *Heat Pipe Theory and Practice* (1976).
[27] E. Schäffer, and P. Wong, "Contact line dynamics near the pinning threshold: A capillary rise and fall experiment," Phys. Rev. E **61**(5), 5257–5277 (2000).
[28] F. Caupin, M.W. Cole, S. Balibar, and J. Treiner, "Absolute limit for the capillary rise of a fluid," EPL **82**(5), 56004 (2008).
[29] P.-G. de Gennes, F. Brochard-Wyart, and D. Quere, *Capillarity and Wetting Phenomena: Drops, Bubbles, Pearls, Waves* (Springer Science & Business Media, 2013).
[30] Y. Li, D. Quéré, C. Lv, and Q. Zheng, "Monostable superrepellent materials," Proc. Natl. Acad. Sci. **114**(13), 3387–3392 (2017).
[31] C. Lv, P. Hao, X. Zhang, and F. He, "Dewetting transitions of dropwise condensation on nanotexture-enhanced superhydrophobic surfaces," ACS Nano **9**(12), 12311–12319 (2015).
[32] H. Wijshoff, "Drop dynamics in the inkjet printing process," Curr. Opin. Colloid Interface Sci. **36**, 20–27 (2018).
[33] S. Shi, C. Lv, and Q. Zheng, "Drop Impact on Two-Tier Monostable Superrepellent Surfaces," ACS Appl. Mater. Interfaces **11**(46), 43698–43707 (2019).
[34] M. Salta, J.A. Wharton, P. Stoodley, S.P. Dennington, L.R. Goodes, S. Werwinski, U. Mart, R.J.K. Wood, and K.R. Stokes, "Designing biomimetic antifouling surfaces," Philos. Trans. R. Soc. Math. Phys. Eng. Sci. **368**(1929), 4729–4754 (2010).
[35] M. Cao, D. Guo, C. Yu, K. Li, M. Liu, and L. Jiang, "Water-Repellent Properties of Superhydrophobic and Lubricant-Infused 'Slippery' Surfaces: A Brief Study on the Functions and Applications," ACS Appl. Mater. Interfaces **8**(6), 3615–3623 (2016).
[36] P. Papadopoulos, L. Mammen, X. Deng, D. Vollmer, and H.-J. Butt, "How superhydrophobicity breaks down," Proc. Natl. Acad. Sci. **110**(9), 3254–3258 (2013).
[37] Y. Li, D. Quéré, C. Lv, and Q. Zheng, "Monostable superrepellent materials," Proc. Natl. Acad. Sci. **114**(13), 3387–3392 (2017).
[38] T. Mouterde, G. Lehoucq, S. Xavier, A. Checco, C.T. Black, A. Rahman, T. Midavaine, C. Clanet, and D. Quéré, "Antifogging abilities of model nanotextures," Nat. Mater. **16**(6), 658–663 (2017).
[39] S. Prakash, E. Xi, and A.J. Patel, "Spontaneous recovery of superhydrophobicity on nanotextured surfaces," Proc. Natl. Acad. Sci. **113**(20), 5508–5513 (2016).
[40] C. Zhu, Y. Gao, Y. Huang, H. Li, S. Meng, J.S. Francisco, and X.C. Zeng, "Controlling states of water droplets on nanostructured surfaces by design," Nanoscale **9**(46), 18240–18245 (2017).

[41] J. Wang, S. Chen, and D. Chen, “Spontaneous transition of a water droplet from the Wenzel state to the Cassie state: a molecular dynamics simulation study,” Phys. Chem. Chem. Phys. **17**(45), 30533–30539 (2015).

[42] D. Chaffart, and L.A. Ricardez-Sandoval, “A three dimensional kinetic Monte Carlo defect-free crystal dissolution model for biological systems, with application to uncertainty analysis and robust optimization,” Comput. Chem. Eng. **157**, 107586 (2022).

[43] D. Chaffart, S.(史松林) Shi, C.(马晨) Ma, C.(吕存景) Lv, and L.A. Ricardez-Sandoval, “A semi-empirical force balance-based model to capture sessile droplet spread on smooth surfaces: A moving front kinetic Monte Carlo study,” Phys. Fluids **35**(3), 032109 (2023).

[44] B.Q. Li, editor , in *Discontinuous Finite Elem. Fluid Dyn. Heat Transf.* (Springer, London, 2006), pp. 429–500.

[45] H.S. Udaykumar, W. Shyy, and M.M. Rao, “Elafint: A Mixed Eulerian–Lagrangian Method for Fluid Flows with Complex and Moving Boundaries,” Int. J. Numer. Methods Fluids **22**(8), 691–712 (1996).

[46] E.-I. Hanzawa, “CLASSICAL SOLUTIONS OF THE STEFAN PROBLEM,” Tohoku Math. J. Second Ser. **33**(3), 297–335 (1981).

[47] L.M. Hocking, “A moving fluid interface on a rough surface,” J. Fluid Mech. **76**(4), 801–817 (1976).

[48] C. Cuchiero, C. Reisinger, and S. Rigger, “Optimal bailout strategies resulting from the drift controlled supercooled Stefan problem,” (2022).

[49] E. Hadjittofis, S.C. Das, G.G.Z. Zhang, and J.Y.Y. Heng, in *Dev. Solid Oral Dos. Forms*, Second Edition (Elsevier Inc, 2017), pp. 225–252.

[50] J.P. Shopple, An Interface-Fitted Finite Element Based Level Set Method : Algorithm, Implementation, Analysis and Applications, UC San Diego, 2009.

[51] S. Quan, and D.P. Schmidt, “A moving mesh interface tracking method for 3D incompressible two-phase flows,” J. Comput. Phys. **221**(2), 761–780 (2007).

[52] L.I. Rubinšteĭn, *The Stefan Problem* (American Mathematical Soc., 2000).

[53] J.M. Hyman, “Numerical methods for tracking interfaces,” Phys. Nonlinear Phenom. **12**(1), 396–407 (1984).

[54] J.A. Sethian, *Level Set Methods and Fast Marching Methods: Evolving Interfaces in Computational Geometry, Fluid Mechanics, Computer Vision, and Materials Science* (Cambridge University Press, 1999).

[55] L. Tan, and N. Zabaras, “A level set simulation of dendritic solidification with combined features of front-tracking and fixed-domain methods,” J. Comput. Phys. **211**(1), 36–63 (2006).

[56] D. Gründing, “An enhanced model for the capillary rise problem,” Int. J. Multiph. Flow **128**, 103210 (2020).

[57] D. Gründing, M. Smuda, T. Antritter, M. Fricke, D. Rettenmaier, F. Kummer, P. Stephan, H. Marschall, and D. Bothe, “A comparative study of transient capillary rise using direct numerical simulations,” Appl. Math. Model. **86**, 142–165 (2020).

[58] H. Ding, and P.D.M. Spelt, “Inertial effects in droplet spreading: a comparison between diffuse-interface and level-set simulations,” J. Fluid Mech. **576**, 287–296 (2007).

[59] D.C. Rapaport, and R. Rapaport Dennis C., *The Art of Molecular Dynamics Simulation* (Cambridge University Press, 2004).

[60] S.A. Hollingsworth, and R.O. Dror, "Molecular Dynamics Simulation for All," Neuron **99**(6), 1129–1143 (2018).
[61] N.H. de Leeuw, S.C. Parker, and J.H. Harding, "Molecular dynamics simulation of crystal dissolution from calcite steps," Phys. Rev. B **60**(19), 13792–13799 (1999).
[62] D.I. Dimitrov, A. Milchev, and K. Binder, "Capillary rise in nanopores: Molecular Dynamics evidence for the Lucas-Washburn equation," Phys. Rev. Lett. **99**(5), 054501 (2007).
[63] P. Raiskinmäki, A. Shakib-Manesh, A. Jäsberg, A. Koponen, J. Merikoski, and J. Timonen, "Lattice-Boltzmann simulation of capillary rise dynamics," J. Stat. Phys. **107**(1), 143–158 (2002).
[64] Y.Y. Yan, and Y.Q. Zu, "A lattice Boltzmann method for incompressible two-phase flows on partial wetting surface with large density ratio," J. Comput. Phys. **227**(1), 763–775 (2007).
[65] H. Kusumaatmaja, and J.M. Yeomans, "Modeling Contact Angle Hysteresis on Chemically Patterned and Superhydrophobic Surfaces," Langmuir **23**(11), 6019–6032 (2007).
[66] W.-Z. Yuan, and L.-Z. Zhang, "Lattice Boltzmann Simulation of Droplets Impacting on Superhydrophobic Surfaces with Randomly Distributed Rough Structures," Langmuir **33**(3), 820–829 (2017).
[67] A.P.J. Jansen, *An Introduction to Kinetic Monte Carlo Simulations of Surface Reactions* (Springer, 2012).
[68] D.T. Gillespie, "A general method for numerically simulating the stochastic time evolution of coupled chemical reactions," J. Comput. Phys. **22**(4), 403–434 (1976).
[69] M.A. Katsoulakis, and D.G. Vlachos, "Coarse-grained stochastic processes and kinetic Monte Carlo simulators for the diffusion of interacting particles," J. Chem. Phys. **119**(18), 9412–9427 (2003).
[70] I. Martin-Bragado, A. Rivera, G. Valles, J.L. Gomez-Selles, and M.J. Caturla, "MMonCa: An Object Kinetic Monte Carlo simulator for damage irradiation evolution and defect diffusion," Comput. Phys. Commun. **184**(12), 2703–2710 (2013).
[71] C. Domain, C.S. Becquart, and L. Malerba, "Simulation of radiation damage in Fe alloys: an object kinetic Monte Carlo approach," J. Nucl. Mater. **335**(1), 121–145 (2004).
[72] J.S.-I. Kwon, M. Nayhouse, P.D. Christofides, and G. Orkoulas, "Modeling and control of protein crystal shape and size in batch crystallization," AIChE J. **59**(7), 2317–2327 (2013).
[73] M. Nayhouse, A. Tran, J.S.-I. Kwon, M. Crose, G. Orkoulas, and P.D. Christofides, "Modeling and control of ibuprofen crystal growth and size distribution," Chem. Eng. Sci. **134**, 414–422 (2015).
[74] S. Rasoulian, and L.A. Ricardez-Sandoval, "Stochastic nonlinear model predictive control applied to a thin film deposition process under uncertainty," Chem. Eng. Sci. **140**, 90–103 (2016).
[75] Y. Lou, and P.D. Christofides, "Estimation and control of surface roughness in thin film growth using kinetic Monte-Carlo models," Chem. Eng. Sci. **58**(14), 3115–3129 (2003).
[76] G. Kimaev, and L.A. Ricardez-Sandoval, "Multilevel Monte Carlo for noise estimation in stochastic multiscale systems," Chem. Eng. Res. Des. **140**, 33–43 (2018).
[77] N. Sitapure, T.H. Kwon, M. Lee, B. Kim, M.S. Kang, and J. Kwon, "Modeling ligand crosslinking for interlocking quantum dots in thin-films," J. Mater. Chem. C **10**(18), 7132–7140 (2022).
[78] S. Rasoulian, and L.A. Ricardez-Sandoval, "A robust nonlinear model predictive controller for a multiscale thin film deposition process," Chem. Eng. Sci. **136**, 38–49 (2015).
[79] B. Wehrli, "Monte Carlo simulations of surface morphologies during mineral dissolution," J. Colloid Interface Sci. **132**(1), 230–242 (1989).
[80] J.M. McCoy, and J.P. LaFemina, "Kinetic Monte Carlo investigation of pit formation at the $CaCO_3(10\bar{1}4)$ surface-water interface," Surf. Sci. **373**(2), 288–299 (1997).

[81] R.E. Williford, D.R. Baer, J.E. Amonette, and A.S. Lea, "Dissolution and growth of (10$\bar{1}$4) calcite in flowing water: estimation of back reaction rates via kinetic Monte Carlo simulations," J. Cryst. Growth **262**(1), 503–518 (2004).

[82] N. Sitapure, T. Qiao, D.H. Son, and J.S.-I. Kwon, "Kinetic Monte Carlo modeling of the equilibrium-based size control of CsPbBr3 perovskite quantum dots in strongly confined regime," Comput. Chem. Eng. **139**, 106872 (2020).

[83] N. Sitapure, R. Epps, M. Abolhasani, and J.S.-I. Kwon, "Multiscale modeling and optimal operation of millifluidic synthesis of perovskite quantum dots: Towards size-controlled continuous manufacturing," Chem. Eng. J. **413**, 127905 (2021).

[84] H. Lee, N. Sitapure, S. Hwang, and J.S.-I. Kwon, "Multiscale modeling of dendrite formation in lithium-ion batteries," Comput. Chem. Eng. **153**, 107415 (2021).

[85] N. Sitapure, H. Lee, F. Ospina-Acevedo, P.B. Balbuena, S. Hwang, and J.S.-I. Kwon, "A computational approach to characterize formation of a passivation layer in lithium metal anodes," AIChE J. **67**(1), e17073 (2021).

[86] S. Pahari, J. Kim, H.-K. Choi, M. Zhang, A. Ji, C.G. Yoo, and J.S.-I. Kwon, "Multiscale kinetic modeling of biomass fractionation in an experiment: Understanding individual reaction mechanisms and cellulose degradation," Chem. Eng. J. **467**, 143021 (2023).

[87] H.-K. Choi, and J.S.-I. Kwon, "Multiscale modeling and multiobjective control of wood fiber morphology in batch pulp digester," AIChE J. **66**(7), e16972 (2020).

[88] H.-K. Choi, and J.S.-I. Kwon, "Modeling and control of cell wall thickness in batch delignification," Comput. Chem. Eng. **128**, 512–523 (2019).

[89] J. Jung, H.-K. Choi, S.H. Son, J.S.-I. Kwon, and J.H. Lee, "Multiscale modeling of fiber deformation: Application to a batch pulp digester for model predictive control of fiber strength," Comput. Chem. Eng. **158**, 107640 (2022).

[90] I. Kurganskaya, and A. Luttge, "Kinetic Monte Carlo Approach To Study Carbonate Dissolution," J. Phys. Chem. C **120**(12), 6482–6492 (2016).

[91] O. Pierre-Louis, and Y. Saito, "Wetting of solid islands on parallel nano-grooves," EPL Europhys. Lett. **86**(4), 46004 (2009).

[92] A. Al-Kattan, F. Errassifi, A.-M. Sautereau, S. Sarda, P. Dufour, A. Barroug, I.D. Santos, C. Combes, D. Grossin, C. Rey, and C. Drouet, "Medical Potentialities of Biomimetic Apatites through Adsorption, Ionic Substitution, and Mineral/Organic Associations: Three Illustrative Examples," Adv. Eng. Mater. **12**(7), B224–B233 (2010).

[93] R.V. Raspopov, É.N. Trushina, I.V. Gmoshinskiĭ, and S.A. Khotimchenko, "Bioavailability of nanoparticles of ferric oxide when used in nutrition. Experimental results in rats," Vopr. Pitan. **80**(3), 25–30 (2011).

[94] L. Wang, J. Barton, L. Hughes, and T.W. Odom, "Shape-Control of Protein Crystals in Patterned Microwells," J. Am. Chem. Soc. **130**(7), 2142–2143 (2008).

[95] G. Yang, N. Kubota, Z. Sha, M. Louhi-Kultanen, and J. Wang, "Crystal Shape Control by Manipulating Supersaturation in Batch Cooling Crystallization," Cryst. Growth Des. **6**(12), 2799–2803 (2006).

[96] M.B. Zimmermann, and F.M. Hilty, "Nanocompounds of iron and zinc: their potential in nutrition," Nanoscale **3**(6), 2390–2398 (2011).

[97] Q. Su, Z.K. Nagy, and C.D. Rielly, "Pharmaceutical crystallisation processes from batch to continuous operation using MSMPR stages: Modelling, design, and control," Chem. Eng. Process. Process Intensif. **89**, 41–53 (2015).

[98] M. Nayhouse, J. Sang-Il Kwon, P.D. Christofides, and G. Orkoulas, "Crystal shape modeling and control in protein crystal growth," Chem. Eng. Sci. **87**, 216–223 (2013).
[99] J.A. Kimber, S.G. Kazarian, and F. Štěpánek, "Modelling of pharmaceutical tablet swelling and dissolution using discrete element method," Chem. Eng. Sci. **69**(1), 394–403 (2012).
[100] J.S.-I. Kwon, M. Nayhouse, and P.D. Christofides, "Multiscale, Multidomain Modeling and Parallel Computation: Application to Crystal Shape Evolution in Crystallization," Ind. Eng. Chem. Res. **54**(47), 11903–11914 (2015).
[101] J.S.-I. Kwon, M. Nayhouse, P.D. Christofides, and G. Orkoulas, "Protein Crystal Shape and Size Control in Batch Crystallization: Comparing Model Predictive Control with Conventional Operating Policies," Ind. Eng. Chem. Res. **53**(13), 5002–5014 (2014).
[102] J. Sang-Il Kwon, M. Nayhouse, P.D. Christofides, and G. Orkoulas, "Modeling and control of shape distribution of protein crystal aggregates," Chem. Eng. Sci. **104**, 484–497 (2013).
[103] J.S.-I. Kwon, M. Nayhouse, G. Orkoulas, and P.D. Christofides, "Enhancing the Crystal Production Rate and Reducing Polydispersity in Continuous Protein Crystallization," Ind. Eng. Chem. Res. **53**(40), 15538–15548 (2014).
[104] N. Sitapure, R.W. Epps, M. Abolhasani, and J. Sang-Il Kwon, "CFD-Based Computational Studies of Quantum Dot Size Control in Slug Flow Crystallizers: Handling Slug-to-Slug Variation," Ind. Eng. Chem. Res. **60**(13), 4930–4941 (2021).
[105] N. Sitapure, and J.S.-I. Kwon, "Neural network-based model predictive control for thin-film chemical deposition of quantum dots using data from a multiscale simulation," Chem. Eng. Res. Des. **183**, 595–607 (2022).
[106] N. Sitapure, and J.S.-I. Kwon, "Exploring the potential of time-series transformers for process modeling and control in chemical systems: An inevitable paradigm shift?," Chem. Eng. Res. Des. **194**, 461–477 (2023).
[107] N. Sitapure, and J.S.-I. Kwon, "A Unified Approach for modeling and control of crystallization of quantum dots (QDs)," Digit. Chem. Eng. **6**, 100077 (2023).
[108] D. Braga, F. Grepioni, L. Maini, and M. Polito, in *Mol. Netw.*, edited by M.W. Hosseini (Springer, Berlin, Heidelberg, 2009), pp. 87–95.
[109] K. Oura, V.G. Lifshits, A.A. Saranin, A.V. Zotov, and M. Katayama, *Surface Science: An Introduction* (Springer Science & Business Media, 2013).
[110] H. Cuppen, H. Meekes, W. Enckevort, and E. Vlieg, "Kink incorporation and step propagation in a non-Kossel model," Surf. Sci. - Surf. SCI **571**, 41–62 (2004).
[111] M. Rak, M. Izdebski, and A. Brozi, "Kinetic Monte Carlo study of crystal growth from solution," Comput. Phys. Commun. **138**(3), 250–263 (2001).
[112] D.G. Vlachos, L.D. Schmidt, and R. Aris, "Kinetics of faceting of crystals in growth, etching, and equilibrium," Phys. Rev. B **47**(9), 4896–4909 (1993).
[113] A. Chatterjee, and D.G. Vlachos, "An overview of spatial microscopic and accelerated kinetic Monte Carlo methods," J. Comput.-Aided Mater. Des. **14**(2), 253–308 (2007).
[114] J.S.-I. Kwon, M. Nayhouse, P.D. Christofides, and G. Orkoulas, "Modeling and control of crystal shape in continuous protein crystallization," Chem. Eng. Sci. **107**, 47–57 (2014).
[115] N. Blagden, M. de Matas, P.T. Gavan, and P. York, "Crystal engineering of active pharmaceutical ingredients to improve solubility and dissolution rates," Adv. Drug Deliv. Rev. **59**(7), 617–630 (2007).
[116] J.D.B. Featherstone, "Prevention and reversal of dental caries: role of low level fluoride," Community Dent. Oral Epidemiol. **27**(1), 31–40 (1999).

[117] E.L. Sjöberg, and D. Rickard, “The influence of experimental design on the rate of calcite dissolution,” Geochim. Cosmochim. Acta **47**(12), 2281–2285 (1983).
[118] L. Chou, R.M. Garrels, and R. Wollast, “Comparative study of the kinetics and mechanisms of dissolution of carbonate minerals,” Chem. Geol. **78**(3), 269–282 (1989).
[119] L.N. Plummer, and T.M.L. Wigley, “The dissolution of calcite in CO2-saturated solutions at 25°C and 1 atmosphere total pressure,” Geochim. Cosmochim. Acta **40**(2), 191–202 (1976).
[120] E.L. Sjöberg, “A fundamental equation for calcite dissolution kinetics,” Geochim. Cosmochim. Acta **40**(4), 441–447 (1976).
[121] L.N. Plummer, and E. Busenberg, “The solubilities of calcite, aragonite and vaterite in CO2-H2O solutions between 0 and 90°C, and an evaluation of the aqueous model for the system CaCO3-CO2-H2O,” Geochim. Cosmochim. Acta **46**(6), 1011–1040 (1982).
[122] E.L. Sjöberg, and D.T. Rickard, “The effect of added dissolved calcium on calcite dissolution kinetics in aqueous solutions at 25°C,” Chem. Geol. **49**(4), 405–413 (1985).
[123] A.C. Lasaga, and A. Luttge, “Variation of Crystal Dissolution Rate Based on a Dissolution Stepwave Model,” Science **291**(5512), 2400–2404 (2001).
[124] A.C. Lasaga, and A. Lüttge, “A model for crystal dissolution,” Eur. J. Mineral. **15**(4), 603–615 (2003).
[125] R.A. Berner, and G.R. Holdren Jr., “Mechanism of feldspar weathering: Some observational evidence,” Geology **5**(6), 369–372 (1977).
[126] I.N. MacInnis, and S.L. Brantley, “Development of etch pit size distributions on dissolving minerals,” Chem. Geol. **105**(1), 31–49 (1993).
[127] Y. Liang, D.R. Baer, J.M. McCoy, J.E. Amonette, and J.P. Lafemina, “Dissolution kinetics at the calcite-water interface,” Geochim. Cosmochim. Acta **60**(23), 4883–4887 (1996).
[128] Y. Liang, and D.R. Baer, “Anisotropic dissolution at the CaCO3(10$\bar{1}$4)—water interface,” Surf. Sci. **373**(2), 275–287 (1997).
[129] N.A.F.A. Samad, G. Sin, K.V. Gernaey, and R. Gani, “Introducing uncertainty analysis of nucleation and crystal growth models in Process Analytical Technology (PAT) system design of crystallization processes,” Eur. J. Pharm. Biopharm. **85**(3, Part B), 911–929 (2013).
[130] A. Lüttge, R.S. Arvidson, and C. Fischer, “A Stochastic Treatment of Crystal Dissolution Kinetics,” Elements **9**(3), 183–188 (2013).
[131] C. Fischer, R.S. Arvidson, and A. Lüttge, “How predictable are dissolution rates of crystalline material?,” Geochim. Cosmochim. Acta **98**, 177–185 (2012).
[132] E. Guyon, J.-P. Hulin, L. Petit, and C.D. Mitescu, *Physical Hydrodynamics* (Oxford University Press, 2015).
[133] F.M. Fowkes, “Additivity Of Intermolecular Forces At Interfaces. I. Determination Of The Contribution To Surface And Interfacial Tensions Of Dispersion Forces In Various Liquids,” J. Phys. Chem. **67**(12), 2538–2541 (1963).
[134] C.H. Bosanquet, “LV. On the flow of liquids into capillary tubes,” Lond. Edinb. Dublin Philos. Mag. J. Sci. **45**(267), 525–531 (1923).
[135] W.C. Jensen, and D. Li, “Determination of line tensions from the capillary rise in a conical tube,” Colloids Surf. Physicochem. Eng. Asp. **156**(1), 519–524 (1999).
[136] P. Roura, and J. Fort, “Local thermodynamic derivation of Young’s equation,” J. Colloid Interface Sci. **272**(2), 420–429 (2004).

[137] N. Verplanck, Y. Coffinier, V. Thomy, and R. Boukherroub, "Wettability Switching Techniques on Superhydrophobic Surfaces," Nanoscale Res. Lett. **2**(12), 577–596 (2007).
[138] K.-Y. Law, "Definitions for Hydrophilicity, Hydrophobicity, and Superhydrophobicity: Getting the Basics Right," J. Phys. Chem. Lett. **5**(4), 686–688 (2014).
[139] M. Pasandideh-Fard, Y.M. Qiao, S. Chandra, and J. Mostaghimi, "Capillary effects during droplet impact on a solid surface," Phys. Fluids **8**(3), 650–659 (1996).
[140] M.J. de Ruijter, J. De Coninck, and G. Oshanin, "Droplet Spreading: Partial Wetting Regime Revisited," Langmuir **15**(6), 2209–2216 (1999).
[141] S. Chen, D. Zhang, S. Shen, X. Liu, and Y. Chen, "Spherical drop impact on solid surfaces: Un-damped oscillation theoretical model," AIP Conf. Proc. **1984**(1), 020032 (2018).
[142] C. Shi, C. Bozhong, Z. Dongqi, L. Xiaohua, and S. Shengqiang, "An undamped oscillation model with two different contact angles for a spherical droplet impacting on solid surface," Вестник Самарского Государственного Технического Университета Серия Физико-Математические Науки **24**(2), 390–400 (2020).
[143] A.-L. Biance, C. Clanet, and D. Quéré, "First steps in the spreading of a liquid droplet," Phys. Rev. E **69**(1), 016301 (2004).
[144] P.-G. de Gennes, F. Brochard-Wyart, and D. Quéré, *Capillarity and Wetting Phenomena: Drops, Bubbles, Pearls, Waves* (Springer, New York, 2004).
[145] H. Hu, and R.G. Larson, "Analysis of the Microfluid Flow in an Evaporating Sessile Droplet," Langmuir **21**(9), 3963–3971 (2005).
[146] H. Masoud, and J.D. Felske, "Analytical solution for inviscid flow inside an evaporating sessile drop," Phys. Rev. E **79**(1), 016301 (2009).
[147] R.M. Manglik, M.A. Jog, S.K. Gande, and V. Ravi, "Damped harmonic system modeling of post-impact drop-spread dynamics on a hydrophobic surface," Phys. Fluids **25**(8), 082112 (2013).
[148] H.-Y. Kim, and J.-H. Chun, "The recoiling of liquid droplets upon collision with solid surfaces," Phys. Fluids **13**(3), 643–659 (2001).
[149] M. Nosonovsky, and B. Bhushan, "Roughness-induced superhydrophobicity: a way to design non-adhesive surfaces," J. Phys. Condens. Matter **20**(22), 225009 (2008).
[150] X.-M. Li, D. Reinhoudt, and M. Crego-Calama, "What do we need for a superhydrophobic surface? A review on the recent progress in the preparation of superhydrophobic surfaces," Chem. Soc. Rev. **36**(8), 1350–1368 (2007).
[151] L. Gao, and T.J. McCarthy, "How Wenzel and Cassie Were Wrong," Langmuir **23**(7), 3762–3765 (2007).
[152] G. McHale, "Cassie and Wenzel: Were They Really So Wrong?," Langmuir **23**(15), 8200–8205 (2007).
[153] B.J. Ryan, and K.M. Poduska, "Roughness effects on contact angle measurements," Am. J. Phys. **76**(11), 1074–1077 (2008).
[154] M.S. Mozumder, H. Zhang, and J. Zhu, "Mimicking Lotus Leaf: Development of Micro-Nanostructured Biomimetic Superhydrophobic Polymeric Surfaces by Ultrafine Powder Coating Technology," Macromol. Mater. Eng. **296**(10), 929–936 (2011).
[155] Y.T. Cheng, D.E. Rodak, C.A. Wong, and C.A. Hayden, "Effects of micro- and nano-structures on the self-cleaning behaviour of lotus leaves," Nanotechnology **17**(5), 1359–1362 (2006).
[156] X. Zhang, F. Shi, J. Niu, Y. Jiang, and Z. Wang, "Superhydrophobic surfaces: from structural control to functional application," J. Mater. Chem. **18**(6), 621–633 (2008).

[157] M. Ma, and R.M. Hill, “Superhydrophobic surfaces,” Curr. Opin. Colloid Interface Sci. **11**(4), 193–202 (2006).
[158] D. Öner, and T.J. McCarthy, “Ultrahydrophobic Surfaces. Effects of Topography Length Scales on Wettability,” Langmuir **16**(20), 7777–7782 (2000).
[159] L. Gao, and T.J. McCarthy, “The ‘Lotus Effect’ Explained: Two Reasons Why Two Length Scales of Topography Are Important,” Langmuir **22**(7), 2966–2967 (2006).
[160] P. Hao, C. Lv, F. Niu, and Y. Yu, “Water droplet impact on superhydrophobic surfaces with microstructures and hierarchical roughness,” Sci. China Phys. Mech. Astron. **57**(7), 1376–1381 (2014).
[161] X. Tian, T. Verho, and R.H.A. Ras, “Moving superhydrophobic surfaces toward real-world applications,” Science **352**(6282), 142–143 (2016).
[162] C.-H. Xue, and J.-Z. Ma, “Long-lived superhydrophobic surfaces,” J. Mater. Chem. A **1**(13), 4146–4161 (2013).
[163] A. Nakajima, K. Hashimoto, and T. Watanabe, in *Mol. Mater. Funct. Polym.*, edited by W.J. Blau, P. Lianos, and U. Schubert (Springer, Vienna, 2001), pp. 31–41.
[164] Y.C. Jung, and B. Bhushan, “Wetting behaviour during evaporation and condensation of water microdroplets on superhydrophobic patterned surfaces,” J. Microsc. **229**(1), 127–140 (2008).
[165] A. Lafuma, and D. Quéré, “Superhydrophobic states,” Nat. Mater. **2**, 457–460 (2003).
[166] R.J. Vrancken, H. Kusumaatmaja, K. Hermans, A.M. Prenen, O. Pierre-Louis, C.W.M. Bastiaansen, and D.J. Broer, “Fully Reversible Transition from Wenzel to Cassie−Baxter States on Corrugated Superhydrophobic Surfaces,” Langmuir **26**(5), 3335–3341 (2010).
[167] N.D. Patil, R. Bhardwaj, and A. Sharma, “Droplet impact dynamics on micropillared hydrophobic surfaces,” Exp. Therm. Fluid Sci. **74**, 195–206 (2016).
[168] K.K. Varanasi, T. Deng, M.F. Hsu, and N. Bhate, in (American Society of Mechanical Engineers Digital Collection, 2009), pp. 637–645.
[169] T. Koishi, K. Yasuoka, S. Fujikawa, T. Ebisuzaki, and X.C. Zeng, “Coexistence and transition between Cassie and Wenzel state on pillared hydrophobic surface,” Proc. Natl. Acad. Sci. **106**(21), 8435–8440 (2009).
[170] J.B. Boreyko, and C.-H. Chen, “Restoring Superhydrophobicity of Lotus Leaves with Vibration-Induced Dewetting,” Phys. Rev. Lett. **103**(17), 174502 (2009).
[171] G. Liu, L. Fu, A.V. Rode, and V.S.J. Craig, “Water Droplet Motion Control on Superhydrophobic Surfaces: Exploiting the Wenzel-to-Cassie Transition,” Langmuir **27**(6), 2595–2600 (2011).
[172] J. Wang, and D. Chen, “Criteria for Entrapped Gas under a Drop on an Ultrahydrophobic Surface,” Langmuir **24**(18), 10174–10180 (2008).
[173] C. Lv, P. Hao, X. Zhang, and F. He, “Dewetting Transitions of Dropwise Condensation on Nanotexture-Enhanced Superhydrophobic Surfaces,” ACS Nano **9**(12), 12311–12319 (2015).
[174] Z. Guo, W. Liu, and B.-L. Su, “Superhydrophobic surfaces: From natural to biomimetic to functional,” J. Colloid Interface Sci. **353**(2), 335–355 (2011).
[175] P.D. Christofides, and A. Armaou, “Control and optimization of multiscale process systems,” Comput. Chem. Eng. **30**(10), 1670–1686 (2006).
[176] D. Chaffart, and L.A. Ricardez-Sandoval, “Robust dynamic optimization in heterogeneous multiscale catalytic flow reactors using polynomial chaos expansion,” J. Process Control **96**(1), 113–131 (2018).

[177] D. Chaffart, S. Rasoulian, and L.A. Ricardez-Sandoval, "Distributional uncertainty analysis and robust optimization in spatially heterogeneous multiscale process systems," AIChE J. **62**(7), 2374–2390 (2016).

[178] M. Alswaitti, M. Albughdadi, and N.A.M. Isa, "Density-based particle swarm optimization algorithm for data clustering," Expert Syst. Appl. **91**, 170–186 (2018).

[179] M. Pant, R. Thangaraj, and A. Abraham, in *Found. Comput. Intell. Vol. 3 Glob. Optim.*, edited by A. Abraham, A.-E. Hassanien, P. Siarry, and A. Engelbrecht (Springer, Berlin, Heidelberg, 2009), pp. 101–128.

[180] Yu.N. Kryuchkov, "Concentration dependence of the mean interparticle distance in disperse systems," Refract. Ind. Ceram. **42**(11), 390–392 (2001).

[181] E. Ruckenstein, P.O. Brunn, and J. Holweg, "Flow-induced creation and destruction of supermicelles in surfactant solutions," Langmuir **4**(2), 350–354 (1988).

[182] J. Gostick, M. Aghighi, J. Hinebaugh, T. Tranter, M.A. Hoeh, H. Day, B. Spellacy, M.H. Sharqawy, A. Bazylak, A. Burns, W. Lehnert, and A. Putz, "OpenPNM: A Pore Network Modeling Package," Comput. Sci. Eng. **18**(4), 60–74 (2016).

[183] B.B. Hanshaw, and W. Back, "Chemical mass-wasting of the northern Yucatan Peninsula by groundwater dissolution," Geology **8**(5), 222–224 (1980).

[184] D. Chaffart, and L.A. Ricardez-Sandoval, "Robust Optimization of a Multiscale Catalytic Reactor System with Spatially-Varying Uncertainty Descriptions using Polynomial Chaos Expansions," Can. J. Chem. Eng. **60**, 128–140 (2017).

[185] G. Kimaev, and L.A. Ricardez-Sandoval, "A comparison of efficient uncertainty quantification techniques for stochastic multiscale systems," AIChE J. **63**(8), 3361–3373 (2017).

[186] M. Herzog, A. Gilg, M. Paffrath, P. Rentrop, and U. Wever, in *Nano Space* (Springer-Verlag, 2008), pp. 161–174.

[187] M.S. Eldred, "Recent advances in non-intrusive polynomial chaos and stochastic collocation methods for uncertainty analysis and design," AIAA Pap. **2274**(2009), 37 (2009).

[188] D. Xiu, *Numerical Methods for Stochastic Computations: A Spectral Method Approach* (Princeton University Press, Princeton, N.J, 2010).

[189] S. Rasoulian, and L.A. Ricardez-Sandoval, "Robust multivariable estimation and control in an epitaxial thin film growth process under uncertainty," J. Process Control **34**, 70–81 (2015).

[190] C.H. Séquin, "Computer simulation of anisotropic crystal etching," Sens. Actuators Phys. **34**, 225–241 (1992).

[191] J. Pal, M. Ganguly, C. Mondal, A. Roy, Y. Negishi, and T. Pal, "Crystal-Plane-Dependent Etching of Cuprous Oxide Nanoparticles of Varied Shapes and Their Application in Visible Light Photocatalysis," J. Phys. Chem. C **117**(46), 24640–24653 (2013).

[192] S. Fang, Y. Xin, L. Ge, C. Han, P. Qiu, and L. Wu, "Facile synthesis of CeO2 hollow structures with controllable morphology by template-engaged etching of Cu2O and their visible light photocatalytic performance," Appl. Catal. B Environ. **179**, 458–467 (2015).

[193] L.D. Britt, P.S. Barie, A.B. Peitzman, and G. Jurkovich, *Acute Care Surgery* (Lippincott Williams & Wilkins, 2012).

[194] C.A. Wunderlich, *Das Verhalten der Eigenwärme in Krankheiten* (O. Wigand, 1870).

[195] G. Kelly, "Body temperature variability (Part 1): a review of the history of body temperature and its variability due to site selection, biological rhythms, fitness, and aging," Altern. Med. Rev. **11**(4), 278–294 (2006).

[196] G.S. Kelly, "Body temperature variability (Part 2): masking influences of body temperature variability and a review of body temperature variability in disease," Altern. Med. Rev. **12**(1), 49–63 (2007).

[197] A.Y. Abuhelwa, D.J.R. Foster, and R.N. Upton, "A Quantitative Review and Meta-Models of the Variability and Factors Affecting Oral Drug Absorption—Part I: Gastrointestinal pH," AAPS J. **18**(5), 1309–1321 (2016).

[198] C. Yw, "Rate-control drug delivery systems: controlled release vs. sustained release.," Med. Prog. Technol. **15**(1–2), 21–46 (1989).

[199] A.A. Deshpande, C.T. Rhodes, N.H. Shah, and A.W. Malick, "Controlled-Release Drug Delivery Systems for Prolonged Gastric Residence: An Overview," Drug Dev. Ind. Pharm. **22**(6), 531–539 (1996).

[200] Y. Ueno, H. Futagawa, Y. Takagi, A. Ueno, and Y. Mizushima, "Drug-incorporating calcium carbonate nanoparticles for a new delivery system," J. Controlled Release **103**(1), 93–98 (2005).

[201] I.E. Grossmann, R. Drabbant, and R.K. Jain, "Incorporating Toxicology in the Synthesis of Industrial Chemical Complexes," Chem. Eng. Commun. **17**(1–6), 151–170 (1982).

[202] N.R. Morrow, and G. Mason, "Recovery of oil by spontaneous imbibition," Curr. Opin. Colloid Interface Sci. **6**(4), 321–337 (2001).

[203] W. Guo, J. Hansson, and W. van der Wijngaart, "Capillary pumping independent of the liquid surface energy and viscosity," Microsyst. Nanoeng. **4**(1), 1–7 (2018).

[204] R. Siegel, "Transient Capillary Rise in Reduced and Zero-Gravity Fields," J. Appl. Mech. **28**(2), 165–170 (1961).

[205] D. Deng, D. Liang, Y. Tang, J. Peng, X. Han, and M. Pan, "Evaluation of capillary performance of sintered porous wicks for loop heat pipe," Exp. Therm. Fluid Sci. **50**, 1–9 (2013).

[206] F. Brochard-Wyart, and P.G. de Gennes, "Dynamics of partial wetting," Adv. Colloid Interface Sci. **39**, 1–11 (1992).

[207] M. Hilpert, "Explicit analytical solutions for liquid infiltration into capillary tubes: Dynamic and constant contact angle," J. Colloid Interface Sci. **344**(1), 198–208 (2010).

[208] K. Dahm, and P. Dearnley, "On the nature, properties and wear response of S-phase (nitrogen-alloyed stainless steel) coatings on Aisi 316l," Proc. Inst. Mech. Eng. Part -J. Mater.-Des. Appl. **214**, 181–199 (2000).

[209] P.G. de Gennes, "Wetting: statics and dynamics," Rev. Mod. Phys. **57**(3), 827–863 (1985).

[210] C. Loehle, and K. Solarik, "Forest growth trends in Canada," For. Chron. **95**, 183–195 (2019).

[211] R.L. Zimdahl, B.K. Cranmer, and W.W. Stroup, "Use of Empirical Equations to Describe Dissipation of Metribuzin and Pendimethalin," Weed Sci. **42**(2), 241–248 (1994).

[212] R. Rioboo, M. Marengo, and C. Tropea, "Time evolution of liquid drop impact onto solid, dry surfaces," Exp. Fluids **33**(1), 112–124 (2002).

[213] D. Caviezel, C. Narayanan, and D. Lakehal, "Adherence and bouncing of liquid droplets impacting on dry surfaces," Microfluid. Nanofluidics **5**(4), 469–478 (2008).

[214] J. Fukai, Y. Shiiba, T. Yamamoto, O. Miyatake, D. Poulikakos, C.M. Megaridis, and Z. Zhao, "Wetting effects on the spreading of a liquid droplet colliding with a flat surface: Experiment and modeling," Phys. Fluids **7**(2), 236–247 (1995).

[215] M. Qin, C. Tang, S. Tong, P. Zhang, and Z. Huang, "On the role of liquid viscosity in affecting droplet spreading on a smooth solid surface," Int. J. Multiph. Flow **117**, 53–63 (2019).

[216] S. Sikalo, M. Marengo, C. Tropea, and E. Ganic, *Analysis of Impact of Droplets on Horizontal Surfaces* (2000), p. 352.

[217] R.M. Manglik, M.A. Jog, S.K. Gande, and V. Ravi, "Damped harmonic system modeling of post-impact drop-spread dynamics on a hydrophobic surface," Phys. Fluids **25**(8), 082112 (2013).

[218] M. Du, H. Zhao, X. Ye, and Z. Zhou, "Fabrication of PDMS Microchannels with Round Profiles Using Glycerol Molds," Key Eng. Mater. **483**, 345–349 (2011).

[219] R. Blossey, "Self-cleaning surfaces — virtual realities," Nat. Mater. **2**(5), 301–306 (2003).

[220] M. Liu, S. Wang, Z. Wei, Y. Song, and L. Jiang, "Bioinspired Design of a Superoleophobic and Low Adhesive Water/Solid Interface," Adv. Mater. **21**(6), 665–669 (2009).

[221] J.-Y. Shiu, C.-W. Kuo, P. Chen, and C.-Y. Mou, "Fabrication of Tunable Superhydrophobic Surfaces by Nanosphere Lithography," Chem. Mater. **16**(4), 561–564 (2004).

[222] A. Tuteja, W. Choi, G.H. McKinley, R.E. Cohen, and M.F. Rubner, "Design Parameters for Superhydrophobicity and Superoleophobicity," MRS Bull. **33**(8), 752–758 (2008).

[223] B. Chang, A. Shah, I. Routa, H. Lipsanen, and Q. Zhou, "Low-height sharp edged patterns for capillary self-alignment assisted hybrid microassembly," J. Micro-Bio Robot. **9**(1), 1–10 (2014).

[224] L. Huang, Y. Yao, Z. Peng, B. Zhang, and S. Chen, "How to Achieve a Monostable Cassie State on a Micropillar-Arrayed Superhydrophobic Surface," J. Phys. Chem. B **125**(3), 883–894 (2021).

[225] T. Cai, Z. Jia, H. Yang, and G. Wang, "Investigation of Cassie-Wenzel Wetting transitions on microstructured surfaces," Colloid Polym. Sci. **294**(5), 833–840 (2016).

[226] W. Zhang, R. Zhang, C. Jiang, and C. Wu, "Effect of pillar height on the wettability of micro-textured surface: Volume-of-fluid simulations," Int. J. Adhes. Adhes. **74**, 64–69 (2017).

[227] Y. Cai, W. Chang, X. Luo, A.M.L. Sousa, K.H.A. Lau, and Y. Qin, "Superhydrophobic structures on 316L stainless steel surfaces machined by nanosecond pulsed laser," Precis. Eng. **52**, 266–275 (2018).

[228] L. Chen, Z. Xiao, P.C.H. Chan, Y.-K. Lee, and Z. Li, "A comparative study of droplet impact dynamics on a dual-scaled superhydrophobic surface and lotus leaf," Appl. Surf. Sci. **257**(21), 8857–8863 (2011).

[229] Y.C. Jung, and B. Bhushan, "Dynamic Effects of Bouncing Water Droplets on Superhydrophobic Surfaces," Langmuir **24**(12), 6262–6269 (2008).

[230] J. Gao, J. Zhao, L. Liu, and W. Xue, "Dimensional effects of polymer pillar arrays on hydrophobicity," Surf. Eng. **32**(2), 125–131 (2016).

[231] D. Rangel-Martinez, K.D.P. Nigam, and L.A. Ricardez-Sandoval, "Machine learning on sustainable energy: A review and outlook on renewable energy systems, catalysis, smart grid and energy storage," Chem. Eng. Res. Des. **174**, 414–441 (2021).

[232] D.B. Trushina, T.N. Borodina, S. Belyakov, and M.N. Antipina, "Calcium carbonate vaterite particles for drug delivery: Advances and challenges," Mater. Today Adv. **14**, 100214 (2022).

[233] H. Masoud, and J.D. Felske, "Analytical solution for Stokes flow inside an evaporating sessile drop: Spherical and cylindrical cap shapes," Phys. Fluids **21**(4), 042102 (2009).

[234] C.J. van Oss, R.F. Giese, and A. Docoslis, "Hyperhydrophobicity of the Water-Air Interface," J. Dispers. Sci. Technol. **26**(5), 585–590 (2005).

[235] F. Schellenberger, N. Encinas, D. Vollmer, and H.-J. Butt, "How Water Advances on Superhydrophobic Surfaces," Phys. Rev. Lett. **116**(9), 096101 (2016).

[236] Y. Jiang, and C.-H. Choi, "Droplet Retention on Superhydrophobic Surfaces: A Critical Review," Adv. Mater. Interfaces **8**(2), 2001205 (2021).

Appendix A

Derivation of Inertial Force Expression

The inertial force acting upon a sessile droplet was previously reported in the literature as follows:[141,142]

$$\vec{F}_{inta} = \left[-\frac{\pi\rho R_{ps}^4\theta}{4R} + \frac{\pi\rho\left(R_{ps}-H_{drop}\right)}{12}\left(2R_{drop}^2 + 3R_{ps}^2\right)\right]\frac{d^2R_{drop}}{dt^2} \quad \text{(A.1)}$$

This expression is derived based on projecting a perfect sphere onto the spherical cap formed by the sessile droplet, as illustrated in Fig. A.1. In both the figure and equation, H_{drop} denotes the height of the sessile droplet above the solid surface, and R_{ps} denotes the radius of the sphere projected onto the droplet cap. These values can be defined based on the droplet contact radius R_{drop} and the contact angle θ as follows:

$$R_{ps} = \frac{R_{drop}}{\sin\theta} \quad \text{(A.2)}$$

$$H_{drop} = R_{drop}\frac{1-\cos\theta}{\sin\theta} \quad \text{(A.3)}$$

By substituting Eqs. (A.2)-(A.3) into Eq. (A.1):

$$\vec{F}_{inta} = \left[-\frac{\pi\rho R_{drop}^4\theta}{4R_{drop}\sin^4\theta} + \frac{\pi\rho\left(\frac{R_{drop}}{\sin\theta}-R_{drop}\frac{1-\cos\theta}{\sin\theta}\right)}{12}\left(2R_{drop}^2 + \frac{3R_{drop}^2}{\sin^2\theta}\right)\right]\frac{d^2R_{drop}}{dt^2} \quad \text{(A.4)}$$

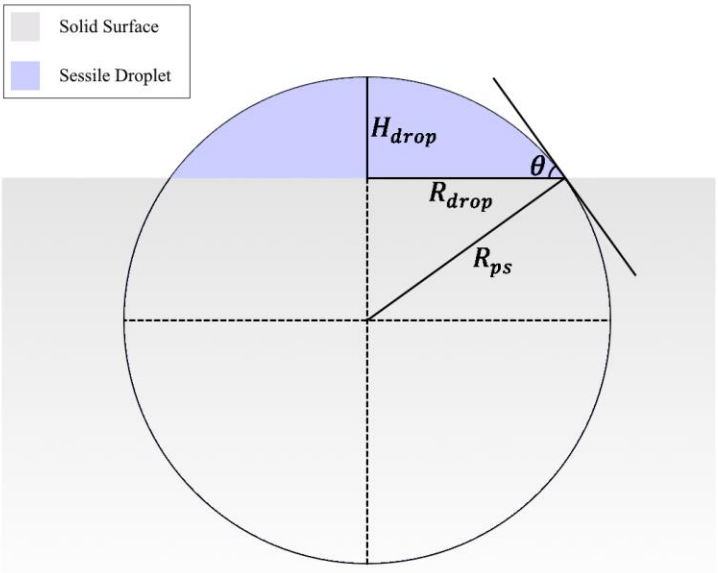

Figure A.1: Projection of a perfect sphere onto the droplet spherical cap

This expression can be simplified as follows:

$$\vec{F}_{inta} = \pi\rho\left[-\frac{R_{drop}^3\theta}{4\,sin^4\,\theta} + \frac{R_{drop}^3\,cos\,\theta}{12\,sin\,\theta}\left(2 + \frac{3}{sin^2\,\theta}\right)\right]\frac{d^2R_{drop}}{dt^2} \tag{A.5}$$

The above expression can be subsequently re-arranged to yield the inertial force expression depicted in Eq. (2.12). In order to provide further analysis about the tendencies of the inertial force term, Fig. A.2 showcases the behaviour of $R_{drop}^3\left[-\frac{\theta}{4\sin^4\theta} + \frac{\cos\theta}{6\sin\theta} + \frac{\cos\theta}{4\sin^3\theta}\right]$ as a function of the contact angle θ for droplets of radii $R_{drop} \in \boldsymbol{R_{drop}} = \{0.1, 0.5, 1, 5, 10\}$ mm. This figure overall showcases that this expression remains negative for all possible values of θ and for all contact radii, and therefore highlights that the inertial force acts in the opposite direction of the acceleration based on the predicted model.

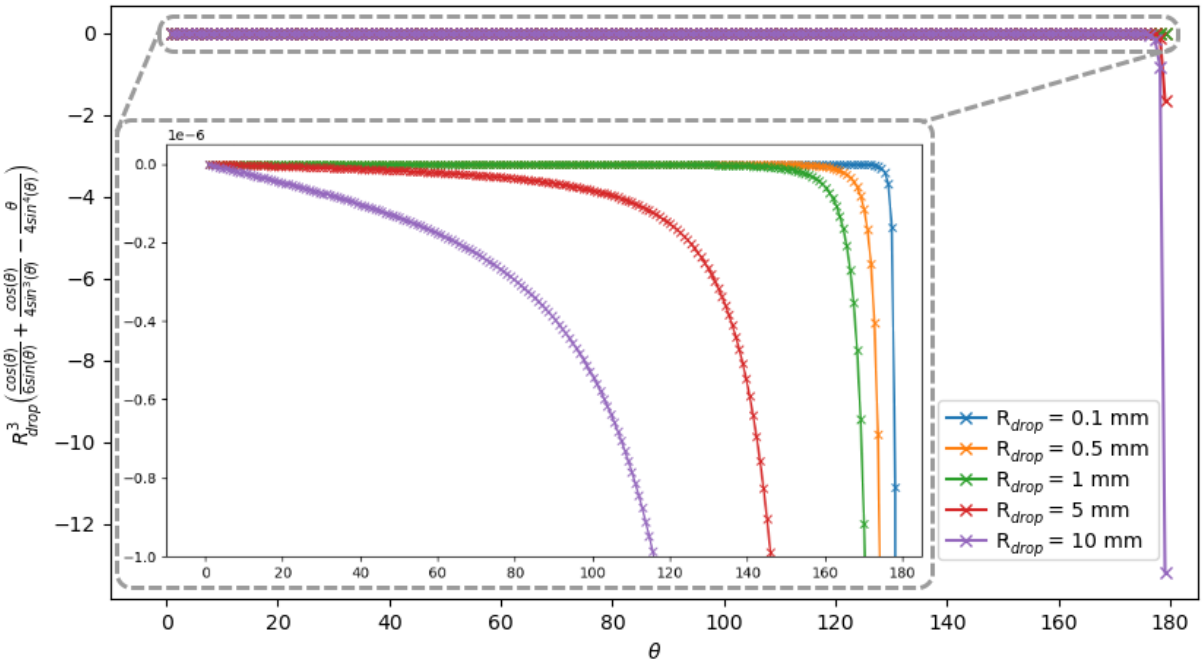

Figure A.2: Plot of the radius and contact angle terms in the inertial force equation $R_{drop}^3\left(\frac{\cos\theta}{6\sin\theta} + \frac{\cos\theta}{4\sin^3\theta} - \frac{\theta}{4\sin^4\theta}\right)$ as a function of θ for various droplet radii. Inset: An enlarged view of the radius and contact angle term using a smaller y-axis scaling to provide a clearer look at the function behaviour at smaller contact angles.

Appendix B

Supplementary Material for Chapter 4

B.1 Standard kMC Algorithm for Crystal Dissolution

The complete standard kMC algorithm implemented in this work to model the crystal dissolution process is summarized according to the following algorithm:

1. Initialize the crystal on the kMC lattice by mapping each crystal particle to its own unique lattice site, as illustrated in Fig. 4.3a.
2. Determine the number of nearest neighbors $\boldsymbol{n_{bd}}$ and the angle configuration $\boldsymbol{\Theta_{n_{bd}}}$ information for each crystal particle.
3. Calculate the kinetic rates of dissolution $W_{cd,\boldsymbol{n_{bd}},\boldsymbol{\Theta_{n_{bd}}}}$ for each molecule according to Eq. (2.3). Tabulate the cumulative sums of the kinetic rates $W_{tot} = \sum_i W_{cd,\boldsymbol{n_{bd}},\boldsymbol{\Theta_{n_{bd}}}}$.
4. Calculate the kMC time increment, δt, according to Eq. (3.11) to determine the time $t + \delta t$ at which the next event will occur.
5. Apply MC sampling to select a crystal molecule to dissolve based on their kinetic rates of dissolution, according to Eq. (3.12).
6. Remove the selected molecule from the kMC lattice and update the nearest neighbor $\boldsymbol{n_{bd}}$ and angle configuration $\boldsymbol{\Theta_{n_{bd}}}$ information for each of the nearest neighbors. Calculate the new kinetic rates of dissolution $W_{cd,\boldsymbol{n_{bd}},\boldsymbol{\Theta_{n_{bd}}}}$ for each of the nearest neighbors according to Eq. (2.3).
7. Repeat Steps 4-6 until the crystal has completely dissolved.

B.2 MFkMC Algorithm for Crystal Dissolution

The complete MFkMC algorithm for crystal dissolution implemented within this study is summarized as follows:

1. Initialize the crystal on the sparse MFkMC lattice by mapping each crystal surface molecule and each adjacent interfacial fluid site to their own unique lattice sites. All bulk phase sites within the solid and the fluid are left empty, as illustrated in Fig. 4.3b.
2. Determine the number of nearest neighbors $\boldsymbol{n_{bd}}$ and angle configuration information $\boldsymbol{\Theta_{n_{bd}}}$ for each surface particle.

3. Calculate the kinetic rates of dissolution $W_{cd,\boldsymbol{n_{bd}},\boldsymbol{\Theta}_{\boldsymbol{n_{bd}}}}$ (i.e. the receding rate $W_{mf,i} \equiv W_{cd,\boldsymbol{n_{bd}},\boldsymbol{\Theta}_{\boldsymbol{n_{bd}}}}$) for each surface molecule according to Eq. (2.3). Tabulate the cumulative sums of the kinetic rates $W_{tot} = \sum_i W_{cd,\boldsymbol{n_{bd}},\boldsymbol{\Theta}_{\boldsymbol{n_{bd}}}}$.
4. Calculate the kMC time increment, δt, according to Eq. (3.11) to determine the time $t + \delta t$ at which the next event will occur.
5. Apply MC sampling to select a surface molecule to dissolve based on their kinetic rates of dissolution, according to Eq. (3.12).
6. Remove the selected ion from the MFkMC lattice and update the nearest neighbor $\boldsymbol{n_{bd}}$ and angle configuration $\boldsymbol{\Theta}_{\boldsymbol{n_{bd}}}$ information for each of the nearest neighbors. Calculate the new kinetic rates of dissolution $W_{cd,\boldsymbol{n_{bd}},\boldsymbol{\Theta}_{\boldsymbol{n_{bd}}}}$ for each of the nearest neighbors according to Eq. (2.3).
7. Initialize any new surface particle sites created by the dissolution of the selected molecule and store their nearest neighbor $\boldsymbol{n_{bd}}$ and angle configuration $\boldsymbol{\Theta}_{\boldsymbol{n_{bd}}}$ information. Calculate the kinetic rates of dissolution $W_{cd,\boldsymbol{n_{bd}},\boldsymbol{\Theta}_{\boldsymbol{n_{bd}}}}$ for each new surface ion according to Eq. (2.3). Similarly, remove any interfacial fluid site that moved into the bulk fluid phase due to the dissolution event.
8. Repeat Steps 4-7 until the crystal has completely dissolved.

Note that since the kinetic rate of dissolution $W_{cd,\boldsymbol{n_{bd}},\boldsymbol{\Theta}_{\boldsymbol{n_{bd}}}}$ (Eq. (2.3)) does not directly depend on the time t or the time increment δt, it does not matter whether δt is calculated before or after the event selection step within the MFkMC algorithm, as discussed in Section 3.3.1. However, the time increment δt was calculated before selecting an event in the MCkMC algorithm as well as the standard kMC algorithm in order to mirror the MFkMC structure presented in Section 3.2.

B.3 Polynomial Chaos Expansion Algorithm

The PCE method implemented within this work can be described according to the following algorithm:

1. Discretize the time domain into *M* different timepoints on which to measure the variability in the process outputs $\boldsymbol{\Psi}$.
2. Define $\mathbf{H} = [\eta_1, \dots, \eta_i, \dots, \eta_\jmath] \in \mathbb{R}^\jmath$ and $\widehat{\mathbf{H}} = [\hat{\eta}_1, \dots, \hat{\eta}_i, \dots, \hat{\eta}_\jmath] \in \mathbb{R}^\jmath$ as the arrays storing the uncertain parameters η_i and the nominal values of the uncertain parameters $\hat{\eta}_i$, respectively. Similarly, define $\boldsymbol{\Psi}(t_m) = \left[\psi_1(t_m), \dots, \psi_j(t_m), \dots, \psi_\jmath(t_m)\right] \in \mathbb{R}^\jmath$ as the array of system outputs ψ_j at timepoint (t_m).
3. Define the probability distribution function (PDF) F_{η_i} for each uncertain parameter η_i as follows:

$$\eta_i \in F_{\eta_i}(\bar{\eta}_i, \sigma_{\eta_i}^2) \tag{B.1}$$

Note that there are numerous different kinds of probability distributions that can be applied to η_i and propagated through the system model using PCE.

4. Define the array of random values $\boldsymbol{\Xi}_{\mathbf{H}} = \left[\xi_{1,\eta_1}, \ldots, \xi_{i,\eta_i}, \ldots, \xi_{\mathcal{I},\eta_\mathcal{I}}\right] \in \mathbb{R}^{\mathcal{I}}$, where ξ_{i,η_i} is generated based on the uncertainty distribution applied to η_i. Note that the standard orthogonal polynomial basis functions $\boldsymbol{b}_{\chi}^{\mathbf{H}}$ (see Eq. (4.1)) used for PCE require ξ_{i,η_i} to be generated from a standard distribution.[187,188] Therefore, in order to define ξ_{i,η_i}, the uncertain parameters η_i must be transformed such that $F_{\xi_{i,\eta_i}}$ has standard distribution properties.[187]
5. Select an orthogonal polynomial basis function $\boldsymbol{b}_{\chi}^{\mathbf{H}}$ to build the PCE approximations based on the probability distribution F_{η_i}. The most commonly used PCE basis functions are the stochastic Askey polynomials, as their weight functions are orthogonal to most standard PDFs.[187]
6. Solve for the PCE coefficients at their corresponding time point, i.e. $\boldsymbol{a}_{\chi}(t_m)$. If the process system can be modelled with a closed-form mathematical expression such as a differential algebraic equation, then $\boldsymbol{a}_{\chi}(t_m)$ can be solved using intrusive approaches (i.e. methods that directly modify the source code), such as Galerkin projection.[186] However, if the process system lacks a closed form as is the case with a kMC-based model, then $\boldsymbol{a}_{\chi}(t_m)$ must be determined using sampling techniques such as non-intrusive spectral projection (NISP)[187,188] or least-squares.[176,184] Note that for these non-intrusive methods, the required number of sample points needed to determine accurate values of $\boldsymbol{a}_{\chi}(t_m)$ is dependent on the number of uncertain parameters $\mathcal{I}$ in **H**. Furthermore, it is necessary to develop a unique PCE model for each system output in $\boldsymbol{\Psi}(t_m)$, and consequently these approaches must be applied to determine $\boldsymbol{a}_{\chi}(t_m)$ for each $\psi_{j}(t_m)$.
7. Use Monte Carlo (MC) sampling to propagate the parametric uncertainty in **H** through the PCE models. The MC sampling method is used to randomly generate values of $\boldsymbol{\Xi}_{\mathbf{H}}$, which are subsequently plugged into the PCE models in order to determine the uncertain system outputs $\boldsymbol{\Psi}(t_m)$.
8. Determine key statistical information about the output distribution $\boldsymbol{\Psi}(t_m)$ such as the mean $\bar{\boldsymbol{\Psi}}(t_m)$, the variance $\sigma^2_{\boldsymbol{\Psi}(t_m)}$, and the upper and lower probabilistic bounds $\boldsymbol{\Psi}^{\varsigma}\left(\alpha_{cf}\middle|t_m\right)$ for $\varsigma \in \{u, l\}$ at a given confidence α_{cf}. Note that the upper (u) and lower (l) bounds can be determined at a specified α_{cf} according to the following expression:

$$\boldsymbol{\Psi}^{\varsigma}\left(\alpha_{cf}\middle|t_m\right) = F^{-1}\left(\Pi\middle|\boldsymbol{\Psi}^{\varsigma}\left(\alpha_{cf}\middle|t_m\right)\right), \Pi \in \left\{1-\frac{\alpha_{cf}}{2}, \frac{\alpha_{cf}}{2}\right\}, \varsigma \in \{u, l\} \tag{B.2}$$

Where $F^{-1}\left(\Pi\middle|\boldsymbol{\Psi}^{\varsigma}\left(\alpha_{cf}\middle|t_m\right)\right)$ denotes the inverse cumulative distribution function of a model output $\boldsymbol{\Psi}^{\varsigma}(t_m)$ at time t_m evaluated at a probability Π for an upper/lower bound ς. Note that in this expression, $\Pi = \frac{\alpha_c}{2}$ for the lower bound $\varsigma = l$ of $\boldsymbol{\Psi}(t_m)$ and $\Pi = 1 - \frac{\alpha_c}{2}$ for the upper bound $\varsigma = u$ of $\boldsymbol{\Psi}(t_m)$.

B.4 Low-order PCE Coefficient Model Algorithm

The LPCM methodology used within this study can be described according to the following steps.

1. Define $\boldsymbol{\omega} = [\omega_1, \dots, \omega_\nu, \dots, \omega_{\mathrm{N}}] \in \mathbb{R}^{\mathrm{N}}$ as the array of process design parameters ω_ν. Sub-divide the region of each ω_ν into N_ν points evenly spaced apart at a distance $\Delta\omega_\nu$ as follows:

$$\omega_{\nu,n_\nu} = \left\{\omega_{\nu,minimum} + (n_\nu - 1)\Delta\omega_\nu \leq \omega_{\nu,n_\nu} \leq \omega_{\nu,maximum},\quad n_\nu = 1,2,3,\dots,N_\nu\right\} \tag{B.3}$$

2. Implement the PCE algorithm described in Section 4.1.2 and Section B.3 to determine the PCE coefficients $\boldsymbol{a}_\chi(t_m)$ at each combination of discretized design parameter realizations ω_{ν,n_ν}.
3. Select reasonable low order models that sufficiently capture the relationship between the input design parameters $\boldsymbol{\omega}$ and the output PCE coefficients $\boldsymbol{a}_\chi(t_m)$. Note that the appropriate model for a given PCE coefficient is problem-dependent and therefore the type of model selected is expected to vary between each coefficient depending on the relationship between $\boldsymbol{a}_\chi(t_m)$ and $\boldsymbol{\omega}$. As a result, the selection of an appropriate model must be performed via data analysis and observations.
4. Use model regression (e.g. least squares) to estimate the coefficients for each of the low-order models selected in Step 3.
5. Use LPCMs to determine the PCE coefficients $\boldsymbol{a}_\chi(t_m)$ for given realizations in $\boldsymbol{\omega}$.
6. Build PCE models to predict the uncertain system outputs $\boldsymbol{\Psi}(t_m)$ based on the determined PCE coefficients $\boldsymbol{a}_\chi(t_m)$.
7. Propagate the uncertainty in $\mathbf{H}$ through the PCE models according to Steps 7-8 in the Polynomial Chaos Expansion Algorithm presented in Section B.3.

B.5 LPCMs and Model Coefficients

The LPCMs developed within the main body of this work were determined using CurveExpert Professional 2.6 in order to fit a large selection of models to the PCE coefficient data. The models were fit to the data using least squares and the optimal model was selected based on the model R-squared values. A total of four different models were selected to predict the various PCE coefficients for the different crystal shapes as a function of the crystal size s:

$$a_\chi(t_m) = b_0 + b_1\omega_\nu \tag{B.4}$$

$$a_\chi(t_m) = b_0\omega_\nu^{b_1} \tag{B.5}$$

$$a_\chi(t_m) = (b_0 + b_1\omega_\nu)^{-\frac{1}{b_2}} \tag{B.6}$$

$$a_\chi(t_m) = -(b_0 + b_1\omega_\nu)^{-\frac{1}{b_2}} \quad \text{(B.7)}$$

where $b_\iota \in \boldsymbol{b} = \{b_0, b_1, b_2\}$ In addition, some of the LPCMs were determined by performing cubic interpolation between the PCE coefficient values for different crystal sizes. The LPCM model and their respective coefficients for each PCE coefficient can be found in Table B.1.

Table B.1. The LPCMs and their respective coefficients developed for each PCE coefficient of every PCE model considered

PCE Model			LPCM Model Equation Number	b_0	b_1	b_2
	Shape (PCE Order)	PCE Coefficient				
t_d	$cube$ (2nd order)	a_0	(B.4)	-0.84224	0.16068	---
		a_1	(B.4)	-0.97554	0.26189	---
		a_2	(B.4)	-0.56377	0.18778	---
	$sphere$ (2nd order)	a_0	(B.4)	-0.91989	0.09183	---
		a_1	(B.4)	-1.29208	0.14570	---
		a_2	(B.4)	-0.89723	0.11779	---
	$tetra$ (2nd order)	a_0	(B.4)	-0.89708	0.05815	---
		a_1	(B.4)	-1.62730	0.10210	---
		a_2	(B.4)	-1.81211	0.09576	---
	$dode$ (2nd order)	a_0	(B.4)	-0.96374	0.09568	---
		a_1	(B.4)	-1.78216	0.17642	---
		a_2	(B.4)	-1.65189	0.14706	---
$n_d(t_0)$	$cube$ (1st order)	a_0	interpolation	---	---	---
		a_1	(B.4)	0.00391	-0.00002	---
	$sphere$ (1st order)	a_0	interpolation	---	---	---
		a_1	(B.4)	0.23898	0.00253	---
	$tetra$	a_0	interpolation	---	---	---

	(1st order)	a_1	(B.4)	-0.21179	0.04967	---
	$dode$ (1st order)	a_0	interpolation	---	---	---
		a_1	(B.4)	0.12869	-0.00014	---
$n_d(t_1)$	$cube$ (2nd order)	a_0	interpolation	---	---	---
		a_1	(B.4)	0.00189	0.00014	---
		a_2	(B.4)	-0.00042	-0.00019	---
	$sphere$ (2nd order)	a_0	interpolation	---	---	---
		a_1	(B.4)	-0.63659	0.05312	---
		a_2	(B.4)	0.87371	-0.04605	---
	$tetra$ (2nd order)	a_0	interpolation	---	---	---
		a_1	(B.4)	-1.23389	0.34059	---
		a_2	(B.4)	0.32734	-0.12472	---
	$dode$ (2nd order)	a_0	interpolation	---	---	---
		a_1	(B.4)	0.93445	0.00261	---
		a_2	(B.4)	-0.40795	-0.00461	---
$n_d(t_2)$	$cube$ (2nd order)	a_0	interpolation	---	---	---
		a_1	(B.5)	0.00032	1.44193	---
		a_2	(B.4)	0.00697	-0.00200	---
	$sphere$ (3rd order)	a_0	interpolation	---	---	---
		a_1	(B.5)	0.00003	3.42081	---
		a_2	(B.7)	0.83473	-0.01597	1.20313
		a_3	(B.6)	1.37123	-0.02638	1.00987
	$tetra$ (2nd order)	a_0	interpolation	---	---	---
		a_1	(B.4)	-5.98787	0.76881	---
		a_2	(B.4)	6.70625	-0.18856	---
	$dode$ (2nd order)	a_0	interpolation	---	---	---
		a_1	(B.4)	-0.50090	0.17431	---
		a_2	(B.4)	2.29997	-0.13864	---

$n_d(t_3)$	$cube$ (2nd order)	a_0	interpolation	---	---	---
		a_1	(B.5)	0.01903	1.43793	---
		a_2	(B.4)	-0.28820	-0.07318	---
	$sphere$ (3rd order)	a_0	interpolation	---	---	---
		a_1	(B.6)	0.28492	-0.00455	0.53484
		a_2	(B.7)	0.02546	-0.00049	1.31775
		a_3	(B.6)	0.09094	-0.00175	1.07971
	$tetra$ (3rd order)	a_0	interpolation	---	---	---
		a_1	(B.6)	0.92498	-0.00090	0.03166
		a_2	(B.7)	0.06273	-0.00067	0.99037
		a_3	(B.6)	0.00413	-0.00005	1.99535
	$dode$ (3rd order)	a_0	interpolation	---	---	---
		a_1	(B.6)	0.02228	-0.00041	1.66899
		a_2	(B.7)	0.64584	-0.00715	0.34057
		a_3	(B.6)	0.01444	-0.00027	2.24202
$n_d(t_4)$	$cube$ (3rd order)	a_0	interpolation	---	---	---
		a_1	(B.6)	0.99984	-0.00001	0.00007
		a_2	(B.5)	-0.10193	2.24183	---
		a_3	(B.6)	0.76145	-0.01118	0.17459
	$sphere$ (3rd order)	a_0	interpolation	---	---	---
		a_1	(B.5)	0.33940	2.06854	---
		a_2	(B.5)	-0.35689	1.97853	---
		a_3	(B.5)	0.12757	2.06392	---
	$tetra$ (3rd order)	a_0	interpolation	---	---	---
		a_1	(B.5)	0.12658	2.08949	---
		a_2	(B.5)	-0.00391	2.84664	---
		a_3	(B.5)	0.00661	2.52132	---
	$dode$	a_0	interpolation	---	---	---

	(3rd order)	a_1	(B.5)	0.04068	2.50382	---
		a_2	(B.5)	-0.02364	2.62881	---
		a_3	(B.5)	0.00002	4.35800	---
$n_d(t_5)$	$cube$ (3rd order)	a_0	interpolation	---	---	---
		a_1	(B.5)	4.01241	1.88967	---
		a_2	(B.5)	-2.29524	1.99928	---
		a_3	(B.5)	0.08310	2.74274	---
	$sphere$ (3rd order)	a_0	interpolation	---	---	---
		a_1	(B.5)	0.46857	2.51041	---
		a_2	(B.5)	-0.13296	2.70205	---
		a_3	(B.5)	0.00911	3.12548	---
	$tetra$ (3rd order)	a_0	interpolation	---	---	---
		a_1	(B.5)	0.45924	2.20206	---
		a_2	(B.5)	-0.07996	2.48306	---
		a_3	(B.5)	0.02786	2.42092	---
	$dode$ (3rd order)	a_0	interpolation	---	---	---
		a_1	(B.5)	0.76445	2.30570	---
		a_2	(B.5)	-0.24732	2.50136	---
		a_3	(B.5)	0.00532	3.22281	---
$n_d(t_6)$	$cube$ (3rd order)	a_0	interpolation	---	---	---
		a_1	(B.5)	12.94864	2.19196	---
		a_2	(B.5)	-3.60917	2.39836	---
		a_3	(B.5)	0.12933	2.97291	---
	$sphere$ (3rd order)	a_0	interpolation	---	---	---
		a_1	(B.5)	0.63611	2.79252	---
		a_2	(B.5)	-0.10325	3.03339	---
		a_3	(B.5)	0.00349	3.45233	---
	$tetra$	a_0	interpolation	---	---	---

	(3rd order)	a_1	(B.5)	0.50886	2.48535	---
		a_2	(B.5)	-0.08757	2.67659	---
		a_3	(B.5)	0.00549	2.88683	---
	$dode$ (3rd order)	a_0	interpolation	---	---	---
		a_1	(B.5)	1.05702	2.64411	---
		a_2	(B.5)	-0.18025	2.89982	---
		a_3	(B.5)	0.00412	3.44685	---
$n_d(t_7)$	$cube$ (3rd order)	a_0	interpolation	---	---	---
		a_1	(B.5)	11.23223	2.67951	---
		a_2	(B.5)	-1.63767	2.96353	---
		a_3	(B.5)	0.04908	3.43487	---
	$sphere$ (2nd order)	a_0	interpolation	---	---	---
		a_1	(B.4)	-23843.57	1281.125	---
		a_2	(B.4)	1975.254	-88.89317	---
	$tetra$ (2nd order)	a_0	interpolation	---	---	---
		a_1	(B.5)	0.00238	3.88246	---
		a_2	(B.5)	-1.52E-06	5.23338	---
	$dode$ (2nd order)	a_0	interpolation	---	---	---
		a_1	(B.5)	1.47798	2.74923	---
		a_2	(B.5)	-0.32766	2.77617	---
$n_d(t_8)$	$cube$ (1st order)	a_0	interpolation	---	---	---
		a_1	(B.4)	0	0	---
	$sphere$ (1st order)	a_0	interpolation	---	---	---
		a_1	(B.4)	0	0	---
	$tetra$ (1st order)	a_0	interpolation	---	---	---
		a_1	(B.4)	0	0	---
	$dode$ (1st order)	a_0	interpolation	---	---	---
		a_1	(B.4)	0	0	---

Appendix C

Supplementary Materials for Chapter 6

C.1 Additional MFkMC Considerations for Droplet Spreading

The sessile droplet system considered in this work consists of a fluid droplet spreading on an ideally-flat two dimensional surface. Under these conditions, the droplet will expand and contract radially with respect to the droplet center, i.e., where the droplet first contacts the surface. However, the lattice-based FB-MFkMC algorithm considered in this work restricts the positions of the droplet-phase and atmospheric-phase interface sites to a square lattice grid in order to significantly reduce computational costs. Consequently, it is necessary to implement additional rules in order to prevent any unrealistic droplet behaviour that might occur due to approximating the radial spread of the spherical cap-shaped droplet using a cartesian grid.

First of all, the rules of standard MFkMC allow for the droplet to advance into any atmospheric-phase interface site and recede from any droplet-phase interface site, regardless of the location of the neighbouring droplet sites. However, the aforementioned nature of droplet spreading necessitates that the droplet can only move radially. Consequently, in order to prevent any non-radial movement, the FB-MFkMC sessile droplet model must only allow the droplet to advance into or recede from a site if one of its neighbouring sites in the direction of the droplet center (i.e., their source sites) are on the droplet side of the interface, as illustrated in Fig. C.1a. This limitation can be expressed by modifying the FB-MFkMC rate equations as follows:

$$W_{\varepsilon,i}\left(x_{\mathcal{R}_i,\phi_i}, y_{\mathcal{R}_i,\phi_i}\right) =$$

$$\begin{cases} Eq.\ (5.4),\ \ \varepsilon = adv\ and\ \left(\left\lfloor\left(x_{\mathcal{R}_i-\lambda,\phi_i}, y_{\mathcal{R}_i-\lambda,\phi_i}\right)\right\rfloor\ or\ \left\lceil\left(x_{\mathcal{R}_i-\lambda,\phi_i}, y_{\mathcal{R}_i-\lambda,\phi_i}\right)\right\rceil\right)\ are\ droplet\ sites \\ Eq.\ (5.5),\ \ \varepsilon = rec\ and\ \left(\left\lfloor\left(x_{\mathcal{R}_i-\lambda,\phi_i}, y_{\mathcal{R}_i-\lambda,\phi_i}\right)\right\rfloor\ or\ \left\lceil\left(x_{\mathcal{R}_i-\lambda,\phi_i}, y_{\mathcal{R}_i-\lambda,\phi_i}\right)\right\rceil\right)\ are\ droplet\ sites \\ 0,\ \ \left\lfloor\left(x_{\mathcal{R}_i-\lambda,\phi_i}, y_{\mathcal{R}_i-\lambda,\phi_i}\right)\right\rfloor\ and\ \left\lceil\left(x_{\mathcal{R}_i-\lambda,\phi_i}, y_{\mathcal{R}_i-\lambda,\phi_i}\right)\right\rceil\ are\ atmosphere\ sites \end{cases} \quad (C.1)$$

where x and y are the cartesian coordinates of a given lattice site i, and the subscripts $\mathcal{R}_i$ and ϕ_i denote the radial and azimuthal polar coordinates of the same lattice site. Note that the floor and ceiling bracket notation is used to handle cases where a site $\left(x_{\mathcal{R}_i,\phi_i}, y_{\mathcal{R}_i,\phi_i}\right)$ has more than one neighbour in the direction of the droplet center (i.e., when $\phi \neq \frac{n\pi}{4}$) and therefore has multiple source sites. In these cases, the droplet is only prevented from moving if both of these sites are atmosphere sites. Another key challenge with lattice-based MFkMC is that the algorithm rules do not prevent the droplet from experiencing breakup while it is receding, as illustrated in Fig. C.1b. Although satellite drops are known to occasionally detach from the main droplet body in experiments, this behaviour is not expected to occur in practice on an ideally flat surface. This behaviour can be overcome by restricting a droplet interface site such that it is only allowed to recede if all of the sites that

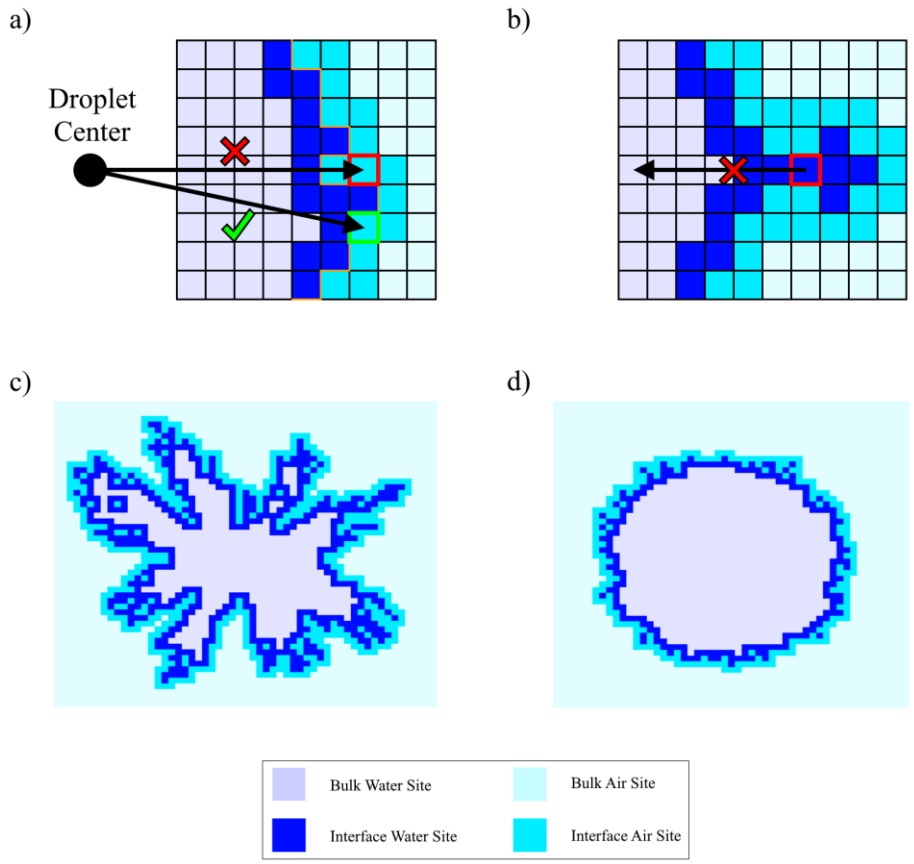

Figure C.1: a) The droplet can progress into an interface atmospheric-phase site only if one of the neighbouring sites in the direction of the droplet center is a droplet-phase site. Consequently, the droplet can proceed into the green site but not the red site; b) Since the droplet-phase interface site in red cannot recede without generating an isolated droplet, it is prohibited from doing so until all of the droplet-phase sites above it have moved into the droplet bulk via recession; c) The MFkMC algorithm on its own will typically result in large deviations in the azimuthal droplet radius due to the stochastic nature of kMC algorithms; d) The droplet is expected to have near-symmetric radial spreading on an ideally flat surface.

use it as a source site (i.e., all the sites in the opposite direction of the droplet center) are atmosphere sites, as follows:

$$W_{\varepsilon,i}\left(x_{\mathcal{R}_i,\phi_i}, y_{\mathcal{R}_i,\phi_i}\right) =$$

$$\begin{cases} Eq.\,(5.4), & \varepsilon = adv \\ Eq.\,(5.5), & \varepsilon = rec \text{ and } \left(\left\lfloor\left(x_{\mathcal{R}_i+\lambda,\phi_i}, y_{\mathcal{R}_i+\lambda,\phi_i}\right)\right\rfloor \text{ and } \left\lceil\left(x_{\mathcal{R}_i+\lambda,\phi_i}, y_{\mathcal{R}_i+\lambda,\phi_i}\right)\right\rceil \text{ are atmosphere sites }\right) \\ 0, & \varepsilon = rec \text{ and } \left(\left\lfloor\left(x_{\mathcal{R}_i+\lambda,\phi_i}, y_{\mathcal{R}_i+\lambda,\phi_i}\right)\right\rfloor \text{ or } \left\lceil\left(x_{\mathcal{R}_i+\lambda,\phi_i}, y_{\mathcal{R}_i+\lambda,\phi_i}\right)\right\rceil \text{ are droplet sites }\right) \end{cases} \quad \text{(C.2)}$$

In addition to the above challenges, the FB-MFkMC method is known to predict uneven droplet spreading on an ideally-flat surface, as depicted in Fig. C.1c. This behaviour is due to the stochastic nature of the algorithm combined with the aforementioned approximation of a droplet's radial spreading using a square lattice. However, the droplet is expected to spread quasi-uniformly, as highlighted in Fig. C.1d, in order to minimize the interfacial energies between the droplet, the solid surface, and the surrounding atmosphere. Although the droplet is expected to experience some fluctuations in its contact radius in practice, the observed deviations in the local radius of the triple contact line are significantly smaller than those predicted by the FB-MFkMC sessile droplet algorithm.[23] This issue can be overcome by adding a weighted penalty term to the rate equations as follows:

$$W_{adv,i,ord} = k' \frac{W_{tot,nc}}{\sum_i W_i} exp\left(\left(\frac{\bar{R}_{drop}+\lambda}{R_{drop,i}+\lambda}\right) sinh^{-1}\left(\frac{v_{drop,i}}{2\lambda k'}\right)\right) \tag{C.3}$$

$$W_{rec,i,ord} = k' \frac{W_{tot,nc}}{\sum_i W_i} exp\left(-\left(\frac{\bar{R}_{drop}+\lambda}{R_{drop,i}-\lambda}\right)^{-1} sinh^{-1}\left(\frac{v_{drop,i}}{2\lambda k'}\right)\right) \tag{C.4}$$

where $R_{drop,i}$ denotes the current local radius of the triple contact line at site i; $\bar{R}_{drop}$ denotes the average droplet contact radius; $v_{drop,i}$ denotes the velocity of the i^{th} droplet contact radius site; and $W_{tot,nc}$ denotes the total sum of all rates without accommodating for the unphysical droplet radius deviations. The penalty terms $\left(\frac{\bar{R}_{drop}+\lambda}{R_{drop,i}+\lambda}\right)$ in Eq. (C.3) and $\left(\frac{\bar{R}_{drop}+\lambda}{R_{drop,i}-\lambda}\right)^{-1}$ in Eq. (C.4) are defined such that it encourages interface sites to recede/advance to a distance λ from the average contact radius $\bar{R}_{drop}$ while simultaneously penalizing sites from advancing/receding too far away from $\bar{R}_{drop}$. As a result, this term will not affect the average spreading behaviour of the droplet but rather will ensure that the fluctuations in the droplet radius remain small. Furthermore, the weighting term $\frac{W_{tot,nc}}{\sum_i W_i}$ in Eqs. (C.3)-(C.4) is added to prevent the penalty term from affecting the calculation of the MFkMC time shown in Eq. (2). Although the penalty term is necessary to prevent unrealistic droplet spreading, its inclusion will significantly affect the temporal evolution of the system without the weighting term. The objective of the penalty term is just to redistribute the probabilities $W_{adv,i}$ and $W_{rec,i}$ so that the FB-MFkMC algorithm does not overly select droplet spreading along a given direction, as observed in Fig. C.1c, and therefore it is not intended to affect the cumulative sum of the interfacial rates, $\sum_i W_i$. Consequently, the weighing term is necessary to ensure that the unrealistic droplet spreading is eliminated without distorting the system temporal information. These restriction equations can be combined into a single equation to capture the rate of the droplet interface movement, as listed in Eqs. (6.1)-(6.3).

C.2 FB-MFkMC Algorithm for Sessile Droplet Spread on a Smooth Surface

The complete FB-MFkMC algorithm to capture sessile droplet spread on an ideally-flat surface can be described as follows:

1. Initialize the system to capture the moment that the droplet contacts the solid surface, as illustrated in Fig. C.2a, by marking the droplet and atmosphere interface sites according to Fig. C.2b. Calculate the initial properties of each interface site i as follows:
    a. Calculate the radial distance $R_{drop,i}$ between the i^{th} site and the droplet center. Note that for atmosphere-phase interface sites, the reported value of the radius should be the location of the nearest droplet interface site (i.e., $R_{drop,i} - \lambda$) as discussed above.
    b. Determine the state of the site's nearest neighbours located at $R_{drop,i} \pm \lambda$ in the direction of the droplet center (i.e., determine whether the sites located at $\left\lfloor \left(x_{\mathcal{R}_i \pm \lambda, \phi_i}, y_{\mathcal{R}_i \pm \lambda, \phi_i}\right) \right\rfloor$ and $\left\lceil \left(x_{\mathcal{R}_i \pm \lambda, \phi_i}, y_{\mathcal{R}_i \pm \lambda, \phi_i}\right) \right\rceil$ are droplet or atmosphere sites). Set the initial velocities for each interface site based on the droplet horizontal impact velocity, $v_{drop,0}$.
    c. Calculate $W_{tot,nc}$ and determine the initial advancing and receding rates for each site according to Eqs. (6.1)-(6.3).
    d. Calculate the average contact radius of the droplet $\bar{R}_{drop}$.
    e. Set the initial time to $t = 0$ s.
2. Determine the time $t + \delta t$ when the droplet interface will move using a randomly generated number ξ_{cont} according to Eq. (3.11). Calculate $W_{tot,nc}$ and update any time-dependent rate equations according to Eqs. (6.1)-(6.3).
3. Apply MC sampling to select a random interface site according to Eq. (3.12). If the selected site is an atmosphere site, then the droplet will advance into this site and change it into a droplet interface site. If the selected site is a droplet site, then the droplet will recede from this site and it will change into an atmosphere interface site. Calculate the new rate for the selected site according to Eqs. (6.1)-(6.3).
4. Check to see if any interface sites have become bulk sites on either side of the interface due to the executed event. Remove any newly formed bulk sites.
5. Check to see if any new interface sites are created from former bulk phase sites on either side of the interface due to the executed event (i.e. formerly blank sites on the surface lattice that now border the interface). Initialize the velocity of the new interface sites based on the velocity of the selected site, calculate $R_{drop,i}$, determine the state of the site's nearest neighbours located at $R_{drop,i} \pm \lambda$ in the

direction of the droplet center, and calculate the movement rates $W_{adv,i}$ and $W_{rec,i}$ for each new interface site according to Eqs. (6.1)-(6.3).

6. Update $\bar{R}_{drop}$ and $W_{tot,nc}$.
7. Repeat Steps 2-6 until the final time $t = t_f$ has been reached.

C.3 Previous Derivation Attempts of the Viscous Damping Force Expression

Due to the lack of mechanistic models for the viscous damping force within the literature, a few different attempts were made to derive these analytical expressions. These attempts were based on integrating the viscous stress tensor across the interface between the droplet and the solid surface as follows:[47]

$$\vec{F}_v(\mathcal{R},\mathfrak{z},t) = \int_0^{2\pi}\int_0^{R_{drop}} \left[-\mu\left(\frac{\delta u_{\mathfrak{z}}(\mathcal{R},\mathfrak{z},t)}{\delta r} + \frac{\delta u_{\mathcal{R}}(\mathcal{R},\mathfrak{z},t)}{\delta_{\mathfrak{z}}}\right)\hat{\boldsymbol{e}}_{\boldsymbol{r}} - 2\mu\frac{\delta u_{\mathfrak{z}}(\mathcal{R},\mathfrak{z},t)}{\delta_{\mathfrak{z}}}\hat{\boldsymbol{e}}_{\mathfrak{z}}\right] dr\, d\phi \qquad \text{(C.5)}$$

where $u_{\mathcal{R}}$ and $u_{\mathfrak{z}}$ are the radial and axial components of the fluid velocity inside the droplet in cylindrical coordinates. In order to solve for the viscous damping force, it is necessary to know the exact velocity profiles inside the droplet at any given point in space and time, and consequently each of the attempted methods utilized different approaches to calculate these parameters. In the first attempt, analytical solutions were found for the

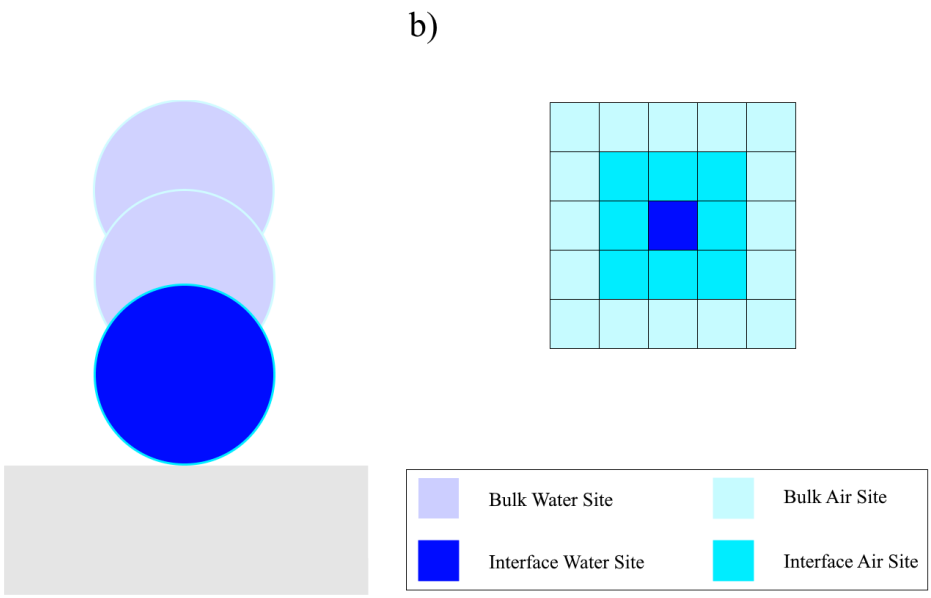

Figure C.2: a) Side view of the droplet when it first impacts the solid surface; b) Initial configuration on the FB-MFkMC lattice for the moment when the droplet first impacts the solid surface

velocity profiles inside a droplet under Stokes flow conditions. These expressions were based on evaporating droplet studies previously reported within the literature, and further details concerning the derivation and assembly of these equations can be found therewithin.[50,51] Note that the aforementioned works within the literature defined their velocity profiles with respect to the evaporation flux experienced by the droplets within their systems. However, the sessile droplet system considered in this work was assumed to undergo negligible evaporation. Instead, the methods reported within the literature were reversed to derive the velocity profiles as a function of the triple contact line velocity. The derived velocity profiles were subsequently coupled with Eq. (C.5) and integrated analytically to calculate the viscous damping force. However, this approach was derived under the assumption that the inertial forces were negligible (i.e. Stokes flow), which is known to be inaccurate for the scenarios considered in this work. Furthermore, the calculated velocity profiles predicted an infinite viscous force acting on the droplet system even under Stokes flow assumptions, which casts doubt on the overall accuracy of the derived velocity profiles themselves. In order to overcome these shortcomings, the velocity profiles inside the droplet were determined by solving the Navier-Stokes equations numerically using CFD-based techniques in COMSOL Multiphysics 5.6. These CFD models were designed to approximate the velocity profiles inside the droplet based on the velocity of the triple contact line, the droplet radius, and the droplet contact angle. The derived velocity profiles were subsequently used to approximate the viscous damping force by numerically solving Eq. (C.5). However, this approach predicted viscous damping forces that were orders of magnitude too small and therefore it did not adequately accommodate for the damping behaviour observed in the studied droplet systems.

Appendix D

Supplementary Material for Chapter 7

When the droplet is advancing or receding overtop of an inter-pillar gap (i.e., when the droplet interface can be represented using a VLV), it will experience different forces compared to when the droplet is advancing or receding on top of the pillars, and consequently it is necessary to modify the force balance to accommodate for these differences. Most notably, liquid droplets are considered to have a contact angle of 180° with air ($\theta_{e,i} = \pi$),[234] where $\theta_{e,i}$ is a binary variable that captures the variability of the contact angle between the VLV and TCL for a given site i as follows:

$$\theta_{e,i} = \begin{cases} \theta_e, & i\ is\ TCL \\ \pi, & i\ is\ VLV \end{cases} \tag{D.1}$$

Accordingly, the capillary force for the VLV can be written as follows:

$$\vec{F}_{cap,VLV}(\boldsymbol{x}, t) = 2\pi R_{drop}(\boldsymbol{x}, t)\gamma_{lv}\big(-1 - cos\,\theta\,(\boldsymbol{x}, t)\big) \tag{D.2}$$

In addition to the capillary force, the droplet is additionally expected to experience pinning along the edges of the pillars when it is receding. While pinned, the droplet interface will remain fixed in place at the transition point between VLV and TCL until the droplet local contact angle exceeds its receding contact angle θ_{rec}, depending on whether the droplet is advancing or receding.[235,236] Although pinning is often associated with the local contact angle, it can also be considered as an energy barrier that must be overcome for de-pinning to occur.[149] In this proposed model, contact line pinning was accommodated in a similar manner to the capillary rise model discussed in Chapter 5 by factoring in an energy barrier angle based on the changes in the droplet height into the capillary force term, as follows:

$$\vec{F}_{cap,pin}(\boldsymbol{x}, t) = 2\pi R_{drop}(\boldsymbol{x}, t)\gamma_{lv}\big(cos\,\theta_e - sin\big(\beta_s(\boldsymbol{x}, t) - \theta(\boldsymbol{x}, t)\big)\big) \tag{D.3}$$

Where $\vec{F}_{cap,pin}(\boldsymbol{x}, t)$ depicts the capillary force when the droplet is pinned while receding at a position $\boldsymbol{x}$ and time t, and $\beta_s(\boldsymbol{x}, t)$ denote the energy barrier angle for receding interfaces at $\boldsymbol{x}$ and t, and can be calculated using Eq. (2.7).

In addition to the above-mentioned changes to the capillary force, the heterogeneous nature of Cassie wetting on an SHS is additionally expected to affect the viscous damping force of a spreading sessile droplet. When a droplet spreads on a solid surface, its viscous force is considered to be proportional to the contact between the droplet fluid and the solid surface due to the derivation of viscous damping for triple contact interface systems.[56] As per its derivation, the viscous damping force term emerges from the boundary condition

of the viscous stress term acting on the fluid/solid interface. Similarly, the boundary condition of the viscous stress term acting on the fluid/atmosphere interface can be re-arranged to yield the capillary force term. Consequently, when a droplet undergoes Cassie wetting on an SHS, the viscous and capillary forces will contribute differently to the overall force balance compared to an ideally flat surface due to the increase in liquid/atmosphere interfaces. This was accommodated within the force balance as follows:

$$\vec{F}_{cap,cw}(\boldsymbol{x},t) = 2\pi(2 - w_{SHS})R_{drop}(\boldsymbol{x},t)\gamma_{lv}\big(\cos\theta_e - \cos\theta\,(\boldsymbol{x},t)\big) \tag{D.4}$$

$$\vec{F}_{v,cw}(\boldsymbol{x},t) = -2\pi w_{SHS} a\mu v_{drop}(\boldsymbol{x},t)V_{Rs}\mathscr{b}^{1/Oh}Oh^{w} \tag{D.5}$$

Where $\vec{F}_{cap,cw}(\boldsymbol{x},t)$ and $\vec{F}_{v,cw}(\boldsymbol{x},t)$ denote the modifications to the capillary and viscous damping forces due to the change in liquid/atmosphere and liquid/solid interfaces from the ideally flat surface case, and w_{SHS} denotes the ratio of the underside of the droplet in contact with the solid surface pillar tops, as listed in Eq. (7.4).

The full force balance for an SHS pillar spreading on an SHS can be determined by combining Eqs. (D.1)-(D.5) with Eq. (6.13) as follows:

$$\mathcal{F}_i \frac{d^2R_{drop,i}}{dt^2} =$$

$$\begin{cases} 2\pi(2 - w_{SHS})R_{drop,i}\gamma_{lv}\big(\cos\theta_e - \sin\big(\beta_{s,i} - \theta_i\big)\big) - 16.1439\pi w_{SHS}\mu v_{drop,i}V_{Rs}0.9975\frac{1}{\sigma_h}Oh^{-0.8314}, & \textit{pillar edge and receding, TCL site} \\ 2\pi(2 - w_{SHS})R_{drop,i}\gamma_{lv}\big(-1 - \sin\big(\beta_{s,i} - \theta_i\big)\big) - 16.1439\pi w_{SHS}\mu v_{drop,i}V_{Rs}0.9975\frac{1}{\sigma_h}Oh^{-0.8314}, & \textit{pillar edge and receding, VLV site} \\ 2\pi(2 - w_{SHS})R_{drop,i}\gamma_{lv}(\cos\theta_e - \cos\theta_i) - 16.1439\pi w_{SHS}\mu v_{drop,i}V_{Rs}0.9975\frac{1}{\sigma_h}Oh^{-0.8314}, & \textit{otherwise, TCL site} \\ 2\pi(2 - w_{SHS})R_{drop,i}\gamma_{lv}(-1 - \cos\theta_i) - 16.1439\pi w_{SHS}\mu v_{drop,i}V_{Rs}0.9975\frac{1}{\sigma_h}Oh^{-0.8314}, & \textit{otherwise, VLV site} \end{cases} \tag{D.6}$$

These equations can be subsequently re-arranged in terms of velocity, as illustrated in Eq. (7.5), and substituted into the SHS-MFkMC rate equations to accommodate for Cassie wetting on an SHS.

In addition to modifying the force balance, it is also necessary to modify the SHS-MFkMC rate equations themselves to prevent unrealistic droplet spreading behaviour from occurring due to the general assumptions of MFkMC. When the SHS-MFkMC algorithm is used to capture Cassie sessile droplet spread on an SHS, this method can frequently encounter phantom pinning when the droplet switches from advancing to receding or vise versa. This phantom pinning does not occur due to any expected pinning phenomena as discussed previously, but rather it occurs due to a discrepancy between the predicted velocities of the droplet interface sites and those of the atmosphere interface sites along the edges of pillars. Recall that the rates for each MFkMC interface site for a given phase is defined as the probability that said phase will recede from the given site and get replaced by the adjacent phase. When this definition is applied to two adjacent droplet and atmosphere interface sites for a sessile droplet model, they provide a complementary pair of rate events that describe the probability that the same section of the droplet interface will either advance or recede, as illustrated in Fig.

D.1a. Consequently, it is expected that the velocities associated with the droplet interface site $v_{drop,di}$ and the atmosphere interface site $v_{drop,ai}$ will be approximately the same at the same point along the interface, as both velocities are supposed to represent the velocity of the triple contact line segment itself. However, when a droplet stops advancing and begins to recede, the VLV interface sites will slow down and reverse speed at a significantly faster rate than the TCL sites on top of the pillars due to the difference in the intrinsic contact angles (i.e., because water and air have a contact angle of 180°, the VLV sites experience a much stronger deceleration from the larger capillary force compared to the TCL sites). As a result, this unexpected pinning creates an impossible jump discontinuity in the interface velocity when the droplet triple interface is located along a pillar edge, as demonstrated in Fig. D.1b. In this case, the droplet interface site predicts that the interface

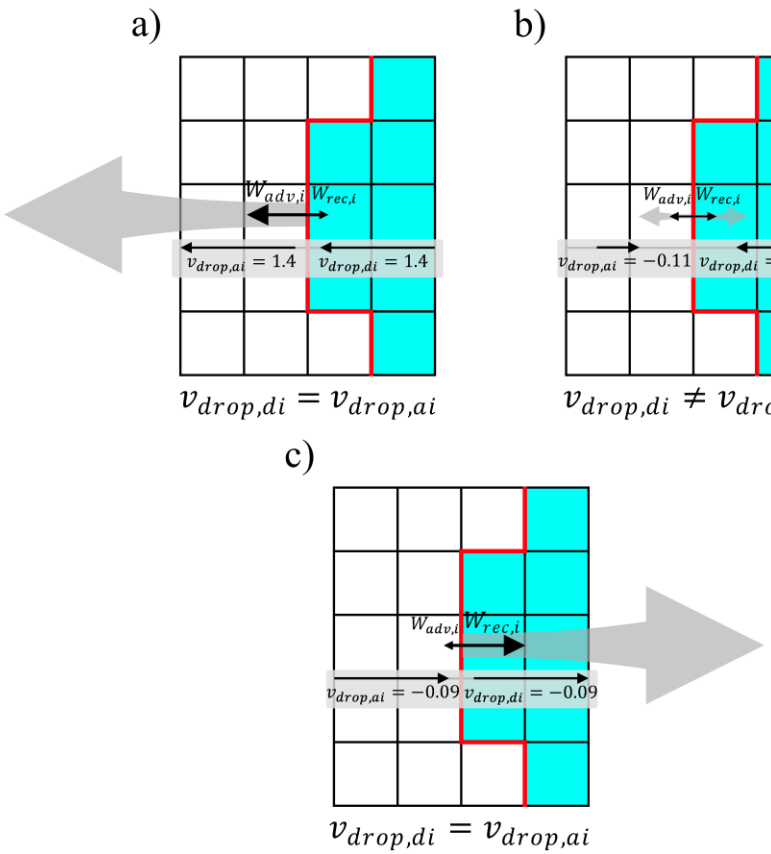

Figure D.1: a) When a droplet is advancing or receding via SHS-MFkMC, the interface velocities predicted by the sites on either side of an interface are typically the same on a smooth surface. b) phantom pinning occurs when a droplet changes direction on the edge of a pillar. This phantom pinning is caused by a jump discontinuity in the predicted interface velocity as calculated by the sites on either side of the interface. c) The jump discontinuity can be eliminated by averaging the two predicted interface velocities, therefore eliminating the jump discontinuity.

has a positive velocity, and therefore should advance. On the other hand, the atmosphere interface site predicts that the interface has a negative velocity, and therefore it should recede. However, it is the atmosphere interface sites that handle droplet advancing events whereas it is the droplet interface sites that handle droplet receding events, and as a result the probability of either event occurring is small. Consequently, the droplet remains pinned on the edges of these pillars and will not advance or recede for a very long time. In order to prevent this issue from occurring, the SHS-MFkMC algorithm was modified with an extra averaging condition, where the velocities of the droplet and atmosphere interface sites are averaged if the interface is on the edge of a pillar. This averaging condition is denoted according to Eqs. (7.6)-(7.7). In particular, Eq. (7.6) calculates the velocity of a TCL interface site as if it was a VLV interface site, and vice versa. Subsequently, Eq. (7.7) averages the expected interface velocity calculated using Eq. (7.5) with the modified velocity calculated using Eq. (7.6) if the interface is on a pillar edge, and otherwise sets the velocity to be the expected velocity (i.e., Eq. (7.5)) if the interface is not on a pillar edge. This velocity averaging approach is expected to eliminate the phantom pinning from occurring when the droplet interface changes direction as it will replace the jump discontinuity in the interface velocity with a single average value that changes based on the underlying physics on both sides of the interface, as illustrated in Fig. D.1c. However, this approach will not affect any other interface sites, where the velocities across the interface are expected to be identical.